

**DEVELOPMENT OF CORROSION
RESISTANT COATINGS FOR
AEROSPACE ALUMINIUM ALLOY
AA2024-T3**

Thesis

Submitted in partial fulfilment of the requirements for the degree of

DOCTOR OF PHILOSOPHY

By

PRAKASHAIAH B G



**DEPARTMENT OF CHEMISTRY
NATIONAL INSTITUTE OF TECHNOLOGY KARNATAKA
SURATHKAL, MANGALORE-575025**

JULY, 2019

D E C L A R A T I O N

by the Ph.D. Research Scholar

I hereby *declare* that the Research Thesis entitled “**Development of corrosion resistant coatings for aerospace aluminium alloy AA2024-T3**” which is being submitted to the **National Institute of Technology Karnataka, Surathkal** in partial fulfilment of the requirements for the award of the Degree of **Doctor of Philosophy in Chemistry** is a *bonafide report of the research work carried out by me*. The material contained in this Research Thesis has not been submitted to any University or Institution for the award of any degree.

Prakashaiah B G

(145026CY14P02)

Department of Chemistry

Place: **NITK - Surathkal**

Date: **25/07/2019**

C E R T I F I C A T E

This is to *certify* that the Research Thesis entitled “**Development of corrosion resistant coatings for aerospace aluminium alloy AA2024-T3**” submitted by **Mr. Prakashaiah B G** (Register Number: 145026CY14P02) as the record of the research work carried out by him, is *accepted as the Research Thesis submission* in partial fulfilment of the requirements for the award of degree of **Doctor of Philosophy**.

Dr. A. Nityananda Shetty

Dr. B. E. Amitha Rani

Research Guides

Chairman - DRPC

AKNOWLEDGEMENT

I wish to express my gratitude to my research supervisors Dr. B. E. Amitha Rani, Principal Scientist, Surface Engineering Division, CSIR-National Aerospace Laboratories, Bangalore, and Dr. A. Nityananda Shetty, Professor, Department of Chemistry, National Institute of Technology Karnataka, Surathkal, for having given me an opportunity to carry out research on corrosion studies under their guidance, with their contributions of time and ideas to make my research experience productive and stimulating. I remain ever grateful to my supervisors, who have made this thesis possible.

I would like to thank the members to RPAC, Dr. Jagannath Nayak, Professor, Department of Metallurgical and Materials Engineering, National Institute of Technology Karnataka, Surathkal, and Dr. D. Krishna Bhat, Professor, Department of Chemistry, National Institute of Technology Karnataka, Surathkal, for their valuable suggestions and inputs throughout this work.

I am obliged to the Directors (Former and Present), National Institute of Technology Karnataka, Surathkal and Heads (Former and Present) of Chemistry Department, National Institute of Technology Karnataka, Surathkal, for the opportunities provided to pursue my Ph.D in NITK. I am thankful to all the faculty of Department of Chemistry, National Institute of Technology Karnataka for their support and help.

I am grateful to Mr. Jitendra J Jadhav, Director, CSIR-National Aerospace Laboratories, Bangalore and Dr. Harish C Barshilia, Head, Surface Engineering Division, CSIR-National Aerospace Laboratories, Bangalore, for providing me the required experimental facilities of the department and CSIR-NAL for the institute fellowship. I am thankful to Dr. J. N. Balaraju, Surface Engineering Division, CSIR-National Aerospace Laboratories, Bangalore, for Salt Spray facility.

It is a pleasure to thank my fellow research scholars, Mr. D. R. Vinay Kumar, Dr. Praveen Kumar, Dr. G. Prasad, Mr. Aranganathan Viswanathan, Mr. M. Gururaj Acharya.

Lastly and most importantly, I wish to thank my parents, B. G. Shivamurthaiah and Shakunthamma, all my family members and friends for their cooperation, care and love. To them I dedicate this thesis

Prakashaiah. B G

ABSTRACT

Five organic molecules, namely, (E)-2-(2-hydroxybenzylidene)hydrazinecarbothioamide (2-MHC), (E)-2-(2,4-dihydroxybenzylidene)hydrazinecarbothioamide (2,4-DHC), (E)-2-(3,4-dihydroxybenzylidene)hydrazinecarbothioamide (3,4-DHC), (E)-2-(2,3,4-trihydroxybenzylidene)hydrazinecarbothioamide (2,3,4-THC) and Bis[[3,4-Dihydroxyphenylmethylene]-carbonothioic dihydrazide] (3,4-DCT) were synthesized and their corrosion inhibition actions on 2024-T3 aluminium alloy were studied in 3.5% NaCl solution. The synthesized inhibitors were found to provide corrosion protection on AA2024-T3 by forming adsorbed layers on the alloy surface. To explore the possibility of using the synthesised inhibitors for corrosion detection applications, the initial studies were carried out on all the five inhibitors. It was found that only 3,4-DHC qualified in the tests, by imparting the colour change at the corrosion sites.

From the five inhibitors studied for their inhibition action, the three most effective inhibitors were employed for coatings applications. An oxide layer was created on the aluminium alloy by anodizing the surface in 10 wt % sulphuric acid and was sealed with the three inhibitors, namely, 2,3,4-THC, 3,4-DHC and 3,4-DCT to evaluate their role in the enhancement of corrosion resistance. The order of the corrosion protection efficiencies of the anodised layer is: Ox < Ox-2,3,4-THC < Ox-3,4-DHC < Ox-3,4-DCT. The effect of corrosion inhibitor addition on the anticorrosion properties of primer coatings on aluminium alloy 2024-T3 was investigated. 3,4-DCT, 3,4-DHC and 2,3,4-THC were supplemented to epoxy primer. The addition of 2,4-DCT and 3,4-DHC to primer coating, offered good barrier properties. The addition of 2,3,4-THC provided active corrosion protection along with good barrier properties. The synthesised inhibitors 3,4-DHC and 2,3,4-THC were added to the hybrid sol to study their effect on the corrosion protection efficiency of the sol-gel coating. Addition of corrosion inhibitors to the coating enhanced the corrosion protection abilities of sol-gel coatings. The order of the corrosion protection efficiencies is: Uncoated < sol-gel coated < sol-gel + 2,3,4-THC coated < sol-gel + 3,4-DHC coated.

Keywords: AA2024-T3, Inhibitors, Anodizing layer, Primer coating, Sol-gel Coating.

CONTENTS

Page No

CHAPTER 1 INTRODUCTION

1.1	INTRODUCTION	1
1.2	ELECTROCHEMICAL THEORY OF CORROSION	1
1.3	TYPES OF CORROSION	2
1.3.1	Uniform attack	2
1.3.2	Galvanic corrosion	2
1.3.3	Crevice corrosion	2
1.3.4	Pitting corrosion	3
1.3.5	Intergranular corrosion	3
1.3.6	Selective leaching	3
1.3.7	Erosion corrosion	3
1.3.8	Stress corrosion	4
1.4	METHODS OF CORROSION PREVENTION	4
1.4.1	Modifying the environmental conditions	4
1.4.2	Alloying	4
1.4.3	Surface coating	5
1.4.3.1	<i>Metallic coating</i>	5
1.4.3.2	<i>Anodizing</i>	6

1.4.4	Cathodic protection	7
1.5	CORROSION INHIBITORS	8
1.5.1	Classifications of inhibitors	8
1.5.1.1	<i>Inorganic inhibitors</i>	8
1.5.1.2	<i>Organic inhibitors</i>	11
1.6	DETERMINATION OF CORROSION RATE	13
1.6.1	DC Electrochemical monitoring techniques	14
1.6.1.1	<i>Tafel extrapolation method</i>	14
1.6.2	AC Electrochemical monitoring techniques	16
1.6.2.1	<i>Electrochemical Impedance Spectroscopy (EIS)</i>	16
1.7	AEROSPACE MATERIAL	19
1.8	LITERATURE REVIEW	20
1.8.1	Corrosion behaviour of AA2024-T3	20
1.8.2	Organic compounds for the corrosion inhibition of AA2024-T3 in sodium chloride solution	21
1.8.3	Anodizing process used for corrosion protection of AA2024-T3	23
1.8.4	Replacement of strontium chromate from the primer coating	25
1.8.5	Addition of inhibitors to the sol-gel coatings	27
1.9	SCOPE AND OBJECTIVES	29

1.9.1	Scope	29
1.9.2	Objectives	32
CHAPTER 2 MATERIAL AND METHODS		
2.1	SAMPLE PREPARATION	33
2.2	SYNTHESIS OF CORROSION INHIBITORS	33
2.2.1	(E)-2-(2-hydroxybenzylidene)hydrazinecarbothioamide (2-MHC)	33
2.2.2	Synthesis of (E)-2-(2,4-dihydroxybenzylidene)hydrazinecarbothioamide (2,4-DHC)	33
2.2.3	Synthesis of (E)-2-(3,4-dihydroxybenzylidene)hydrazinecarbothioamide (3,4-DHC)	34
2.2.4	Synthesis of (E)-2-(2,3,4-trihydroxybenzylidene)hydrazinecarbothioamide (2,3,4-THC)	34
2.2.5	Synthesis of Bis [[3,4-Dihydroxyphenylmethylene] carbonothioicdihydrazide] (3,4-DCT)	35
2.3	CORROSION MEDIA	36
2.4	ELECTROCHEMICAL STUDIES	36
2.5	SURFACE CHARACTERIZATIONS	36
2.6	X-RAY PHOTOELECTRON SPECTROSCOPY	37
2.7	SUBSTRATE PREPARATION FOR COATING APPLICATIONS	37
2.8	ANODIZING OF AA2024-T3 SURFACE	37
2.9	PRIMER COATED SUBSTRATE PREPARATION	38

2.10	PREPARATION OF THE SOL-GEL COATINGS	38
2.11	SOL-GEL COATING METHOD	38
2.12	CHARACTERIZATION OF COATED SUBSTRATE	39
2.13	ACCELERATED SALT SPRAY TEST	39

CHAPTER 3 RESULTS AND DISCUSSION

3.1	INHIBITION EFFECT OF CORROSION INHIBITOR FOR ALUMINIUM ALLOY 2024-T3 IN 3.5 % NaCl SOLUTION	40
3.1.1	Characterization of the inhibitors	40
	3.1.1.1 NMR and elemental analysis	40
3.1.2	Electrochemical impedance spectroscopy (EIS) studies	44
3.1.3	Potentiodynamic polarization studies	58
3.1.4	Surface morphology	60
3.1.5	X-ray photoelectron spectroscopy	63
3.2	(E)-2-(3,4-DIHYDROXYBENZILIDINE)HYDRAZINECARBO THIOAMIDE (3,4-DHC) AS AN INHIBITOR FOR CORROSION DETECTION	68
3.2.1	Detection of pitting corrosion on AA2024-T3 in 3.5 % NaCl solution	68
3.2.2	Corrosion detection mechanism of the synthesized inhibitor	72
3.3	EFFECT OF INHIBITOR INCORPORATION IN OXIDE LAYER ON THE CORROSION BEHAVIOUR OF ALUMINIUM ALLOY 2024-T3	74

3.3.1	Open circuit potential measurement	74
3.3.2	Electrochemical impedance spectroscopy	75
3.3.3	Potentiodynamic polarization studies	87
3.3.4	Surface characterization of anodized AA2024-T3	89
3.3.5	Salt spray analysis	91
3.4	EFFECT OF INHIBITORS ON THE ANTICORROSION PROPERTIES OF EPOXY PRIMER COATING ON ALUMINIUM ALLOY 2024-T3	94
3.4.1	Electrochemical impedance spectroscopy studies	94
3.4.2	Corrosion studies on artificial defect area	100
3.4.3	Salt spray analysis	106
3.5	EFFECT OF INHIBITION ON THE ANTICORROSION PROPERTIES OF SOL-GEL COATING ON ALUMINIUM ALLOY AA2024-T3	113
3.5.1	Electrochemical impedance spectroscopy	113
3.5.2	Surface characterization after corrosion	123
3.5.3	Adhesion strength of the sol-gel coating	125
 CHAPTER 4 SUMMARY AND CONCLUSION		
4.1	SUMMARY	126
4.2	CONCLUSIONS	127
4.3	SCOPE FOR FUTURE WORK	128

REFERENCES	129
RESEARCH PUBLICATIONS	139
CURRICULUM VITAE	

LIST OF FIGURES

Fig. No.	Caption	Page No.
1.1	Potentiodynamic polarization diagram: electrochemical behaviour of a metal in a solution (a) in the presence of the anodic inhibitor (b) in the absence of the inhibitor.	9
1.2	Potentiodynamic polarization diagram: electrochemical behaviour of the metal in a solution (a) in the presence of a cathodic inhibitor (b) in the absence of an inhibitor.	10
1.3	Theoretical polarization diagrams: electrochemical behaviour of a metal in a solution containing (a) a mixed inhibitor; (b) no inhibitor.	12
1.4	Tafel plots.	15
1.5	Nyquist plot.	18
1.6	Bode plots.	18
1.7	Coating layers.	32
2.1	The synthesis scheme of inhibitors.	35
2.2	The synthesis scheme of 3,4-DCT.	35
3.1	¹ H-NMR spectra of 2,4-DHC.	40
3.2	¹ H-NMR spectra of 3,4-DHC.	41
3.3	¹ H-NMR spectra of 2,3,4-THC.	42

3.4	¹ H-NMR spectra of 3,4-DCT.	43
3.5 (a)	Nyquist plots for the corrosion of AA2024-T3 at different immersion times in 3.5 % NaCl solution.	45
3.5 (b)	Nyquist plots for the corrosion of AA2024-T3 at different immersion times in 3.5 % NaCl solution in the presence of 1 mM of 2-MHC.	45
3.5 (c)	Nyquist plots for the corrosion of AA2024-T3 at different immersion times in 3.5 % NaCl solution in the presence of 1 mM of 2,4-DHC.	46
3.5 (d)	Nyquist plots for the corrosion of AA2024-T3 at different immersion times in 3.5 % NaCl solution in the presence 1 mM of 2,3,4-THC.	46
3.5 (e)	Nyquist plots for the corrosion of AA2024-T3 at different immersion times in 3.5 % NaCl solution in the presence of 1 mM of 3,4-DHC.	47
3.5 (f)	Nyquist plots for the corrosion of AA2024-T3 at different immersion times in 3.5 % NaCl solution in the presence of 1 mM of 3,4-DCT.	47
3.6	Equivalent circuits used for fitting the experimental EIS spectra of AA2024-T3 in 3.5 % NaCl solution, (a) in the absence of inhibitors; (b) in the presence of inhibitors 2-MHC, 2,4-DHC and 2,3,4-THC (c) in the presence of 3,4-DHC (d) in the presence of 3,4-DCT.	48
3.7	Variation of polarization resistance of AA2024-T3 with immersion time in 3.5 % NaCl solution in the absence and in the presence of inhibitors.	51

3.8	Variation of inhibition efficiency of inhibitors on AA2024-T3 with immersion time in 3.5 % NaCl solution.	51
3.9 (a)	Bode plots for the corrosion of AA2024-T3 at different immersion times in 3.5 % NaCl solution.	53
3.9 (b)	Bode plots for the corrosion of AA2024-T3 at different immersion times in 3.5 % NaCl solution in the presence of 1 mM of 2-MHC.	53
3.9 (c)	Bode plots for the corrosion of AA2024-T3 at different immersion times in 3.5 % NaCl solution in the presence of 1 mM of 2,4-DHC.	54
3.9 (d)	Bode plots for the corrosion of AA2024-T3 at different immersion times in 3.5 % NaCl solution in the presence of 1 mM of 2,3,4-THC.	54
3.9 (e)	Bode plots for the corrosion of AA2024-T3 at different immersion times in 3.5 % NaCl solution in the presence of 1 mM of 3,4-DHC.	55
3.9 (f)	Bode plots for the corrosion of AA2024-T3 at different immersion times in 3.5 % NaCl solution in the presence of 1 mM of 3,4-DCT.	55
3.10	Potentiodynamic polarization curves for the corrosion of AA2024-T3 in 3.5 % NaCl solution in the absence and in the presence of inhibitors after 2 h immersion.	59
3.11	Potentiodynamic polarization curves for the corrosion of AA2024-T3 in 3.5 % NaCl solution in the absence and in the presence of inhibitors after 24 h immersion.	59
3.12	FESEM images and EDX spectra of AA2024-T3 alloy surface after 7 days of immersion in 3.5 % NaCl solution.	60

3.13	FESEM images of AA2024-T3 alloy surface after 7 days of immersion in: (a) (b) 3.5 % NaCl solution + 2-MHC, (c) (d) 3.5 % NaCl solution + 2,4-DHC, (e) (f) 3.5 % NaCl solution + 2,3,4-THC.	62
3.14	FESEM images of AA2024-T3 alloy surface after 7 days of immersion in: (a) (b) 3.5 % NaCl solution + 3,4-DHC, (c) (d) 3.5 % NaCl solution + 3,4-DCT.	63
3.15	XPS survey spectrum of AA2024-T3 surfaces after 7 days of immersion in 3.5 % NaCl solution in the absence and in the presence of the inhibitors.	64
3.16	The magnified individual peaks in the XPS spectra of AA2024-T3 surfaces after 7 days of immersion in 3.5 % NaCl solution in the absence and in the presence of inhibitors (a) O1s, (b) Al2p (c) N1s (d) C1s ionization peaks.	65
3.17	The deconvulated O 1s ionization peaks of AA2024-T3 surface immersed for 7 days in 3.5 % NaCl solution.	66
3.18	The deconvulated O 1s ionization peaks of AA2024-T3 surface immersed for 7 days in 3.5 % NaCl solution in the presence of 3,4-DHC.	67
3.19	Optical images of the AA2024-T3 surface after immersion in 3.5 % NaCl solution in the presence of 3,4-DHC at different exposure times (50 x).	68
3.20	Images of the pitting area after 7 days of immersion in 3.5 % NaCl solution in the presence of 3,4-DHC (a), (b) Optical images (200x), (c) (d) FESEM images	69

3.21	FESEM image and EDX spectra of the alloy surface AA2024-T3 after 7 days of immersion in 3.5 % NaCl solution in the presence of 3,4-DHC.	70
3.22	Photographic images of AA2024-T3 after 7 days of immersion in (a) 3.5% NaCl solution (b) 3.5% NaCl solution in the presence of 3,4-DHC.	71
3.23	The UV-vis absorption spectra of 3,4-DHC in the presence of different concentrations of Al ³⁺ ions.	72
3.24	¹ H-NMR spectra of 3,4-DHC and 3,4-DHC + Al ³⁺ .	73
3.25	The sensing mechanism of the inhibitor for Al ³⁺ .	73
3.26	Variation of open circuit potential of the anodized AA2024-T3 with immersion time in 3.5 % NaCl solution.	75
3.27 (a)	Nyquist plots for the corrosion of anodized AA2024-T3 at different immersion times in 3.5 % NaCl solution.	76
3.27 (b)	Nyquist plots for the corrosion of anodized AA2024-T3 with 2,3,4- THC sealing (Ox-2,3,4-THC) at different immersion times in 3.5 % NaCl solution.	76
3.27 (c)	Nyquist plots for the corrosion of anodized AA2024-T3 with 3,4-DHC sealing (Ox-3,4-DHC) at different immersion times in 3.5 % NaCl solution.	77
3.27 (d)	Nyquist plots for the corrosion of anodized AA2024-T3 with 3,4-DCT sealing (Ox-3,4-DCT) at different immersion times in 3.5 % NaCl solution.	77
3.28	Equivalent circuits used to fit experimental data for the corrosion of anodised and inhibitor incorporated alloy surface.	80

3.29	Variation of porous oxide layer resistance of the anodized AA2024-T3 with immersion time in the absence and in the presence of the inhibitors in 3.5 % NaCl solution.	82
3.30	Variation of inner barrier oxide layer resistance of the anodized AA2024-T3 with immersion time in the absence and in the presence of the inhibitors in 3.5 % NaCl solution.	82
3.31	Variation of polarization resistance of the anodized AA2024-T3 with immersion time in the absence and in the presence of the inhibitors in 3.5 % NaCl solution.	83
3.32	Bode plots for the corrosion of anodized AA2024-T3 in 3.5 % NaCl solution at different immersion times.	84
3.33 (a)	Bode plots for the corrosion of anodized AA2024-T3 sealed with 2,3,4-THC in 3.5 % NaCl solution at different immersion times.	85
3.33 (b)	Bode plots for the corrosion of anodized AA2024-T3 sealed with 2,3,4-DHC in 3.5 % NaCl solution at different immersion times.	86
3.33 (c)	Bode plots for the corrosion of anodized AA2024-T3 sealed with 3,4-DCT in 3.5 % NaCl solution at different immersion times.	86
3.34	Potentiodynamic polarization curves for the corrosion of anodized AA2024-T3 without and with sealing after 336 h of immersion in 3.5 % NaCl solution.	88
3.35	Photographic images of as prepared samples.	90
3.36	FESEM images of as prepared samples (a) Ox, (b) Ox-2,3,4-THC, (c) Ox-3,4-DHC, (d) Ox-3,4-DCT (e) Cross sectional image.	91
3.37	Photographs of Ox and Ox-HWS coupons after salt spray exposures.	92

3.38	Photographs of Ox-2,3,4-THC, Ox-3,4-DHC, and Ox-3,4-DCT coupons after salt spray exposures.	93
3.39	Bode plots for the corrosion of AA2024-T3 alloy surface coated with primer coating in 3.5 % NaCl solution at different immersion times.	95
3.40 (a)	Bode plots for the corrosion of AA2024-T3 alloy surface coated with 3,4-DCT doped primer coating in 3.5 % NaCl solution at different immersion times.	96
3.40 (b)	Bode plots for the corrosion of AA2024-T3 alloy surface coated with 3,4-DHC doped primer coating in 3.5 % NaCl solution at different immersion times.	96
3.40 (c)	Bode plots for the corrosion of AA2024-T3 alloy surface coated with 2,3,4-THC doped primer coating in 3.5 % NaCl solution at different immersion times.	97
3.41	Equivalent circuits used to fit the experimental impedance data of primer coating, over the exposure periods (a) up to 168 h, (b) above 216 h up to 384 h and (c) above 456 h up to 504 h.	98
3.42	Plots of variation of polarization resistance (R_p) with time for the primer coating and inhibitor doped primer coatings.	100
3.43	Bode plots for the primer coating with artificial defect at different immersion times, in 3.5 % NaCl solution.	101
3.44 (a)	Bode plots for the primer coating doped with 3,4-DCT, with scribes at different immersion times, in 3.5 % NaCl solution.	101
3.44 (b)	Bode plots for the primer coating doped with 3,4-DHC, with scribes at different immersion times, in 3.5 % NaCl solution.	102

3.44 (c)	Bode plots for the primer coating doped with 2,3,4-THC, with scribes at different immersion times, in 3.5 % NaCl solution.	102
3.45	Equivalent circuit used to fit the experimental impedance data for the coatings with scribe (a) blank, 3,4-DCT doped and 3,4-DHC doped primer coating over an exposure period of 168 h; and 2,3,4-DHC doped primer coating up to an exposure period of 48 h, (b) 2,3,4-DHC doped primer coating for an exposure period above 48 h up to 168 h.	104
3.46	Variation of polarization resistance (R_p) with time for the primer coating in the absence and in the presence of inhibitors with scribe.	106
3.47	Images of (a) primer coating (b) primer coating with scribe after salt spray tests for 1000 h.	107
3.48	Schematic representation of blister formation and corrosion of the alloy surface under primer coating.	107
3.49	FE-SEM cross sectional images of the primer coating after salt spray test for 1000 h.	108
3.50	Images of (a) 3,4-DCT doped primer coating, (b) 3,4-DHC doped primer coating and (c) 2,3,4-THC doped primer coating after salt spray tests for 1000 h.	109
3.51	Images of (a) 3,4-DCT doped primer coating, (b) 3,4-DHC doped primer coating and (c) 2,3,4-THC doped primer coating, with scribes after salt spray tests for 1000 h.	110
3.52	FE-SEM images of the scribe area taken after 1000 h salt spray test, (a) primer coating, (b) 3,4-DCT doped primer coating, (c)	111

	3,4-DHC doped primer coating, (d) 2,3,4-THC doped primer coating.	
3.53	FE-SEM cross sectional images of (a) 3,4-DCT doped primer coating, (b) 3,4-DHC doped primer coating, (c) 2,3,4-THC doped primer coating, post salt spray analysis.	112
3.54	Nyquist plots for the corrosion of surface treated AA2024-T3 (uncoated) at different immersion times in 3.5 % NaCl solution.	113
3.55 (a)	Nyquist plots for the corrosion of sol-gel coated AA2024-T3 at different immersion times in 3.5 % NaCl solution.	115
3.55 (b)	Nyquist plots for the corrosion of 2,3,4- THC doped sol-gel coated AA2024-T3 at different immersion times in 3.5 % NaCl solution.	115
3.55 (c)	Nyquist plots for the corrosion of 3,4- DHC doped sol-gel coated AA2024-T3 at different immersion times in 3.5 % NaCl solution.	116
3.56	Equivalent circuit used to fit the experimental data for the sol-gel coating in the absence and in the presence of the inhibitors.	117
3.57	Variation of polarization resistance of the uncoated and sol-gel coated AA2024-T3 with immersion time in 3.5 % NaCl solution.	120
3.58 (a)	Bode magnitude and phase angle plots for the corrosion of uncoated AA 2024-T3 aluminium alloy at different immersion times in 3.5 % NaCl solution.	121
3.58 (b)	Bode magnitude and phase angle plots for the corrosion of sol-gel coated AA 2024-T3 aluminium alloy at different immersion times in 3.5 % NaCl solution.	122

3.58 (c)	Bode magnitude and phase angle plots for the corrosion of 2,3,4-THC doped sol-gel coated AA 2024-T3 aluminium alloy at different immersion times in 3.5 % NaCl solution.	122
3.58 (d)	Bode magnitude and phase angle plots for the corrosion of 3,4-DHC doped sol-gel coated AA 2024-T3 aluminium alloy at different immersion times in 3.5 % NaCl solution.	123
3.59	Photographs of (a) Sol-gel coated, (b) Sol-gel + 2,3,4-THC coated, (c) Sol-gel + 3,4-DHC coated sample surfaces after 168 h of immersion in 3.5 % NaCl solution.	124
3.60	FESEM images of (a) Sol-gel coated, (b) 2,3,4-THC doped sol-gel coated and (c) 3,4-DHC doped sol-gel coated sample surfaces after 168 h of immersion in 3.5 % NaCl solution.	125
3.61	Optical images of the different sol-gel coated samples after the cross-hatch test according to ASTM D3359: (a) Sol-gel coating, (b) 2,3,4-THC doped sol-gel coating, (c) 3,4-DHC doped sol-gel coating.	125

LIST OF TABLES

Table No.	Captions	Page No.
1.1	The composition of AA2024 T3 alloy	19
1.2	Corrosion inhibitors for AA2024-T3.	22
1.3	Anodizing process used for corrosion protection of AA2024-T3.	24
1.4	Addition of inhibitors to the primer coatings for corrosion protection of AA2024-T3.	26
1.5	Addition of inhibitors to the sol-gel coatings for corrosion protection of AA2024-T3.	27
3.1	The electrochemical impedance parameters for the corrosion of AA2024-T3 in the absence and in the presence of inhibitors in 3.5 % NaCl solution at different immersion times.	56
3.2	EDX results of the elemental composition (atomic %) of AA2024-T3 surface after 7 days of immersion in 3.5 % NaCl solution in the absence and in the presence of inhibitors.	61
3.3	XPS results of the elemental composition (atomic %) of AA2024-T3 surfaces after 7 days immersion in 3.5 % NaCl solution in the absence and in the presence of inhibitors.	67
3.4	EDX results of the elemental composition (atomic %) of AA2024-T3 surface after 7 days of immersion in 3.5 % NaCl solution in the presence and in the absence of 3,4-DHC.	71
3.5	The electrochemical impedance parameters for the corrosion of anodised and inhibitor sealed anodised AA2024-T3 alloy surface in 3.5 % NaCl solution at different immersion time.	81

3.6	Potentiodynamic polarization data for the corrosion of anodized AA2024-T3 without and with sealing in 3.5 % NaCl solution, after 336 h of immersion.	89
3.7	Impedance parameters for the corrosion of AA2024-T3 alloy coated with the primer coating in the absence and in the presence of inhibitors.	99
3.8	Impedance parameters for the corrosion of AA2024-T3 alloy coated with the primer coating in the absence and in the presence of inhibitors with scribe.	105
3.9	Impedance parameters for the corrosion of different sol-gel coated AA2024-T3 alloy in 3.5 % NaCl solution.	119

LIST OF ABBREVIATIONS

2-MHC	:	(E)-2-(2-hydroxybenzylidene)hydrazinecarbothioamide
2,4-DHC	:	(E)-2-(2,4-dihydroxybenzylidene)hydrazinecarbothioamide
3,4-DHC	:	(E)-2-(3,4-dihydroxybenzylidene)hydrazinecarbothioamide
2,3,4-THC	:	(E)-2-(2,3,4-trihydroxybenzylidene)hydrazinecarbothioamide
2-MBT	:	2-mercaptobenzothiazole
¹H-NMR	:	Proto nuclear magnetic resonance
AC	:	Alternating current
ASTM	:	American Society for Testing and Materials
BTA	:	2,5-dimercapto benzotriazolate
CAA	:	Chromic acid anodizing
CPE	:	Constant phase element
DC	:	Direct current
DEDTC	:	N,N- diethyldithiocarbamate
DEODMES	:	Diethoxydimethylsilane
DMTD	:	1,3,4 thiadiazolate
EDX	:	Energy dispersive X-ray analysis
EIS	:	Electrochemical impedance spectroscopy
FESEM	:	Field emission scanning electron microscope
GPTMS	:	3-glycidoxypropyl –trimethoxysilane

HF	: High frequency
LF	: Low frequency
MPTMS	: Methacryloxypropyltrimethoxysilane
MTEOS	: Methyltriethoxysilane
OCP	: Open circuit potential
PhTMS	: Phenyltrimethoxysilane
SCE	: Saturated calomel electrode
TEOS	: Tetraethylorthosilicate
TMOS	: Tetramethoxysilane
TPOZ	: Zirconium (IV) propoxide
XPS	: X-ray photoelectron spectrometer

LIST OF SYMBOLS

ω	: Angular frequency
$Z(\omega)$: Angular frequency dependent impedance
β_a	: Anodic slope
R_b	: Barrier layer resistance
Q_b	: Barrier layer capacitance
C_{dl}	: Capacitance of the electrical double layer
β_c	: Cathodic slope
R_{ct}	: Charge transfer resistance
Q_{dl}	: Constant phase element associated with electrical double layer : capacitance
Q_f	: Constant phase element associated with inhibitor thin film capacitance
Q_{ox}	: Constant phase element associated with oxide layer capacitance
i_{corr}	: Corrosion current density
E_{corr}	: Corrosion potential
n	: CPE exponent
D	: Density of the corroding species,
R_f	: Film resistance
ω_{max}	: Frequency at which the imaginary component of the impedance is : maximum
Z''	: Imaginary impedance
Z	: Impedance
η	: Inhibition efficiency
Q_{in}	: Inhibitor layer capacitance
R_{in}	: Inhibitor layer resistance
θ	: Phase angle

E_{pit}	:	Pitting potential
R_p	:	Polarization resistance in the absence of the inhibitor
$R_{p(inh)}$:	Polarization resistance in the presence of the inhibitor
R_{po}	:	Porous oxide layer resistance
Q_{po}	:	Porous oxide layer capacitance
Q_{coat}	:	Primer coating capacitance
R_{coat}	:	Primer coating resistance
R_{ox}	:	Oxide layer resistance
R_{sol}	:	Solution resistance
W	:	Warburg resistance

1.1 INTRODUCTION

Corrosion is the destructive result of a series of chemical or electrochemical reactions between a metal or metal alloy and its environment. In nature, metals are present in minerals and the amount of energy required to extract the metals from their minerals are liberated during the corrosion reaction. Corrosion reaction returns the metal to its minerals, from which the metal is extracted. Corrosion is defined in different ways, but the usual interpretation of the term is “an attack on a metallic material by the reaction with its environment”.

1.2 ELECTROCHEMICAL THEORY OF CORROSION

The electrochemical reaction on the metal or metal alloy surface can be used to explain the corrosion problems of the metals and its alloy. These are often called wet corrosion since aqueous medium or moist air is required for the corrosion to take place. According to electrochemical theory, corrosion takes place due to the formation of anodic and cathodic sites on the same metal surface or when two different metals are in contact with each other in a conducting medium.

The anodic oxidation reaction is of the general form:

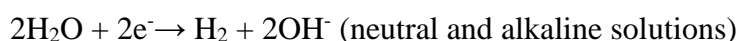
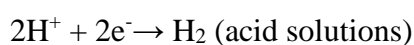
At the anode



The anodic reaction is responsible for the dissolution of the metal into metal ions. There are many cathodic reactions, depending upon the environment. These cathodic reactions are either one or many as shown below.

At the cathode

1. Evolution of hydrogen from acid or neutral solutions:



2. Reduction of dissolved oxygen in acid or neutral solutions:



1.3 TYPES OF CORROSION

Corrosion is classified into eight types, which are briefly explained in the following sections.

1.3.1 Uniform attack

Uniform corrosion or general corrosion, is the attack of metal and its alloy at essentially the same rate, uniformly distributed over the entire exposed surface of the metal. This type of corrosion is possible when the metal surface and the corrosion environment are both uniform throughout.

1.3.2 Galvanic corrosion

Galvanic corrosion tends to occur when dissimilar conducting materials are connected electrically and exposed to an electrolyte. The following fundamental requirements, therefore, have to be met for galvanic corrosion:

1. Dissimilar metals.
2. Electrical contact between the dissimilar conducting materials (can be direct contact or a secondary connection such as electrical path).
3. Electrolyte (the corrosive medium) in contact with the dissimilar conducting materials.

1.3.3 Crevice corrosion

Crevice corrosion is a form of localized corrosive attack. It occurs at narrow openings or spaces between two metal surfaces or between metals and nonmetal surfaces. A concentration cell forms with the crevice being depleted of oxygen. This differential aeration between the crevice (microenvironment) and the external surface

(bulk environment) gives the crevice an anodic character. This can contribute to a highly corrosive condition in the crevice. Some examples of crevices are flanges, deposits, washers, rolled tube ends, threaded joints, etc.

1.3.4 Pitting corrosion

Pitting corrosion is a localized, accelerated form of corrosion by which cavities or "holes" are produced in the material. Pitting is considered to be more dangerous than uniform corrosion damage because it is more difficult to detect, predict and design against. Pitting corrosion can produce pits with their mouth open (uncovered) or covered with a semi-permeable membrane of corrosion products.

1.3.5 Intergranular corrosion

Intergranular corrosion consists of a localized attack, where a narrow path is corroded out preferentially along grain boundaries of a metal. This type of corrosion may have extreme effects on mechanical properties, resulting in a loss of strength and ductility.

1.3.6 Selective leaching

It is also known as parting or dealloying, is the selective removal of one element from an alloy leaving an altered residual structure. The most common example is the selective removal of zinc in the brass alloy (dezincification).

1.3.7 Erosion corrosion

Erosion corrosion is the corrosion of a specimen in a corrosive medium in the presence of an abrading action on the metal surface. The abrading action may be due to the movement of the medium or of the metal. Under the abrading action, the protective film on the metal surface is damaged and the surface is under continued attack by the medium.

1.3.8 Stress corrosion

Stress corrosion cracking (SCC) refers to the cracking caused by the simultaneous presence of tensile stress and a corrosive environment. The stressed region acts as the anode and develops fine cracks which migrate in the metal in a direction perpendicular to the direction of the stress applied.

1.4 METHODS OF CORROSION PREVENTION

1.4.1 Modifying the environmental conditions

The corrosion rate can be reduced by modifying the environment by the following methods

- (a) Deaeration: The presence of increased amounts of oxygen is harmful since it increases the corrosion rate. Deaeration aims at the removal of dissolved oxygen. Dissolved oxygen can be removed by deaeration or by adding some chemical substances like sodium carbonate.
- (b) Dehumidification: In this method, moisture from the air is removed by lowering the relative humidity of the surrounding air. This can be achieved by adding silica gel which can absorb moisture preferentially on its surface.
- (c) Inhibitors: Here, some chemical substances are added to the corrosive environment in small quantities. These inhibitors substantially reduce the rate of corrosion.

1.4.2 Alloying

Both corrosion resistance and strength of many metals can be improved by alloying, e-g. Stainless steels containing chromium produce a coherent oxide film which protects the steel from further attack. The other non-corrosive alloys are German silver, Aluminium bronze, nickel bronze, duralumin, etc.

1.4.3 Surface coating

Corrosion of metal surfaces is a common phenomenon. To protect a metal surface from corrosion, the contact between the metal and the corrosive environment is to be cut off. This is done by coating the surface of the metal with a continuous, non-porous material, inert to the corrosive atmosphere. Such a coating is referred to as surface coating or protective coating. In addition to protective action, such coatings also give a decorative effect and reduce wear and tear.

Objectives of coating surfaces

- Corrosion prevention.
- Enhancement of wear and scratch resistance
- Increasing the hardness
- Insulating electrically/thermally
- Imparting decorative colour

1.4.3.1 *Metallic coatings*

Surfacing coatings made up of metals are known as metallic coatings. These coatings separate the base metal from the corrosive environment and also function as an effective barrier for the protection of base metals. The metal which is coated upon is known as the base metal. The metal applied as a coating is referred to as coat metal. The different methods used for metal coating are:

- i) Hot dipping
 - Galvanization
 - Tinning
- ii) Metal spraying
- iii) Cladding.
- iv) Cementation
 - Sherardizing – Cementation with zinc powder is called sherardizing.
 - Chromizing - Cementation with 55% chromium powder & 45% alumina is called chromizing

- Calorizing – Cementation with Aluminium and alumina powder is called calorizing
- v) Electroplating or electrodeposition.

1.4.3.2 Anodizing

Anodizing is an electrochemical oxidation process for producing a stable Aluminium oxide layer on the surface of Aluminium and its alloys. Anodizing process is carried out in a wide variety of the electrolytes by applying AC, DC or a combination of both. In order to produce a stable Aluminium oxide layer, the Aluminium or its alloys must be used as anode and another appropriate metal or alloy as a cathode.

Advantages of the anodizing process

- Increases the corrosion resistance
- Increases in surface hardness and abrasion resistance
- Provides better adhesion for paint primers
- Provides electrical and thermal insulation
- Porous layer allows for colouring and sealing of the coating

There are three principal types of aluminium anodizing processes. Type I is chromic acid anodizing, Type II is sulphuric acid anodizing and Type III is sulphuric acid hard anodizing (sulphuric acid alone or with additives). The other less frequently used anodizing processes, use sulphuric acid with phosphoric acid, tartaric acid, oxalic acid, sulfophthalic acid sulfosalicylic acid. The acidic anodizing process produces the porous oxide film on the surface. These pores in the oxide film permit the corrosive ions and water to reach the substrate surface and initiate the corrosion. The porous oxide layer is sealed by prolonged immersion in hot water. In this process oxide is converted into its hydrate form, the resulted swelling reduces the porosity of the layer.

The change in properties produced by sealing are basically

- Reduction of primer coating adhesion
- Reduction in hardness and abrasion resistance
- Reduction of thermal resistance

- Reduction of the retention of dyes
- Increases in the corrosion resistance
- Increases in impedance of the oxide film

1.4.4 Cathodic protection

The principle involved in cathodic protection is to force the metal to behave like a cathode. Since there will not be any anodic area on the metal, corrosion does not occur. There are two methods of cathodic protection.

- (a) Sacrificial anodic method.
- (b) Impressed voltage method

(a) Sacrificial anodic method

In this technique, a more active metal is connected to the metal structure to be protected so that all the corrosion is concentrated at the more active metal and thus saving the metal structure from corrosion. This method is used for the protection of sea-going vessels such as ships and boats. Sheets of zinc or magnesium are hung around the hull of the ship. Zinc and magnesium being anodic to iron get corroded. Since they are sacrificed in the process of saving iron (anode), they are called sacrificial anodes. The corroded sacrificial anode is replaced by a fresh one when consumed completely. Important applications of sacrificial anodic protection are as follows:

- Protection from soil corrosion of underground cables and pipelines.
- Magnesium sheets are inserted into domestic water boilers to prevent the formation of rust.

(b) Impressed voltage method

In this method, an impressed current is applied in the opposite direction to nullify the corrosion current and converting the corroding metal from anode to cathode. This can be accomplished by applying a sufficient amount of direct current from a battery to an anode buried in the soil and connected to the corroding metal structure which is to be protected. The anode is in a backfill (composed of gypsum) so as to increase the

electrical contact with the soil. Since in this method, current from an external source is impressed on the system, this is called the impressed current method.

1.5 CORROSION INHIBITORS

Inhibitors are substances or mixtures that in low concentrations and in aggressive environments inhibit /prevent or minimize the corrosion.

1.5.1 Classification of Inhibitors

The corrosion inhibitors can be chemicals either synthetic or natural and could be classified based on

- The chemical nature - organic or inorganic;
- The mechanism of action - anodic inhibitor, cathodic inhibitor or mixed inhibitor and
- As oxidants or non-oxidants.

In general, the inorganic inhibitors have cathodic or anodic protection, while organic inhibitors exhibit both cathodic and anodic protection and the protective action is by film adsorption.

1.5.1.1 Inorganic inhibitors

Anodic inhibitors

Anodic inhibitor (also called passivation inhibitors) reduce the rate of anodic reaction, by forming an adsorbed film on the metal, and supporting the natural passivation of the metal surface, thereby blocking the anode from coming in contact with the corrosion medium. In general, the inhibitors react with the corrosion product formed, resulting in a cohesive and insoluble film on the metal surface.

Figure 1.1 shows a potentiodynamic polarization diagram of metal in a solution in the presence of an anodic inhibitor. The anodic reaction is affected by the corrosion inhibitor and the corrosion potential of the metal is shifted to a more positive value. As well, the value of the current decreases in the presence of the corrosion inhibitor.

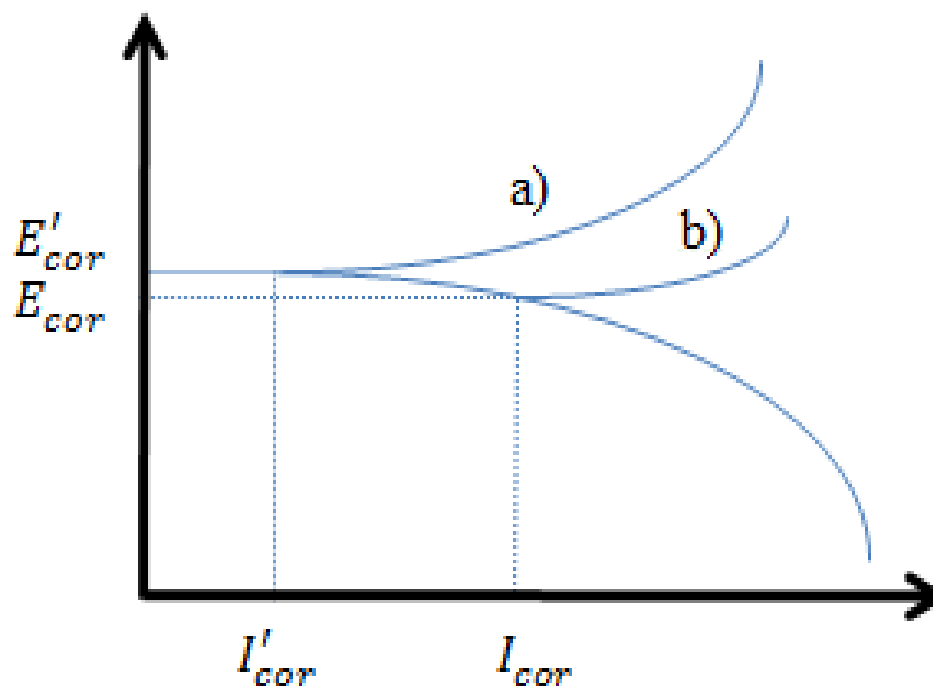


Figure 1.1 Potentiodynamic polarization diagram: electrochemical behaviour of a metal in a solution (a) in the presence of the anodic inhibitor (b) in the absence of the inhibitor.

The anodic inhibitors react with metallic ions (M^{n+}) produced on the anode, forming generally, insoluble products which are deposited on the metal surface as insoluble films. When the concentrations of the inhibitor become sufficiently high, the cathodic current density at the primary passivation potential becomes higher than the critical anodic current density, shifting the potential to a noble side, and, consequently, the metal is passivated.

For the anodic inhibition effect, it is very important that the inhibitor concentrations should be high enough in the solution. The addition of an inappropriate amount of the inhibitor results in incomplete coverage of the anodic surface by the protective film, leaving sites of the metal exposed, thus causing localized corrosion. Some examples of anodic inorganic inhibitors are nitrates, molybdates, chromates, phosphates, hydroxides and silicates.

Cathodic inhibitors:

During the corrosion process, the cathodic corrosion inhibitors prevent/retard the cathodic reaction on the metal surface. These inhibitors may themselves adhere on the cathode surface forming a surface film. They may also have metal ions capable of forming product due to alkalinity and thus producing insoluble compounds that precipitate selectively on cathodic sites, forming a compact and adherent film over the cathodic surface, restricting the diffusion of reducible species in these areas. Figure 1.2 depicts a polarization curve of the metal in the solution containing a cathodic inhibitor. When the cathodic reaction is affected the corrosion potential is shifted to a more negative value.

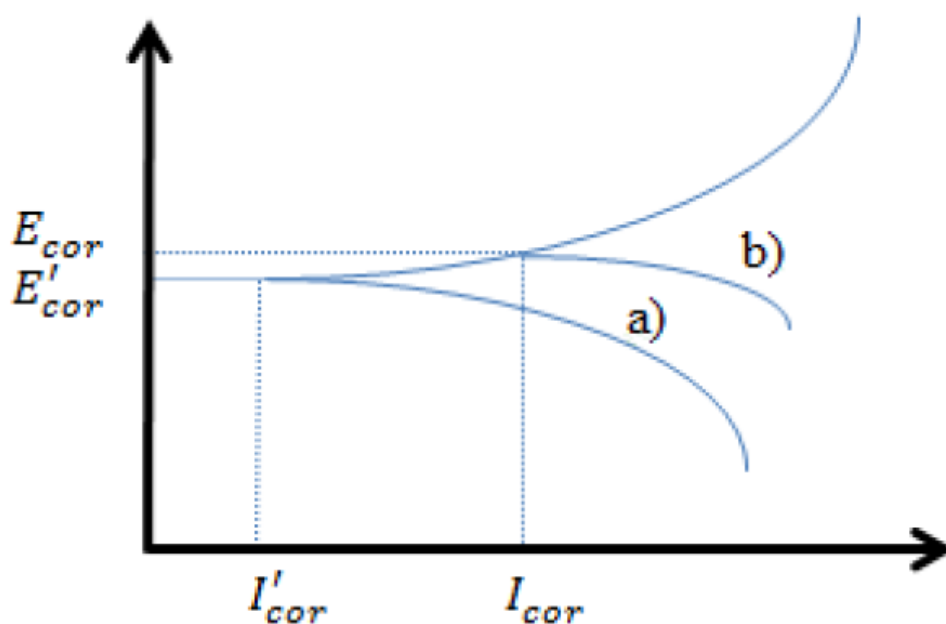


Figure 1.2 Potentiodynamic polarization diagram: electrochemical behaviour of the metal in a solution (a) in the presence of a cathodic inhibitor (b) in the absence of an inhibitor.

The cathodic inhibitors form barrier layers over the metal surface, covering it. Thus, they restrict the metal contact with the environment, even if immersed completely, preventing the occurrence of the cathodic reaction and in turn preventing the corrosion reaction. Even incomplete coverage of the cathodic region results in a

decrease in the corrosion rate. Therefore, they are considerably more secure than an anodic inhibitor.

Some examples of inorganic cathodic inhibitors are the ions of the magnesium, zinc, and nickel that reacts with the hydroxyl (OH^-) of the water forming the insoluble hydroxides as ($\text{Mg}(\text{OH})_2$, $\text{Zn}(\text{OH})_2$, $\text{Ni}(\text{OH})_2$) which are deposited on the cathodic site of the metal surface, protecting it. Also can be cited polyphosphates, phosphonates, tannins, lignins and calcium salts as examples that present the same inhibition mechanism. A similar inhibitory mechanism can be witnessed in hard waters, due to the effect of the magnesium or calcium bicarbonate present in it. When temporary hard water flows over the metal it promotes the nucleation of carbonates and forms the precipitates on the metal surface. These precipitates cover the cathodic area and protect the metal from corrosion. The oxides and salts of antimony, arsenic, and bismuth, which deposit the respective metals on the cathode region and retard the liberation of hydrogen as the cathodic reaction, due to their higher hydrogen overvoltage.

1.5.1.2 Organic inhibitor

Organic compounds used as inhibitors, occasionally, act as cathodic, anodic or mixed inhibitors. As a general rule, they act through a process of surface adsorption, forming a surface film. Naturally, molecules exhibiting a strong affinity for metal surfaces show good inhibition efficiency. These inhibitors build up a protective hydrophobic film of adsorbed molecules on the metal surface, which provides a barrier to the dissolution of the metal in the electrolyte. They must be soluble or dispersible in the medium surrounding the metal.

Figure 1.3, shows theoretical polarization curves, showing the effect of the organic inhibitor. The addition of the inhibitor does not alter the corrosion potential, but the current decreases from I_{corr} to I'_{corr} .

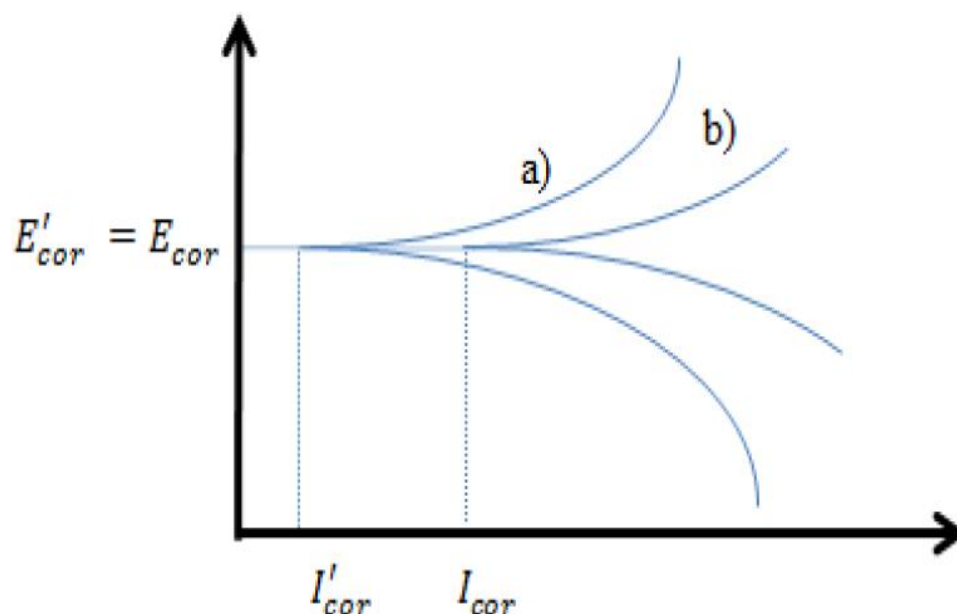


Figure 1.3 Theoretical polarization diagrams: electrochemical behaviour of a metal in a solution containing (a) a mixed inhibitor; (b) no inhibitor.

The efficiency of an organic inhibitor depends on:

- Chemical structure, like the size of the organic molecule.
- Aromaticity and/or conjugated bonding, and the carbon chain length.
- Type and number of bonding atoms or groups in the molecule (either π or σ).
- Nature and the charges of the metal surface, and mode of adsorption.
- The ability of a layer to become compact or cross-linked.
- Capability to form a complex with the metal atom/ions.
- Type of the electrolyte solution, and solubility of the inhibitor in the environment.

The efficiency of these organic corrosion inhibitors is related to the presence of polar functional groups with S, O or N atoms, heterocyclic moieties and pi electrons in the compounds. The polar functional site is usually regarded as the reaction center for the establishment of the adsorption process. The organic inhibitor that contains oxygen, nitrogen and/or sulfur is adsorbed on the metallic surface blocking the active corrosion sites. As the metal surface covered is proportional to the inhibitor concentration, the concentration of the inhibitor in the medium is critical.

Some examples of organic inhibitors are amines, urea, mercaptobenzothiazole (MBT), triazole derivatives, aldehydes, heterocyclic nitrogen compounds, sulfur-containing compounds, acetylenic compounds, ascorbic acid, succinic acid, tryptamine, caffeine and extracts of natural substances. Some inhibitors act in the vapor phase (volatile corrosion inhibitors). The examples are dicioexilamonio benzoate, diisopropyl ammonium nitrite or benzoate, ethanolamine benzoate or carbonate and the combination of urea and sodium nitrite.

1.6 DETERMINATION OF CORROSION RATE

The electrochemical techniques can be used to study the rate of corrosion reactions and their mechanisms. Unlike weight loss or gravimetric methods, electrochemical methods are quicker to determine and analyze the electrochemical properties. Electrochemical corrosion testing is a simple and fast way to determine the corrosion resistance of metals in a particular environment. The mixed potential theory forms the basis for two electrochemical methods used to determine the corrosion rate. These are Tafel extrapolation and linear polarization techniques. According to a mixed potential theory, any electrochemical reaction can be divided into two or more partial oxidation and reduction reactions. Electrochemical techniques can be used to measure the kinetics of the electrochemical process, in a specific environment and also to measure the oxidizing power of the environment.

The corrosion rate can be electrochemically determined by a number of methods that measure the corrosion current density, which is converted to corrosion rate using Faraday's laws,

$$\text{Corrosion rate (mm y}^{-1}\text{)} = \frac{0.00327 (E.W) i_{\text{corr}}}{D} \quad (1.1)$$

where i_{corr} = corrosion current density, $\mu\text{A cm}^{-2}$

$E.W$ = equivalent weight of the corroding species (atomic wt. / oxidation number)

D = density of the corroding species, g cm^{-3}

The electrochemical corrosion measurement techniques are classified into two types:

- a) DC Electrochemical monitoring techniques
- b) AC Electrochemical monitoring techniques.

1.6.1 DC Electrochemical monitoring techniques

DC electrochemical monitoring techniques are potentiodynamic corrosion testing techniques. These methods involve changing the potential of the working electrode and measuring the current produced as a function of time or potential. When an electrode is polarized, it can cause current to flow via electrochemical reactions that occur at the electrode surfaces. The amount of current generated is controlled by the kinetics of the reactions and the diffusion of reactants both towards and away from the electrode. DC polarization technique utilizes a typical three-electrode system. The metal sample is used as the working electrode. Inert metal like platinum constitutes the auxiliary electrode. The potential of the working electrode is measured with respect to a reference electrode.

1.6.1.1 Tafel extrapolation method

The Tafel extrapolation method can be used to determine the corrosion rate of metal when metallic dissolution is under activation control. This technique uses data obtained from cathodic and anodic polarization measurements. The Tafel plots are generated by applying a potential of 300 mV in both the positive and negative directions from the open circuit potential against a reference electrode. The current density is measured and usually plotted on a logarithmic scale. As shown in Figure 1.4, a typical Tafel plot consists of anodic and cathodic branches and the intersection of these branches can be projected on the X and Y axes to give the values of i_{corr} and E_{corr} , by drawing tangents to the anodic and cathodic regions of the Tafel curve. The corrosion potential (E_{corr}) or the open-circuit potential is the potential a metal will assume when placed in contact with a conductive medium. The value of the corrosion potential is determined by the potentials of half-reactions of the corrosion process. E_{corr} is a characteristic of the corroding system. The Tafel plot provides a direct measure of the corrosion current, which can be used to calculate the corrosion rate.

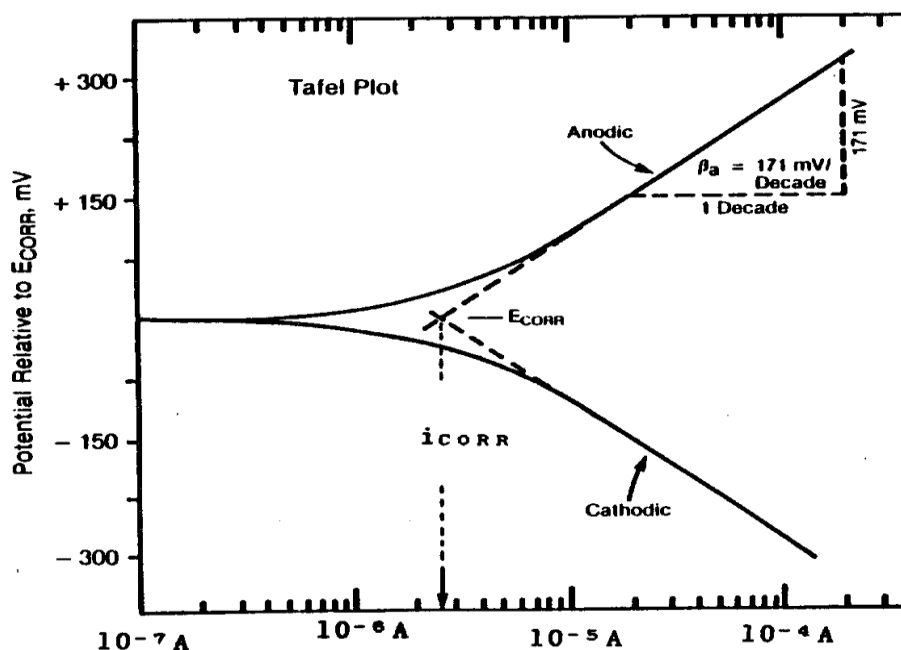


Figure 1.4 Tafel plots.

The slopes of the linear portions of this plot are called the Tafel constants, which are used to calculate the polarization resistance using the Stern-Geary equation.

$$R_p = \frac{B}{i_{corr}} \quad (1.2)$$

$$B = \frac{\beta_a \beta_c}{2.303(\beta_a + \beta_c)} \quad (1.3)$$

where β_a & β_c are the Tafel proportionality constants for the anodic and the cathodic reactions, respectively. The corrosion rate is calculated using equation 1, explained in the earlier section.

Advantages of Tafel extrapolation method

- It is possible to measure very low corrosion rates.
- It can be used for continuous monitoring the corrosion rate of a system.
- This technique is more rapid than conventional weight loss methods.
- The Tafel constants β_a and β_c can be used with linear polarization data.

Disadvantages of Tafel extrapolation method

- The test electrode can be polarized only a limited number of times because some degree of electrode surface roughening occurs with each polarization.
- The method can be applied only to systems containing one reduction process since Tafel region is distorted if more than one reduction process occurs.
- The system gets disturbed due to the polarization of material under test by several hundred mV from corrosion potential.

1.6.2 AC Electrochemical monitoring techniques

1.6.2.1 Electrochemical Impedance Spectroscopy (EIS)

The response of corroding electrodes to small amplitude alternating potential signals of widely varying frequency is analyzed by electrochemical impedance spectroscopy (EIS). EIS can determine in principle a number of fundamental parameters relating to electrochemical kinetics and has been the subject of vigorous research.

The time-dependent current response $I(t)$ of an electrode surface to a sinusoidal alternating potential signal $V(t)$ is expressed as an angular frequency dependent impedance $Z(\omega)$,

$$Z(\omega) = V(t)/I(t) \quad (1.4)$$

where 't' is the time,

$$V(t) = V_0 \sin \omega t \quad (1.5)$$

$$I(t) = I_0 \sin(\omega t + \theta) \quad (1.6)$$

θ = phase angle between $V(t)$ and $I(t)$.

Electrochemical impedance spectroscopy (EIS) method can be applied to the corroding systems for characterization and analysis of complex interfaces. In electrochemical impedance experiments, a small AC voltage perturbation is applied

to an electrode/solution interface, the resulting alternate current intensity is measured, and the corresponding electrical impedance is obtained. Electrochemical impedance is usually measured by applying an AC potential to an electrochemical cell and measuring the current through the cell. The data obtained is then modeled as equivalent electrical circuits and information about the processes occurring at the solution metal interface can be obtained. EIS can be used appropriately in the following areas of corrosion measurement.

- Rapid estimation of corrosion rates.
- Estimation of extremely low corrosion rate and metal contamination rate.
- Estimation of corrosion rates in low conductivity media.
- Rapid assessment of corrosion inhibitor performance in aqueous and non-aqueous media.
- Rapid evaluation of coatings.

Various processes at the surface absorb electrical energy at discrete frequencies, causing a time lag and a measurable phase angle θ , between the time-dependent excitation and response signals. These processes have been simulated by resistive-capacitive electrical networks. The impedance, $Z(\omega)$ may be expressed in terms of real $Z^1(\omega)$ and imaginary $Z^{11}(\omega)$ components.

$$Z(\omega) = Z^1(\omega) + Z^{11}(\omega) \quad (1.7)$$

The impedance behaviour of an electrode may be expressed in Nyquist plots of $Z^{11}(\omega)$ as a function of $Z^1(\omega)$ (Figure 1.5) or in Bode plot of $\log |Z|$ and $\log \theta$ versus frequency f in cycles per second (hertz) (Figure 1.6), where $\omega = 2\pi f$. An important part of the EIS analysis is to create an “equivalent circuit” of the system using resistors and capacitors in series and in parallel. The physical behaviour of the corrosion system can be simulated and quantified with this circuit to gain insight into the important processes in the corrosion system. The impedance spectra are modeled by assuming a circuit made up of resistors, capacitors, and inductors and then fitting that circuit to the spectra to extract values of circuit elements. The values may then relate to physical phenomena to verify that the circuit model is a reasonable representation of the corrosion process.

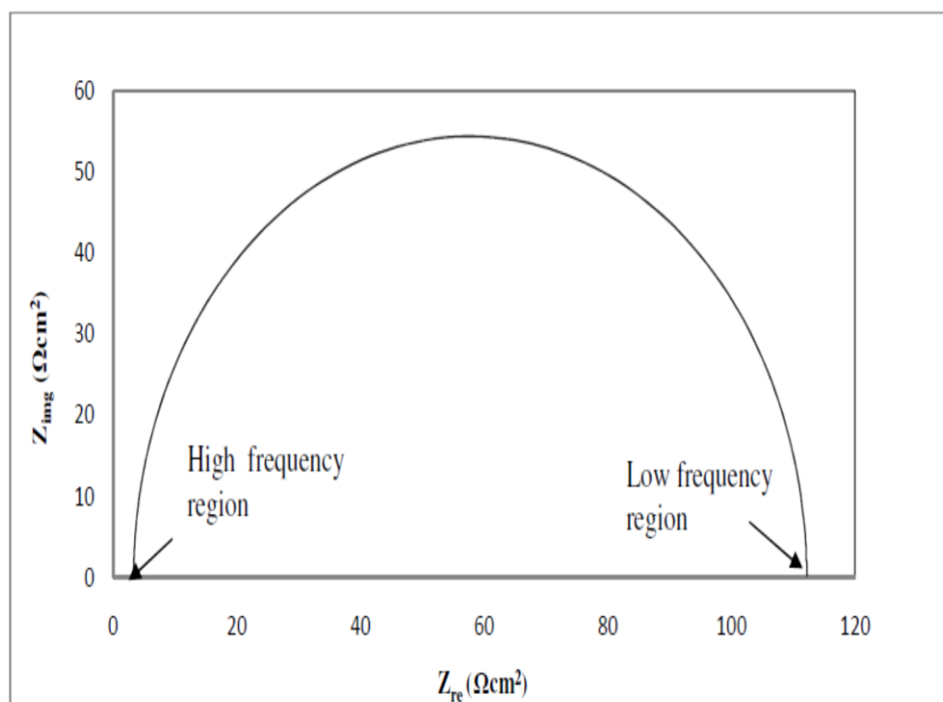


Figure 1.5 Nyquist plot.

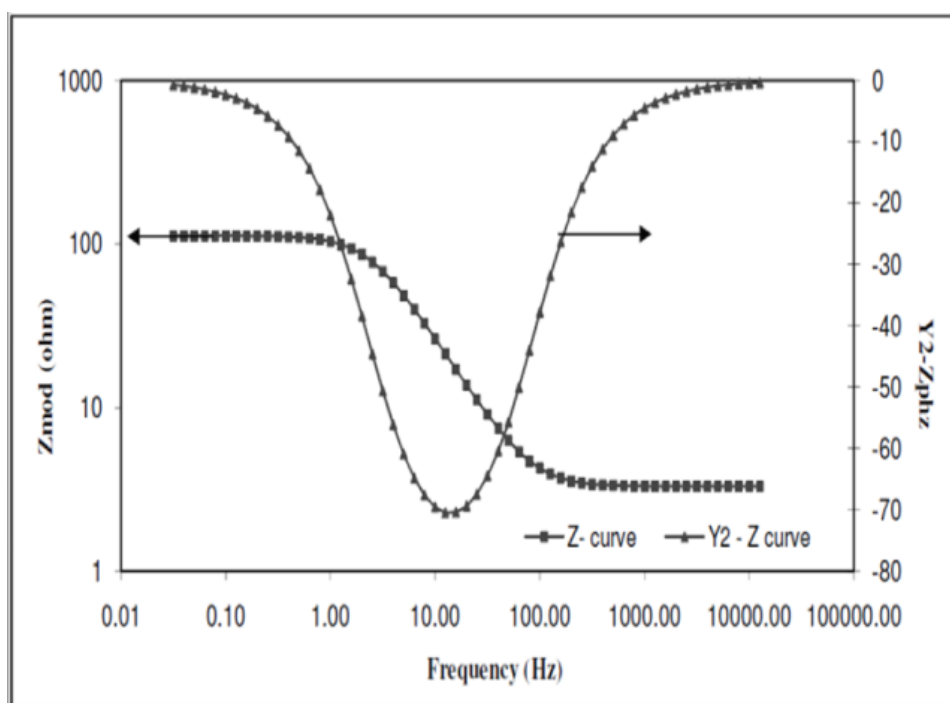


Figure 1.6 Bode plots.

The Nyquist plot shows a semicircle, with increasing frequency in the counter clockwise direction as shown in Figure 1.5. At very high frequency, the imaginary component Z^{11} disappears, leaving only the solution resistance, R_s . At very low frequency, Z^{11} again disappears, leaving a sum of R_s and the Faradaic reaction resistance or polarization resistance R_p . The Faradaic reaction resistance or polarization R_p is inversely proportional to the corrosion rate. R_s measured at high frequency can be subtracted from the sum of $R_p + R_s$ at low frequency to give a compensated value of R_p free of ohmic interferences.

1.7 AEROSPACE MATERIALS

Aluminium alloys are extensively used in aerospace applications due to their high strength-to-weight ratio. Their improved mechanical properties are attributed to the addition of alloying elements that precipitate into fine particles during age-hardening after solid-solution heat treatment. However, during the solidification process, coarse constituent particles, or intermetallic compounds, also segregate throughout the alloy with a resulting heterogeneous microstructure that is susceptible to localized corrosion.

Materials used for aerospace application, in particular, aircraft manufacturing are required to meet stringent specifications like durability, damage tolerance, corrosion resistance, lightweight in order to reduce fuel consumption and expenditure cost. Aluminium and its alloys have been found to satisfy these requirements considerably.

Aluminium alloys are classified into two major groups as wrought and casting alloys based on the fabrication method. The most commonly used alloy is AA2024, which is a wrought alloy, composed of the elements as shown in Table 1.1.

Table 1.1 The composition of AA2024 T3 alloy

Element	Al	Cu	Mg	Zn	Fe	Mn	Cr	Si
(Wt %)	93.52	4.24	1.26	0.08	0.15	0.65	<0.01	0.06

This alloy is cold worked, specifically to improve the strength and mechanical properties that are stabilized at room temperature. Hence, the alloy is called AA2024-T3.

The attractive properties of the alloy are due to the presence of alloying elements:

- **Copper** imparts appreciable solubility and age-hardening character.
- **Manganese** provides substantial strengthening.
- **Silicon** lowers melting point, increases fluidity and strength.
- **Magnesium** and **Zinc** give high strength.

Other properties of AA2024-T3 are

- High strength to weight ratio.
- Good fatigue resistance.
- Lightweight.
- Susceptible to thermal shock.
- Good thermal and electrical properties.
- High reflectivity.
- Ductility does not decrease during the strengthening heat treatment.
- Possesses lower specific gravity.

However, AA2024-T3 shows low corrosion resistance due to the presence of intermetallics, forming electrochemical cells.

1.8 LITERATURE REVIEW

1.8.1 Corrosion behaviour of AA2024-T3

Aluminium alloys, in general, find potential applications in automotive, aerospace industries, aviation industries, household appliances, ship buildings and military hardware due to their high strength, low density and high stiffness. 2024-T3 aluminium alloy, one of the widely used aluminium alloys in aerospace applications, possesses the high strength to weight ratio and high damage tolerance resulting from the presence of copper and magnesium as the major alloying elements and suitable thermo mechanical processing (Hashimoto et al. 2016). Despite possessing advantageous mechanical

properties, the utility of the alloy is limited by its high susceptibility to corrosion, arising out of the presence of the intermetallic particles which differ in their potentials from that of the alloy matrix (Boag et al. 2009 Qafsaoui et al. 2015 Zhang et al. 2016).

There are a number of reports available in the literature, discussing the corrosion mechanism of 2024-T3 aluminium alloy in aqueous media containing chloride ions (Buchheit et al. 1997 Fonseca et al. 2002 Liu et al. 2005 Yasakau et al. 2006 Hashimoto et al. 2016). The 2024-T3 aluminium alloy is mainly composed of three main intermetallic inclusions, namely, Al_2CuMg (S phase), Al_2Cu and $\text{Al}_7\text{Cu}_2\text{Fe}$. $\text{Al}_7\text{Cu}_2\text{Fe}$ is the representative composition of different types of particles containing Al, Cu, Fe as major constituents; Mn and Si as minor constituents found in 2024-T3 (Birbilis et al. 2016). The role of these intermetallic inclusions has been investigated and found that the S phase acts as an active phase towards corrosion (Buchheit et al. 1997), while Al_2Cu and $\text{Al}_6(\text{Cu, Mn, Fe})$ act as noble phases (Zhang et al. 2016). The S phase particles, accounting for about 60% of the intermetallic particles in 2024-T3 aluminium alloys, are reported to be initiation sites for localized corrosion of the alloy (Boag et al. 2011 Hughes et al. 2011 King et al. 2011, 2012). In the initial stages of corrosion, the active S phase undergoes dealloying corrosion with the chemical and electrochemical dissolution of Mg and Al from S phase, simultaneously enriching it with copper. The dealloyed S phase, enriched with copper acts as an effective cathodic site for the preferential corrosion of the alloy matrix. Thus, an effective corrosion inhibition strategy for 2024-T3 aluminium alloy needs suppression of the dealloying of S phase and also protection of the alloy matrix from corrosion. The hexavalent chromate coatings are known to offer corrosion protection to high strength aluminium alloys due to the formation of strongly protective oxide (Cr_2O_3) layer on the metal surface. However, the usage of chromium (VI) has been banned due to its innate carcinogenic properties.

1.8.2 Organic compounds for the corrosion inhibition of AA2024-T3 in sodium chloride solution

A large number of investigations have been carried out using organic compounds as corrosion inhibitors for AA2024-T3 alloy in sodium chloride solution. Organic

compounds consisting of heteroatoms, such as O, N or S and multiple bonds or aromatic rings act as good corrosion inhibitors on metal and alloy surfaces. The electron rich active sites on these molecules facilitate easy adsorption of the molecules of these compounds on the metal/alloy surface. Some of the important inhibitors used for AA2024-T3 alloy are given in Table. 1.2

Table.1.2 Corrosion inhibitors for AA2024-T3.

Electrolyte	Inhibitors	Results	Reference
0.005 M NaCl	1,2,4-triazole, 3-amino-1,2,4-triazole, benzotriazole and 2-mercaptobenzothiazole.	Benzotriazole and 2-mercapto -benzothiazole act as effective corrosion inhibitors for AA-2024 alloy.	(Zheludkevich et al. 2005)
0.05 M NaCl	Cerium cinnamate.	Cerium cinnamate act as a mixed type inhibitor, suppress the dealloying of second phase particle and Al-matrix.	(Shi et al. 2011)
	Vanadate	Corrosion inhibition of AA2024-T3 by the formation of inhibitor layer on reactive sites (second phase particle)	(Iannuzzi and Frankel 2007)
	Cerium nitrate	The thin layer of inhibitor covers the entire alloy surface and controls both the anodic and the cathodic behaviour.	(Paussa et al. 2012)
	Cerium tartrate	Cerium tartrate offers both anodic and cathodic inhibition.	(Tianhui et al. 2015)
	Several commercially available organic compounds	8-hydroxyquinoline, quinaldic acid and salicylaldoxime are effective	(Lamaka et al. 2007)

		corrosion inhibitors for AA2024-T3.	
	Cerium molybdate nanowires	Cerium molybdate nanowires suppress the corrosion activity on the cathodic sites.	(Yasakau et al. 2012)
	Benzotriazole and cerium chloride	Benzotriazole and cerium chloride are effective corrosion inhibitors for AA2024.	(Coelho et al. 2018)
5 % NaCl	2,5-dimercapto benzotriazolate (BTA), N,N-diethyldithiocarbamate (DEDTC), 1,3,4 thiadiazolate(DMTD), and ferrocyanide	Order of inhibition efficiency is ferrocyanide < BTA < DEDTC \approx DMDT.	(Williams et al. 2010)

1.8.3 Anodizing process used for corrosion protection of AA2024-T3

In aerospace industry, aluminium alloys are protected by three different layers. The lowermost layer is the anodized layer. Chromic acid anodizing (CAA) is a widely used method for formation of an oxide layer. But the method is not preferred due to its carcinogenic effect. Hence, the eco-friendly anodizing process is needed to replace the CAA. Some alternative process has been developed for the replacement of CAA and their details are given Table 1.3.

Table. 1.3 Anodizing process used for corrosion protection of AA2024-T3.

Anodizing electrolyte	Sealing agent	Remarks	Reference
H ₂ SO ₄ (10% (v/v))	KMnO ₄ (9.5 g/L), Na ₂ MoO ₄ (5 g/L) and LiNO ₃ (4 g/l)	Incorporation of Mn and Mo into the oxide layer improves the corrosion protection properties.	(Yoganandan et al. 2016)
H ₂ SO ₄ (20 wt %)	Hot Ni(CH ₃ CO ₂) ₂ (5 g/L). Cold Ni(CH ₃ CO ₂) ₂ (5 g/L), Cold saturated Ni(CH ₃ CO ₂) ₂ (180 g/L) Hot water sealing	All sealing methods decrease the pore size of the oxide layer. Hot Ni(CH ₃ CO ₂) ₂ sealing reduces the pore size and also deposits on the air oxide interface.	(Hu et al. 2015)
H ₂ SO ₄ (0.41M) + C ₄ H ₆ O ₆ (0.53 M)	Hot water sealing	Combination of H ₂ SO ₄ and C ₄ H ₆ O ₆ leads to the formation of a low porous oxide layer.	(Boisier et al. 2008)
H ₂ SO ₄ (0.46M) + C ₄ H ₆ O ₆ (0.53 M)	Zn(NO ₃) ₂ ·6H ₂ O (0.01 mol) + NH ₄ NO ₃ (0.06 mol) (LDH-NO ₃) Zn(NO ₃) ₂ ·6H ₂ O (0.01 mol) + NaVO ₃ (0.1 M) (LDH-VO _x) Hot water sealing	LDH-based sealing improved the active protection of anodized AA2024. Coating sustainable up to 168 h.	(Kuznetsov et al. 2016)
H ₂ SO ₄ (0.46 M) + C ₄ H ₆ O ₆ (0.53 M) (TSA)	Without sealing	Na ₂ MoO ₄ ·2H ₂ O addition to anodizing bath enhanced corrosion protection behaviour of	(García-Rubio et al. 2009)

H ₂ SO ₄ (0.46 M) + C ₄ H ₆ O ₆ (0.53 M) + Na ₂ MoO ₄ .2H ₂ O (0.25 M)		anodised AA2024 substrate.	
H ₂ SO ₄ (40 g/L) + C ₄ H ₆ O ₆ (80 g/L)	Hot water TEOS (20 %v/v) + GPTMS (10 %v/v)	Hybrid sol-gel sealing increased the corrosion resistive properties of the oxide layer, compared to the classical hot water sealing.	(Capelossi et al. 2014)
H ₂ SO ₄ (55 g/L) + C ₄ H ₆ O ₆ (88 g/L)	Hot water NiF ₂ (4g/L) followed by hot water sealing Hot K ₂ Cr ₂ O ₇ (50g/L) KMnO ₄ + Na ₂ MoO ₄ + LiNO ₃	KMnO ₄ + Na ₂ MoO ₄ + LiNO ₃ sealing reagent shows excellent corrosion resistance.	(Wang et al. 2018)

1.8.4 Replacement of strontium chromate from the primer coating

The second most important layer is the primer layer, which is generally epoxy based. Primers play an important role in maintaining the integrity of the airframe although their role is often misunderstood and underestimated because it is invisible after the topcoat finish is applied. The primer paints, also fill in the porosity of the base layer and provide sustained adherence with the top paint layer, the polyurethane paint (Twite and Bierwagen 1998; Bierwagen and Tallman 2001). Epoxy primer is normally used to coat steel, aluminium and composites before painting. They have excellent anti-corrosive properties due to the presence of hexavalent chromium pigments - strontium chromate. However, the industry is abuzz with looking for chrome-free green alternatives, as hexavalent chromium is a proven potential carcinogen. Some of the

important inhibitors used for replacement of strontium chromate from primer, are given in Table. 1.4

Table. 1.4 Addition of inhibitors to the primer coatings for corrosion protection of AA2024-T3.

Corrosion inhibitor	Remarks	Reference
2-mercaptobenzothiazole (2-MBT) 2-MBT loaded mesoporous silica nanocontainers 2-MBT loaded spherical hollow silica particles	The direct addition of 2-MBT to the primer coating not sufficient to provide the anticorrosion activities. Addition of inhibitor encapsulated nanoparticles to the primer coating leads to the increase in the barrier and self-healing properties.	(Borisova et al. 2013)
Benzotriazole, 2-mercaptobenzothiazole and lithium carbonate	Order of inhibition efficiency on AA2024-T3 is: 2-MBT > BTA > Li ₂ CO ₃ . Only Li ₂ CO ₃ incorporated coating demonstrated effective corrosion in the scribe area.	(Visser et al. 2018)
Lithium carbonate and lithium oxalate	Lithium salt loaded primer coating demonstrates the active corrosion inhibition.	(Visser et al. 2015)
Cerium tartrate	Cerium tartrate loaded coatings shows the healing properties on artificial defected areas.	(Hu et al. 2017)
2-mercaptobenzothiazole and 2-methylbenzothiazole encapsulated polyelectrolyte nanocapsules.	Addition of inhibitor encapsulated polyelectrolyte nanocapsules to the primer coating leads to an increase in the barrier and self-healing properties.	(Kopeć et al. 2015)

1.8.5 Addition of inhibitors to the sol-gel coatings

The sol-gel coatings seem to be a promising replacement to the versatile hexavalent chromium coating. Sol-gel and hybrid coatings are green, easy to fabricate and tunable for various applications. In addition, they have the advantage of being compatible with the top coat paints due to the formation of chemical bonding which is possible by choosing optimal functional groups in the top coat and silanes of the sol-gel, enabling enhanced adhesion. Generally, sol-gel coatings have pinholes, which enable percolation of the corrosion species towards the metal surface and initiate the corrosion process. Many kinds of additives have been used to increase the corrosion protection performance of sol-gel coatings. Some of the important additives are listed in Table. 1.5.

Table. 1.5 Addition of inhibitors to the sol-gel coatings for corrosion protection of AA2024-T3.

Coating precursors	Corrosion media	Remarks	Reference
3-glycidoxypropyl – trimethoxysilane (GPTMS), Zirconium (IV) propoxide (TPOZ)	0.5 % NaCl	The addition of 8-hydroxyquinoline and cerium, benzotriazole to the sol-gel film sufficiently decreases the barrier properties of sol-gel films and does not provide adequate corrosion protection.	(Yasakau et al. 2008)
Methacryloxypropyltri methoxysilane (MPTMS), Tetraethylorthosilicate (TEOS), phenyltrimethoxysi-lane (PhTMS)	0.5% NaCl + 0.35% (NH ₄) ₂ SO ₄	The addition strontium aluminium polyphosphate to the methacryloxy based sol–gel coating leads to an increase in the barrier properties. The addition benzotriazole to the sol-gel coating leads to a	(Raps et al. 2009)

		deterioration of the barrier properties.	
(Tetraethyl orthosilicate (TEOS) + 3-methacryloxypropyl trimethoxysilane (MPS))-SiO ₂ (TEOS+MPS)-SiO ₂ -5 or 10 % CeNO ₃	3.5 % NaCl	The addition of cerium nitrate to the sol-gel coatings diminish the barrier properties.	(Rosero-Navarro et al. 2008)
Tetramethoxysilane (TMOS), 3-glycidoxypropyltrimethoxysilane (GPTMS), diethylenetriamine	0.005 M NaCl	The addition of 8-hydroxyquinoline increases the corrosion resistance of the sol-gel film and shows the self-healing properties.	(Tian et al. 2015)
Diethoxydimethylsilane (DEODMES), Methyltriethoxysilane (MTEOS), Tetrapropoxyzirconium (TPOZ)	5 % NaCl	Addition of high content of chloranil does not provide adequate corrosion protection due to the disorganization of the sol-gel system.	(Quinet et al. 2007)
Tetramethoxysilane (TMOS), 3-glycidoxypropyltrimethoxysilane (GPTMS)	0.35 wt.% (NH ₄) ₂ SO ₄ + 0.05 wt.% NaCl	The addition of Ce(NO ₃) ₃ and CeCl ₃ in silane solution significantly improves the corrosion resistance of sol-gel coating.	(Shi et al. 2010)
Methyltriethoxysilane (MTEOS)	3.5 % NaCl	The incorporation of cerium nitrate inhibitor to the sol-gel system improves corrosion protection on aluminium alloy.	(Lakshmi et al. 2013)

1.9 SCOPE AND OBJECTIVES

1.9.1 Scope

All metals and metal alloys suffer from corrosion due to various environmental factors. The simplest way of protecting them from corrosion is to apply an external protective paint layer. A well-painted structure is easier to maintain. Paints not only add to the aesthetics by providing the desired appearance but also add to the weight of the structure - a critical factor in aircraft. Paints generally refer to and include primers, enamels, and various finishing formulations.

The aerospace paint system is three-tiered. The lowermost layer is often a conversion coating or anodizing layer measuring about 5-60 μm in thickness (Habazaki et al. 2004 Balaraju et al. 2011). Over this layer is the primer layer, generally epoxy based. Primers play an important role to maintaining the integrity of the airframe although their role is often misunderstood and underestimated because it is invisible after the topcoat finish is applied. The primer paints, also fill in the porosity of the base layer and for sustained adherence with the top paint layer, the polyurethane paint.

The naturally formed oxide layer on the aluminium alloy not sufficient to offers effective corrosion protection against the aggressive environment. The barrier properties of these aluminium alloy can be improved by the anodizing method through the formation of an oxide layer on the alloy surface. Chromic acid anodizing (CAA) is a widely used method for the formation of an oxide layer containing hexavalent chromium ions (Cr (VI)) and trivalent chromium ions (Cr (III)), which offers the excellent barrier and corrosion resistance. But the Cr (VI) is not preferred for the anodizing process due to its carcinogenic effect. Hence, the eco-friendly anodizing process is needed to replace the Cr (VI). Thus researchers have focused on the replacement of Cr (VI) from the anodizing process. Some alternative processes have been developed for the replacement of CAA using different anodization baths such as phosphoric acid, sulphuric acid, sulphuric acid – boric acid mixture, sulphuric acid – boric acid – phosphoric acid mixture, sulphuric acid - tartaric acid mixture, etc (Miera et al. 2010 Elabar et al. 2017 Elaish et al. 2018 Torrescano-Alvarez et al. 2018).

Sulphuric acid anodizing process generally produces microcracks and porous surface (Moutarlier et al. 2005 Miera et al. 2008). These pores and cracks will permit the corrosive ions and water to reach the substrate surface and initiate the corrosion. The porous oxide layer is sealed by prolonged immersion in hot water. In this process oxide is converted into its hydrate form, and the resulted swelling reduces the porosity of the layer. But it is not very effective due to reduction in the abrasion resistance; and the sealing process is not enough to provide the effective corrosion resistance due to the presence of intermetallic particles. Nickel acetate, cobalt acetate, cerium ions, and sodium dichromate or potassium dichromate are used as sealing elements to fill the porosity and to enhance the corrosion resistance (Balaraju et al. 2011). The aim of the present investigation is to synthesise effective corrosion inhibitors for AA2024-T3 and to incorporate them into the oxide layer formed on aluminium alloy by an immersion process.

The second layer, epoxy primer is normally used to coat steel, aluminium, and composites before painting. They have excellent anti-corrosive properties due to the presence of hexavalent chromium pigment, strontium chromate. However, the industry is abuzz with looking for chrome-free green alternatives, as hexavalent chromium is a proven potential carcinogen. Several alternatives to hexavalent chromium have been investigated, and some of the reported ones include less toxic trivalent chromium (Pearlstein and Agarawala 1994 Qi et al. 2015), rare-earth based inhibitors (such as cerium ions and lanthanide ions) (Birbilis et al. 2005 Zheludkevich et al. 2005a Ho et al. 2006 Markley et al. 2007 Hongwei Shi et al. 2011 Matter et al. 2012 Shi et al. 2014), vanadate based compounds and organic based inhibitors (thiazole derivatives, benzotriazole, 8- hydroxyquinoline, thiosemicarbazone derivatives, 2-mercaptobenzothiazole, salicylaldoxime, quinaldic acid) (Zheludkevich et al. 2005b Yasakau et al. 2008 Marcelin and P  b  re 2015). Organic corrosion inhibitor molecules could also be potential alternatives to the hexavalent chromium pigment, strontium chromate

The sol-gel coatings seem to be a promising replacement to the versatile hexavalent chromium coating. Sol-gel and hybrid coatings are green, easy to fabricate and tunable for various applications. In addition, they have the advantage of being

compatible with the top coat paints due to the formation of chemical bonding which is possible by choosing optimal functional groups in the top coat and silanes of the sol-gel, enabling enhanced adhesion. Generally, sol-gel coatings have pinholes, which enable percolation of the corrosion species towards the metal surface and initiate the corrosion process. Many kind of additives have been used to increase the corrosion protection performers of sol-gel coatings. The organic inhibitors such as benzotriazole and 8-hydroxyquinoline have shown promising corrosion protection on AA2024 in 3.5 % NaCl solution (Lamaka et al. 2007 Marcelin and Pébère 2015). The direct addition of organic inhibitors into the sol-gel coatings could cause leaching of the inhibitor, alterations in the coating integrity and influence on the stability of the system (Yasakau et al. 2008 Raps et al. 2009). To overcome these shortcomings, the inhibitors are packaged in nano-containers and doped into the coatings (Abdullayev and Lvov 2010 Kartsonakis et al. 2012 Maia et al. 2012, 2013 Wei et al. 2015 Shi et al. 2017). The addition of nano-containers to the sol-gel matrix, converts the passive barrier coatings into active ‘smart’ coatings with self-protecting properties.

Organic compounds consisting of hetero atoms, such as O, N or S and multiple bonds or aromatic rings act as good corrosion inhibitors on metal and alloy surfaces. The electron rich active sites on these molecules facilitate easy adsorption of the molecules of these compounds on the metal/alloy surfaces (Bentiss et al. 2005 Lebrini et al. 2006). Aromatic derivatives of thiosemicarbazone possess the combination of all the above bonding sites and are expected to act as good corrosion inhibitors.

In the present work, five different thiosemicarbazone derivatives have been synthesised. The inhibitive impact of the compounds on the corrosion of 2024-T3 aluminium alloy has been studied and reported.

Very little work has been reported on the development of complete chromium free coatings for AA2024-T3. The aim of the present work is also the replacement of chromium ions from aerospace coating system (Figure1.7).

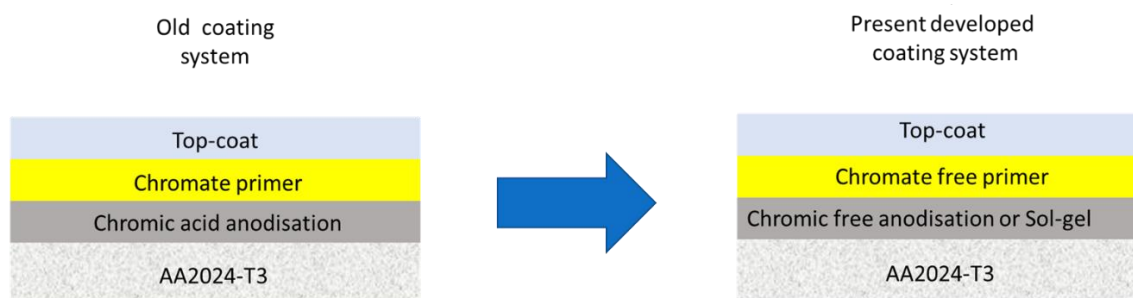


Figure 1.7 Coating layers.

1.9.2 Objectives

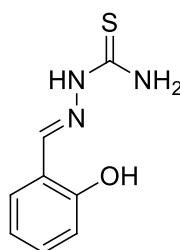
1. To study the corrosion behaviour of aluminium alloy AA2024-T3 specimen in a corrosion medium of sodium chloride (3.5 wt. %).
2. To synthesize thiosemicarbazone derivatives, Bis [[3,4-Dihydroxyphenylmethylene]carbonothioicdihydrazide] and investigate their corrosion inhibitor performance on aluminium alloy AA2024-T3 in a sodium chloride medium.
3. To develop the chromium free anodizing coatings.
4. To replace Strontium chromate from primer coatings.
5. To develop a sustained anticorrosion sol-gel coating system.
6. To further improve the anticorrosion of sol-gel coatings by adding the synthesised organic inhibitor.
7. To validate the coating according to ASTM standard in the salt chamber.

2.1 SAMPLE PREPARATION

The specimens of AA2024-T3 aluminium alloy were used as working sample. The samples were well polished with 400, 800, 1200 and 2500 grade silicon carbide paper and finally on a polishing wheel with alumina (1 μm) to obtain a mirror finish. The samples were sonicated in Milli-Q water for 10 minutes and air dried at room temperature.

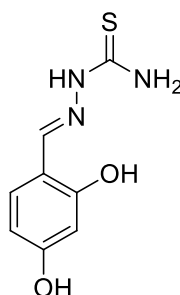
2.2 SYNTHESIS OF CORROSION INHIBITORS

2.2.1 (E)-2-(2-hydroxybenzylidene)hydrazinecarbothioamide (2-MHC)



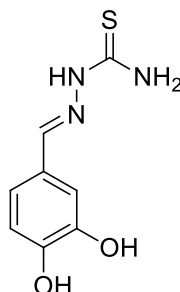
2-MHC was purchased from Ms.Sigma Aldrich.

2.2.2 Synthesis of (E)-2-(2,4-dihydroxybenzylidene)hydrazinecarbothioamide (2,4-DHC)



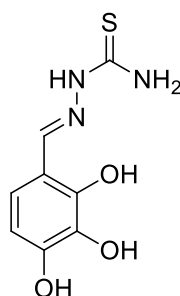
The mixture of 2,4-dihydroxybenzaldehyde (10 mM, 1.38 g) and thiosemicarbazide (10 mM, 0.91 g) was dissolved in 30 mL of absolute ethanol and refluxed for 12 h. The reaction mixture was cooled to room temperature, and the resulted precipitate was filtered and recrystallized with ethanol to yield titled compound as a white solid (yield 85%).

2.2.3 Synthesis of (E)-2-(3,4-dihydroxybenzylidene)hydrazinecarbothioamide (3,4-DHC)



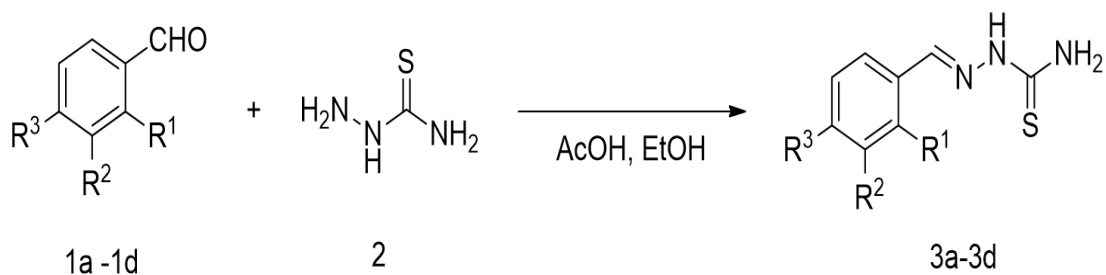
Prepared from 3,4-dihydroxybenzaldehyde and thiosemicarbazide by following the same procedure as described above in 2.2.2. The product was obtained as yellow crystals (80% yield).

2.2.4 Synthesis of (E)-2-(2,3,4-trihydroxybenzylidene)hydrazinecarbothioamide (2,3,4-THC)



Prepared from 2,3,4-trihydroxybenzaldehyde and thiosemicarbazide by following the same procedure as described above in 2.2.2. The product was obtained as yellow crystals (85% yield).

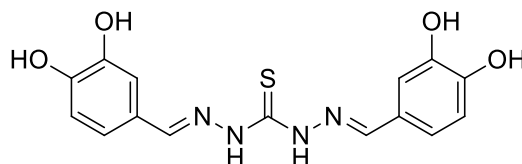
The general synthesis scheme of the inhibitors is shown in Figure 2.1.



Compound 1	R ¹	R ²	R ³	Compound 3
1a	OH	H	H	3a (2-MHC)
1b	OH	H	OH	3b (2,4-DHC)
1c	H	OH	OH	3c (3,4-DHC)
1d	OH	OH	OH	3d (2,3,4-THC)

Figure 2.1 The synthesis scheme of inhibitors.

2.2.5 Synthesis of Bis ((3,4-Dihydroxyphenylmethylene)-carbonothioic dihydrazide) (3,4-DCT)



A mixture of 3,4-dihydroxybenzaldehyde (10 mM, 1.38 g) and thiocarbonylhydrazide (5 mM, 0.530 g) in 60 mL of ethanol+water (1:1) was refluxed for 12 h. Initially the solution turned turbid and later became a clear solution. The reaction mixture was cooled to room temperature, and the resultant precipitate was filtered and recrystallized with ethanol+water as a green solid (75% yield).

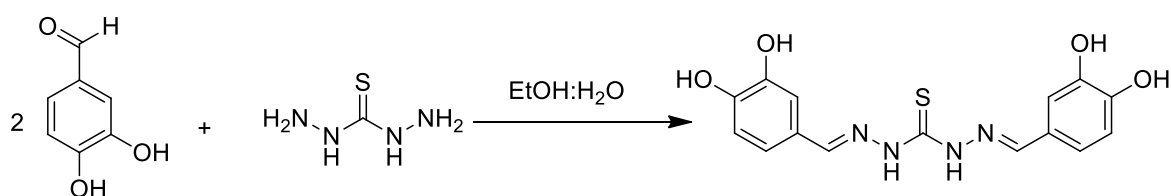


Figure 2.2 The synthesis scheme of 3,4-DCT.

2.3 CORROSION MEDIA

A standard 3.5 % NaCl solution was prepared by dissolving sodium chloride in Milli-Q water. An appropriate known weight of the inhibitors were added to 3.5 % NaCl solution and stirred for 24 h at room temperature to obtain 1 mM solution.

2.4 ELECTROCHEMICAL STUDIES

The electrochemical measurements were carried out using CH instruments electrochemical work station (CHI660E) in naturally aerated 3.5% NaCl solution in the absence and in the presence of different inhibitors. The corrosion cell set up employed was a three electrode cell comprising of the test coupon as the working electrode (1 cm² exposure area), a platinum electrode as counter electrode and saturated calomel electrode used as the reference electrode. The alloy coupon was immersed in 3.5% NaCl in the absence and in the presence of the inhibitor and allowed to establish a steady state open circuit potential (OCP). The electrochemical impedance measurements were carried out at different immersion times in the same 3.5% NaCl solution in the absence and in the presence of the inhibitors. The scanned frequency ranged from 100 kHz to 10 MHz with a small amplitude (10 mV) ac perturbation about the OCP. The corrosion characteristics were analyzed through Nyquist plots and Bode plots. The impedance behaviour of the specimen was simulated with a suitable equivalent electrical circuit using ZsimWin software program; and the various impedance parameters were evaluated.

The potentiodynamic polarization studies were performed on the alloy specimen by applying a cathodic potential drift of -250 mV and an anodic potential drift of +250 mV with respect to the OCP at a scan rate of 1 mV s⁻¹. The simultaneously developed current potential curves (potentiodynamic polarization curves) were analyzed.

2.5 SURFACE CHARACTERIZATIONS

The surface morphologies of the corroded aluminium alloy substrate in the absence and in the presence of inhibitors were analyzed by field emission scanning electron microscopy (FE-SEM) and energy dispersive X-ray analysis (EDX) using Carl Zeiss,

Supra 40 VP, attached with EDX analyser, under an operating voltage of 10 kV and probe current of ≈ 100 pA. The corroded samples were washed with water and dried at room temperature before subjecting to surface analysis.

2.6 X-RAY PHOTOELECTRON SPECTROSCOPY

The chemical composition of the corroded alloy sample surfaces, immersed in the corrosion media in the absence and presence of the inhibitors were investigated by XPS analysis using X-ray photoelectron spectrometer (SPECES surface nano analysis). XPS spectra of components O 1s, Al 2p, C 1s and N 1s on the aluminium alloy surface were recorded with non-monochromatic Al K α radiations (1486.6 eV) under high vacuum (5×10^{-9} mbar); and C 1 s peak located at 284.6 eV was used as a reference peak. The survey spectra were obtained under 70 eV pass energy, while the individual spectra of Al 2p, O 1s, C 1s and N 1s were obtained under 40 eV pass energy. The spectra fitting was carried out using PeakFit v4.12 software.

2.7 SUBSTRATE PREPARATION FOR COATING APPLICATIONS

The working substrate, aluminium alloy 2024-T3 was degreased with acetone and ethanol. The coupons were then cleaned using alkaline solution (sodium carbonate and sodium phosphate) by immersion for 5 minutes at 60° C, followed by dipping in 0.5 M NaOH solution at 30° C for 5 minutes, washed with 20% HNO₃ solution for 2 minutes at 25°C and finally with distilled water. After the surface cleaning, the specimens were dried and used for coating application.

2.8 ANODIZATION OF AA2024-T3 SURFACE

Surface treated aluminium alloy samples were anodized using 10 wt % sulphuric acid electrolyte by applying a constant voltage of 12 V for a duration of 1 h. The obtained samples were rinsed with distilled water and air dried. The anodized oxide layers, containing pores were sealed with the synthesised inhibitors by immersing them in ethanol-water (1:1 v/v) solutions of the inhibitors at 50°c for 1 h. the inhibitor sealed anodized coupons were rinsed with distilled water, air dried and used for further characterization.

2.9 PRIMER COATED SUBSTRATE PREPARATION

The commercially available Southguard epoxy white primer (EA21Z01) was used in the present study. The primer coating without inhibitor was used as a reference and it was prepared by mixing the Southguard epoxy white primer (EA21Z01) and epoxy thinner (ST30Z288) in an 8:2 volume ratio. The hardener was added later to the epoxy primer in a 1:1 volume ratio with mechanical stirring to make a homogenous mixture.

The effect of adding the synthesised inhibitors, on the anticorrosion nature of the epoxy coating was studied by incorporating them in the coating. The inhibitor doped epoxy coatings were prepared by adding 10 mg of inhibitors per mL of the epoxy resin under constant stirring for an optimum dispersal. The coatings were applied on AA2024-T3 substrate by the manual spray method.

2.10 PREPARATION OF THE SOL-GEL COATINGS

The hybrid sol-gel was prepared by mixing two sol-gel precursors, S1 and S2 in a defined molar ratio. The first sol S1 was prepared by mixing the sol-gel precursor, 3-glycidoxypropyltrimethoxysilane (GPTMS), in a closed container, with acidified water (0.05 M HNO₃) (as a catalyst) in 2:1 molar ratio, followed with constant stirring for 1h to complete the hydrolysis and condensation reactions. Subsequently, the inhibitor solution in 2-propanol (10 mg/mL) was added to the prepared sol and stirred for 1 h. The second sol-gel precursor (S2), zirconium propoxide was prepared by the addition of ethylacetoacetate in 1:1 molar ratio. The sol was stirred for 1h to stabilize the zirconium propoxide - ethylacetoacetate complex. Acidified water added dropwise in the molar ratio 3:1 to the sol S2 with continuous stirring for 1 h. In the final step, the obtained second sol (S2) was added dropwise to the first sol (S1) to form the final hybrid sol-gel. The final sol was stirred for 2 h at room temperature.

2.11 SOL-GEL COATING METHOD

The ormosil coated substrates were fabricated by the dip coating method, using an automatic sequential layer by layer deposition system (M/s IEICOS Ltd), with a dipping time of 90 s and dipping speed of 1.5 mm s⁻¹.

2.12 CHARACTERIZATION OF COATED SUBSTRATE

Surface morphology of the uncoated and coated samples was studied using field emission scanning electron microscope and the surface composition was analysed by energy dispersive X-ray (EDX). Adhesion of the coatings was evaluated by the Tape pull cross hatch (ASTM D3359) method, using a cross-hatch cutter, Model Elcometer 107. The obtained results are represented on a scale of 0-5, 5 for a poorly adhesive coating through 0 for a very good adhesive coating.

The deterioration of coating systems in 3.5 % sodium chloride solution were examined by electrochemical impedance spectroscopy (EIS) method. The impedance spectra were recorded in a frequency range of 10^5 Hz to 10^{-2} Hz with an AC amplitude of 10 mV, periodically from 24 h to 336 h for anodized aluminium alloy, 24 h to 504 h for primer coated aluminium alloy and 24 h to 168 h for sol-gel coated aluminium alloy. The resultant impedance plots were fitted with the suitable electrical equivalent circuits using ZsimWin software program.

2.13 ACCELERATED SALT SPRAY TEST

The anticorrosion behaviour of the coated alloy sample was examined by exposing the coated alloy to a salt fog environment created by spraying 5 wt. % aqueous sodium chloride solution at 35 °C, according to ASTM B117 standard.

3.1 INHIBITION EFFECT OF CARBOTHIOAMIDE AND CARBONOTHIOICDIHYDRAZIDE DERIVATIVES ON ALUMINIUM ALLOY 2024-T3 IN 3.5 % NaCl SOLUTION

3.1.1 Characterisation of the inhibitors

3.1.1.1 NMR and elemental analysis

(a) (*E*)-2-(2,4-dihydroxybenzylidene)hydrazinecarbothioamide (2,4-DHC)

The ^1H NMR spectrum of 2,4-DHC is shown in Figure 3.1. The different peaks are assigned as follows:

^1H NMR (DMSO); δ ppm, 11.14 (s, 1H, NHCS), 9.720 (s, 2H, Ar-OH), 8.23 (s, 1H, Ar-CH=N), 7.91 (s, 1H, NH), 7.71 (s, 1H, NH), 7.64 (d, 1H, $J = 8.4$ Hz), 6.28 (d, 1H, $J = 2.4$ Hz), 6.24 (d.d, 1H, $J = 2.4$ Hz and 8.8 Hz).

CHNS analysis of $\text{C}_8\text{H}_9\text{N}_3\text{O}_2\text{S}$; Found (Calculated) (%) C = 46.10 (45.49), H = 4.38 (4.29), N = 20.08 (19.89) and S = 15.44 (15.18).

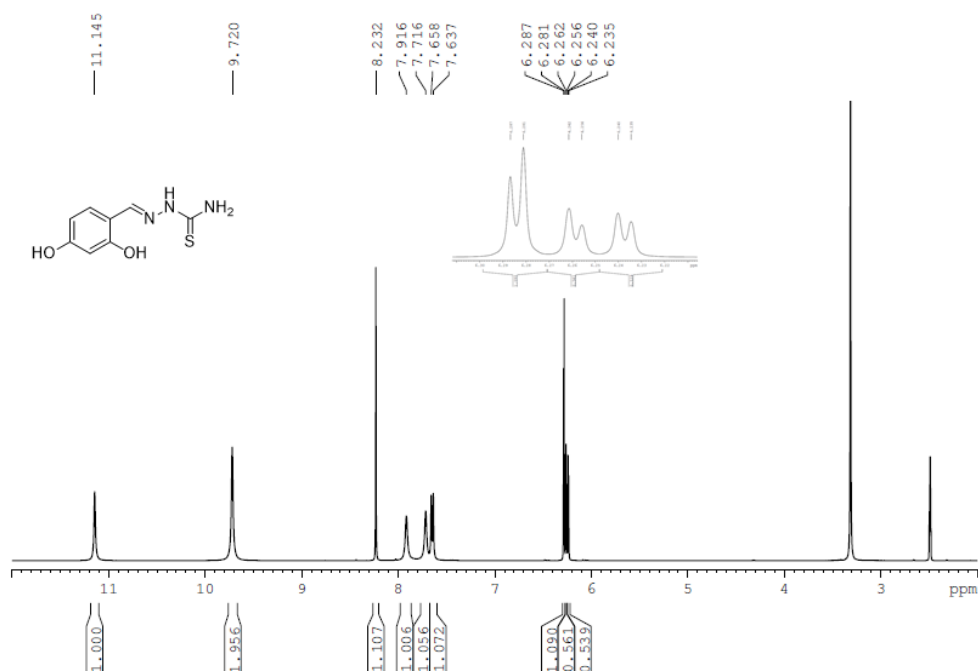


Figure 3.1 ^1H -NMR spectrum of 2,4-DHC.

(b)(E)-2-(3,4-dihydroxybenzylidene)hydrazinecarbothioamide (3,4-DHC)

The ^1H NMR spectrum of 3,4-DHC is shown in Figure 3.2. The different peaks are assigned as follows:

^1H NMR. 11.19 (s, 1H, NHCS), 9.44 (s, 1H, Ar-OH), 8.97 (s, 1H, Ar-OH), 8.02 (s, 1H, NH), 7.89 (s, 1H, CH=N), 7.70 (s, 1H, NH), 7.18 (d, 1H), 7.03 (d,d, 1H), 6.75 (d, 1H).

CHNS analysis of $\text{C}_8\text{H}_9\text{N}_3\text{O}_2\text{S}$; Found (Calculated) (%) C = 46.12 (45.49), H = 4.28 (4.29), N = 20.01 (19.89) and S = 15.20 (15.18).

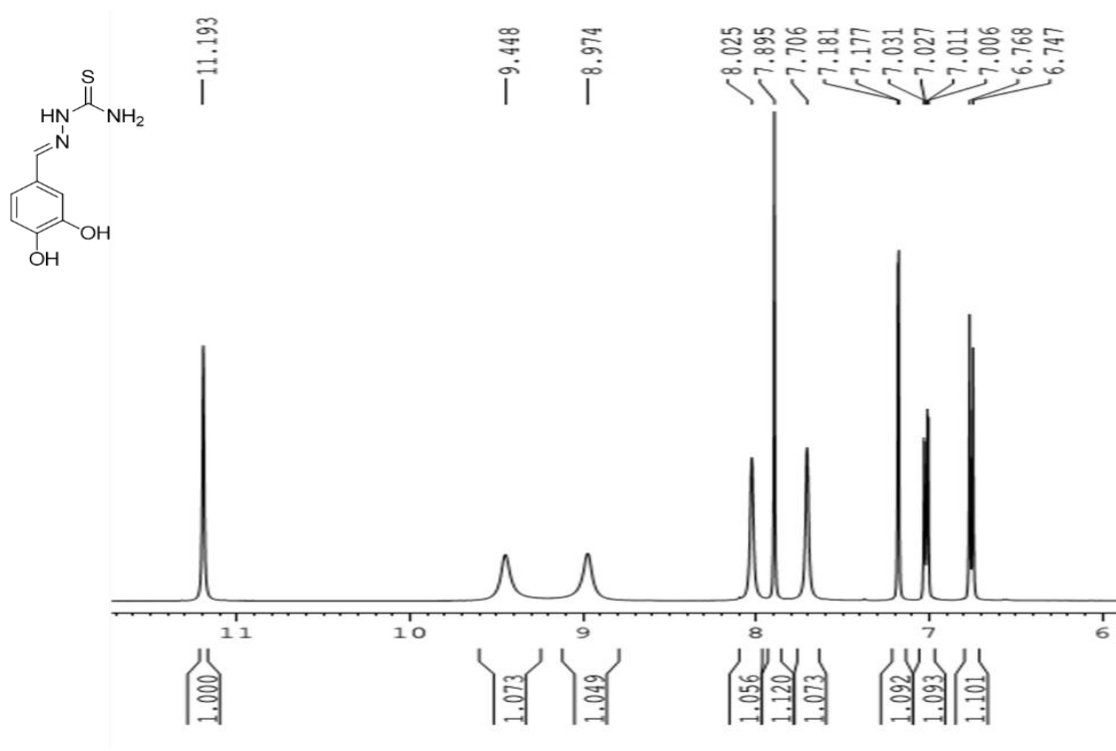


Figure 3.2 ^1H -NMR spectrum of 3,4-DHC.

(c) (*E*)-2-(2, 3, 4-trihydroxybenzylidene)hydrazinecarbothioamide (2,3,4-THC)

The ^1H NMR spectrum of 2,3,4-THC is shown in Figure 3.3. The different peaks are assigned as follows:

^1H NMR (DMSO); δ ppm, 11.17 (s, 1H, NHCS), 9.47 (s, 1H, Ar-OH), 8.94 (s, 1H, Ar-OH), 8.39 (s, 1H, Ar-CH=N), 8.22 (s, 1H, Ar-OH), 7.92 (s, 1H, NH), 7.72 (s, 1H, NH), 7.10 (d, 1H, $J = 8.8$ Hz) 6.32 (d, 1H, $J = 8.8$ Hz)

CHNS analysis of $\text{C}_8\text{H}_9\text{N}_3\text{O}_3\text{S}$; Found (Calculated) (%) C 43.14 (42.28), H 4.19 (3.99), N 18.47 (18.49) and S 14.21 (14.11).

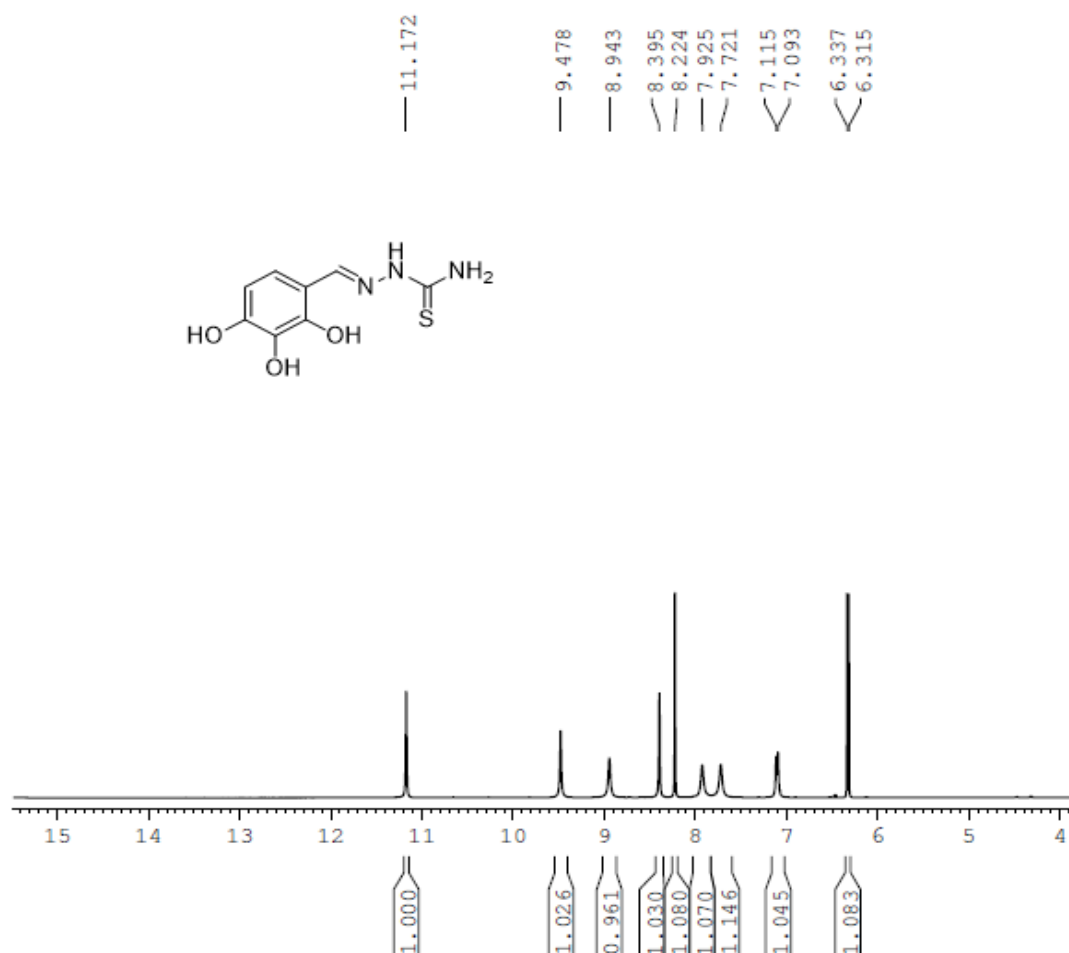


Figure 3.3 ^1H -NMR spectrum of 2,3,4-THC.

(d) Bis ((3,4-Dihydroxyphenylmethylene)carbonothioicdihydrazide) (3,4-DCT)

The ^1H NMR spectrum of 3,4-DCT is shown in Figure 3.4. The different peaks are assigned as follows:

^1H -NMR- (400 MHz [D6] DMSO) 6.78-6.80 (2H, d), 6.95-7.06 (2H, d), 7.28 (2H, s), 7.97-8.37 (2H, br), 9.34 (4H, br), 11.25-11.50 (2H, br)

CHNS analysis of $\text{C}_{14}\text{H}_{14}\text{N}_4\text{O}_4\text{S}$; Found (Calculated) (%) C = 52.20 (52.02), H = 4.18 (4.07), N = 16.29 (16.18) and S = 9.28 (9.26).

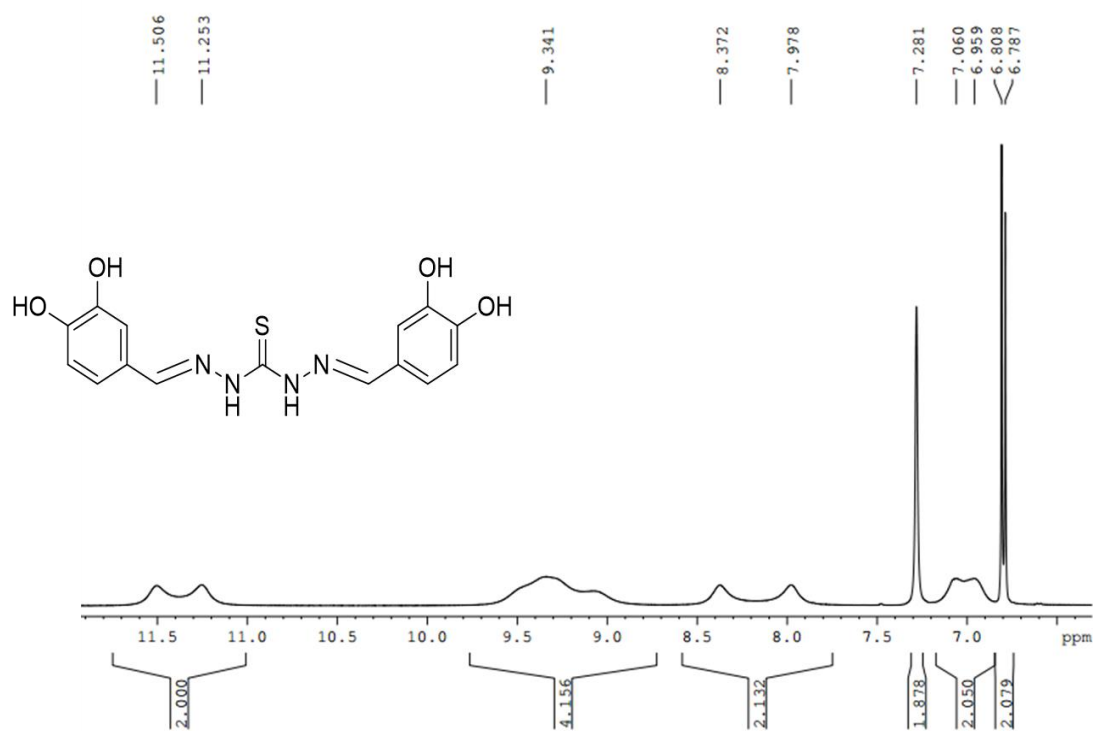


Figure 3.4 ^1H -NMR spectrum of 3,4-DCT.

3.1.2 Electrochemical impedance spectroscopy (EIS) studies

The inhibition efficiencies of the synthesised compounds were evaluated by electrochemical impedance spectroscopy (EIS) measurements at different immersion times. The spectra, presented in terms of Nyquist plots for the corrosion of 2024-T3 aluminium alloy in 3.5% NaCl solution in the absence and in the presence of the inhibitors, (namely 2-MHC, 2,4-DHC, 2,3,4-THC, 3,4-DHC and 3,4-DCT), (1 mM) at different immersion times are shown in Figure 3.5.

The Nyquist plots shown in Figure 3.5 are associated with a large capacitive loop at higher frequency (HF) region and a small capacitive loop at lower frequency (LF) region. The higher frequency capacitive loop could be accounted for the charge transfer reaction during the corrosion process occurring at the metal/oxide/electrolyte interface. The charge transfer occurs through the formation of Al^{3+} , OH^- and O^{2-} at the metal/surface film/electrolyte interface. The second capacitive loop at the lower frequency region could be due to the diffusion of ions or electrolyte ingress through the corrosion product/inhibitor layer (Dinodi and Shetty 2014). The Nyquist plot for the corrosion of the alloy retains its shape on the addition of the inhibitors, but the diameter of the loop increases in the presence of inhibitors, indicating the inhibitive action of inhibitors on the corrosion process, without altering the mechanism of corrosion.

The impedance spectra were analyzed by using appropriate equivalent circuits (EC) that tentatively model the physical processes occurring at the metal-electrolyte interface and give an insight in understanding the electrochemical reactions taking place at the electrode/electrolyte interface. The ECs used to analyze the impedance spectra in the absence and in the presence of the inhibitors are shown in Figure 3.6

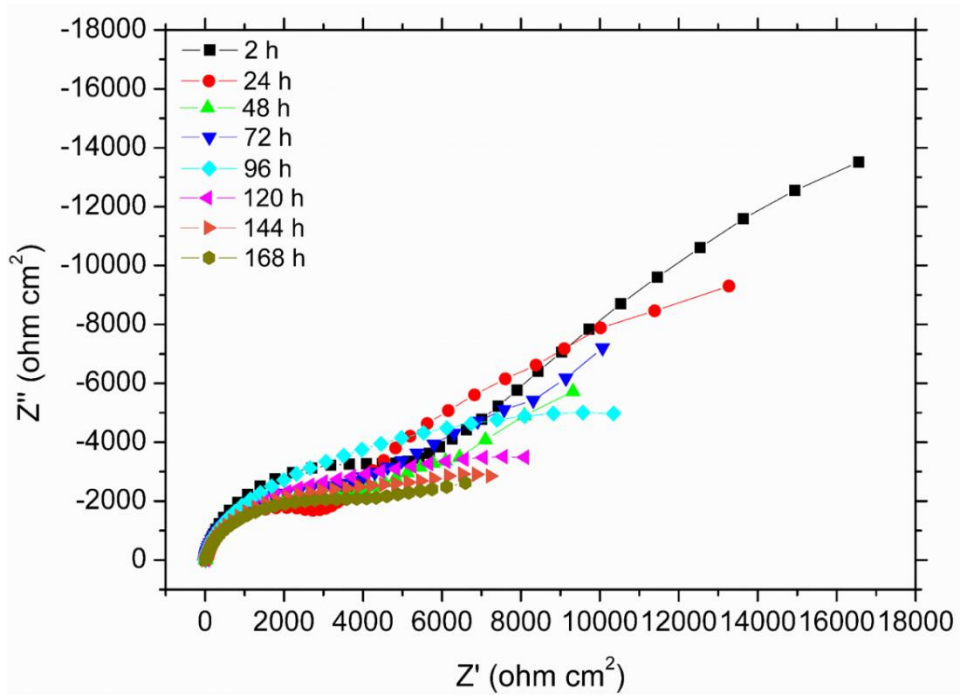


Figure 3.5 (a) Nyquist plots for the corrosion of AA2024-T3 at different immersion times in 3.5 % NaCl solution.

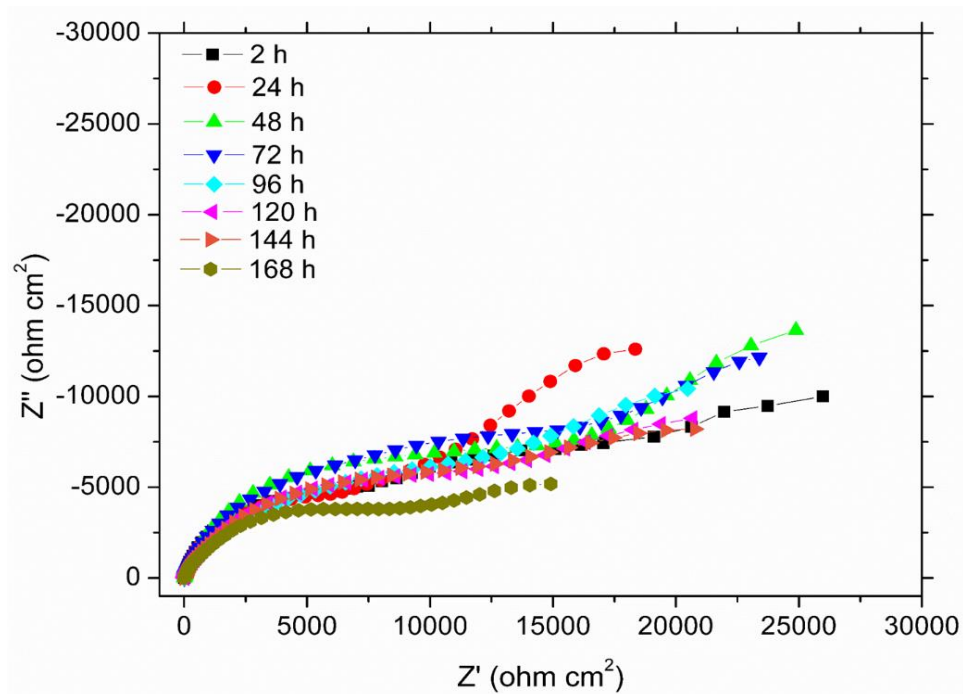


Figure 3.5 (b) Nyquist plots for the corrosion of AA2024-T3 at different immersion times in 3.5 % NaCl solution in the presence of 1 mM of 2-MHC.

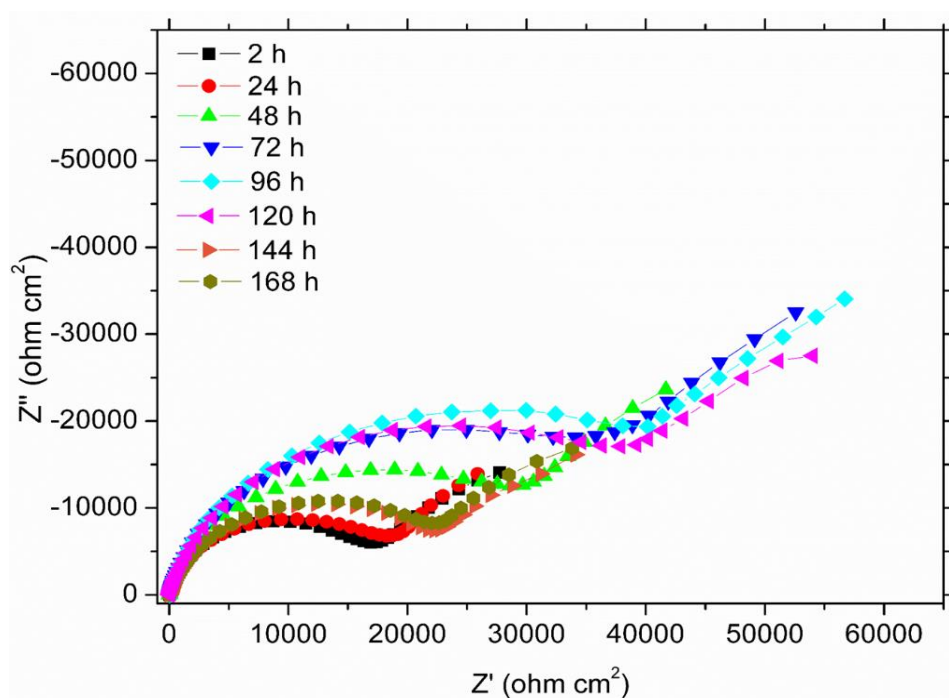


Figure 3.5 (c) Nyquist plots for the corrosion of AA2024-T3 at different immersion times in 3.5 % NaCl solution in the presence of 1 mM of 2,4-DHC.

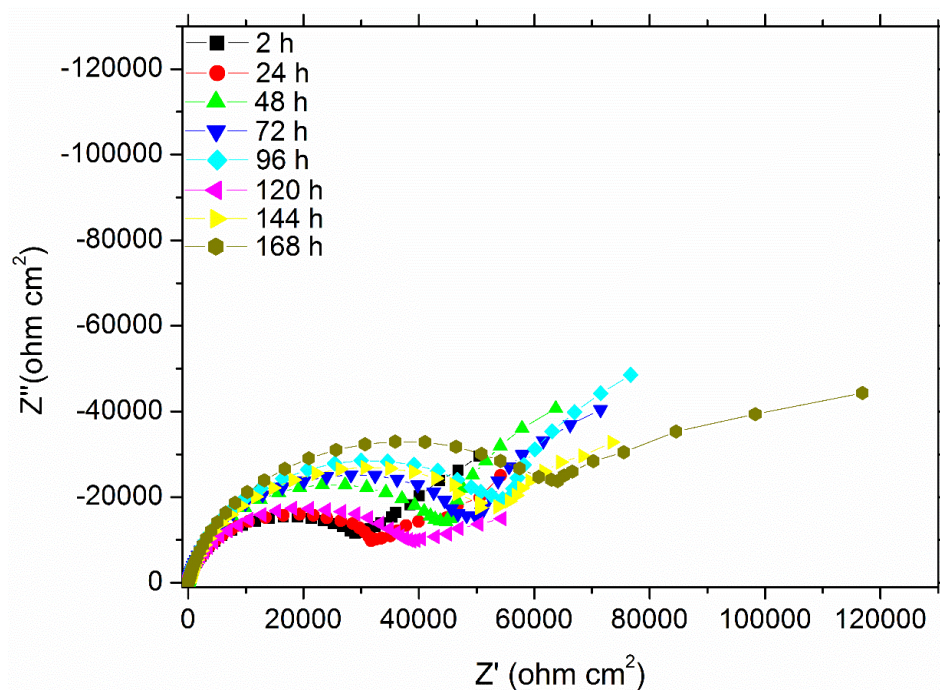


Figure 3.5 (d) Nyquist plots for the corrosion of AA2024-T3 at different immersion times in 3.5 % NaCl solution in the presence 1 mM of 2,3,4-THC.

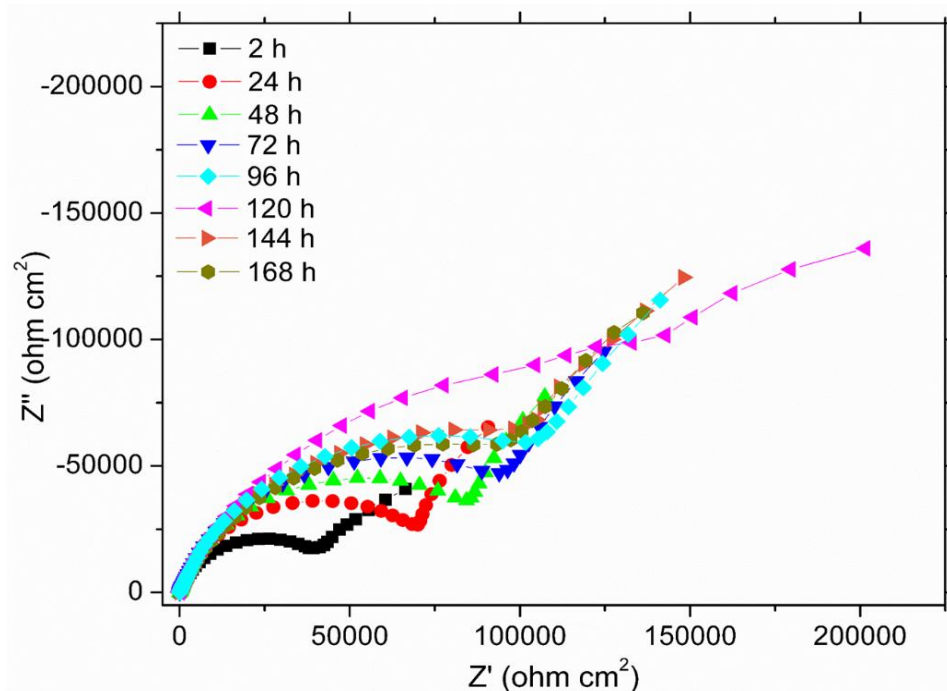


Figure 3.5 (e) Nyquist plots for the corrosion of AA2024-T3 at different immersion times in 3.5 % NaCl solution in the presence of 1 mM of 3,4-DHC.

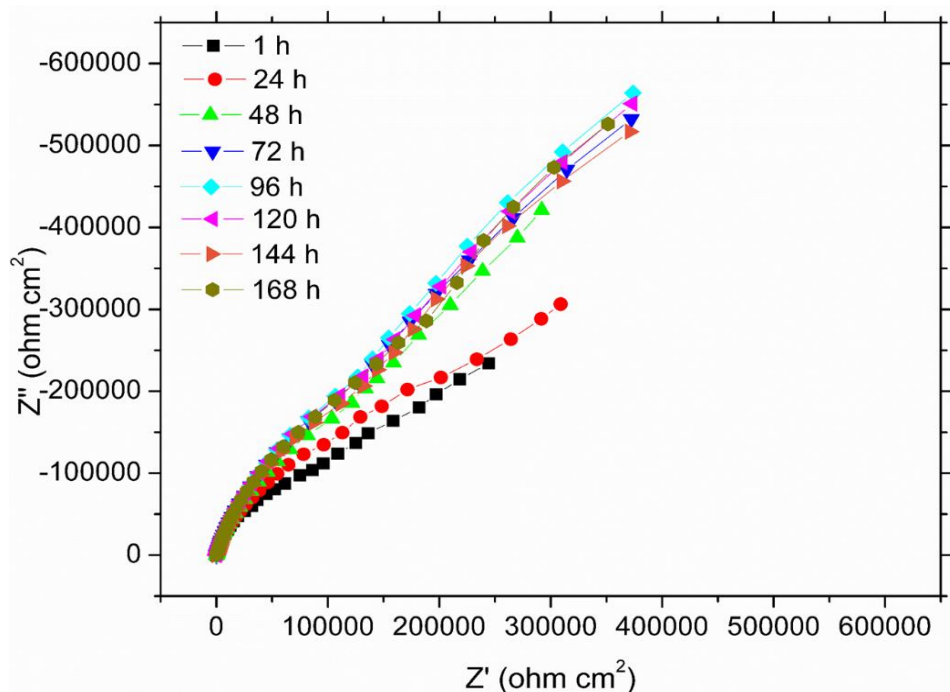


Figure 3.5 (f) Nyquist plots for the corrosion of AA2024-T3 at different immersion times in 3.5 % NaCl solution in the presence of 1 mM of 3,4-DCT.

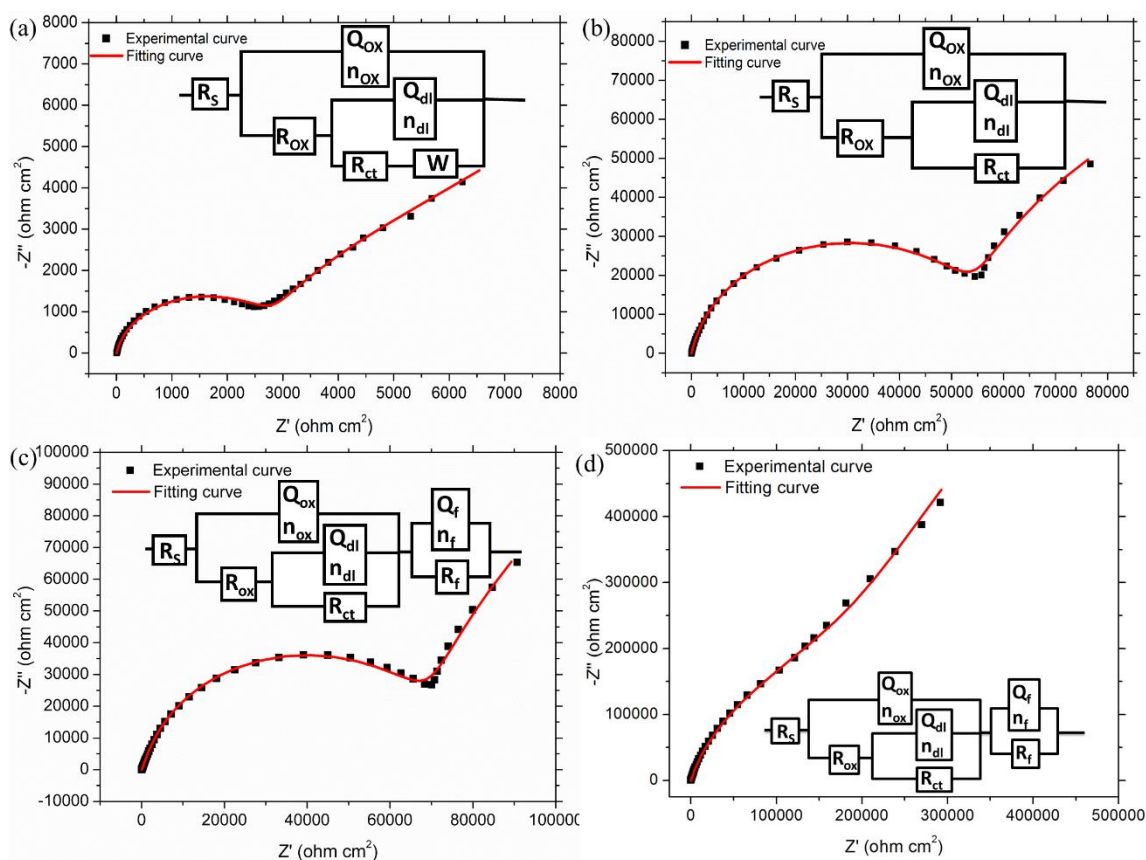


Figure 3.6 Equivalent circuits used for fitting the experimental EIS spectra of AA2024-T3 in 3.5 % NaCl solution, (a) in the absence of inhibitors; (b) in the presence of inhibitors 2-MHC, 2,4-DHC and 2,3,4-THC (c) in the presence of 3,4-DHC (d) in the presence of 3,4-DCT.

In the absence of the inhibitors, the equivalent circuit (Figure 3.6 a) comprises of 6 elements, namely, solution resistance (R_{sol}), resistance of the surface film of oxide layer (R_{ox}), capacitance of the surface film in terms of a constant phase element, CPE, (Q_{ox}), double layer capacitance (Q_{dl}), charge transfer resistance (R_{ct}) and Warburg resistance (W) due to the ionic diffusion of a part of the corrosion product. The CPE is used in place of the ideal capacitive element for a better fit of depressed capacitive loops, resulting from frequency dispersion due to the inhomogeneous nature of the electrode surface (Jüttner 1990). In the presence of all the inhibitors, the Warburg resistance disappears as the inhibitor layer does not allow the ionic diffusion.

In the presence of 3,4-DHC and 3,4-DCT, along with the disappearance of Warburg resistance, an additional time-constants appears as shown in Figure 3.6 c and

Figure 3.6 d. The additional time constant is due to the formation of an adsorbed inhibitor layer on the alloy surface. The additional circuit components include the film resistance (R_f) of the adsorbed inhibitor film and the capacitance (Q_f) due to the dielectric nature of the inhibitor layer. The real capacitance after accounting for inhomogeneity of the electrode surface, is deduced using the following relation (Eq. (3.1)) (Mansfeld et al. 1992).

$$C = Q (\omega_{\max})^{n-1} \quad (3.1)$$

where Q is the CPE constant, ω_{\max} is the frequency at which the imaginary part of the impedance (Z'') has a maximum and n is a CPE exponent which is a measure of the unevenness of the electrode surface.

The inhibition efficiency of the inhibitor was calculated from the polarization resistance (R_p), which is inversely proportional to the corrosion rate, according to the following expression (Eq. (3.2)).

$$\eta(\%) = \frac{R_{p(inh)} - R_p}{R_{p(inh)}} \times 100 \quad (3.2)$$

where, $R_{p(inh)}$ and R_p are the polarization resistances in the presence and in the absence of the inhibitor. The polarization resistance values in the absence of the inhibitors and in the presence of inhibitors, 2-MHC, 2,4-DHC and 2,3,4-THC, were calculated from the ECs in Figure 3.6, using Eq. (3.3).

$$R_p = R_{ox} + R_{ct} \quad (3.3)$$

In the presence of inhibitors, 3,4-DHC and 3,4-DCT the R_p value were calculated using Eq. (3.4).

$$R_p = R_{ox} + R_{ct} + R_f \quad (3.4)$$

The impedance parameters for the corrosion of 2024-T3 aluminium alloy in 3.5% NaCl solution in the absence and in the presence of the inhibitors are presented in Table 3.1. From Figure 3.5, it is observed that the presence of inhibitors in the corrosion medium decreases the corrosion rate, as indicated by the increased diameter of the semicircular

loops of the Nyquist plots. Similar trend is also indicated by the increased R_p values for the corrosion of the alloy in the presence of the inhibitor compounds. The above facts are indicative of the inhibitive action of the inhibitor compounds.

From Figure 3.5 a, it is observed that the diameter of the capacitive loop decreases with the increase in immersion time, which is accounted for the increased dissolution of the protective oxide layer on the surface of the alloy surface, leading to increased corrosion on the alloy surface. The same trend is reflected by the decreasing R_p values with the exposure time as shown in Table 3.1. In the presence of inhibitors, as seen in Figure 3.5, the diameter of the capacitive loop increases with the increase in exposure time and decreases on further increase in the exposure time. The initial increase in the diameters of the loops and corresponding decrease in corrosion rate, may be attributed to the increasing adsorption of the inhibitor molecule with time on the alloy surface. The subsequent decrease in the diameters of the loops may be due to the subsequent desorption of the inhibitor molecules from the surface of the alloy and also due to the enhanced corrosion on the relatively small surface areas on the alloy surface, which are not covered by the inhibitor layers.

The variations of polarization resistance (R_p) and inhibition efficiency (η %) with exposure time for the corrosion of the alloy in the absence and presence of the inhibitors are shown in Figure 3.7 and Figure 3.8, respectively, which corroborate the above observations. In the presence of 2,4-DHC, 2,3,4-THC and 3,4-DCT R_p increases steadily up to 96 h, and in the presence of 3,4-DHC R_p increases steadily up to 120 h indicating a gradual development of inhibitor film on the alloy surface (Hongwei Shi et al. 2011). However, in the presence of MHC, the trend is not regular. It is clear from the figure that even at higher exposure period of 168 h, 3,4-DCT molecules show very high corrosion protection efficiency.

Figures 3.7 and 3.8 and Table 3.1 also demonstrate that R_p value and inhibition efficiency increase in the presence of inhibitors in the order: 2-MHC < 2,4-DHC < 2,3,4-THC < 3,4-DHC < 3,4-DCT.

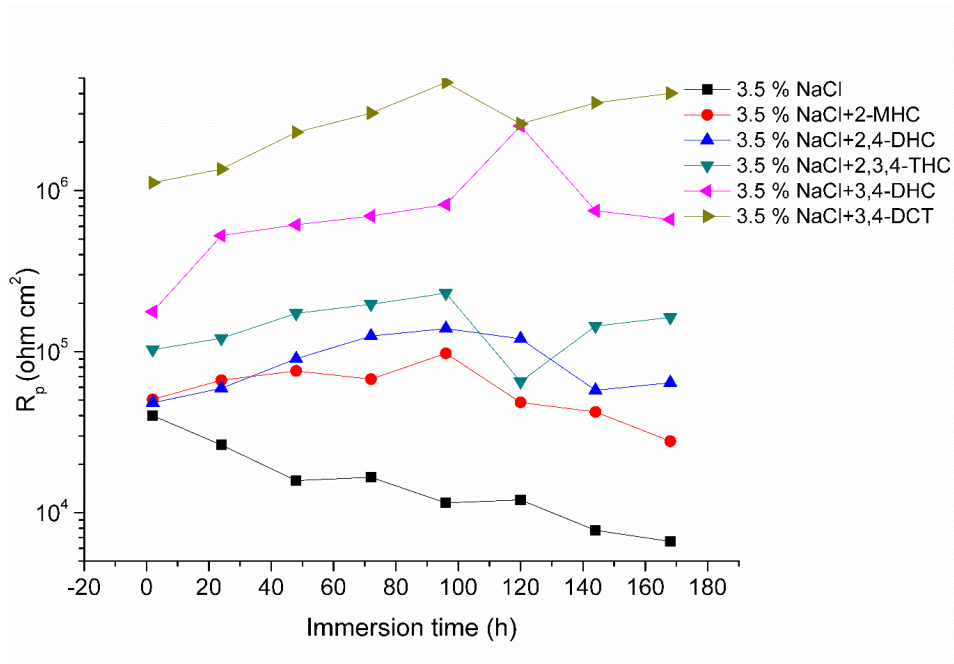


Figure 3.7 Variation of polarization resistance of AA2024-T3 with immersion time in 3.5 % NaCl solution in the absence and in the presence of inhibitors.

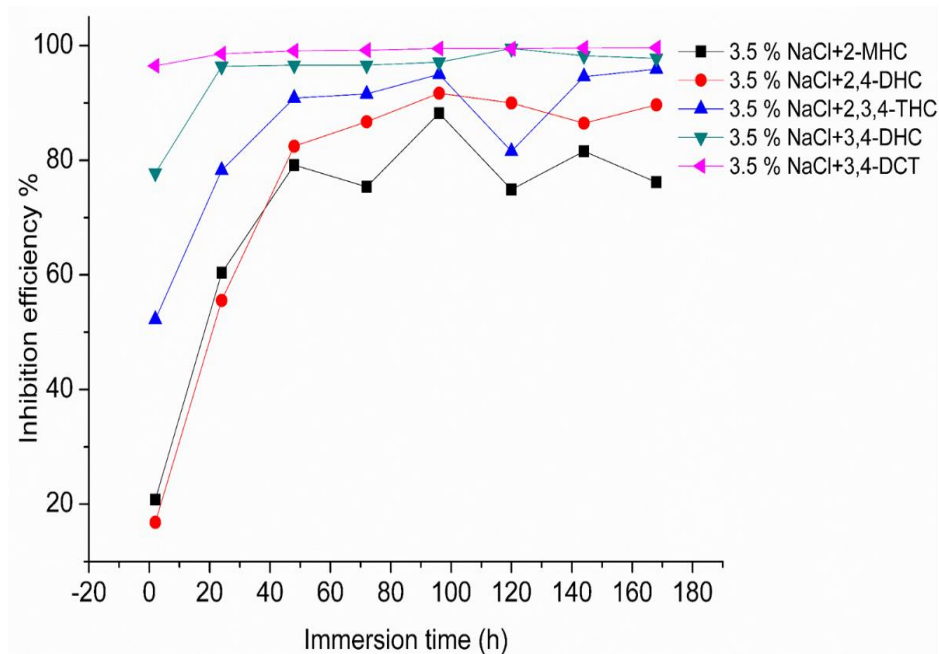


Figure 3.8 Variation of inhibition efficiency of inhibitors on AA2024-T3 with immersion time in 3.5 % NaCl solution.

The inherent limitation of the Nyquist plots is that they do not show the exact frequencies at which the impedance values are measured. This limitation is overcome by plotting Bode plots, which display frequency specific impedance behaviour of the system. Figure 3.9 represents the Bode magnitude and Bode phase angle plots for the corrosion of 2024-T3 aluminium alloy in 3.5% NaCl solution in the absence and in the presence of inhibitors, at different exposure times. It is seen from the magnitude plots that the low frequency impedance modules ($|Z|$), which is the measure of protection against corrosion, has increased in the presence of all the five inhibitors. Similarly, it is also observed that the medium frequency phase maximum (θ_{\max}) increases in the presence of the inhibitors. The medium frequency behaviour is due to the diffusion through the surface films and hence the increase in θ_{\max} implies a better barrier effect by the inhibitor layers against the corrosive ingress (Gao et al. 2010).

It can be seen from the phase angle plots that in the absence of inhibitors, the impedance spectra represents two time constants at approximately 0.018 Hz and 25 Hz. The two time constants can be assigned to the electron charge transfer process across the double layer at the interface and to the native oxide layer (Rosero-Navarro et al. 2008). In the presence of inhibitors (2-MHC, 2,4-DHC and 2,3,4-THC), the middle frequency time constant associated with the Bode phase angle plot is extended over a wide range of frequencies (Figure 3.9(b – d)), revealing that it is composed of both the adsorbed inhibitor layer resistance and the native aluminium oxide layer resistance.

In the presence of 3,4-DHC and 3,4-DCT, the phase angle plot clearly represents three time constants at approximately 10^4 Hz, 1 Hz and 0.015 Hz. The three time constants can be assigned to the electron charge transfer process across the double layer at the interface, to the native oxide layer and to the inhibitor layer. The medium frequency phase maximum (θ_{\max}) is distributed over a wide range of frequencies (Figure 3.9 e and Figure 3.9 f), confirming the presence of the inhibitor layer on the alloy surface. The frequency spread of the phase angle is maximum in the presence of 3,4-DCT in comparison with those in the presence of 3,4-DHC, 2,3,4-THC, 2,4-DHC and 2-MHC.

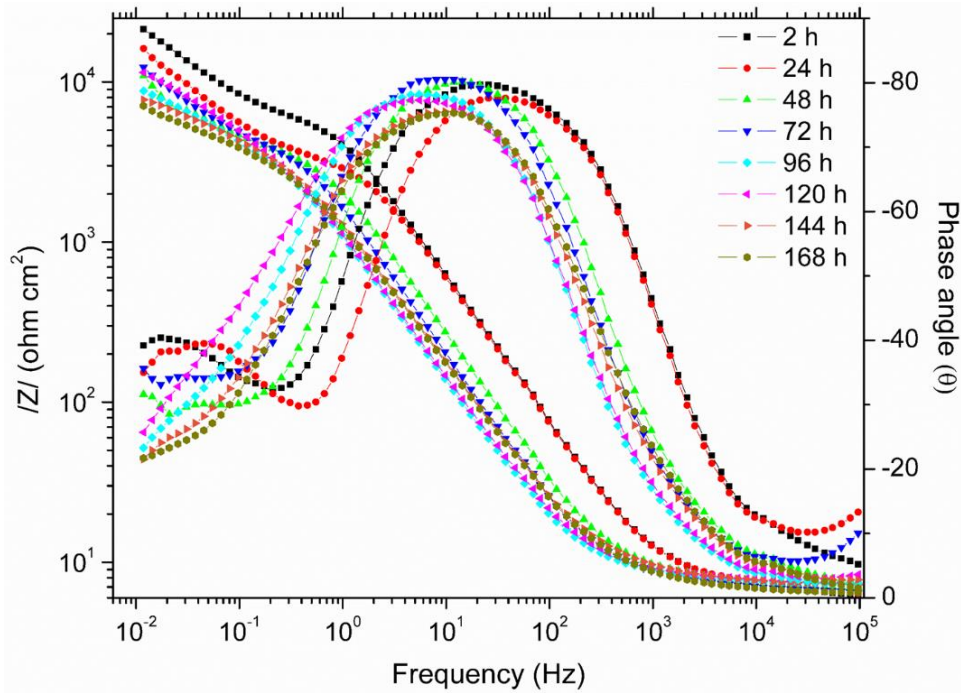


Figure 3.9 (a) Bode plots for the corrosion of AA2024-T3 at different immersion times in 3.5 % NaCl solution.

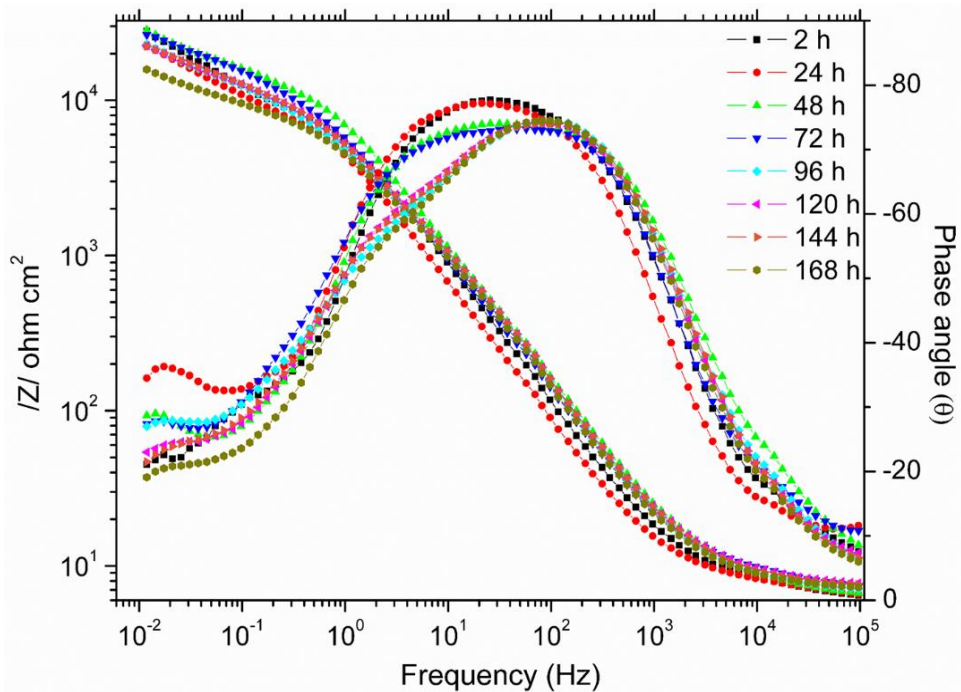


Figure 3.9 (b) Bode plots for the corrosion of AA2024-T3 at different immersion times in 3.5 % NaCl solution in the presence of 1 mM of 2-MHC.

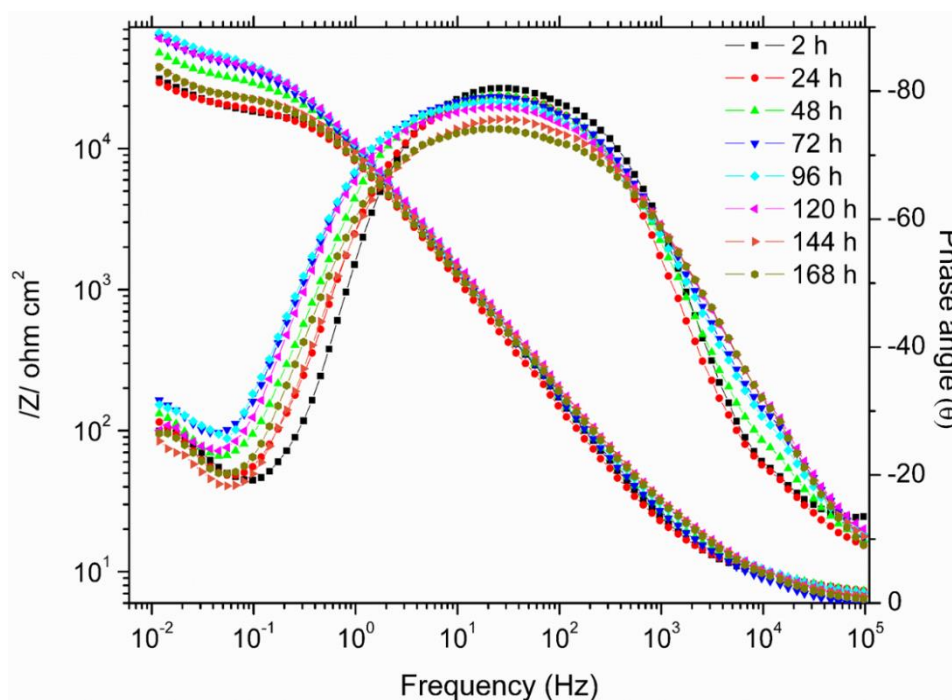


Figure 3.9 (c) Bode plots for the corrosion of AA2024-T3 at different immersion times in 3.5 % NaCl solution in the presence of 1 mM of 2,4-DHC.

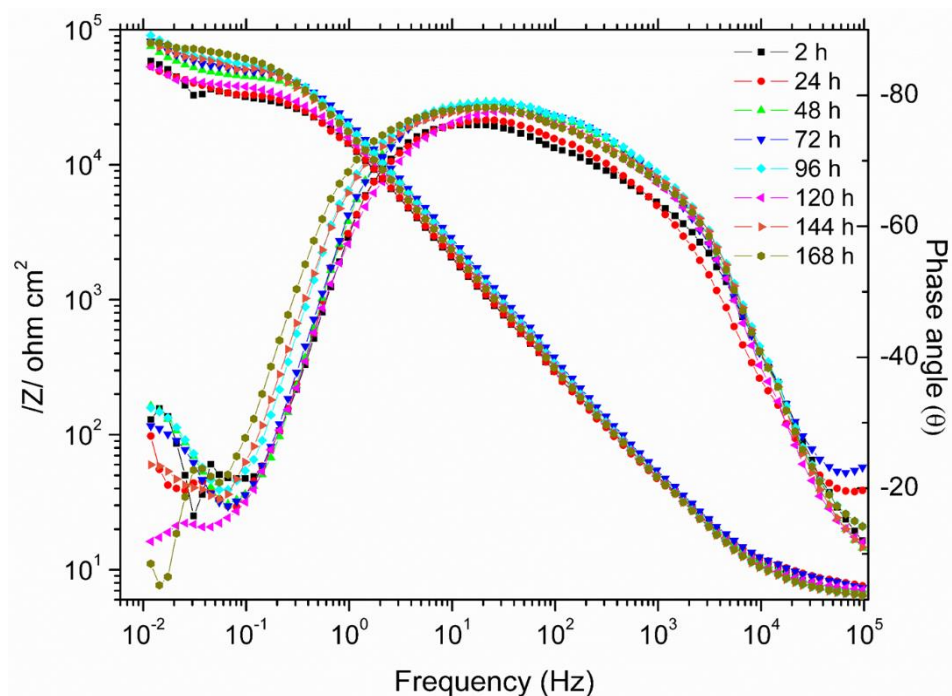


Figure 3.9 (d) Bode plots for the corrosion of AA2024-T3 at different immersion times in 3.5 % NaCl solution in the presence of 1 mM of 2,3,4-THC.

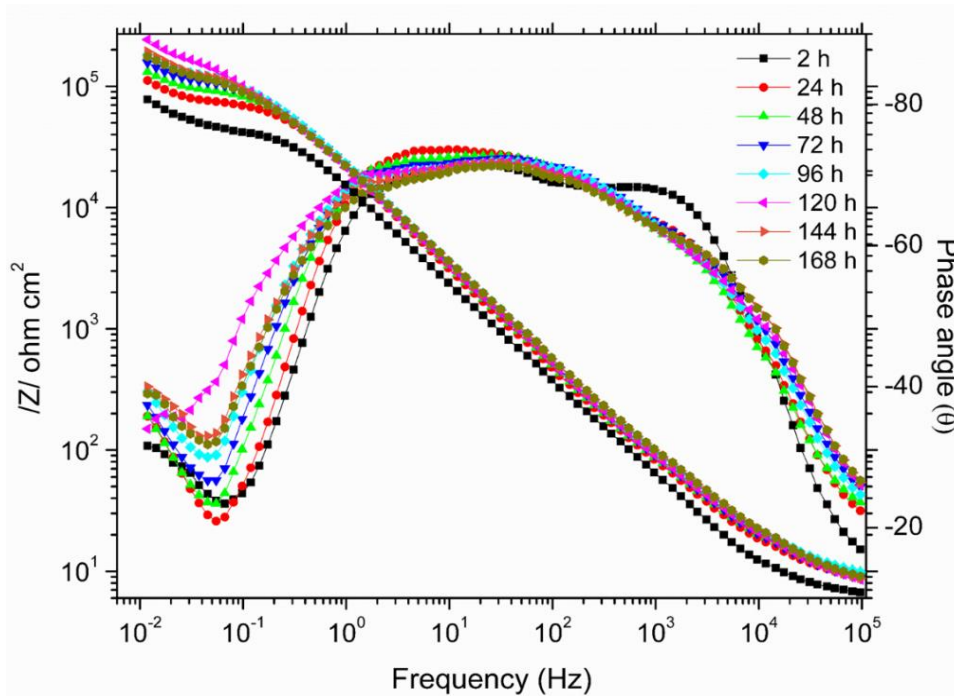


Figure 3.9 (e) Bode plots for the corrosion of AA2024-T3 at different immersion times in 3.5 % NaCl solution in the presence of 1 mM of 3,4-DHC.

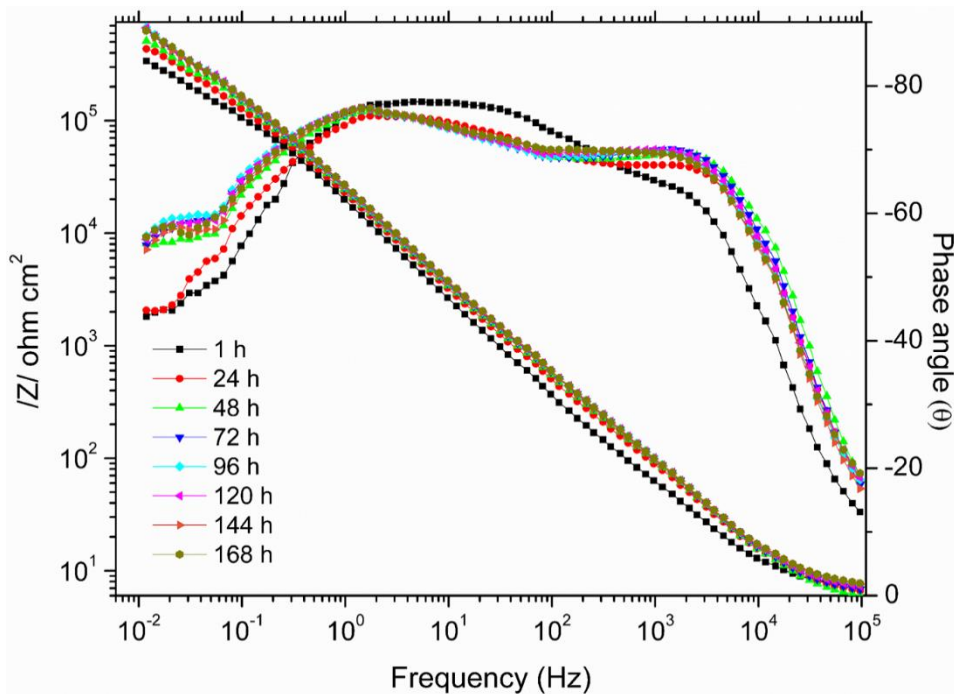


Figure 3.9 (f) Bode plots for the corrosion of AA2024-T3 at different immersion times in 3.5 % NaCl solution in the presence of 1 mM of 3,4-DCT.

Table 3.1 The electrochemical impedance parameters for the corrosion of AA2024-T3 in the absence and in the presence of inhibitors in 3.5 % NaCl solution at different immersion times.

Medium	Immersion Time (h)	R_{ox} ($\Omega \text{ cm}^2$)	R_{ct} ($\Omega \text{ cm}^2$)	R_f ($\Omega \text{ cm}^2$)	R_p ($\Omega \text{ cm}^2$)	η (%)
3.5 % NaCl	2	7.29×10^3	3.27×10^4	-	4×10^4	-
	24	3.94×10^3	2.23×10^4	-	2.63×10^4	-
	48	4.52×10^3	1.13×10^4	-	1.58×10^4	-
	72	5.35×10^3	1.12×10^4	-	1.66×10^4	-
	96	5.44×10^3	6.06×10^3	-	1.15×10^4	-
	120	7.24×10^3	4.76×10^3	-	1.20×10^4	-
	144	5.3×10^3	2.48×10^3	-	7.77×10^3	-
3.5 % NaCl + 2-MHC	2	1.98×10^4	3.07×10^4	-	5.05×10^4	20.79
	24	1.02×10^4	5.62×10^4	-	6.64×10^4	60.35
	48	1.65×10^4	5.95×10^4	-	7.60×10^4	79.18
	72	1.47×10^4	5.27×10^4	-	6.74×10^4	75.37
	96	1.29×10^4	8.47×10^4	-	9.76×10^4	88.21
	120	1.087×10^4	3.75×10^4	-	4.84×10^4	74.90
	144	1.076×10^4	3.14×10^4	-	4.22×10^4	81.57
3.5 % NaCl + 2,4-DHC	2	1.96×10^4	2.84×10^4	-	4.81×10^4	16.83
	24	2.10×10^4	3.82×10^4	-	5.92×10^4	55.55
	48	3.52×10^4	5.50×10^4	-	9.02×10^4	82.46
	72	4.73×10^4	7.76×10^4	-	1.25×10^5	86.72
	96	5.33×10^4	8.57×10^4	-	1.39×10^5	91.72
	120	4.96×10^4	7.04×10^4	-	1.20×10^5	90
	144	2.69×10^4	3.06×10^4	-	5.75×10^4	86.48
168	2.81×10^4	3.61×10^4	-	6.42×10^4	89.68	

Medium	Immersion Time (h)	R_{ox} ($\Omega \text{ cm}^2$)	R_{ct} ($\Omega \text{ cm}^2$)	R_f ($\Omega \text{ cm}^2$)	R_p ($\Omega \text{ cm}^2$)	η (%)
3.5 % NaCl + 2,3,4-THC	2	3.98×10^4	6.34×10^4	-	1.03×10^5	52.23
	24	4.07×10^4	8.03×10^4	-	1.21×10^5	78.26
	48	5.34×10^4	1.19×10^5	-	1.73×10^5	90.86
	72	5.97×10^4	1.37×10^5	-	1.97×10^5	91.57
	96	6.76×10^4	1.63×10^5	-	2.31×10^5	95.02
	120	4.33×10^4	2.18×10^4	-	6.51×10^4	81.56
	144	6.53×10^4	7.87×10^4	-	1.44×10^5	94.60
	168	8.15×10^4	8.21×10^4	-	1.63×10^5	95.93
3.5 % NaCl + 3,4 DHC	2	3.95×10^4	1.35×10^5	2.79×10^3	1.77×10^5	77.79
	24	1.30×10^4	4.51×10^5	6.14×10^4	5.26×10^5	96.38
	48	1.62×10^4	5.24×10^5	7.42×10^4	6.14×10^5	96.59
	72	2.05×10^4	5.91×10^5	8.38×10^4	6.95×10^5	96.60
	96	2.55×10^4	7.03×10^5	9.17×10^4	8.20×10^5	97.13
	120	3.62×10^4	2.11×10^6	4.52×10^4	2.52×10^6	99.51
	144	4.31×10^4	6.36×10^5	7.02×10^4	7.49×10^5	98.26
	168	3.13×10^4	5.53×10^5	7.72×10^4	6.62×10^5	97.80
3.5 % NaCl + 3,4-DCT	2	6.47×10^3	4.31×10^5	6.88×10^5	1.12×10^6	96.50
	24	1.14×10^3	4.70×10^5	8.92×10^5	1.36×10^6	98.60
	48	1.92×10^3	2.64×10^5	2.04×10^6	2.30×10^6	99.09
	72	1.26×10^3	2.79×10^5	2.75×10^6	3.03×10^6	99.22
	96	2.86×10^3	9.02×10^5	3.78×10^6	4.69×10^6	99.49
	120	2.33×10^3	2.79×10^5	2.02×10^6	2.30×10^6	99.46
	144	1.21×10^3	9.84×10^4	3.42×10^6	3.51×10^6	99.62
	168	1.16×10^3	8.78×10^4	3.94×10^6	4.02×10^6	99.63

3.1.3 Potentiodynamic polarization studies

The potentiodynamic polarization curves for the corrosion of 2024-T3 aluminium alloy after 2 h and 24 h immersion in 3.5% NaCl solution, in the absence and in the presence of inhibitors are shown in Figure 3.10 and Figure 3.11, respectively. The potentiodynamic polarization curves cannot be used for 2024-T3 aluminium alloy as a quantitative analysis because of localized corrosion (Lamaka et al. 2007). The cathodic and anodic polarization curves do not exhibit well defined Tafel regions. The nonexistence of distinct Tafel region in the cathodic polarization curve is due to the diffusion limitations of oxygen reduction reactions. On the anodic region, it is due to the presence of pitting potential. However, the polarization curves can be used for qualitative studies on the inhibition effects of the synthesised inhibitors.

The addition of inhibitors leads to the reduction of the cathodic current, indicating the decrease in the reduction of oxygen on copper rich intermetallics particles. Further, on increasing the exposure time (24 h), further dropping of cathodic current was observed due to the strong inhibition action of inhibitors on cathodic sites. These results suggest that, the inhibitor molecules are slowly adsorbed on the cathodic site, reducing the cathodic reaction.

The anodic polarization curves of AA204-T3 are associated with two breakdown potentials. The first breakdown potential could be related to the dissolution of secondary phase intermetallic particles and the second breakdown potential observed at more positive potential region could be attributed to the intergranular attack (Lamaka et al. 2007). After 2h immersion, slight variation of anodic currents is observed on the addition of inhibitor. The variation is much more defined after 24 h immersion. The addition of inhibitors decreases the anode density. The observations demonstrate, the ability of the inhibitors to control the metal dissolution from the alloy surface.

From Figure 3.10 and Figure 3.11 it can be observed that the addition of inhibitor makes the corrosion potential to shift towards both the anodic region and the cathodic region. However, the shift is not large enough to designate the inhibitors distinctly as

anodic inhibitor or cathodic inhibitor. Therefore, the inhibitors can be considered as mixed inhibitors.

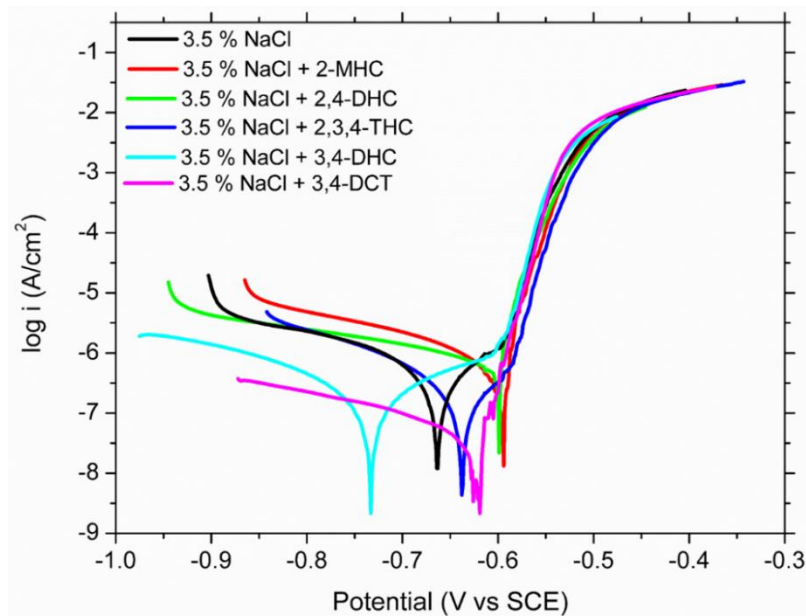


Figure 3.10 Potentiodynamic polarization curves for the corrosion of AA2024-T3 in 3.5 % NaCl solution in the absence and in the presence of inhibitors after 2 h immersion.

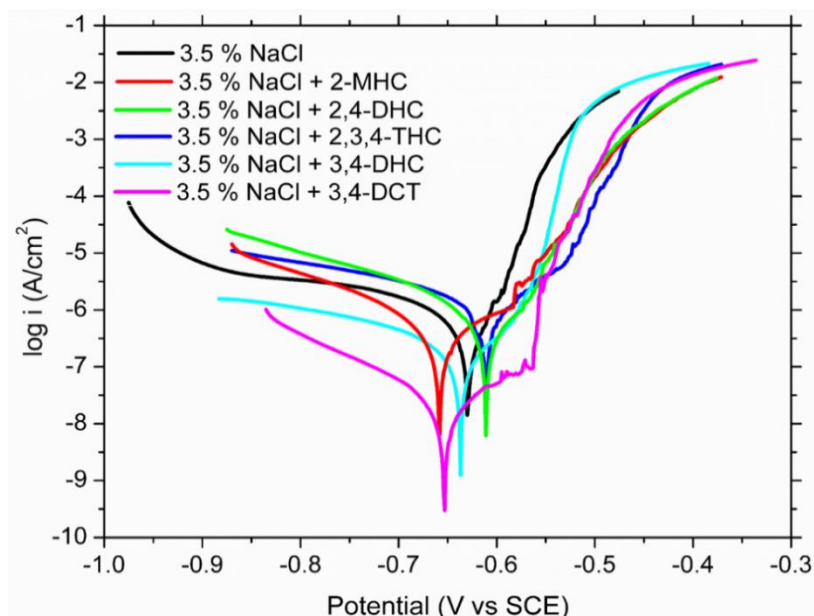


Figure 3.11 Potentiodynamic polarization curves for the corrosion of AA2024-T3 in 3.5 % NaCl solution in the absence and in the presence of inhibitors after 24 h immersion.

3.1.4 Surface morphology

The surface morphologies of the corroded 2024-T3 aluminium alloy samples in 3.5% NaCl solution, in the absence and presence of the inhibitors were analyzed by recording the FESEM images of the samples; and the surface compositions were determined from their EDX spectra. Figure 3.12 shows the FESEM images EDX spectra of the corroded surface of the alloy after 7 days of immersion in 3.5% NaCl solution in the absence of the inhibitors. The corresponding EDX results are summarized in Table 3.2. The FESEM image of the corroded alloy surface in the absence of the inhibitors (Figure 3.12(a)) depicts the degraded metal matrix.

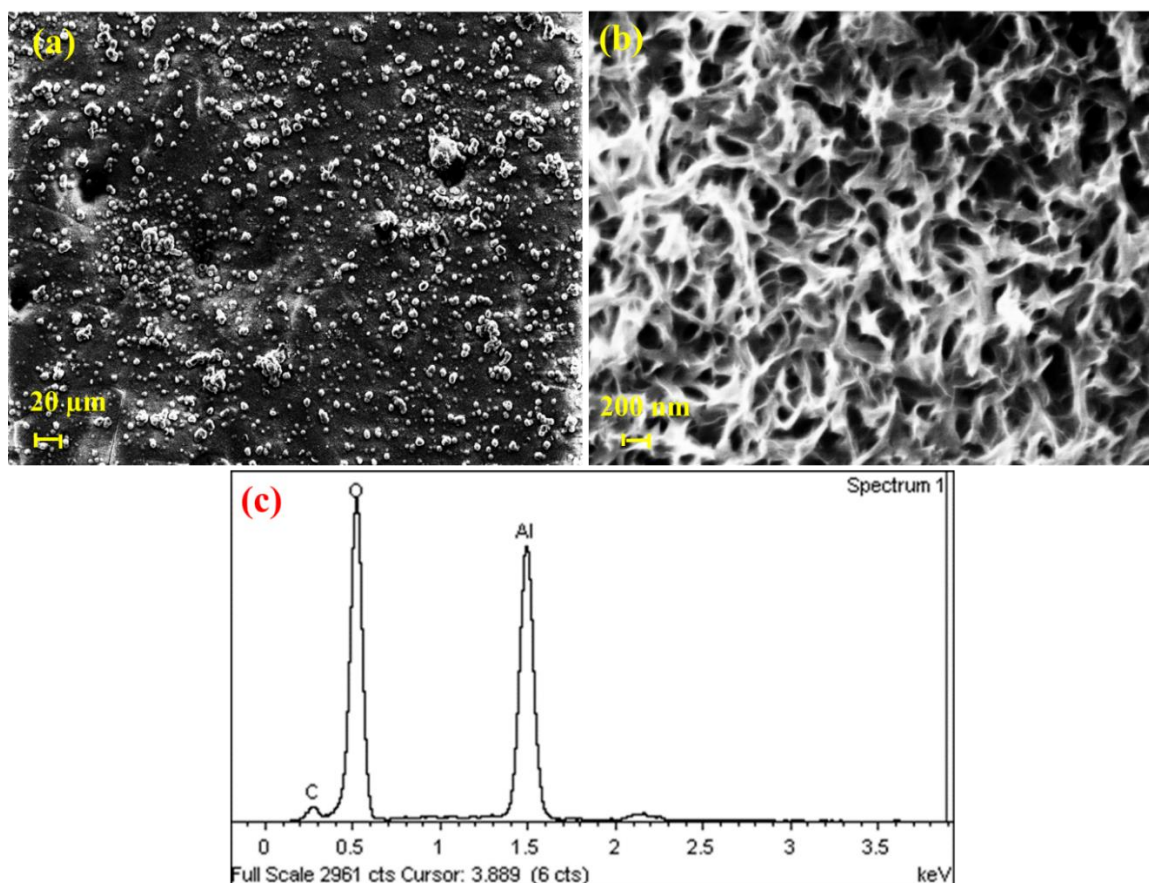


Figure 3.12 FESEM images and EDX spectra of AA2024-T3 alloy surface after 7 days of immersion in 3.5 % NaCl solution.

The EDX analysis results reveal the presence of Al and O on the surface of the alloy; the presence of high atomic percentage of O indicates the presence of corrosion

product such as $\text{Al}_2\text{O}_3/\text{Al}(\text{OH})_3$. The corroded surface appears to be micro porous in nature (Figure 3.12 b), which would permit the ingress of corrosion media to the underlying fresh alloy surface, continuing the corrosion process.

Table 3.2 EDX results of the elemental composition (atomic %) of AA2024-T3 surface after 7 days of immersion in 3.5 % NaCl solution in the absence and in the presence of inhibitors.

Medium	Al	Cu	Mg	O	C	N	S
3.5 % NaCl	23.96	-	-	67.58	8.46	-	-
3.5 % NaCl + 2-MHC	22.63	0.26	-	64.02	11.34	1.46	0.28
3.5 % NaCl + 2,4-DHC	63.27	1.84	0.92	17.80	15.04	0.90	0.23
3.5 % NaCl + 2,3,4-THC	67.13	1.65	0.97	7.14	19.79	3.12	0.20
3.5 % NaCl + 3,4-DHC	65.45	1.41	0.97	6.50	20.08	3.47	1.12
3.5 % NaCl + 3,4-DCT	67.86	1.78	0.91	5.35	17.98	5.11	1.02

The FESEM images, in the presence of the inhibitors, show that the aluminium alloy matrix is less deteriorated, without any severe corrosion attack by the medium, whereas, the corrosion around the intermetallic particles is still observed to some extent (Figure 3.13 and Figure 3.14). It is also observed from the images that in the presence of 2,3,4-THC, 3,4-DHC and 3,4-DCT, the alloy surface is very smooth and no distinct corrosion cavities are observed around the intermetallic particles. The alloy surface in the presence of 3,4-DCT, 3,4 DHC and 2,3,4-THC is with maximum smoothness and least defected intermetallic particles, indicating its better corrosion inhibition capability than 2-MHC and 2,4-DHC. The EDX results (Table 3.2) show a relatively lower oxygen content on the alloy surface, in the presence of inhibitors. Also, the presence of C, N and S confirms the presence of inhibitor molecules on the surfaces of the alloy. Therefore it is not unjustified to assume the formation of inhibitor layers on the surface of the alloy, acting as barriers between the corrosion media and the alloy surface.

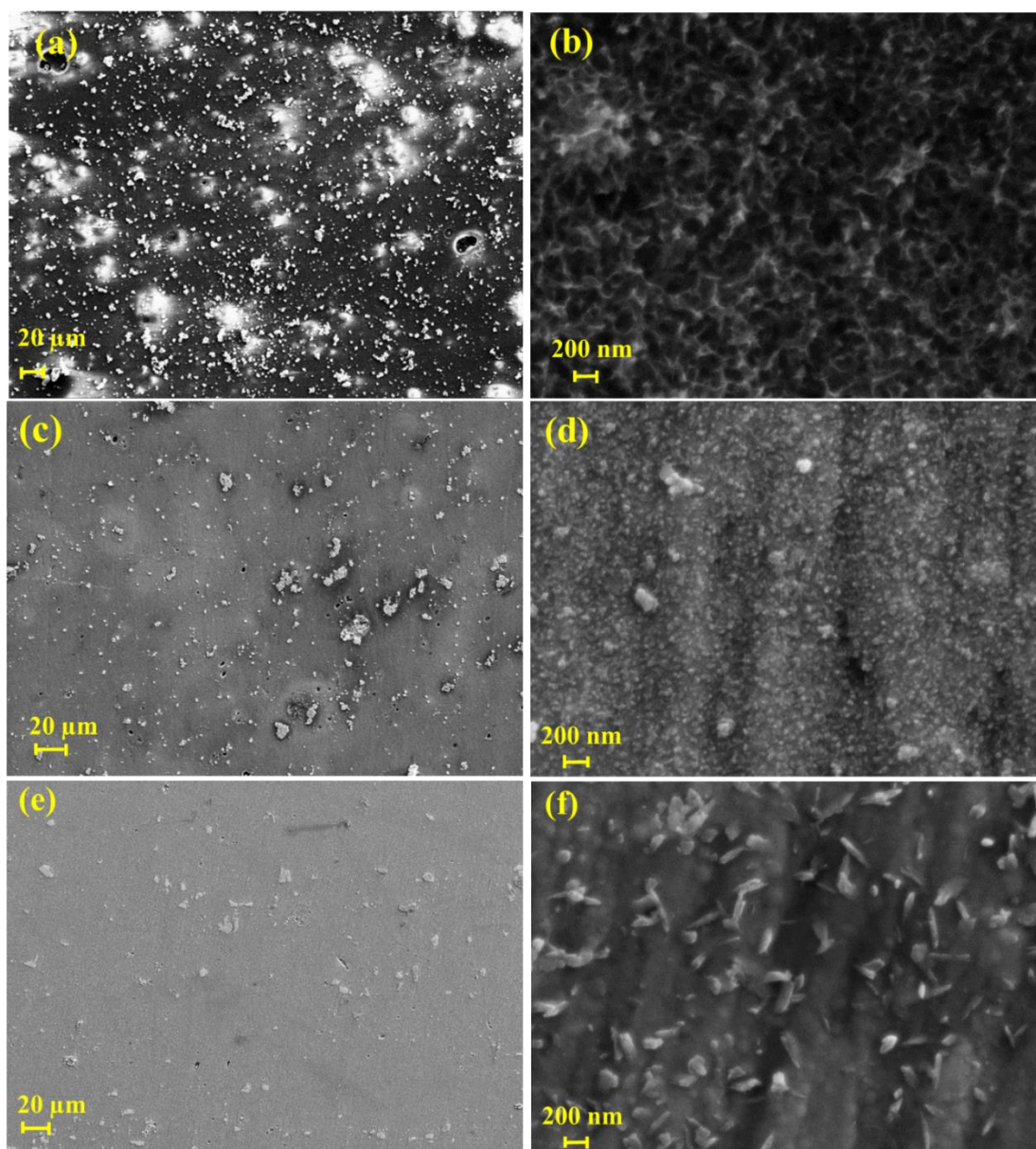


Figure 3.13 FESEM images of AA2024-T3 alloy surface after 7 days of immersion in: (a) (b) 3.5 % NaCl solution + 2-MHC, (c) (d) 3.5 % NaCl solution + 2,4-DHC, (e) (f) 3.5 % NaCl solution + 2,3,4-THC.

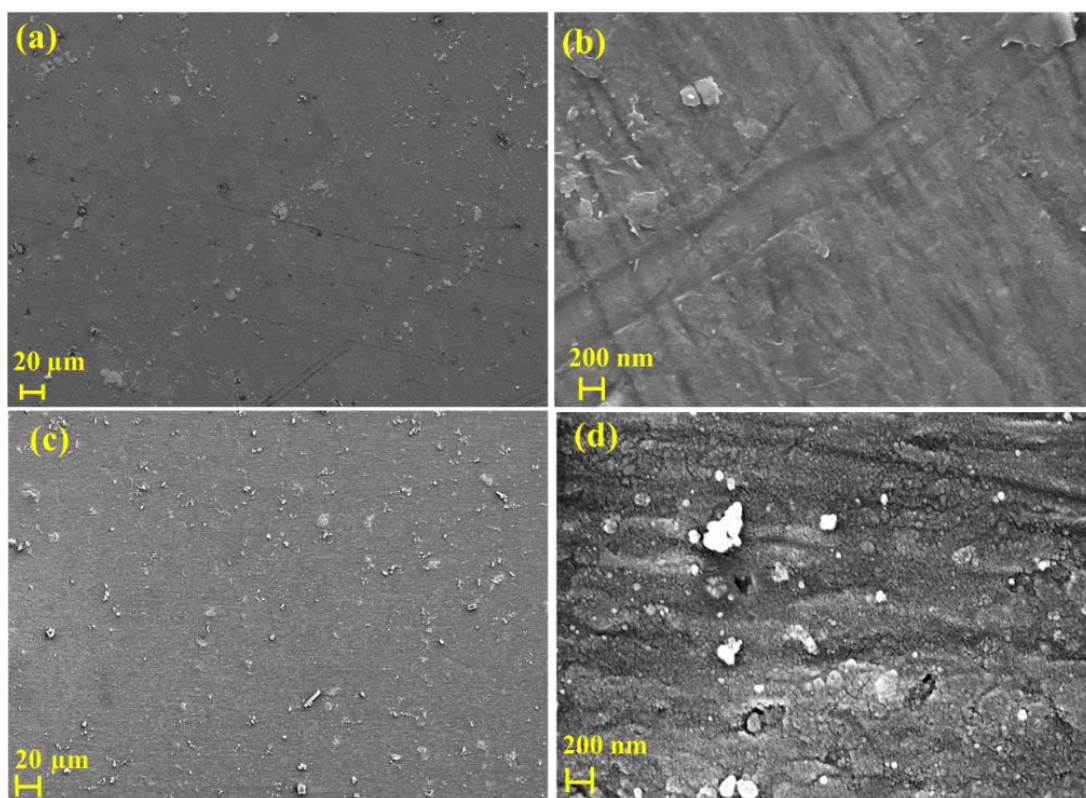


Figure 3.14 FESEM images of AA2024-T3 alloy surface after 7 days of immersion in: (a) (b) 3.5 % NaCl solution + 3,4-DHC, (c) (d) 3.5 % NaCl solution + 3,4-DCT.

3.1.5 X-ray photoelectron spectroscopy

The XPS survey spectra of the aluminium alloy surfaces after 7 days of immersion in 3.5% NaCl, in the absence and in the presence of inhibitors, are shown in Figure 3.15. The corresponding atomic percentages of Al, O, C and N are listed in Table 3.3. The presence of oxygen content on the surface, in the absence of the inhibitors, comes from the corrosion product such as $\text{Al}_2\text{O}_3/\text{Al}(\text{OH})_3$. In the presence of the inhibitors, the O of $-\text{OH}$ groups in the inhibitors also contribute to the oxygen content. The O1s band is composed of multiple parts, the O1s peak at ~ 531 eV corresponding to Al_2O_3 and the peak at ~ 532 eV corresponding to $-\text{OH}$ group from $\text{Al}(\text{OH})_3$ (Djebaili et al. Bo et al. 1993).

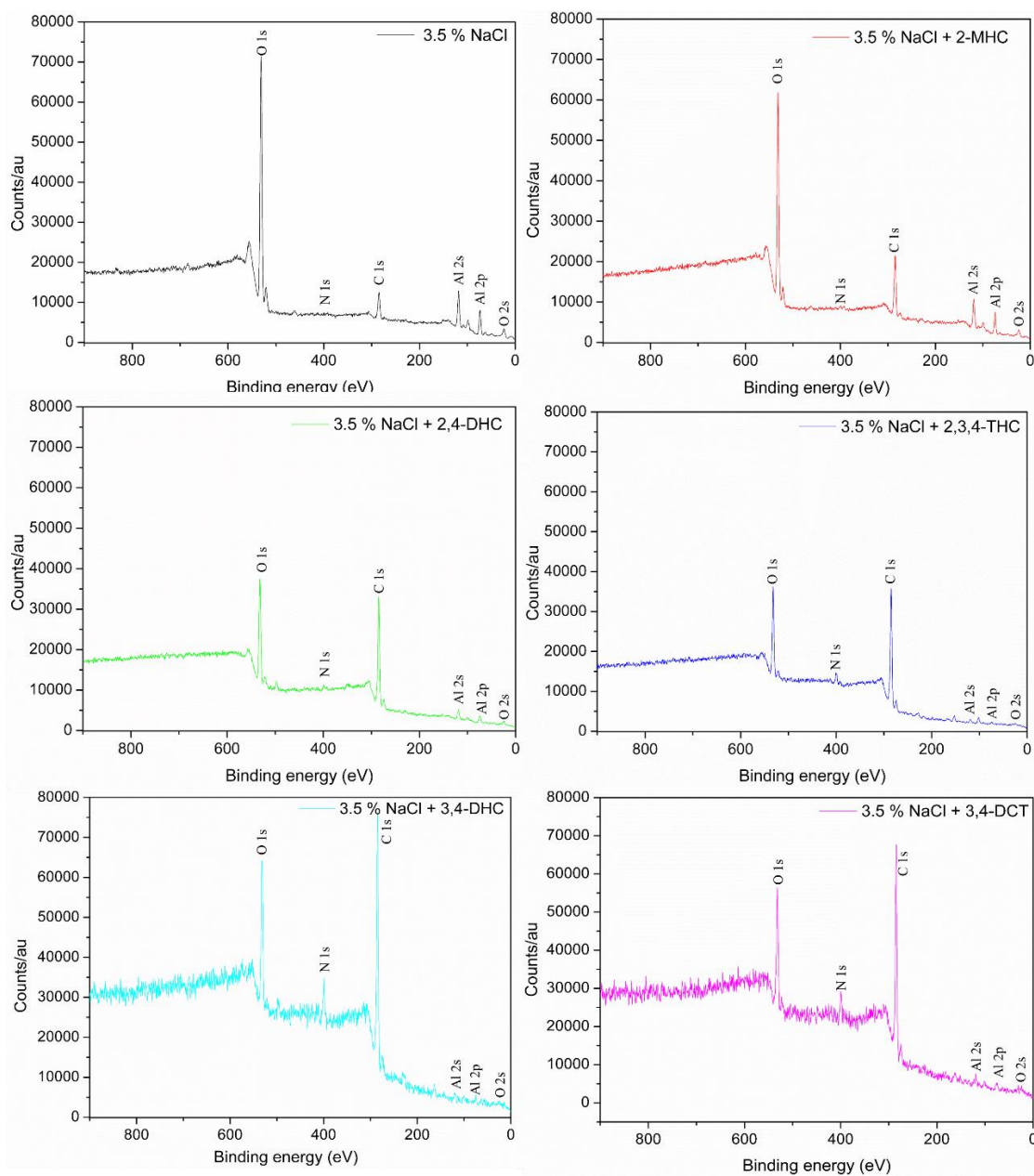


Figure 3.15 XPS survey spectrum of AA2024-T3 surfaces after 7 days of immersion in 3.5 % NaCl solution in the absence and in the presence of the inhibitors.

The magnified individual peaks corresponding to O 1s, Al 2p, N 1s and C 1s are shown in Figure 3.16. In the absence of inhibitors, the center of O 1s peak (Figure 3.16(a)) appears at 531.15 eV and is composed of various peaks. The deconvoluted peak of O1s is shown in Figure 3.17, consisting of a O1s peak at 530.75 eV corresponding to Al_2O_3 and another peak at 531.90 eV corresponding to hydroxyl (-

OH) group from $\text{Al}(\text{OH})_3$. In the presence of the inhibitors, the center of the O1s peak shifts towards higher binding energy (Figure 3.18).

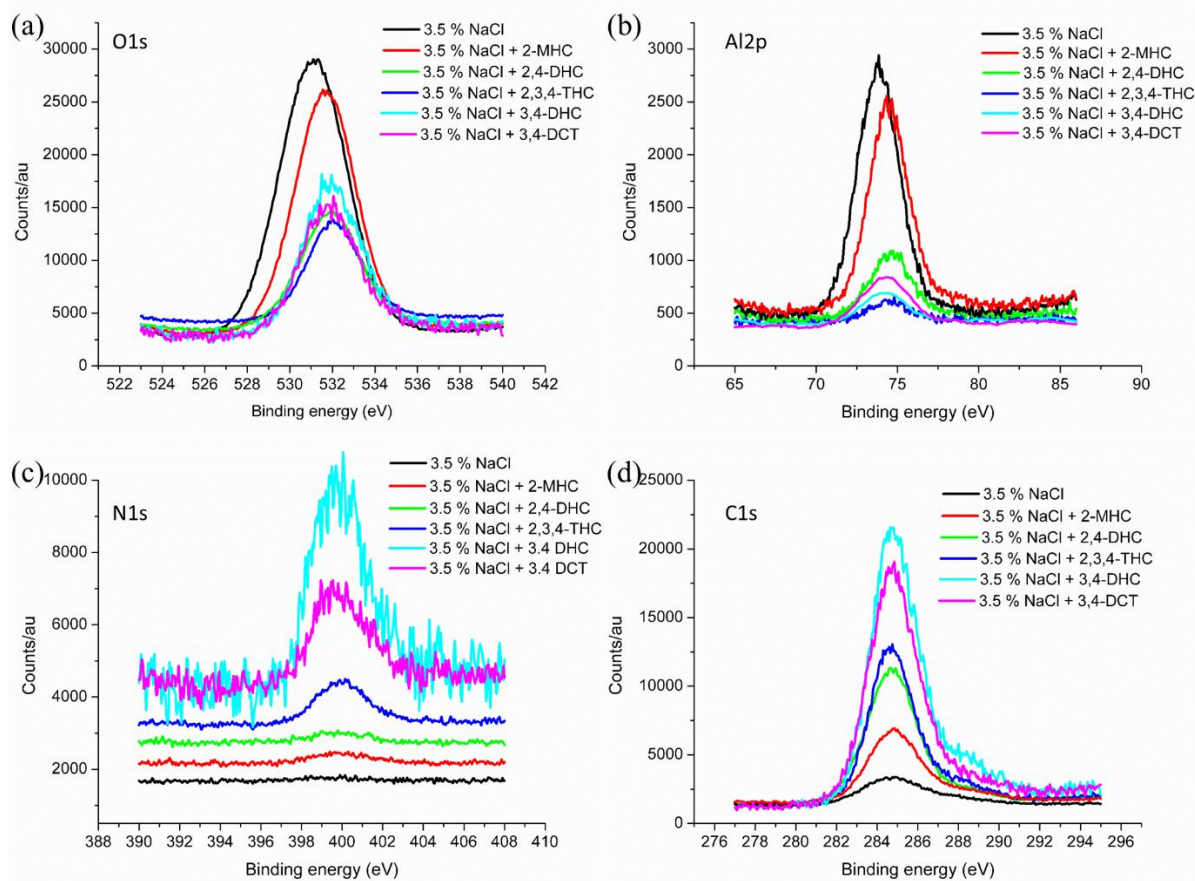


Figure 3.16 The magnified individual peaks in the XPS spectra of AA2024-T3 surfaces after 7 days of immersion in 3.5 % NaCl solution in the absence and in the presence of inhibitors (a) O1s, (b) Al2p (c) N1s (d) C1s ionization peaks.

The shift in the centers of O1s peak, in the presence of inhibitors are: 531.65 eV in the presence of 2-MHC, 531.9 eV in the presence of 2,4-DHC, 532.12 eV in the presence of 2,3,4- THC, 531.94 eV in the presence of 3,4-DHC, 531.92 eV in the presence of 3,4-DCT. These shifts may be due to the presence of –OH groups of the inhibitor molecules as an adsorbed thin layer on the substrate surface. It is also observed that the intensity of the O 1s peak is reduced. The oxygen content on the surface of the alloy in the presence of inhibitors is in the order, 2-MHC (50.88%) > 2,4-DHC (27.56%) > 2,3,4-THC (22.26%) > 3,4-DHC (19.76%) > 3,4-DCT (18.79%) ;

correspondingly the inhibition efficiency in the order, 2-MHC < 2,4-DHC < 2,3,4-THC < 3,4-DHC < 3,4-DCT.

In the Al 2p ionization peaks (Figure 3.16(b)), the center of the band at 73.88 eV in the absence of the inhibitors is shifted to 74.44 eV, 74.54 eV, 74.53 eV, 74.41 eV and 74.31eV in the presence of 2-MHC, 2,4-DHC, 2,3,4-THC, 3,4-DHC and 3,4-DCT respectively. The intensity of the peak decreases in the presence of the inhibitors as the inhibitors form the surface layers on the alloy. From the extent of reduction in the intensity of the peak, the order of corrosion protection of the inhibitors are in accordance with the earlier discussions. The presence of inhibitor molecules on the surface of the alloy is further supported by the presence of N 1s and C 1s ionization peaks in the presence of inhibitors.

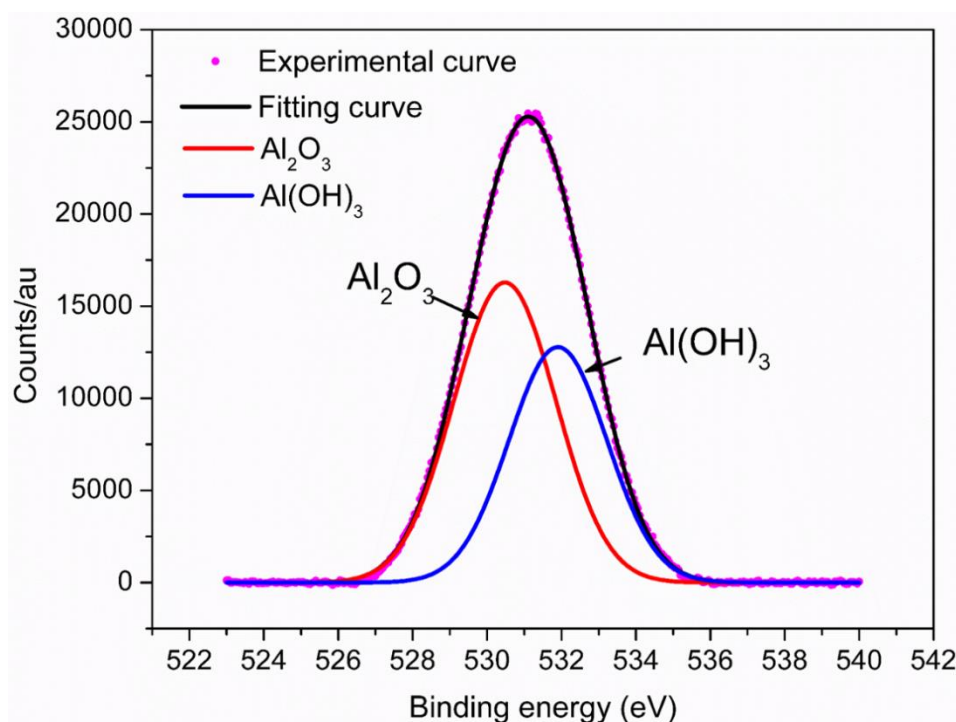


Figure 3.17 The deconvoluted O 1s ionization peaks of AA2024-T3 surface immersed for 7 days in 3.5 % NaCl solution.

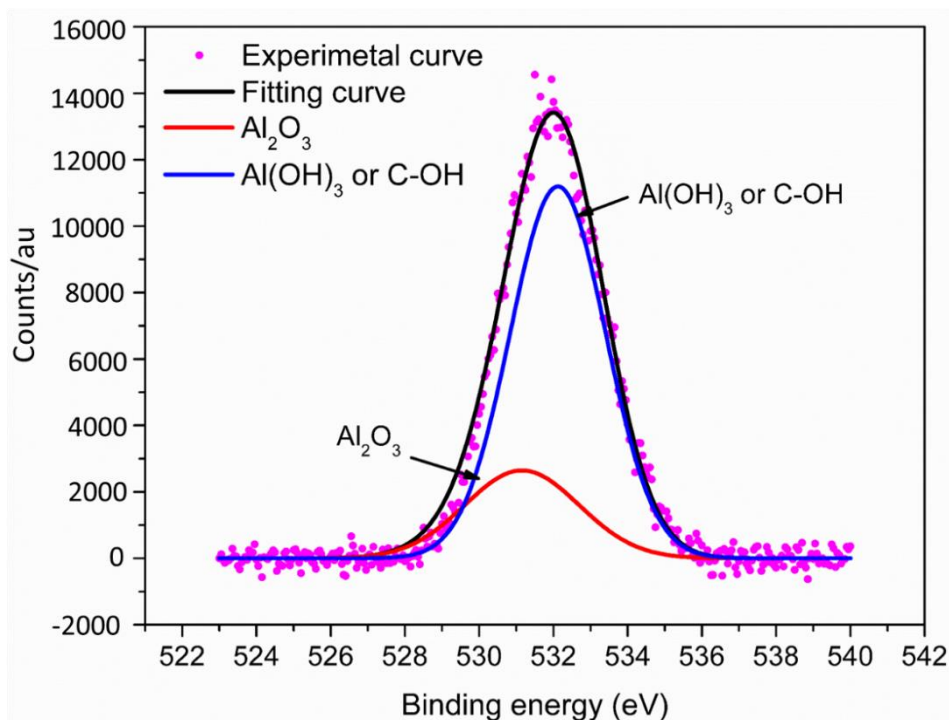


Figure 3.18 The deconvoluted O 1s ionization peaks of AA2024-T3 surface immersed for 7 days in 3.5 % NaCl solution in the presence of 3,4-DHC.

Table 3.3 XPS results of the elemental composition (atomic %) of AA2024-T3 surfaces after 7 days immersion in 3.5 % NaCl solution in the absence and in the presence of inhibitors.

Medium	C	Al	O	N
3.5 % NaCl	13.95	23.067	62.97	-
3.5 % NaCl + 2-MHC	29.52	18.476	50.88	1.120
3.5 % NaCl + 2,4-DHC	63.99	7.247	27.556	1.199
3.5 % NaCl + 2,3,4-THC	69.4	2.32	22.26	4.33
3.5 % NaCl + 3,4-DHC	72.23	1.66	19.76	6.18
3.5 % NaCl + 3,4-DCT	67.92	5.19	18.79	6.52

3.2 (E)-2-(3,4-DIHYDROXYBENZILIDINE)HYDRAZINECARBO- THIOAMIDE (3,4-DHC) AS AN INHIBITOR FOR CORROSION DETECTION

To explore the possibility of using the synthesised inhibitors for corrosion detection applications, the initial studies were carried out on all the five inhibitors. It was found that only 3,4-DHC qualified in the tests, by imparting the colour change at the corrosion sites. The detailed studies on its corrosion detection properties were carried out and the same are discussed here under.

3.2.1 Detection of pitting corrosion on AA2024-T3 in 3.5 % NaCl solution

In order to understand the mechanism of corrosion detection on AA2024-T3, the samples were immersed for different time periods in sodium chloride solution in the presence of the 3,4-DHC. The results were analysed by optical microscopy and FE-SEM images. The optical microscopy images of the samples are shown in Figure 3.19.

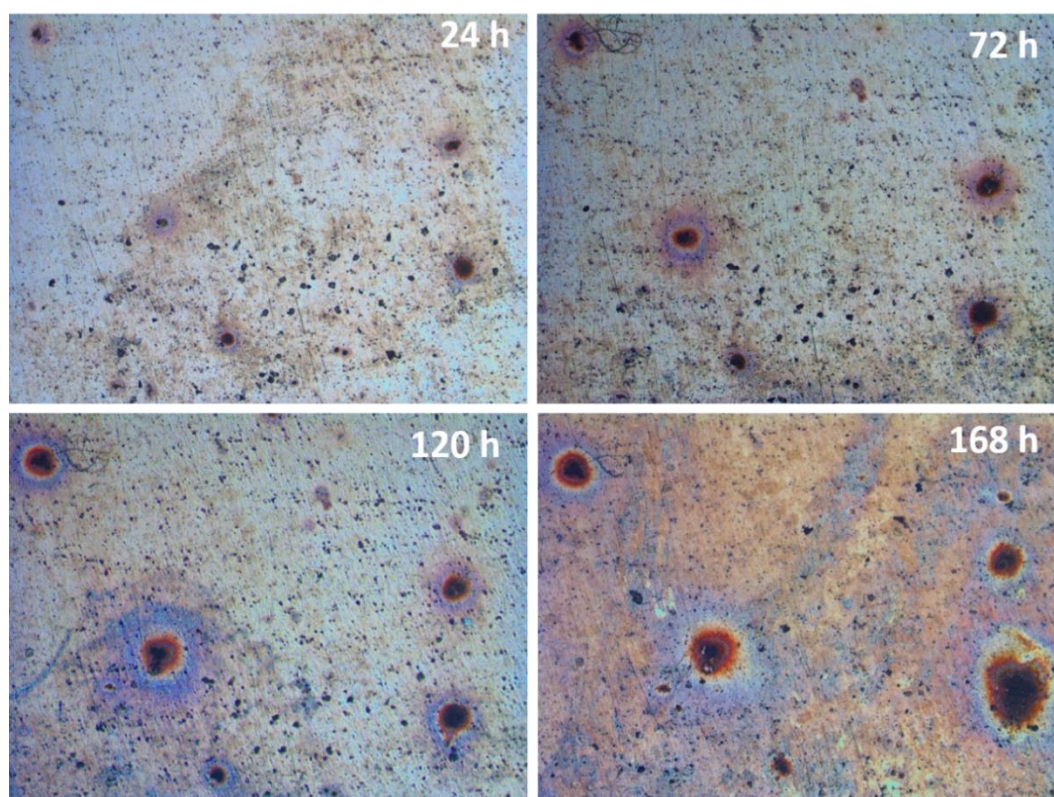


Figure 3.19 Optical images of the AA2024-T3 surface after immersion in 3.5 % NaCl solution in the presence of 3,4-DHC at different exposure times (50 x).

Initially, no color change was observed on the alloy surface. However, after 24 h of exposure, a small bright circular spot was observed under an optical microscope (Figure 3.19). This bright area probably indicates the onset of pitting corrosion on the alloy surface. The bright red color on the pitting area is due to the complex formed by the inhibitor molecules with the Al^{3+} ions produced due to the corrosion of the alloy surface. The complex formed, precipitates on the pitting area, covering the metal surface on the substrate. The bright spot increases in size, with increased exposure time.

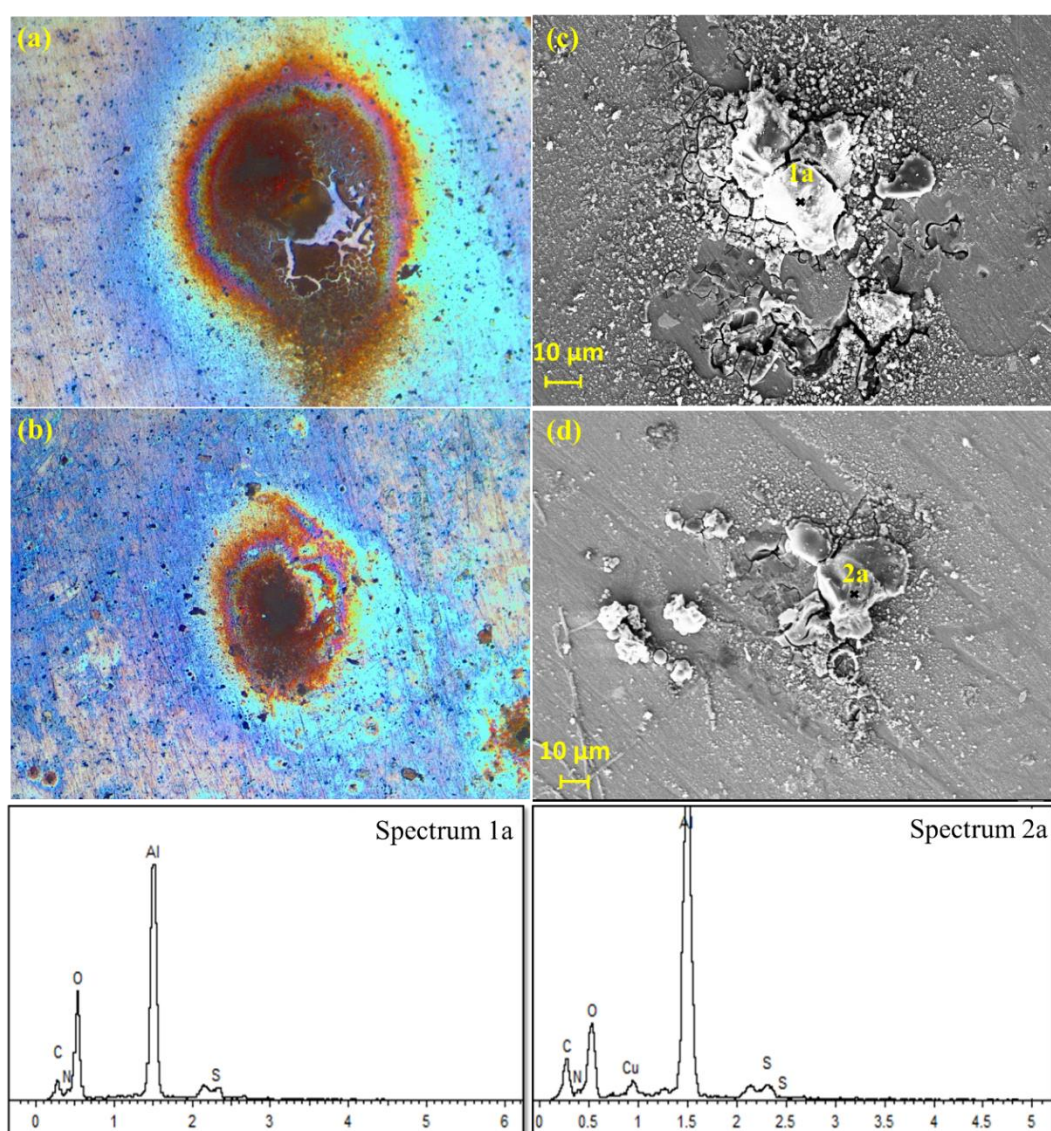


Figure 3.20 Images of the pitting area after 7 days of immersion in 3.5 % NaCl solution in the presence of 3,4-DHC (a), (b) Optical images (200x), (c) (d) FESEM images.

Figure 3.20 demonstrates the higher magnification optical images and FE-SEM images of the pitted AA2024-T3 surface of the alloy after 7 days of exposure in sodium chloride solution in the presence of 3,4-DHC. The respective EDX spectra at selected regions (Spectrum 1a and 2a) are given in Figure 3.20 and the data are tabulated in Table 3.4. The precipitated metal-inhibitor complex layer clearly seen the Figure 3.20 c & d. The EDX results disclose the existence of Al, Cu, (from the substrate) C, N, O and S (from the inhibitor molecules) on the surface of the alloy, confirming the presence of inhibitor molecules on the corroded area. The inhibitor layer act as a barrier layer between the alloy surface and the corrosive media.

Figure. 3.21, shows the FESEM image of the inhibitor deposited alloy surface. It clearly demonstrates the presence of inhibitor layer on the substrate. EDX was carried out on substrate and inhibitor layer; and the respective spectra are presented in Figure 3.21 and the elemental composition are given in Table. 3.4. From EDX data, increasing of carbon, nitrogen and sulphur content in the precipitated layer, conforms the presence of inhibitor in the precipitated layer on the alloy surface.

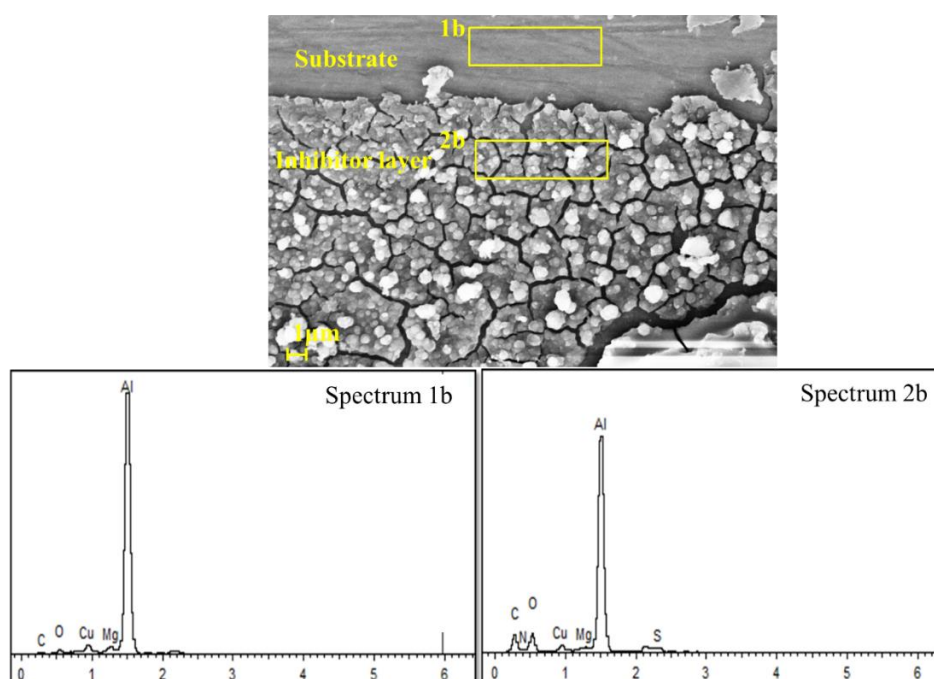


Figure 3.21 FESEM image and EDX spectra of the alloy surface AA2024-T3 after 7 days of immersion in 3.5 % NaCl solution in the presence of 3,4-DHC.

Table 3.4 EDX results of the elemental composition (atomic %) of AA2024-T3 surface after 7 days of immersion in 3.5 % NaCl solution in the presence and in the absence of 3,4-DHC.

Positions	Al	Cu	Mg	C	N	S	O
1a	29.70	-	-	21.63	5.05	1.73	41.89
2a	32.36	1.15	-	33.64	6.23	1.42	25.19
1b	81.81	1.84	1.46	9.76	1.23	-	3.89
2b	42.24	0.92	0.23	38.98	2.77	0.95	13.91

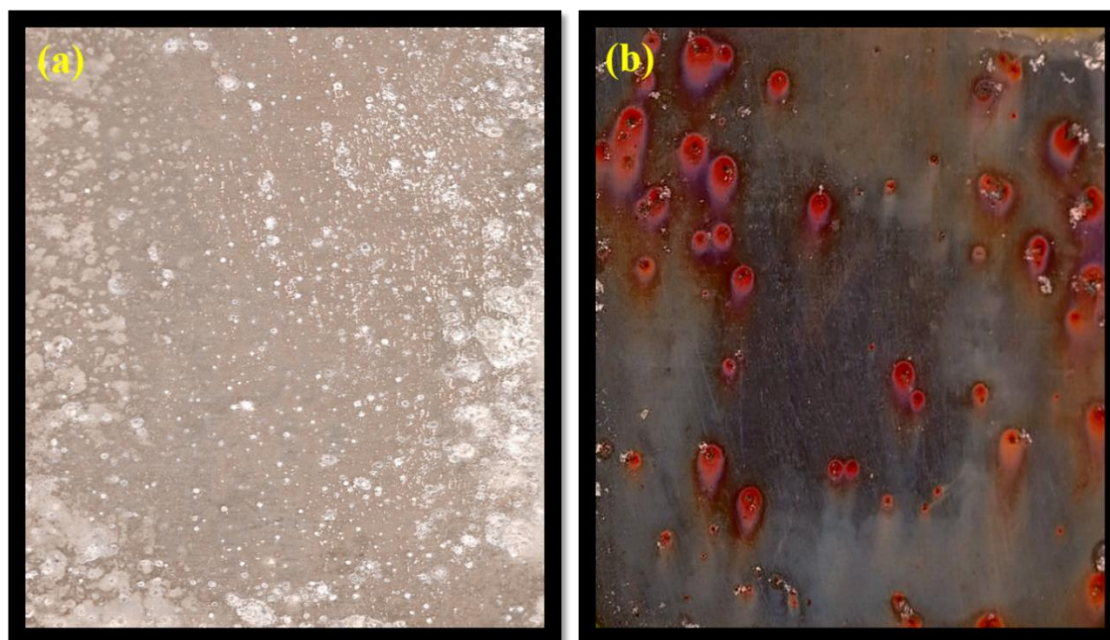


Figure 3.22 Photographic images of AA2024-T3 after 7 days of immersion in (a) 3.5% NaCl solution (b) 3.5% NaCl solution in the presence of 3,4-DHC.

The photographic images of the AA2024-T3 substrate are presented in Figure 3.22, obtained after 7 days of exposure in sodium chloride solution in the absence and in the presence of 3,4-DHC. It can be observed that the sample immersed in blank sodium chloride solution is substantially corroded with visible pitting, whereas lesser degradation was observed in the sample immersed in sodium chloride solution in the presence of 3,4-DHC. These findings confirm that 3,4-DHC molecules have the ability

to control the metal dissolution from the alloy surface and also to help detecting the pitting corrosion on the alloy surface.

3.2.2 Corrosion detection mechanism of the synthesised inhibitor

The binding behaviour of the inhibitor towards Al^{3+} ion was examined by UV- vis spectroscopy in $\text{H}_2\text{O}/\text{DMSO}$ (2/3, v/v). The UV-vis spectra of 3,4-DHC, in the presence of different concentrations of Al^{3+} , are shown in Figure 3.23. The inhibitor (10 μM) shows the absorption maximum (λ_{max}) at 330 nm. The addition of Al^{3+} ions shows significant redshift (λ_{max} , 334 nm) and also, a new absorption peak appears at 373 nm. The absorbance at 334 nm decreases and at 373 nm increases with the increase in Al^{3+} concentration. These observations are indicative of the formation of a complex between inhibitor molecules and Al^{3+} .

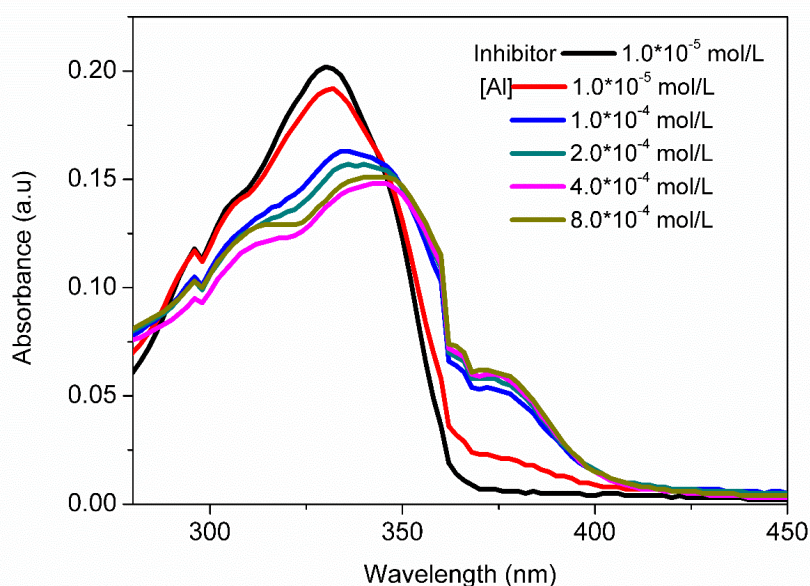


Figure 3.23 The UV-vis absorption spectra of 3,4-DHC in the presence of different concentrations of Al^{3+} ions.

The complexation of Al^{3+} with the inhibitor molecules was further confirmed by ^1H NMR. The ^1H NMR spectra of 3,4-DHC with and without the addition of Al^{3+} ions are shown in Figure 3.24. The results showed that, on the addition of the Al^{3+} ions, the oxygen atoms of the hydroxyl group participate in the complexation with Al^{3+} ions. This complexation is observed only as a change in the chemical shift of the hydroxyl

group hydrogen atom in the spectra. The visible bright red color observed on the alloy surface is of the complex formed.

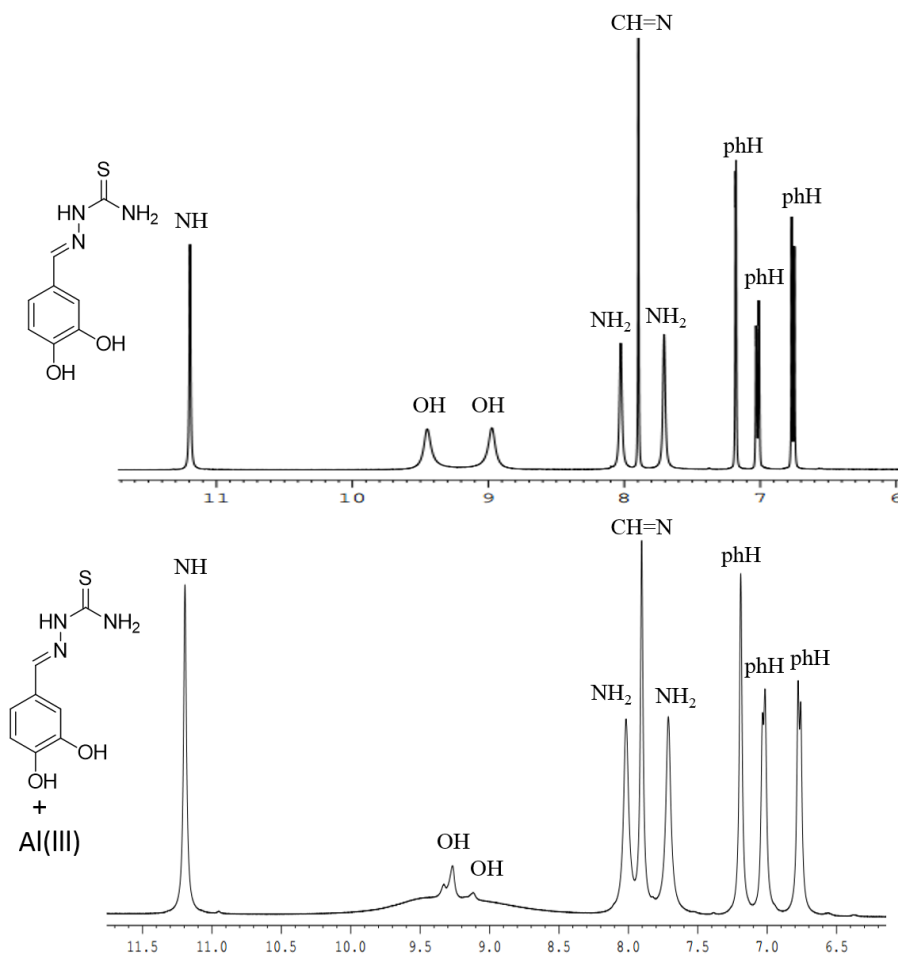


Figure 3.24 $^1\text{H-NMR}$ spectra of 3,4-DHC and 3,4-DHC + Al^{3+} .

The mechanism for the appearance of visible bright red colour, appears to be due to the prohibition of the photoinduced electron transfer (PET) between the electron rich groups (hydroxyl group) to lack electronic group (C=N bond of Schiff base) on introducing Al^{3+} . The mechanism is schematically presented in Figure 3.25 (Lei et al. 2016).

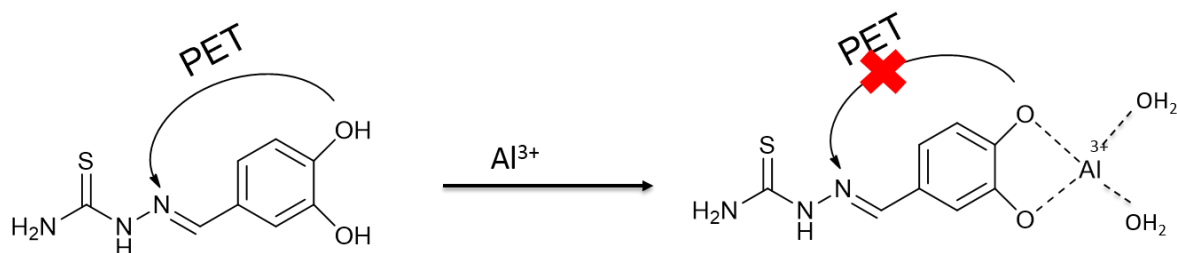


Figure 3.25 The sensing mechanism of the inhibitor for Al^{3+} .

3.3 EFFECT OF INHIBITOR INCORPORATION IN OXIDE LAYER ON THE CORROSION BEHAVIOUR OF ALUMINIUM ALLOY 2024-T3

From the five inhibitors studied for their inhibition action, the three most effective inhibitors were employed for coatings applications. An oxide layer was created on the aluminium alloy by anodizing the surface using 10 wt % sulphuric acid (plain oxide layer- Ox) and was sealed with the three inhibitors, namely, (E)-2-(2,3,4-trihydroxybenzylidene)hydrazinecarbothioamide (2,3,4-THC), (E)-2-(3,4-dihydroxybenzylidene)hydrazinecarbothioamide (3,4-DHC) and Bis ((3,4-Dihydroxyphenylmethylene) carbonothioicdihydrazide) (3,4-DCT) to evaluate their role in the enhancement of corrosion resistance. The coatings are designated as Ox-2,3,4-THC, Ox-3,4-DHC and Ox-3,4-DCT, respectively.

3.3.1 Open circuit potential measurement

The variation of open circuit potential (OCP) with exposure time can be used for characterizing the anticorrosion potential stability of the anodized aluminium alloy with and without sealing. The OCP cannot be used for the analysis of corrosion kinetics, but can be used to predict and characterize the corrosion susceptibility (Danilidis et al. 2007 Zhang et al. 2008). The time-dependent OCP curves for Ox, Ox-2,3,4-THC, Ox-3,4-DHC, and Ox-3,4-DCT are shown in Figure 3.26.

For the anodized aluminium alloy without sealing, the open circuit potential decreases from -0.6216 V (24 h) to -0.6797 V (72 h), which may be due to the penetration of corrosive ions through the porous oxide layer. Further, with the increase in the immersion time, the OCP increases and it ranges between -0.6314 V to -0.588 V. This may be attributed to the gradual formation of insoluble corrosion product such as aluminium oxide on the surface. The relative ratio of the formation of the oxide layer and its dissolution in the corrosion medium decide the OCP. However, in the case of Ox-2,3,4-THC, Ox-3,4-DHC, and Ox-3,4-DCT, the OCP shifts towards the positive potential and higher OCP values are maintained up to 336 h, as compared to Ox. These results confirm that, the oxide layer on the surface of the alloy is stabilized by the incorporation of inhibitor molecules. For the alloy sample with Ox-3,4-DCT coating,

initially a slight variation in the OCP value is observed from 24 h to 120 h, but after that the OCP value significantly shifted towards positive potentials. This may be due to the higher inhibition action of the inhibitor molecules and better stabilization of the oxide layer. Generally, the OCP value for a given system is inversely proportional to the corrosion rate (Balaraju et al 2011). Thus, according to the above results the order of corrosion protection could be started as Ox < Ox-2,3,4-THC < Ox-3,4-DHC < Ox-3,4-DCT.

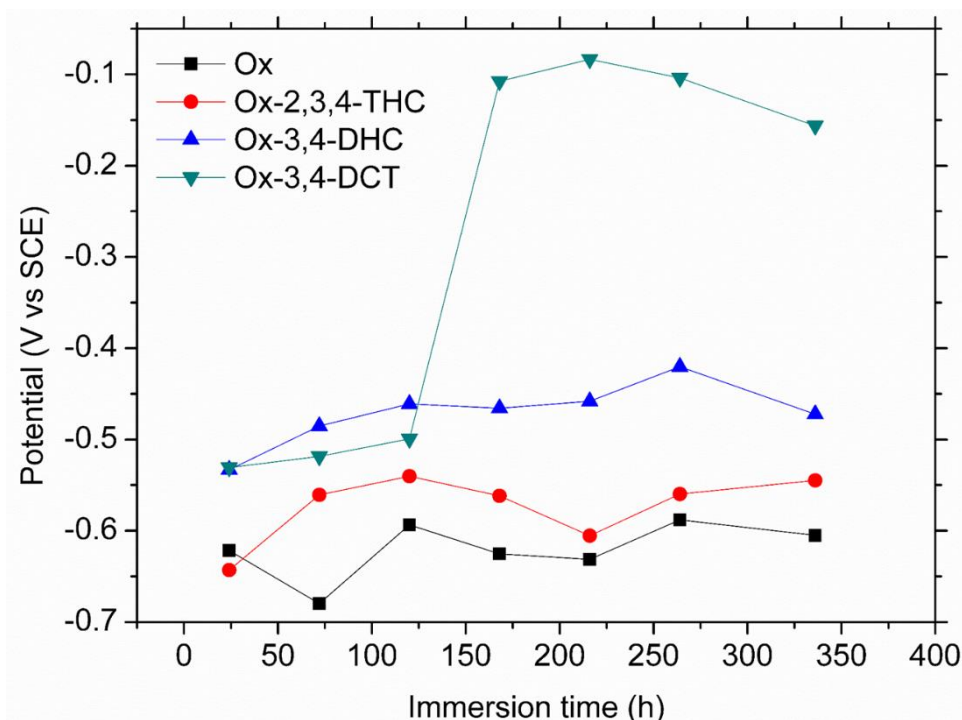


Figure 3.26 Variation of open circuit potential of the anodized AA2024-T3 with immersion time in 3.5 % NaCl solution.

3.3.2 Electrochemical impedance spectroscopy

The corrosion protection properties of the unsealed and sealed anodized aluminium alloy surface were analyzed by electrochemical impedance spectroscopy (EIS) measurements at different immersion times in sodium chloride solution (3.5 wt %). Nyquist plots for Ox, Ox-2,3,4-THC, Ox-3,4-DHC, and Ox-3,4-DCT are shown in Figure 3.27.

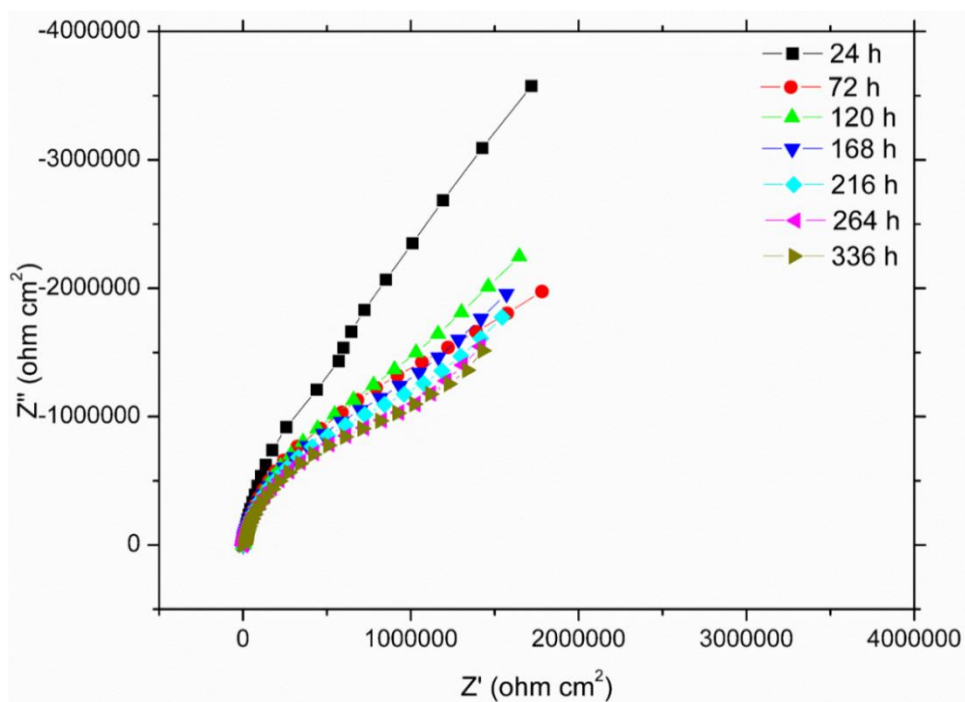


Figure 3.27 (a) Nyquist plots for the corrosion of anodized AA2024-T3 at different immersion times in 3.5 % NaCl solution.

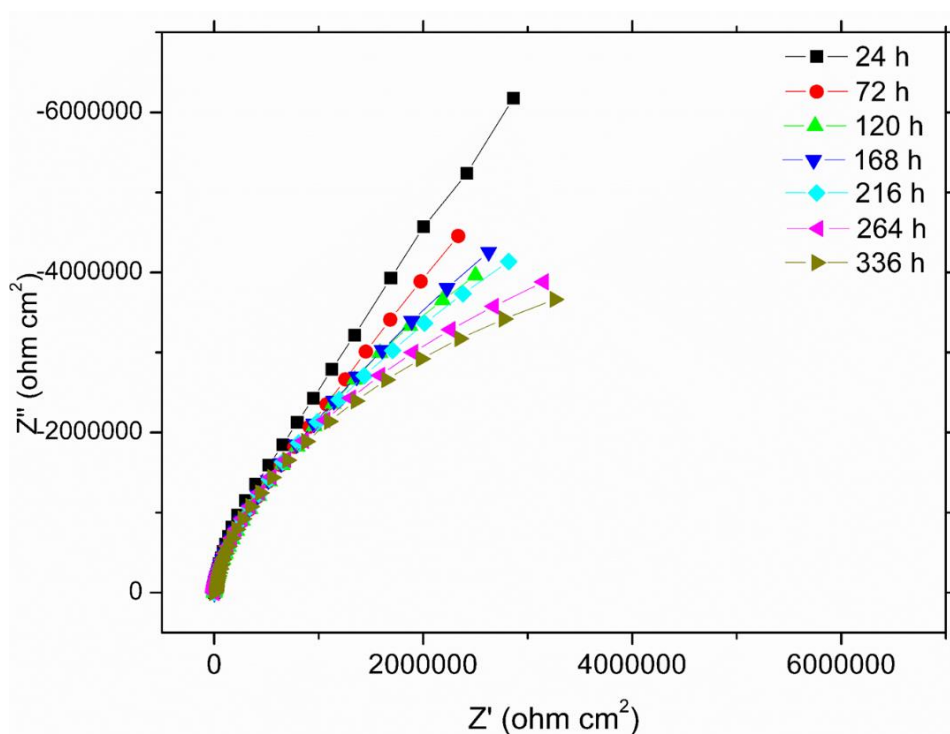


Figure 3.27 (b) Nyquist plots for the corrosion of anodized AA2024-T3 with 2,3,4-THC sealing (Ox-2,3,4-THC) at different immersion times in 3.5 % NaCl solution.

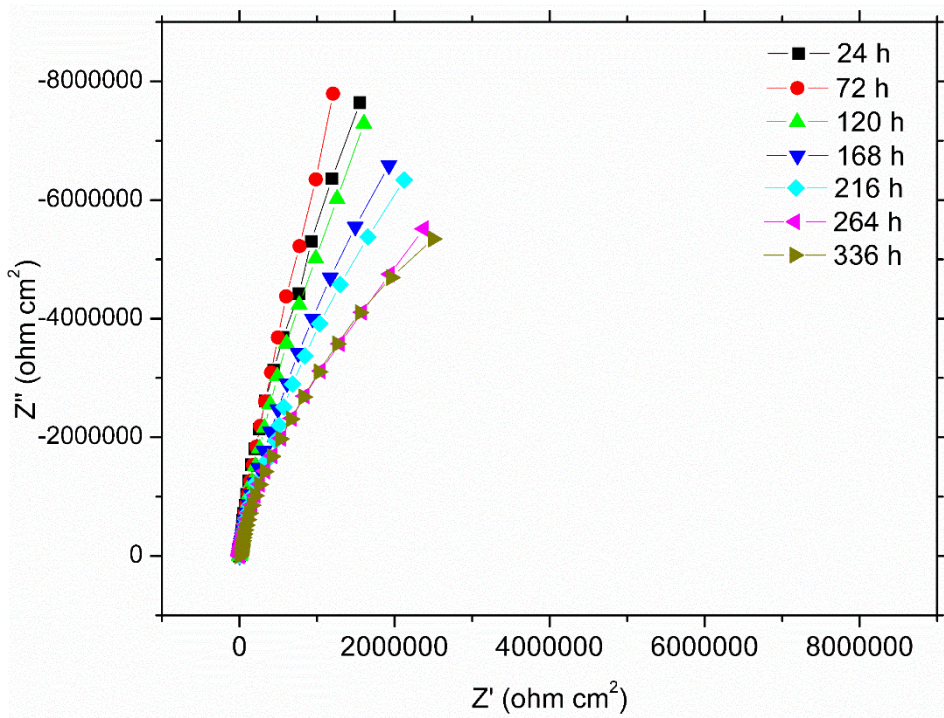


Figure 3.27 (c) Nyquist plots for the corrosion of anodized AA2024-T3 with 3,4-DHC sealing (Ox-3,4-DHC) at different immersion times in 3.5 % NaCl solution.

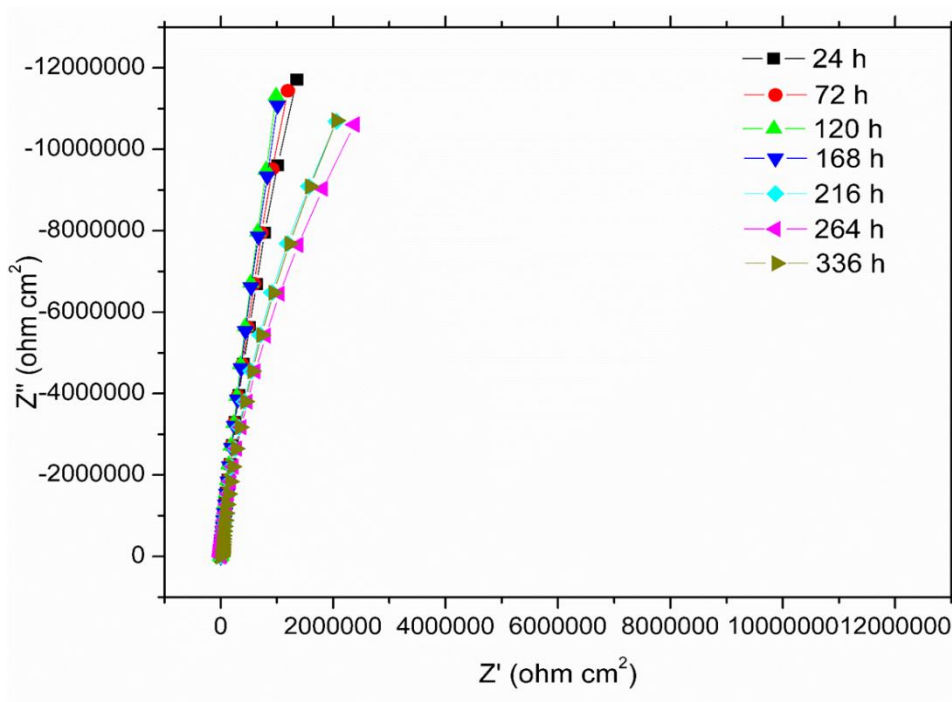


Figure 3.27 (d) Nyquist plots for the corrosion of anodized AA2024-T3 with 3,4-DCT sealing (Ox-3,4-DCT) at different immersion times in 3.5 % NaCl solution.

The Nyquist plots for the corrosion of unsealed anodized aluminium alloy surface at different immersion times, in 3.5 % NaCl solution are shown in Figure 3.27a. The Nyquist curves exhibit incompleting semicircles, consisting of two capacitive loops, the first capacitive loop corresponds to the porosity of the oxide layer and the second one is due to the barrier nature of the oxide layer (Yu and Cao 2003, Huang et al. 2008). With the increase in the immersion time, the diameter of the capacitive loop decreases. This is due to the increased dissolution of the protective oxide layer on the surface, leading to the increased corrosion on the alloy surface.

The time-dependent Nyquist plots for the corrosion of the inhibitor incorporated anodized aluminium alloy surface are shown in Figure 3.27 b, c and d. The incorporation of inhibitors to the oxide layer significantly affects the anticorrosion behaviour of the anodized aluminium alloy. The radial diameters of the arcs clearly increase with the sealing of the inhibitors. These results indicate that the corrosion rate decreases with the incorporation of inhibitors to the oxide layer.

The impedance spectra were analyzed by fitting with suitable equivalent electrical circuit model, to understand the electrochemical reactions occurring on the anodized substrate in the electrolyte solution. The equivalent electrical circuit model for the corrosion of Ox, Ox-2,3,4-THC, Ox-3,4-DHC, and Ox-3,4-DCT in sodium chloride solution are shown in Figure 3.28. The impedance spectra obtained for the anodized aluminium alloy (Ox) is associated with three time constants at 24 h immersion time (Figure 3.28a). The first time constant results from the capacitance of the porous oxide layer, the second time constant accounts for the inner oxide layer and the third time constant relates to the charge transfer reaction taking place at the metal/oxide/electrolyte interface during the corrosion process. The charge transfer reaction takes place through the formation of Al^{3+} , OH^- , and O^2 at the metal/electrolyte interface. Diffusion of these ions creates a Warburg impedance (W), after 24 h of immersion, as depicted in the equivalent electrical circuit given in Figure 3.28b. These observations are in line with the reports in the literature that, the interpretation of impedance data from the oxide layer formed aluminium alloy is generally explained from the three-time constant (Mansfeld and Kendig 1988 Suay et al. 2003 Boisier et al. 2008). In the equivalent electrical circuit model, R_s is the solution resistance between

the working and the reference electrode. R_{po} is the porous oxide layer resistance, Q_{po} is the porous oxide layer capacitance, R_b is the barrier layer resistance, Q_b is the barrier layer capacitance, R_{ct} is the charge transfer resistance, Q_{dl} is the double layer resistance and W is the Warburg resistance. In 2,3,4-THC incorporated oxide layer (Ox-2,3,4-THC), the Warburg resistance disappears due to the presence of the inhibitor layer which does not permit the ion diffusion (Figure 3.28a). The impedance spectra for Ox-3,4-DHC, is associated with two time constants at initial immersion time from 24 h to 120 h (Figure 3.28c). The presence of thick inhibitor (3,4-DHC) layer does not allow the electrolyte to interact with the internal surface. With further exposure from 120 h to 336 h, an additional time constant appears due to the defect created on the 3,4-DHC incorporated oxide layer, which may allow the corrosive ions to the alloy surface, relevant equivalent electrical circuit model given is Figure 3.28a. The 3,4-DCT sealed oxide layer (Ox-3,4-DCT) samples are fitted with two time constants and are sustainable up to 336 h as corroborated with the equivalent electric circuit model given in Figure 3.28c. These results suggest the presence of a stable inhibitor layer. Thus, the present study clearly confirms that, Ox-3,4-DCT layer have good barrier properties compared to Ox, Ox-2,3,4-THC and Ox-3,4-DHC.

The important fitted parameters include porous oxide layer resistance (R_{po}), inner barrier oxide layer resistance (R_b), charge transfer resistance (R_{ct}) and polarization resistance ($R_p=R_{po}+R_b$ or $R_p=R_{po}+R_b+R_{ct}$) and are tabulated in Table 3.5.

The anodizing process produces a porous oxide layer, which can readily accept the organic molecules. The incorporation of inhibitors into the oxide layer causes a drastic change in the corrosion barrier stability of the anodizing layer as measured by the impedance spectra. The analysis of the porous oxide layer resistance, inner barrier oxide layer resistance and polarization resistance shows the anticorrosion stability of the formed oxide layer during immersion studies.

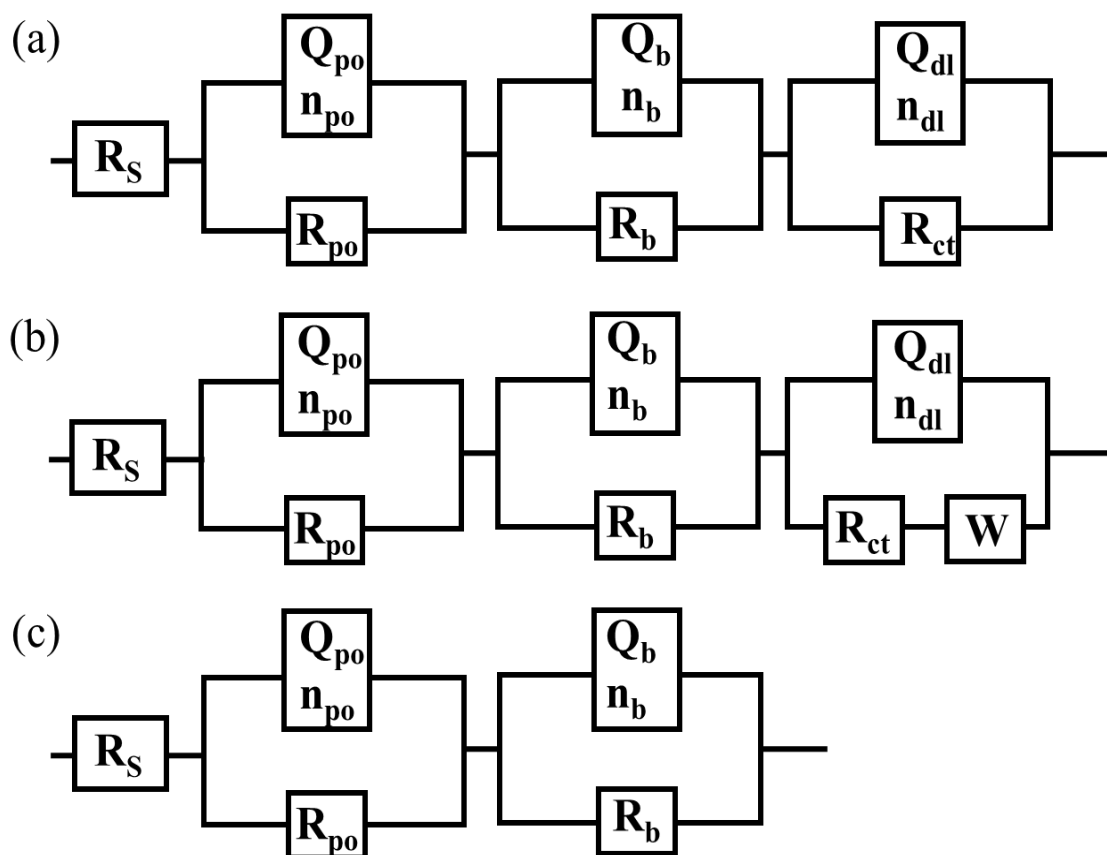


Figure 3.28 Equivalent circuits used to fit experimental data for the corrosion of anodised and inhibitor incorporated alloy surface.

The Figures 3.29, 3.30 and 3.31 represents the variation of porous oxide layer resistance, inner barrier oxide layer resistance and polarization resistance of the Ox, Ox-2,3,4-THC, Ox-3,4-DHC, and Ox-3,4-DCT during the immersion in sodium chloride solution. Inhibitor incorporated oxide layers (Ox-2,3,4-THC, Ox-3,4-DHC, and Ox-3,4-DCT) show higher R_{po} , R_b and R_p value during immersion studies compared to the anodized alloy without sealing. These results confirm that the presence of inhibitors enhances the anticorrosion behaviour of the oxide layer. R_p value is inversely proportional to corrosion rate. Thus, from acquired results, the order of corrosion protection efficiency is Ox < Ox-2,3,4-THC < Ox-3,4-DHC < Ox-3,4-DCT.

Table 3.5 The electrochemical impedance parameters for the corrosion of anodised and inhibitor sealed anodised AA2024-T3 alloy surface in 3.5 % NaCl solution at different immersion time.

Coating	Immersion time (h)	R_{po} ($\Omega \text{ cm}^2$)	R_b ($\Omega \text{ cm}^2$)	R_{ct} ($\Omega \text{ cm}^2$)	W ($\Omega \text{ cm}^2$)	R_p ($\Omega \text{ cm}^2$)	η (%)
Ox	24	1.323×10^2	1.243×10^2	5.08×10^7	-	5.080×10^7	-
	72	9.492×10^1	5.720×10^2	2.203×10^6	1.789×10^{-6}	2.203×10^6	-
	120	2.223×10^2	1.090×10^3	1.407×10^6	1.197×10^{-6}	1.408×10^6	-
	168	6.286×10^2	4.992×10^3	6.662×10^5	1.328×10^{-6}	6.718×10^5	-
	216	3.234×10^2	3.077×10^3	1.428×10^6	1.723×10^{-6}	1.431×10^6	-
	264	2.746×10^2	3.399×10^3	1.256×10^6	2.036×10^{-6}	1.259×10^6	-
	336	2.421×10^2	4.644×10^3	1.266×10^6	2.069×10^{-6}	1.270×10^6	-
Ox-2,3,4-	24	1.100×10^2	9.34×10^5	1.716×10^7	-	1.809×10^7	-180
THC	72	3.520×10^2	1.281×10^6	1.694×10^7	-	1.822×10^7	87.90
	120	8.036×10^2	1.614×10^6	1.433×10^7	-	1.594×10^7	91.16
	168	9.384×10^2	1.543×10^6	1.388×10^7	-	1.542×10^7	95.64
	216	1.118×10^3	1.654×10^6	1.192×10^7	-	1.357×10^7	89.45
	264	1.620×10^3	2.414×10^6	9.984×10^6	-	1.239×10^7	89.83
	336	1.758×10^3	6.185×10^5	9.703×10^6	-	1.032×10^7	87.69
Ox-3,4-	24	9.13×10^2	1.018×10^8	-	-	1.018×10^8	50.09
DHC	72	1.177×10^3	1.518×10^8	-	-	1.518×10^8	98.54
	120	1.578×10^3	6.592×10^7	-	-	6.592×10^7	97.86
	168	1.980×10^3	1.097×10^6	4.075×10^7	-	4.184×10^7	99.96
	216	1.831×10^3	2.424×10^6	4.824×10^7	-	5.066×10^7	97.17
	264	1.939×10^3	2.086×10^6	2.610×10^7	-	2.818×10^7	95.53
	336	1.749×10^3	2.104×10^6	2.434×10^7	-	2.644×10^7	95.19
Ox-3,4-	24	1.086×10^3	2.532×10^8	-	-	2.532×10^8	79.93
DCT	72	2.018×10^3	2.931×10^8	-	-	2.931×10^8	99.24
	120	3.353×10^3	4.619×10^9	-	-	4.619×10^9	99.96
	168	6.793×10^3	1.819×10^9	-	-	1.819×10^9	99.96
	216	7.863×10^3	1.220×10^9	-	-	1.220×10^9	99.88
	264	9.847×10^3	4.007×10^8	-	-	4.008×10^8	99.68
	336	8.758×10^3	1.221×10^8	-	-	1.221×10^8	98.95

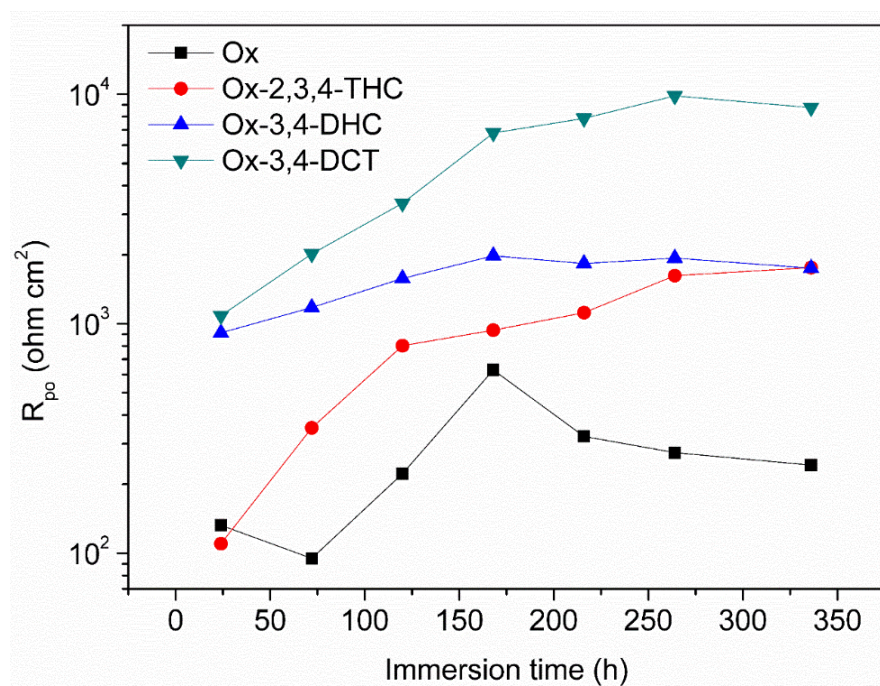


Figure 3.29 Variation of porous oxide layer resistance of the anodized AA2024-T3 with immersion time in the absence and in the presence of the inhibitors in 3.5 % NaCl solution.

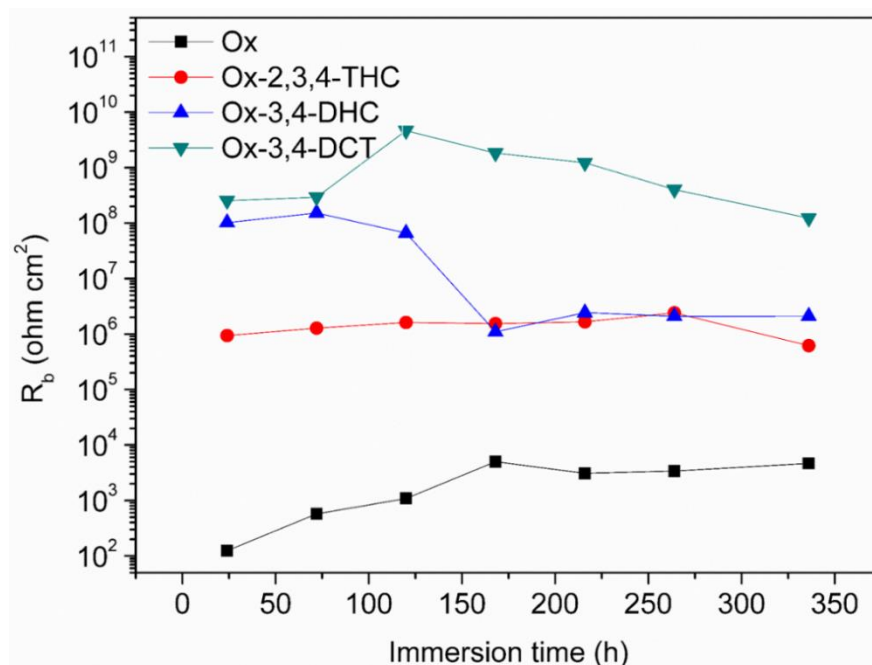


Figure 3.30 Variation of inner barrier oxide layer resistance of the anodized AA2024-T3 with immersion time in the absence and in the presence of the inhibitors in 3.5 % NaCl solution.

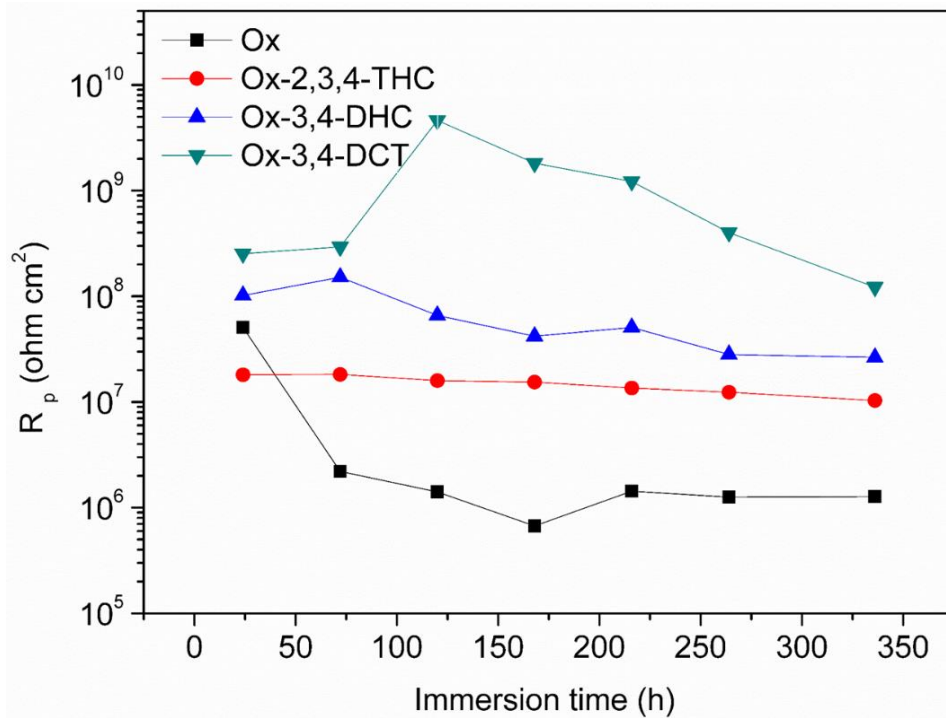


Figure 3.31 Variation of polarization resistance of the anodized AA2024-T3 with immersion time in the absence and in the presence of the inhibitors in 3.5 % NaCl solution.

The impedance spectra for the corrosion of anodizing aluminium alloy with and without inhibitors, can also be represented as Bode impedance plots and Bode phase angle plots. The plots were obtained at different immersion times in 3.5 % NaCl solution. The impedance spectra for the anodized aluminium alloy without sealing, are shown in Figure 3.32.

Generally, the Aluminium oxide layer on the alloy surface is associated with an under lying very thin nonporous oxide layer and thick porous oxide layer, partially hydrated on the top of it. The impedance spectra for anodized AA2024-T3, clearly shows three typical regions. The impedance modules at $/Z/_{10^5 \text{ Hz}}$ is attributed to the capacitive behaviour of the thick porous oxide layer. These parameters give the valuable information regarding to the hydration reaction within the pores. The impedance modules at middle frequency is related to the capacitive behaviour of the inner barrier layer. These two parameters are the deciding factors for corrosion

protection behaviour of the formed oxide layer. Low frequency impedance modules is attributed to the charge transfer reaction occurring on the alloy surface.

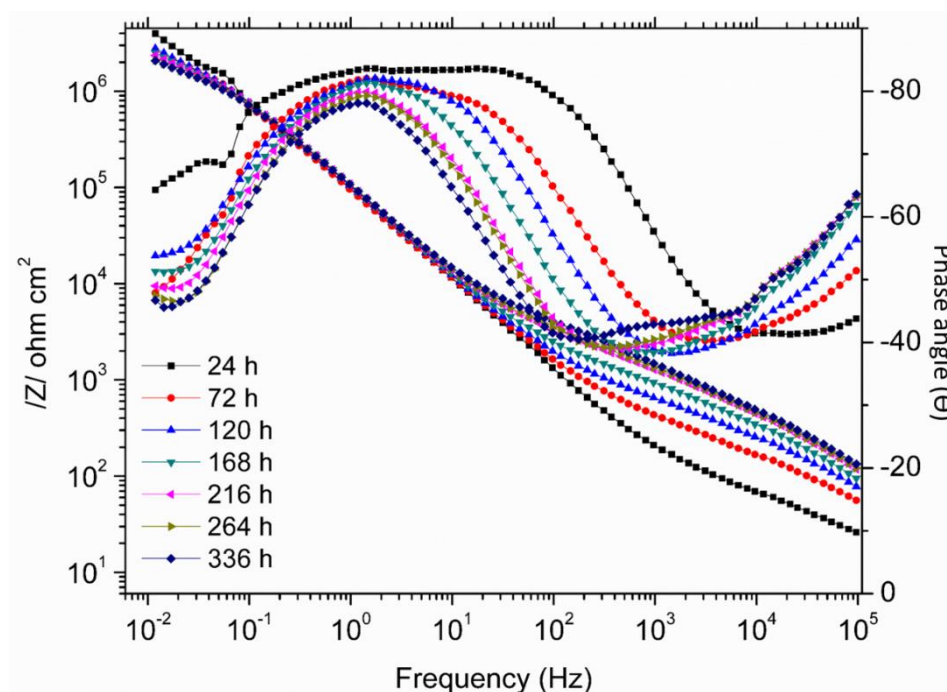


Figure 3.32 Bode plots for the corrosion of anodized AA2024-T3 in 3.5 % NaCl solution at different immersion times.

Impedance modules at $|Z|_{10^5 \text{ Hz}}$, slightly increases with the increase in the immersion time, due to the blocking of pores through hydration reaction. The low-frequency impedance modules ($|Z|$) can be used for monitoring of corrosion protection potential of the coating system. The impedance modules at $|Z|_{0.01 \text{ Hz}}$ decreases gradually with the increase in the immersion time. Simultaneously, the phase angle at the middle-frequency range shifts to low frequency and the phase angle at low frequency decreases significantly as the immersion time increases (Figure 3.32). These results suggest that the resistance of the oxide layer decreases, as a result of the electrolyte penetration through the porous oxide layer, reaching the alloy surface and thus activating the surface corrosion. Overall, the impedance spectra suggest that the unsealed anodized aluminium alloy surface are significantly corroded during immersion in sodium chloride solution.

The Bode plots presented in Figure 3.33 are for the corrosion of anodized AA2024-T3 surface sealed with inhibitors, 2,3,4-THC, 3,4-DHC, and 3,4-DCT. The impedance modules at $/Z/_{0.01\text{Hz}}$ is comparatively high during immersion studies compared with that of the plain oxide layer. This result suggests that, the corrosion rate decreases with the incorporation of inhibitors into the oxide layer. Similarly, it is also observed that the low frequency phase angle increases and the middle frequency phase maximum (Θ_{max}) increases and broadens in the presence of the inhibitors in the porous oxide layer. The increase and the broadening of θ_{max} implies a better barrier effect by the presence of the inhibitor in porous oxide layer against corrosive ingress.

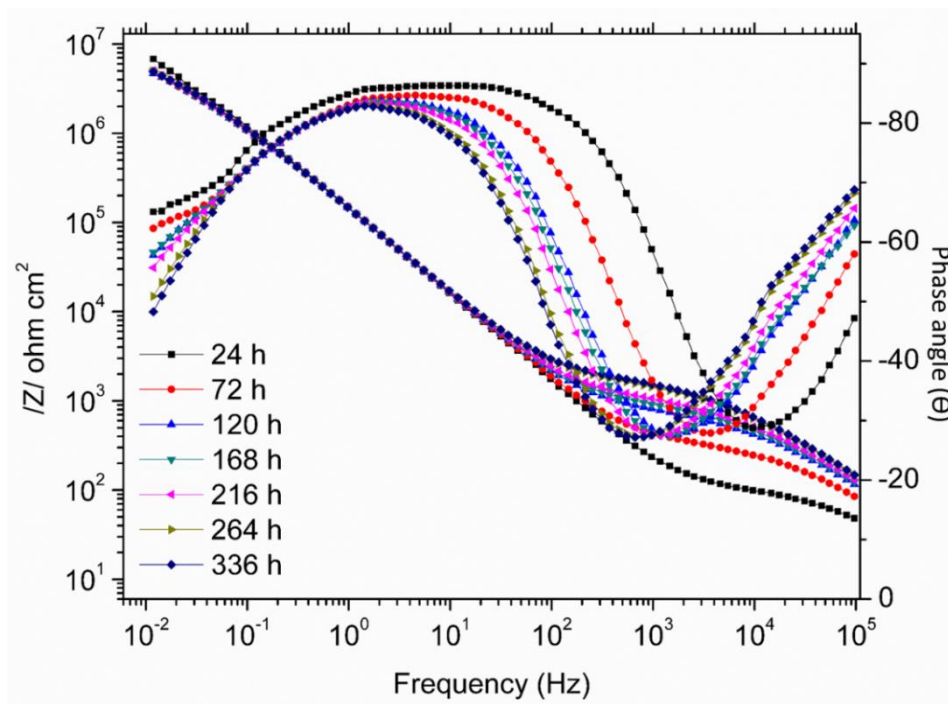


Figure 3.33 (a) Bode plots for the corrosion of anodized AA2024-T3 sealed with 2,3,4-THC in 3.5 %NaCl solution at different immersion times.

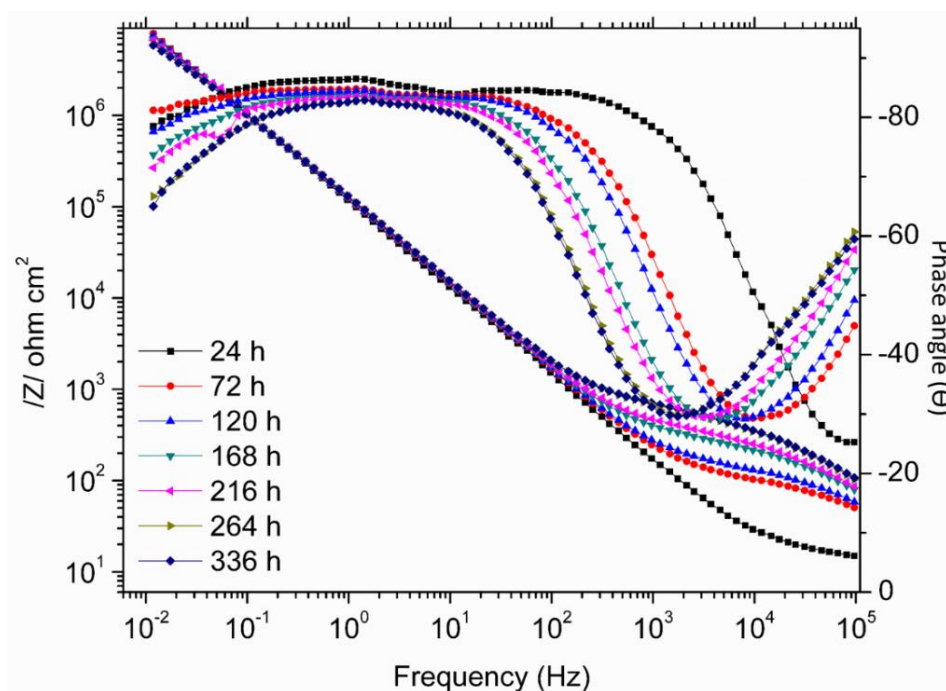


Figure 3.33 (b) Bode plots for the corrosion of anodized AA2024-T3 sealed with 2,3,4-DHC in 3.5 % NaCl solution at different immersion times.

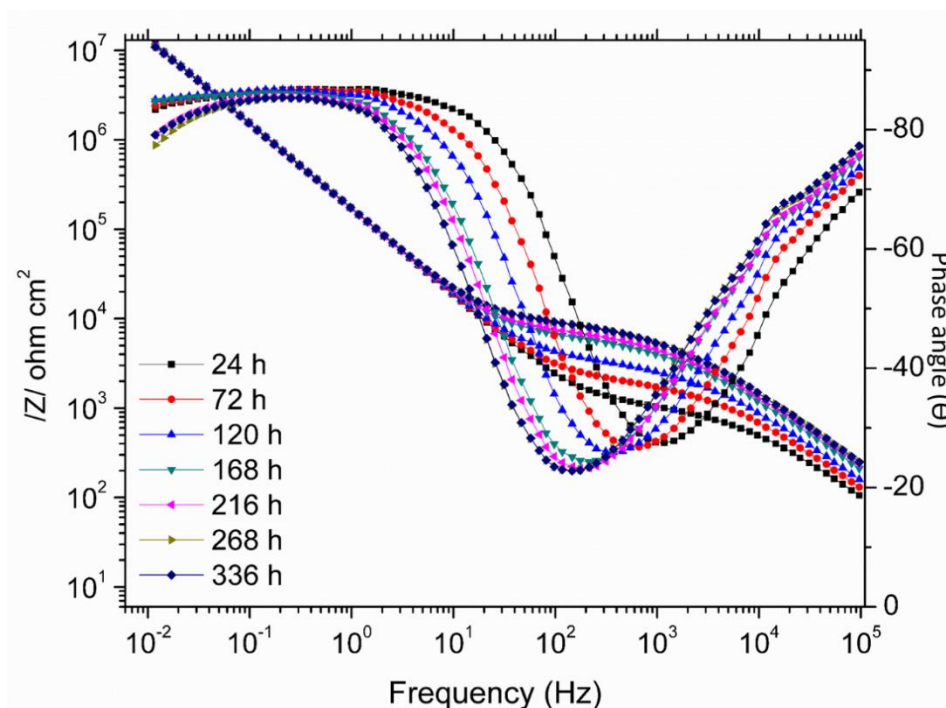


Figure 3.33 (c) Bode plots for the corrosion of anodized AA2024-T3 sealed with 3,4-DCT in 3.5 % NaCl solution at different immersion times.

It can be seen from the phase angle plots that in the presence of inhibitors, the impedance spectra represent three time constants for Ox-2,3,4-THC. The three time constants can be assigned to the electron charge transfer process across the double layer at the interface and to the formed oxide layer. In the case of Ox-3,4-DHC, the two time constants associated with the Bode phase angle plot is extended over a wide range of frequencies at initial immersion time from 24 h to 120 h. With further extension in the immersion time, one more time constant appears at low frequency due to the defect created on the 3,4-DHC incorporated oxide layer, which may allow the corrosive ions to the alloy surface. The phase angle plot represents the two time constant for Ox-3,4-DCT and the same number of time constants are maintained upto 336 h. These results suggest the presence of a stable inhibitor layer, which is non-permeable to the corrosive ions and prevent them from reaching the alloy surface. The frequency spread of the phase angle is maximum in the case of Ox-3,4-DCT in comparison with those in the presence of Ox, Ox-2,3,4-THC and Ox-3,4-DHC.

3.3.3 Potentiodynamic polarization studies

The potentiodynamic polarization curves can be used to monitor the corrosion rate of a metal and its alloy. The potentiodynamic polarization curve for the corrosion of anodized aluminium alloy with and without sealing with different inhibitors, after 336 h of immersion in 3.5 % NaCl solution are shown in Figure 3.34.

In the case of anodized AA2024-T3 without sealing, the anodic curve does not possess a well-defined Tafel region, due to the presence of pitting corrosion at -0.569 V. Hence, corrosion current density (i_{corr}) was calculated by extrapolating the Tafel region of the cathodic curve to the corrosion potential (E_{corr}). In the presence of inhibitors in the oxide layer, the pitting potential disappears, as the presence of inhibitor molecules do not permit the metal dissolution. In this case, the i_{corr} was calculated by extrapolating the Tafel regions of the anodic and cathodic curves to the E_{corr} . The measured electrochemical parameters including corrosion potential (E_{corr}), pitting potential (E_{pit}), corrosion current density (i_{corr}), and polarization resistance (R_{pol}) are summarized in Table 3.6. The i_{corr} was calculated using Stern-Geary equation (Eq. (3.5)).

$$i_{corr} = \frac{B}{R_{pol}} \quad (3.5)$$

$$B = \frac{\beta_a \beta_c}{2.303 (\beta_a + \beta_c)} \quad (3.6)$$

B is the proportionality constant, β_a is the anodic slope, β_c is the cathodic slope.

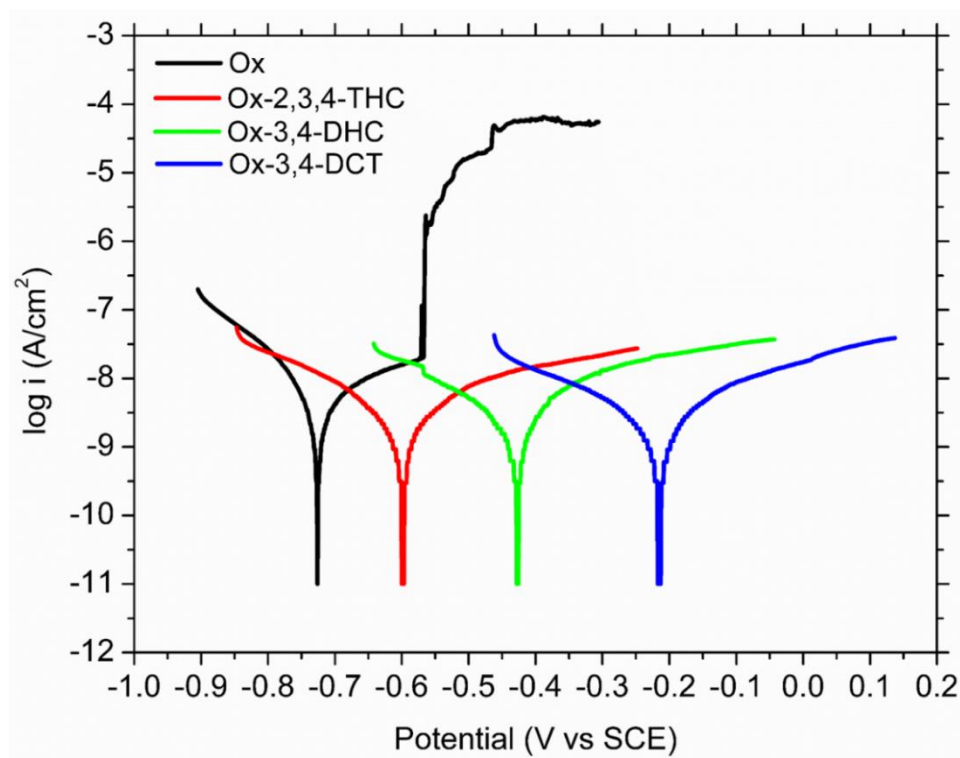


Figure 3.34 Potentiodynamic polarization curves for the corrosion of anodized AA2024-T3 without and with sealing after 336 h of immersion in 3.5 % NaCl solution.

The anodic polarization curve is attributed to the metal dissolution on the alloy surface. In the absence of inhibitor in the oxide layer, a sudden increase of current density from -0.569 V (E_{pit}) is observed, as a result of the pitting corrosion due to the porous oxide layer. The E_{pit} disappears in the presence of the inhibitor in the oxide layer. These results confirm that, the incorporation of inhibitors avoids the electrolyte access to the metal surface, thereby avoiding the metal dissolution. It is evident from the data tabulated in Table 3.6 that the corrosion current density decreases in the presence of the inhibitor in the oxide layer. Simultaneously, R_{pol} (R_{pol} inversely

proportional to corrosion rate) value increases in the presence of inhibitor, in the order of Ox < Ox-2,3,4-THC < Ox-3,4-DHC < Ox-3,4-DCT.

The corrosion potential (E_{corr}), a thermodynamic factor, is an indicator of the corrosion tendency. In porous oxide layer, the E_{corr} appears at -0.7272 V, while in the presence of inhibitors in porous oxide layer, the E_{corr} value is shifted toward the positive potential (-0.5988 V - Ox-2,3,4-THC, -0.4281 V - Ox-3,4-DHC, -0.2151 - Ox-3,4-DCT). Thus indicating the improvement of corrosion resistance of anodized aluminium alloy AA2024-T3 by sealing of inhibitors. These findings corroborate well with the EIS measurements.

Table 3.6 Potentiodynamic polarization data for the corrosion of anodized AA2024-T3 without and with sealing in 3.5 % NaCl solution, after 336 h of immersion.

Coating	E_{corr} (V/SCE)	E_{pit} (V/SCE)	i_{corr} (A cm ⁻²)	R_{pol} (Ω cm ²)
Ox	-0.7272	-0.569	6.028×10^{-9}	5.184×10^6
Ox-2,3,4-THC	-0.5988	-	2.762×10^{-9}	1.289×10^7
Ox-3,4-DHC	-0.4281	-	2.676×10^{-9}	1.386×10^7
Ox-3,4-DCT	-0.2151	-	2.559×10^{-9}	1.526×10^7

3.3.4 Surface characterization of anodized AA2024-T3

Photographic images of the as prepared samples are presented in Figure 3.35. In as prepared condition, Ox surface appears colourless, Ox-2,3,4-THC surface appears orange, Ox-3,4-DHC surface appears light orange, and Ox-3,4-DCT surface appears slightly greenish.

Anodized AA2024-T3 surfaces were characterized by the FE-SEM method in order to understand the surface microstructure before and after sealing. In general, the presence of intermetallic particles in the matrix, produces voids and cracks in the oxide layer. The anodized alloy surface appears regular, with micro cracks and cavities.

Surface analysis of Ox, Ox-2,3,4-THC and Ox-3,4-DHC, clearly shows the presence of cracks and cavities of about 1-2 μ m width. The visible cavity structures on the surface could be attributed to the presence of intermetallic particles. In the case of Ox-3,4-DCT (Figure 3.36d), the surface appears uniform, with minor cracks and no evidence of cavities. The thickness of formed oxide layer was approximately 6-8 μ m (Figure 3.36e).

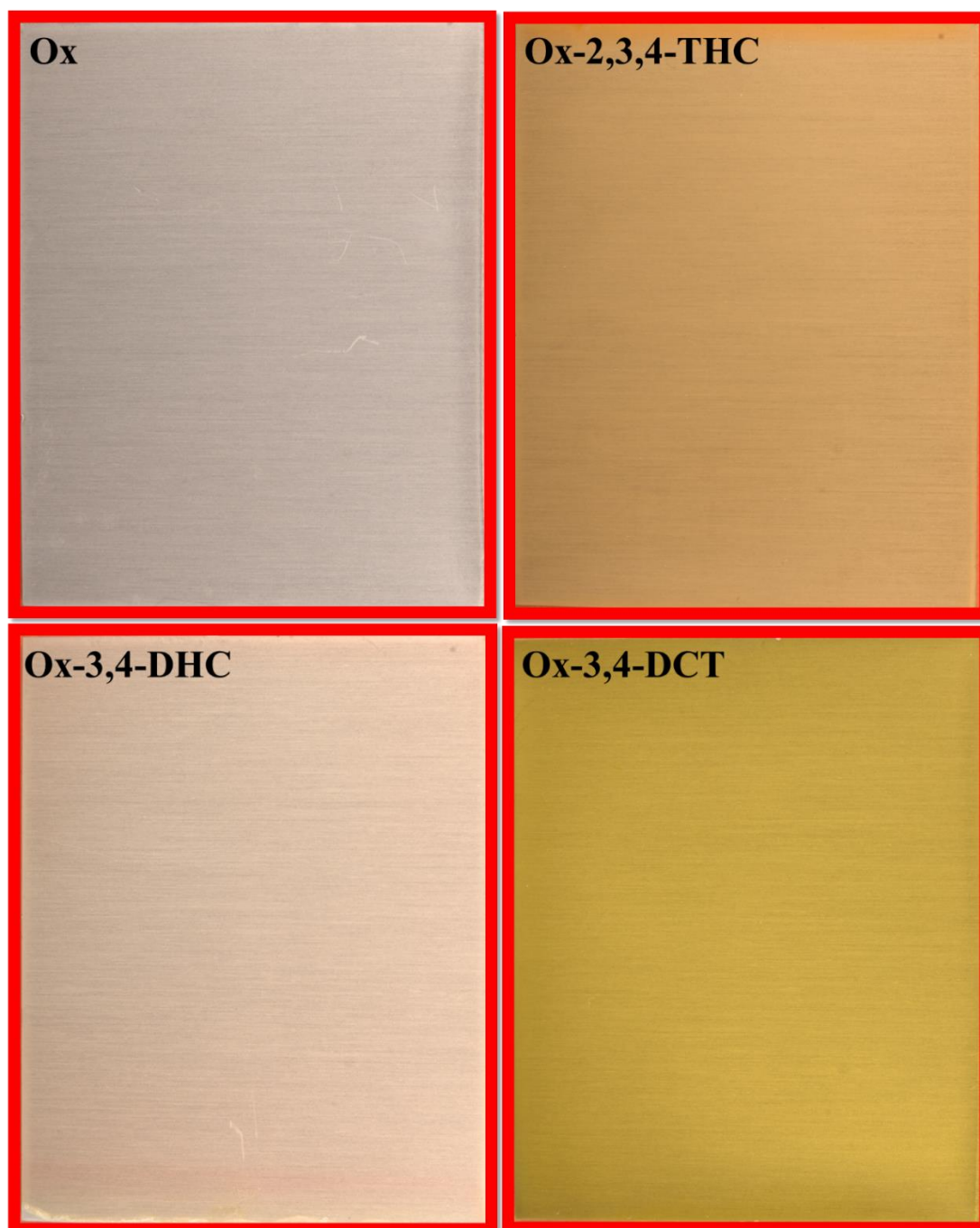


Figure 3.35 Photographic images of as prepared samples.

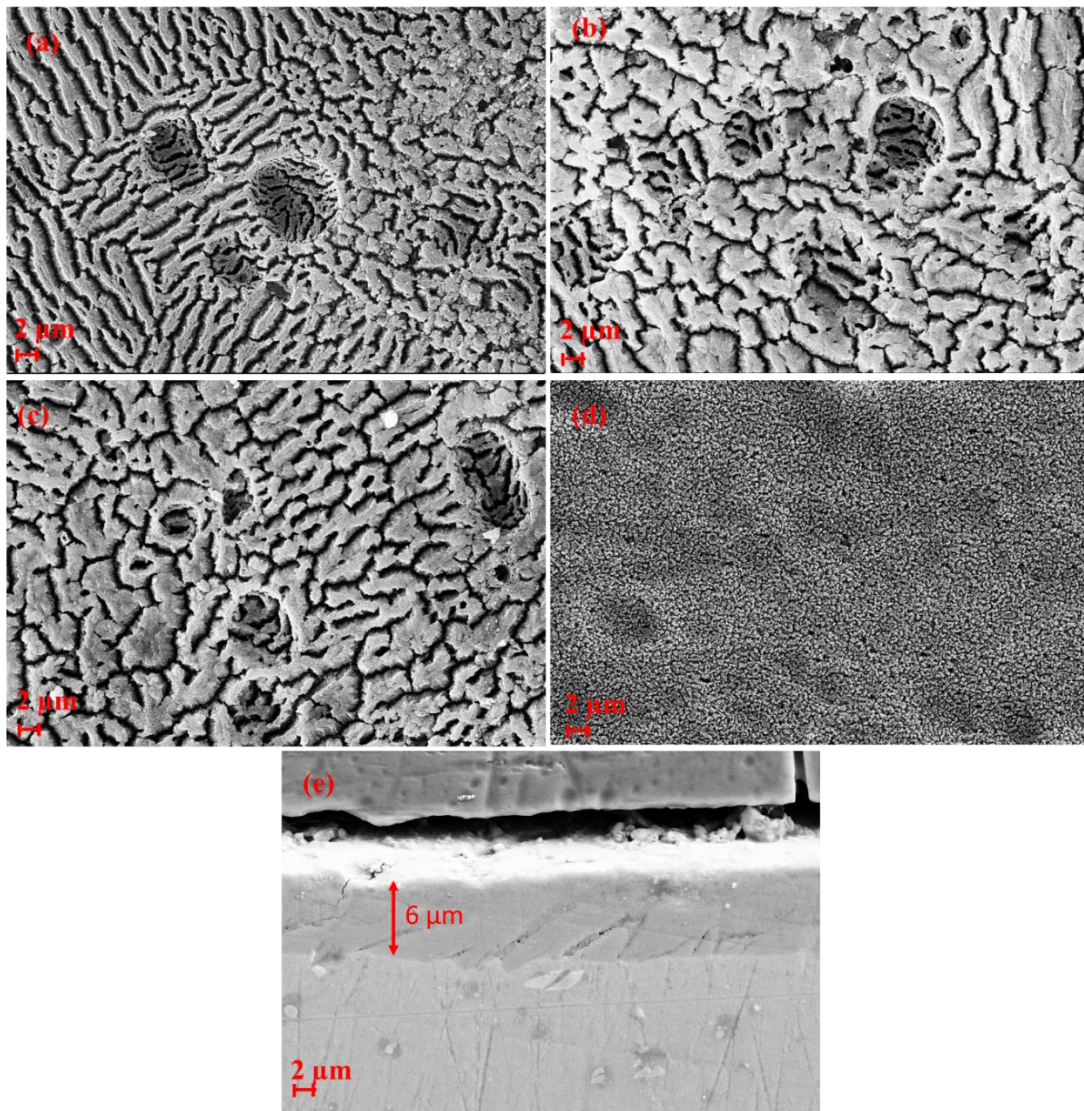


Figure 3.36 FESEM images of as prepared samples (a) Ox, (b) Ox-2,3,4-THC, (c) Ox-3,4-DHC, (d) Ox-3,4-DCT (e) Cross sectional image.

3.3.5 Salt spray analysis

Anticorrosion performances of Ox, Ox-HWS (Ox-hot water sealed), Ox-2,3,4-THC, Ox-3,4-DHC and Ox-3,4-DCT samples were tested by salt spray tests up to 504 h, according to ASTM B117. Normally, the porous oxide layer is sealed by long immersion in hot water (Ox-HWS), and this sample was used as a reference in salt spray test. The samples were observed at different time intervals (168 h, 336 h and 504 h) and their photographs are shown in Figures 3.37 & 3.38. With time, the deterioration of metal surface and existence of decay products are visually observable on the anodized

AA2024-T3 without sealing and hot water sealing samples (Figure 3.37). In the case of sealing with 2,3,4-THC, 3,4-DHC, and 3,4-DCT, the samples are sustainable up to 504 h with no evidence of corrosion (Figure 3.38). These results confirm that, the incorporated inhibitors enhance the anticorrosion performance of the oxide layer. Thus, these molecules can be used as effective sealants in the anodizing process.

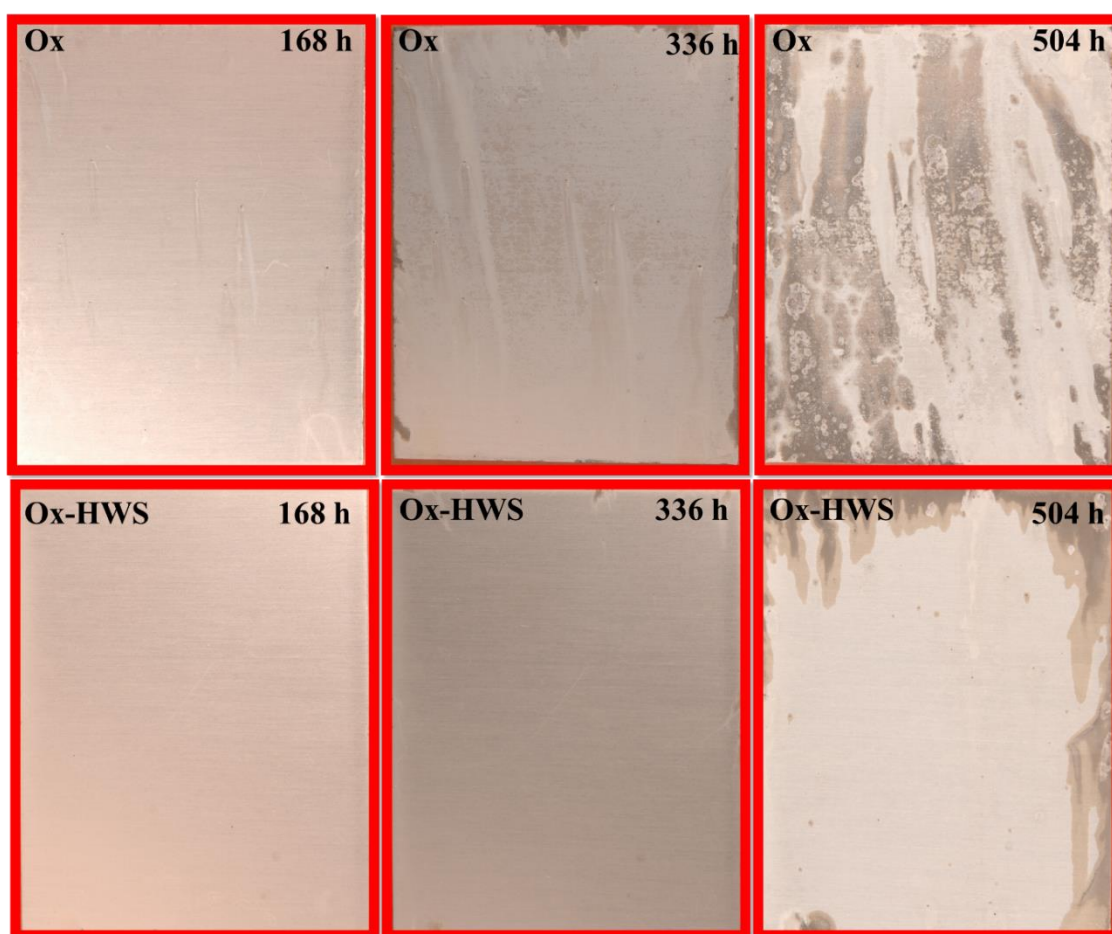


Figure 3.37 Photographs of Ox and Ox-HWS coupons after salt spray exposures.



Figure 3.38 Photographs of Ox-2,3,4-THC, Ox-3,4-DHC, and Ox-3,4-DCT coupons after salt spray exposures.

3.4 EFFECT OF INHIBITORS ON THE ANTICORROSION PROPERTIES OF EPOXY PRIMER COATING ON ALUMINIUM ALLOY 2024-T3

Effect of corrosion inhibitor addition on the anticorrosion properties of primer coatings on aluminium alloy 2024-T3 was investigated. 3,4-DCT, 3,4-DHC, 2,3,4-THC were supplemented to epoxy primer generally used in aircraft paint systems and anticorrosion protection property was examined using electrochemical impedance spectroscopy and salt spray test.

3.4.1 Electrochemical impedance spectroscopy studies

The impedance spectra for the corrosion of primer coated Aluminium alloy in 3.5 % NaCl solution at different immersion times, represented as Bode plots, are presented in Figure 3.39.

Up to 168 h of exposure, the impedance at low frequency ($/Z/_{0.01\text{Hz}}$) is higher than $10^8 \Omega \text{ cm}^2$, indicating that the primer coating blocks the alloy surface completely from coming in contact with the corrosion environment. After 240 h of immersion, $/Z/_{0.01\text{Hz}}$ value decreases with the increase in exposure period, as a result of the corrosive medium ingress through the coated primer layer and reaching the alloy surface; and thus activating the surface corrosion. The phase angle value at a higher frequency (HF) is ascribed to the coating capacitance which decreases with the increase in immersion time (Figure 3.39). From 24 h to 168 h, the phase angle plots are associated with a large time constant. The further increase in immersion time results in the appearance of an additional time constant at the LF region. This is attributed to the corrosion reactions resulting from the diffusion of electrolyte to the alloy surface. These results suggest that primer coating alone has poor barrier property and offered corrosion protection only up to 168 h of exposure in the corrosive medium.

The time-dependent impedance spectra for inhibitors incorporated primer coatings are presented in Figure 3.40. The addition of inhibitors to the primer coating significantly affects the anticorrosion behaviour of the primer coated alloy. The impedance modules at $/Z/_{0.01\text{Hz}}$ is higher than $10^8 \Omega \text{ cm}^2$ and sustains the same up to 504 h, indicating that the inhibitor incorporated primer coating covers the alloy surface

more completely and thus preventing the ingress of corrosive ions through the coating layer. The large time constants in the phase angle plots, over the entire exposure period, indicate sustainable coatings. The results confirm that the corrosion protection property of the primer coating increases by the inclusion of inhibitors.

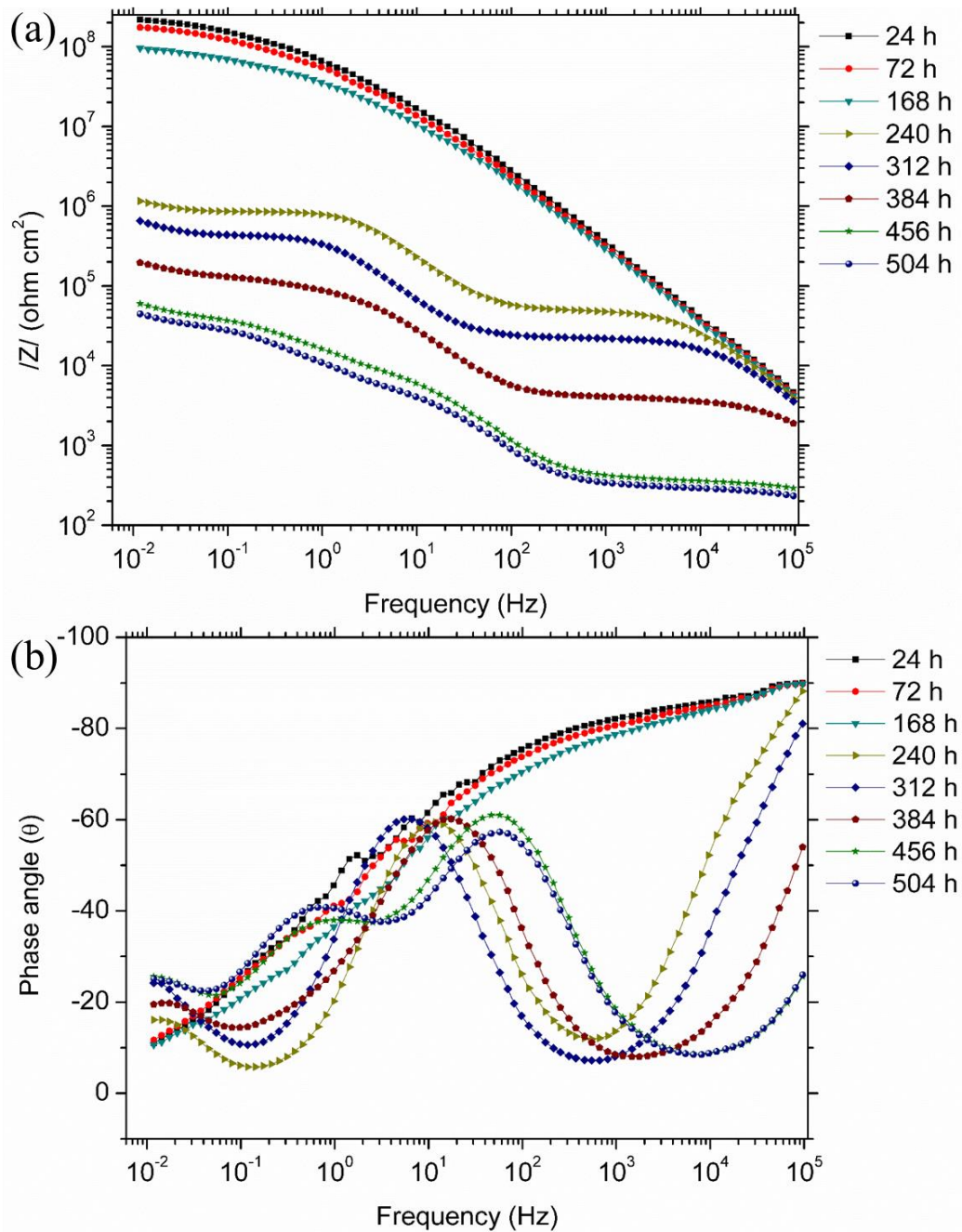


Figure 3.39 Bode plots for the corrosion of AA2024-T3 alloy surface coated with primer coating in 3.5 % NaCl solution at different immersion times.

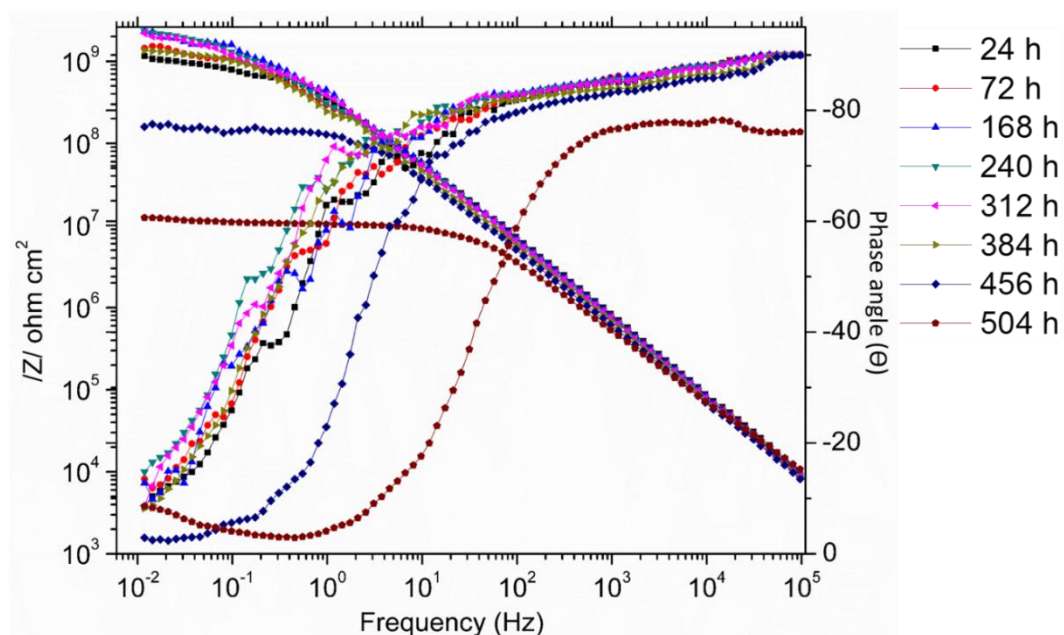


Figure 3.40 (a) Bode plots for the corrosion of AA2024-T3 alloy surface coated with 3,4-DCT doped primer coating in 3.5 % NaCl solution at different immersion times.

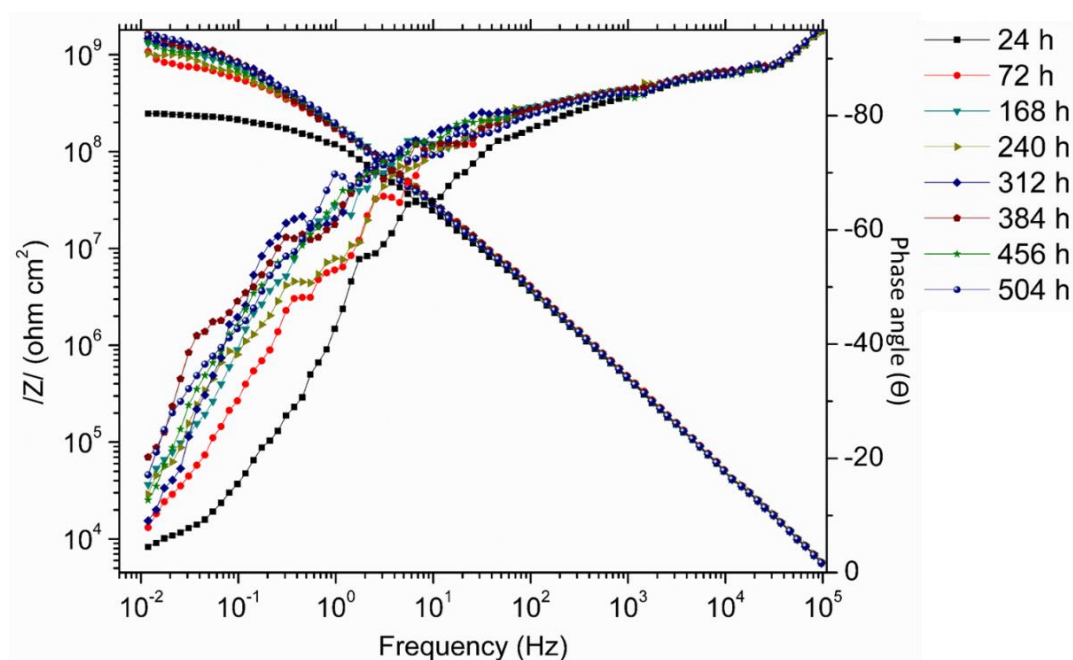


Figure 3.40 (b) Bode plots for the corrosion of AA2024-T3 alloy surface coated with 3,4-DHC doped primer coating in 3.5 % NaCl solution at different immersion times.

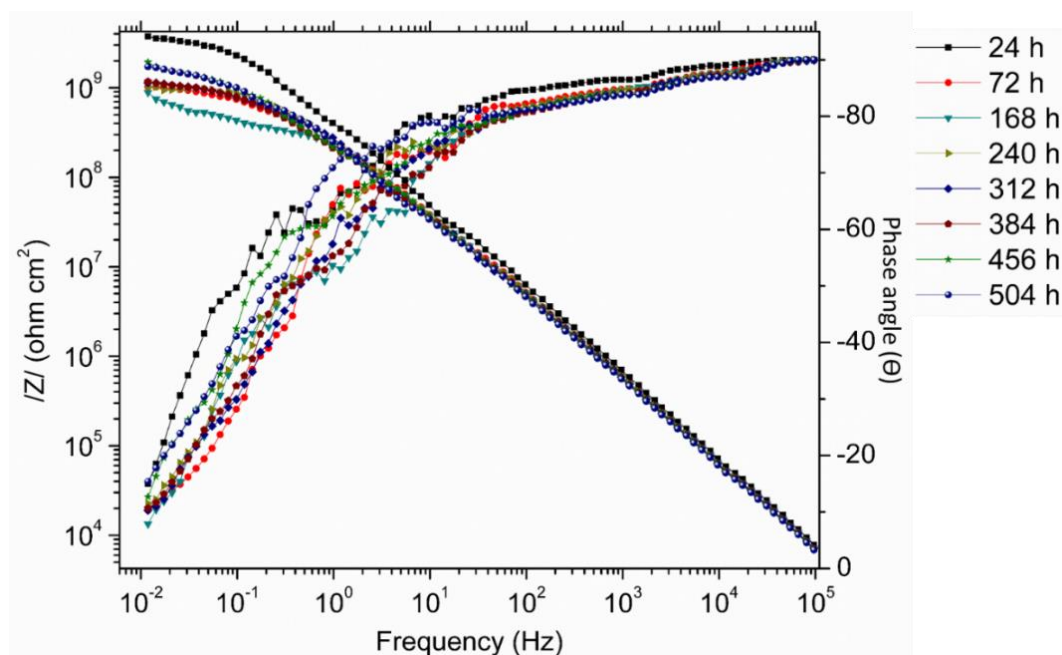


Figure 3.40 (c) Bode plots for the corrosion of AA2024-T3 alloy surface coated with 2,3,4-THC doped primer coating in 3.5 % NaCl solution at different immersion times.

The impedance spectra were fitted with suitable equivalent circuit (EC) models to understand the processes that take place on the substrate/solution interface. The impedance spectra of the primer coating are associated with two time constants at initial immersion from 24 h to 168 h (Figure 3.41 a). The first one pertains to the primer coating layer and the second one corresponds to the oxide layer; and are generated by the penetration of the ions through the primer coating. The equivalent circuit is composed of, solution resistance (R_s), primer coating resistance (R_{coat}), the primer coating capacitance (Q_{coat}), oxide layer resistance (R_{ox}) and oxide layer capacitance (Q_{ox}). With the further extension in exposure period from 168 h to 384 h, an additional time constant appears due to the cracks developed in the primer and oxide layers, which permit percolation of ions to the alloy surface. Thus, the two extra components are inserted in the circuit model to explain the charge transfer resistance (R_{ct}) and double layer capacitance (Q_{dl}) (Figure 3.41 b). Above 456 h, up to 504 h, an additional Warburg element (W) appears, which represents the diffusion of the corrosion product ions from the surface through the surface films (Figure 3.41 c). The impedance spectra of the inhibitor doped primer coating are fitted with two time

constants and are sustainable up to 504 h. This result further strengthens the hypothesis that, inhibitor enhances the barrier efficiency of the primer coating.

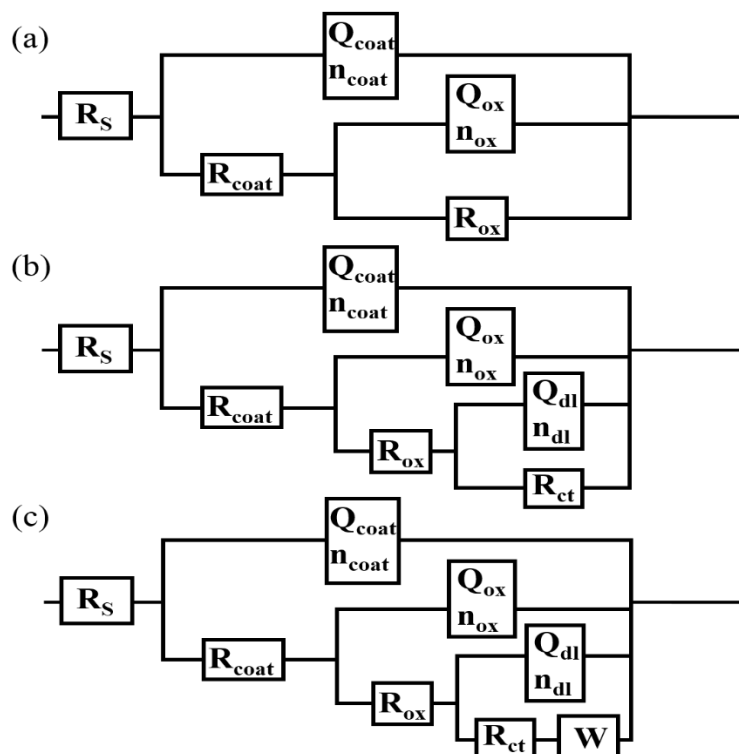


Figure 3.41 Equivalent circuits used to fit the experimental impedance data of primer coating, over the exposure periods (a) up to 168 h, (b) above 216 h up to 384 h and (c) above 456 h up to 504 h.

Table 3.7 lists the impedance parameters. The polarization resistance (R_p) values were calculated as the sums of R_{coat} and R_{ox} when two time constants are present and as the sums of R_{coat} , R_{ox} and R_{ct} in the presence of three time constants. The R_p value is used for predicting the corrosion protection property of the primer layer during immersion. The results of the variation of polarization resistance with immersion time, for different coatings are shown in Figure 3.42. Inhibitor doped primer coatings show higher polarization resistances compared to the undoped primer coatings, over the entire immersion period, implying good protection properties and higher water penetration resistance of the coating layer. The inhibition efficiencies of the coatings in the present study are in the order: Primer < Primer + 3,4-DCT < Primer + 3,4-DHC ~ Primer + 2,3,4-THC.

Table. 3.7 Impedance parameters for the corrosion of AA2024-T3 alloy coated with the primer coating in the absence and in the presence of inhibitors.

Coating	Immersion time (h)	R_{coat} ($\Omega \text{ cm}^2$)	R_{ox} ($\Omega \text{ cm}^2$)	R_{ct} ($\Omega \text{ cm}^2$)	W (S cm^{-2})	R_{p} ($\Omega \text{ cm}^2$)
Primer	24	3.061×10^5	2.680×10^8	-	-	2.683×10^8
	72	3.436×10^5	2.291×10^8	-	-	2.294×10^8
	168	2.695×10^5	1.15×10^8	-	-	1.152×10^8
	240	4.754×10^4	8.259×10^5	6.739×10^5	-	1.547×10^6
	312	2.142×10^4	4.234×10^5	5.816×10^5	-	1.026×10^6
	384	3.898×10^3	1.155×10^5	9.893×10^4	-	2.183×10^5
	456	2.171×10^2	5.050×10^3	4.158×10^4	1.272×10^{-4}	4.684×10^4
	504	1.882×10^2	6.449×10^3	2.157×10^4	1.608×10^{-4}	2.820×10^4
	-Primer + 3,4- DCT	24	6.221×10^6	1.171×10^9	-	-
72		8.733×10^5	1.701×10^9	-	-	1.701×10^9
168		6.124×10^5	2.013×10^9	-	-	2.013×10^9
240		5.101×10^5	2.704×10^9	-	-	2.704×10^9
312		6.302×10^5	2.261×10^9	-	-	2.261×10^9
384		2.874×10^5	1.442×10^9	-	-	1.442×10^9
456		2.957×10^5	1.560×10^8	-	-	1.562×10^8
504		2.027×10^5	1.041×10^8	-	-	1.043×10^8
Primer + 3,4- DHC		24	2.593×10^5	2.572×10^8	-	-
	72	9.427×10^5	1.048×10^9	-	-	1.048×10^9
	168	3.829×10^5	1.534×10^9	-	-	1.534×10^9
	240	1.034×10^6	1.505×10^9	-	-	1.506×10^9
	312	3.773×10^5	1.762×10^9	-	-	1.762×10^9
	384	3.118×10^5	2.370×10^9	-	-	2.370×10^9
	456	3.120×10^5	1.538×10^9	-	-	1.538×10^9
	504	4.648×10^5	2.018×10^9	-	-	2.018×10^9
	Primer + 2,3,4- THC	24	1.257×10^6	5.136×10^9	-	-
72		1.462×10^6	1.120×10^9	-	-	1.121×10^9
168		1.268×10^6	1.819×10^9	-	-	1.820×10^9
240		3.237×10^5	1.249×10^9	-	-	1.249×10^9
312		3.979×10^6	1.285×10^9	-	-	1.286×10^9
384		5.207×10^5	1.343×10^9	-	-	1.343×10^9
456		3.975×10^5	2.167×10^9	-	-	2.167×10^9
504	3.593×10^5	1.993×10^9	-	-	1.993×10^9	

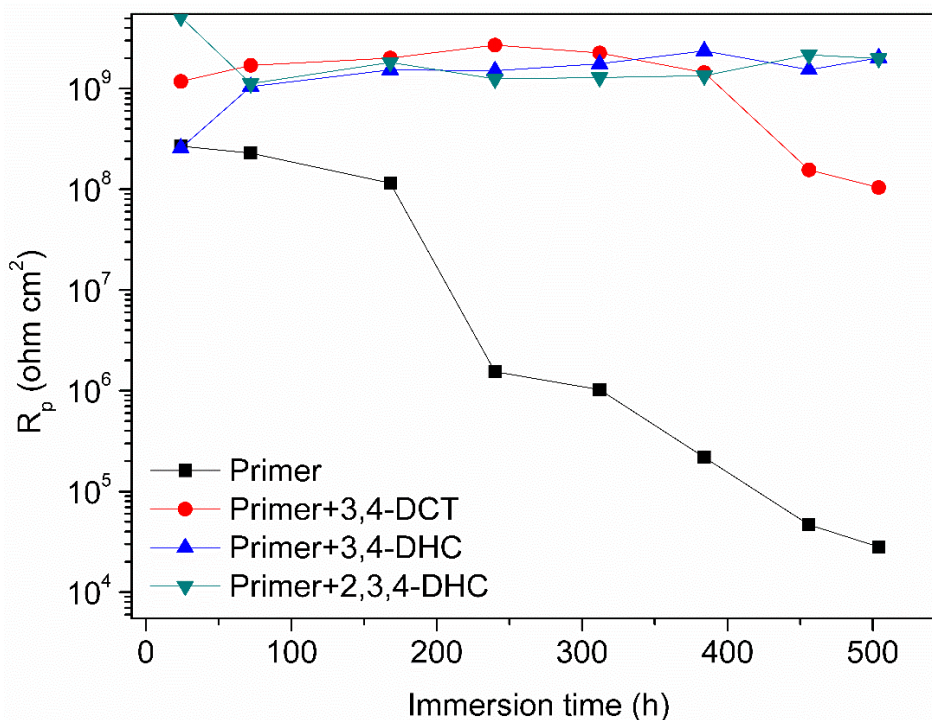


Figure 3.42 Plots of variation of polarization resistance (R_p) with time for the primer coating and inhibitor doped primer coatings.

3.4.2 Corrosion studies on artificial defect area

EIS studies were carried out on the simulated artificial defect areas to examine the active corrosion behaviour of the blank primer coating and the inhibitor doped primer coatings. The Bode plots of the Aluminium alloy substrates covered by blank primer coating with an artificial defect, at different exposure periods, in aqueous sodium chloride solution are depicted in Figure 3.43. The total impedance value of the primer coated system is not largely altered with the variation in immersion time. The Bode plots presented in Figure 3.43 show the presence of two-time constants. The first time constant at 10^{-4} Hz to 1 Hz, corresponds to the oxide layer and the second time constant around 10^{-1} Hz to 10^{-2} Hz, depicts the charge transfer reaction taking place at the alloy surface.

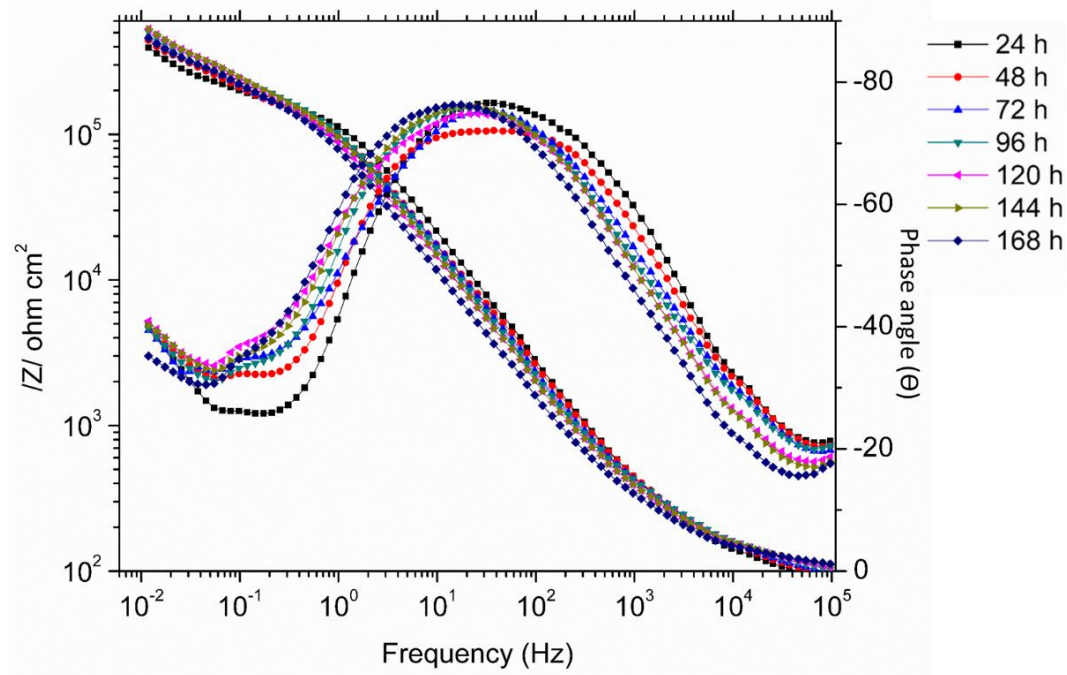


Figure 3.43 Bode plots for the primer coating with an artificial defect at different immersion times, in 3.5 % NaCl solution.

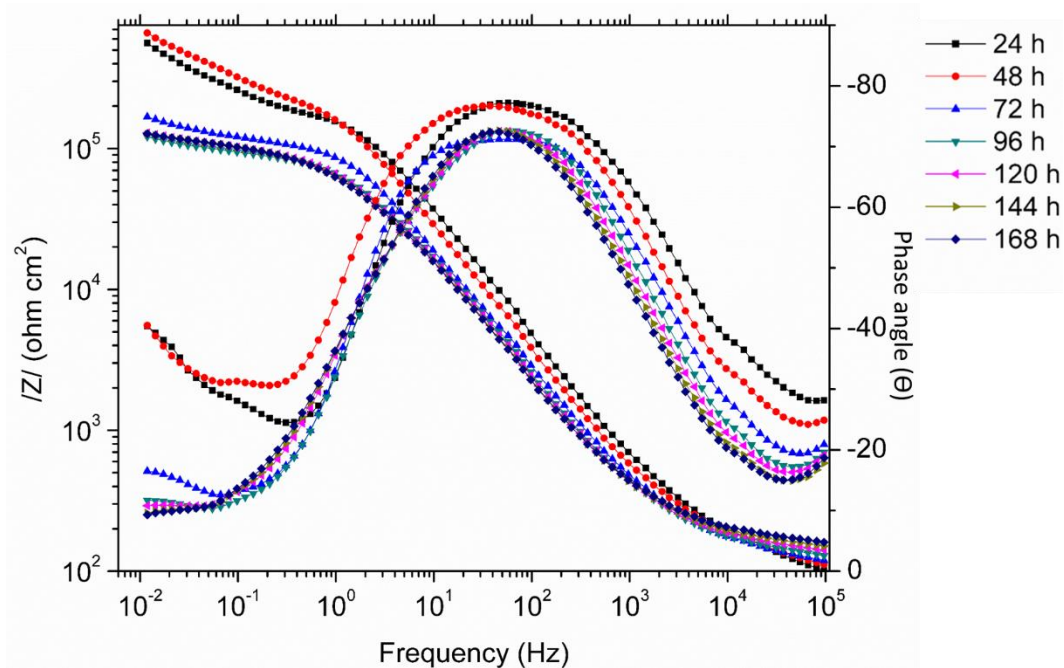


Figure 3.44 (a) Bode plots for the primer coating doped with 3,4-DCT, with scribes at different immersion times, in 3.5 % NaCl solution.

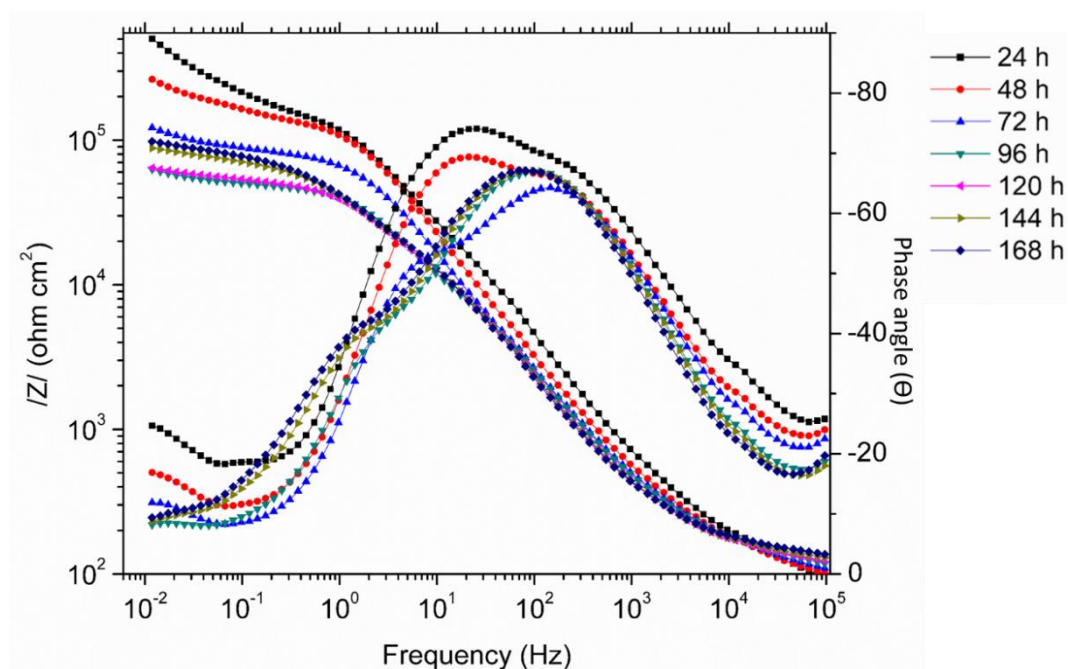


Figure 3.44 (b) Bode plots for the primer coating doped with 3,4-DHC, with scribes at different immersion times, in 3.5 % NaCl solution.

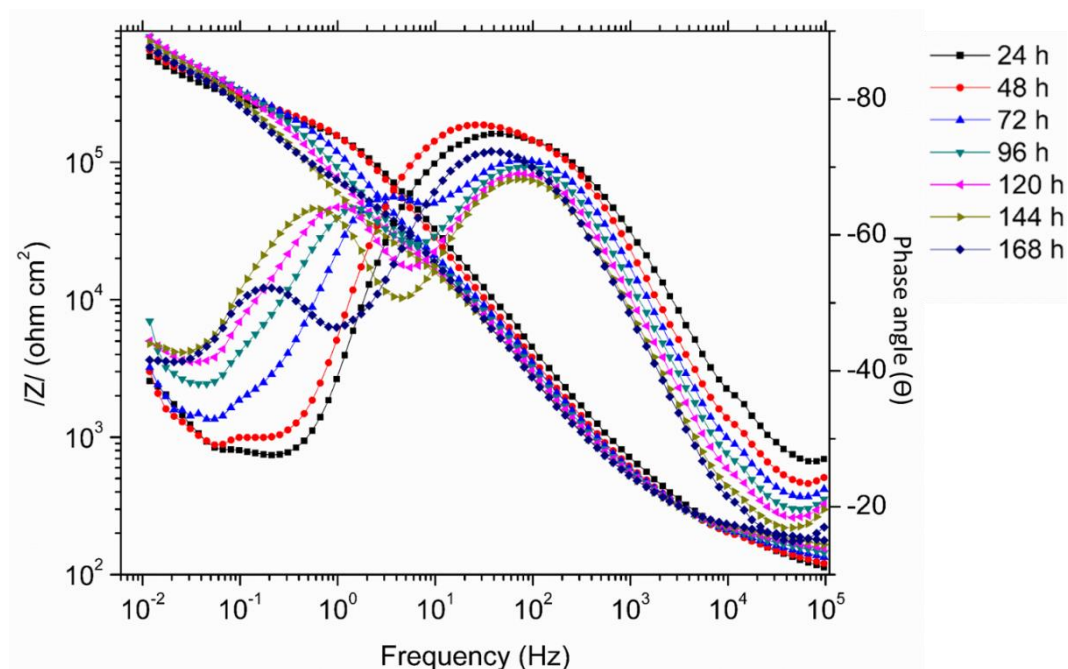


Figure 3.44 (c) Bode plots for the primer coating doped with 2,3,4-THC, with scribes at different immersion times, in 3.5 % NaCl solution.

In the presence of inhibitors, 3,4-DCT and 3,4-DHC, the total impedance value declines as the immersion time increases (Figures 3.44 a and 3.44 b). This finding confirms that the corrosion is initiated on the artificial defected area and spreads over the alloy surface due to delamination of the primer layer. The primer layer delamination initiated from the artificially defected area is due to the poor adhesion properties. These results are suggestive of the fact that the addition of 3,4-DCT and 3,4-DHC negatively affects the adhesion properties of the primer layer and the two compounds do not show the active corrosion protection efficiency.

However, in the presence of 2,3,4-THC, the total impedance value is higher than that for the blank primer coated system. From 24 h to 48 h, the impedance spectra is associated with two time constants (Figure 3.44c). They correspond to the oxide layer on the alloy surface and the charge transfer reaction on the artificial defect area. When the exposure period is further increased, one more time constant is observed in the LF region. The additional time constant may be due to the release of the 2,3,4-THC molecules from the primer layer along the scribed area, resulting in the formation of inhibitor layer. These results suggest that 2,3,4-THC doped primer coated system offers active corrosion protection.

The active corrosion barrier mechanism of the primer layer was analyzed using the relevant equivalent circuit model fitted on the impedance curves. The impedance spectra of the artificially defected blank primer coating, 3,4-DCT doped coating and 3,4-DHC doped primer coating are fitted with two time constants incorporated equivalent circuit model (Figure 3.45a). The equivalent circuit comprises of oxide layer resistance (R_{ox}), oxide layer capacitance (Q_{ox} and n_{ox}), double layer capacitance (Q_{dl} and n_{dl}) and charge transfer resistance (R_{ct}).

In the presence of 2,3,4-THC, up to 48 h of exposure period, the impedance curves are fitted with the ECs, presented in Figure 3.45a. For further increase in the exposure period up to 168 h, the impedance curves are fitted with the EC model depicted in Figure 3.45b. The additional two new components in the circuit model are the inhibitor layer resistance (R_{in}) and its capacitance (Q_{in}). Some of the important fitted parameters are tabulated in Table 3.8.

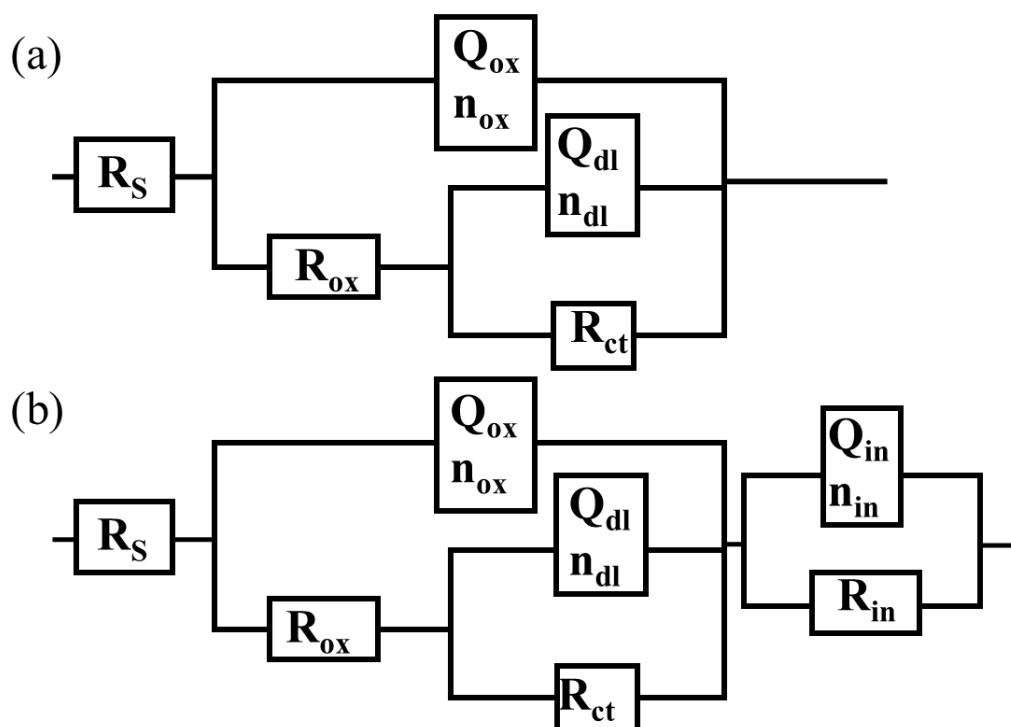


Figure 3.45 Equivalent circuit used to fit the experimental impedance data for the coatings with scribe (a) blank, 3,4-DCT doped and 3,4-DHC doped primer coating over an exposure period of 168 h; and 2,3,4-DHC doped primer coating up to an exposure period of 48 h, (b) 2,3,4-DHC doped primer coating for an exposure period above 48 h up to 168 h.

The active corrosion inhibition properties of the coating system can be explained in terms of R_p values. Figure 3.46 depicts the variation of polarization resistance with immersion time during the corrosion analysis. It is seen from Figure 3.46 that R_p decreases when the immersion time increases, in the presence of 3,4-DCT and 3,4-DHC in the primer coating; and also the values are lower than that for the blank primer coating. These observations are indicative of the fact that the corrosion rate increases and the inhibition effect decreases as the exposure period is increased. In the presence of 2,3,4-THC in primer coating, the R_p value increases with the exposure period up to 120 h and decreases thereafter. The gradual growth of R_p value is due to the formation of an inhibitor layer by 2,3,4-THC, released from the primer layer along the artificial defect area.

Table 3.8 Impedance parameters for the corrosion of AA2024-T3 alloy coated with the primer coating in the absence and in the presence of inhibitors with scribe.

Coating	Immersion time (h)	R_{ox} ($\Omega \text{ cm}^2$)	R_{ct} ($\Omega \text{ cm}^2$)	R_{in} ($\Omega \text{ cm}^2$)	R_p ($\Omega \text{ cm}^2$)
Primer	24	1.944×10^5	1.535×10^6	-	1.729×10^6
	48	2.174×10^5	1.479×10^6	-	1.217×10^6
	72	2.136×10^5	1.588×10^6	-	1.801×10^6
	96	2.777×10^5	1.543×10^6	-	1.820×10^6
	120	2.863×10^5	2.109×10^6	-	2.395×10^6
	144	2.831×10^5	1.390×10^6	-	1.673×10^6
	168	2.811×10^5	7.912×10^5	-	1.072×10^6
-Primer + 3,4-DCT	24	2.186×10^5	1.515×10^6	-	1.733×10^6
	48	2.944×10^5	2.495×10^6	-	2.789×10^6
	72	1.284×10^5	8.479×10^4	-	2.131×10^5
	96	9.580×10^4	5.559×10^4	-	1.513×10^5
	120	1.010×10^5	7.201×10^4	-	1.730×10^5
	144	9.694×10^4	7.165×10^4	-	1.685×10^5
	168	9.704×10^4	6.570×10^4	-	1.627×10^5
Primer + 3,4-DHC	24	2.022×10^5	1.446×10^6	-	1.648×10^6
	48	1.743×10^5	2.380×10^5	-	4.123×10^5
	72	9.680×10^4	7.097×10^4	-	1.677×10^5
	96	5.473×10^4	2.723×10^4	-	8.196×10^4
	120	4.542×10^4	3.134×10^4	-	7.676×10^4
	144	4.273×10^4	5.401×10^4	-	9.674×10^4
	168	4.618×10^4	5.754×10^4	-	1.037×10^5
Primer + 2,3,4-THC	24	2.687×10^5	1.390×10^6	-	1.658×10^6
	48	3.049×10^5	1.949×10^6	-	2.253×10^6
	72	2.240×10^4	1.812×10^5	5.625×10^6	5.828×10^6
	96	2.075×10^4	1.754×10^5	7.789×10^6	7.985×10^6
	120	1.602×10^4	1.847×10^5	1×10^7	1.020×10^7
	144	5.619×10^4	3.601×10^5	1.563×10^6	1.979×10^6
	168	9.266×10^4	2.866×10^5	1.468×10^6	1.847×10^6

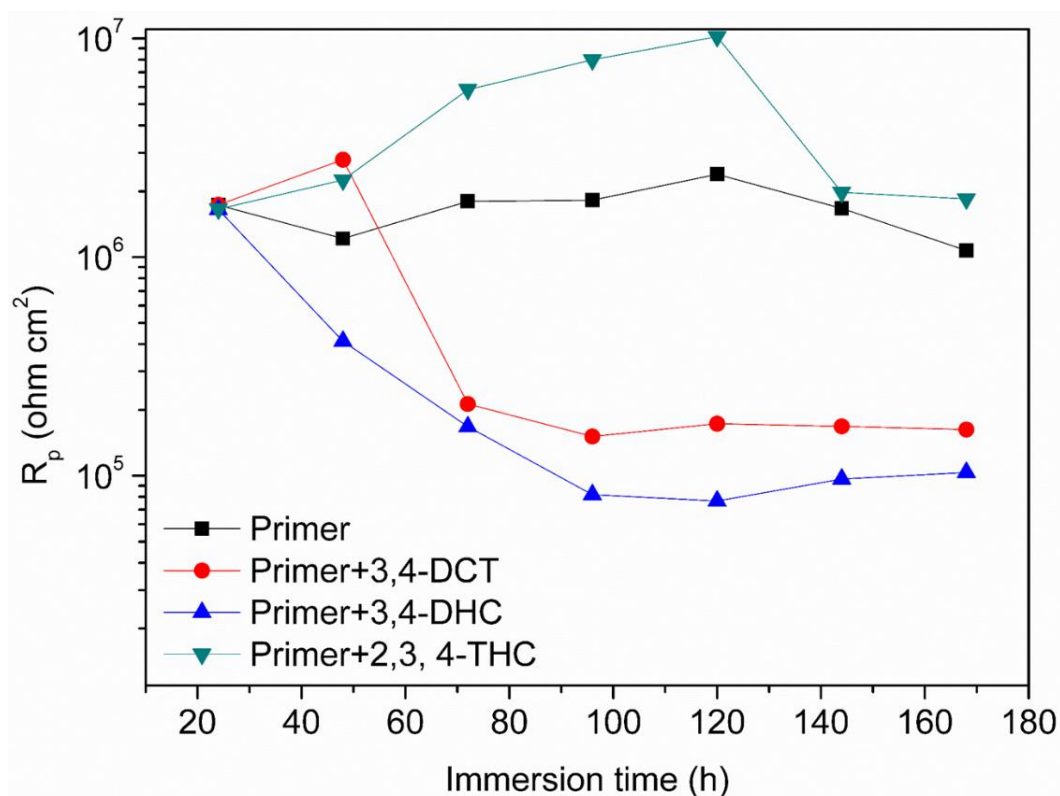


Figure 3.46 Variation of polarization resistance (R_p) with time for the primer coating in the absence and in the presence of inhibitors with scribe.

3.4.3 Salt spray analysis

The salt spray analysis was performed up to 1000 h, according to ASTM B117. The salt spray results support the observations of the EIS studies. Figure 3.47 presents the images of the specimen surfaces after the salt spray analysis of the blank primer coated alloy surface. The blister formation is observed on the primer coated system, due to the diffusion of corrosion medium through the primer layer. The coating acts as a semi permeable membrane, ions may diffuse through the coating and the corrosive ions accumulate at the coating substrate interface, leading to blistering. Schematic representation of blister formation is shown in Figure 3.48. The diffused corrosive ions could initiate corrosion.

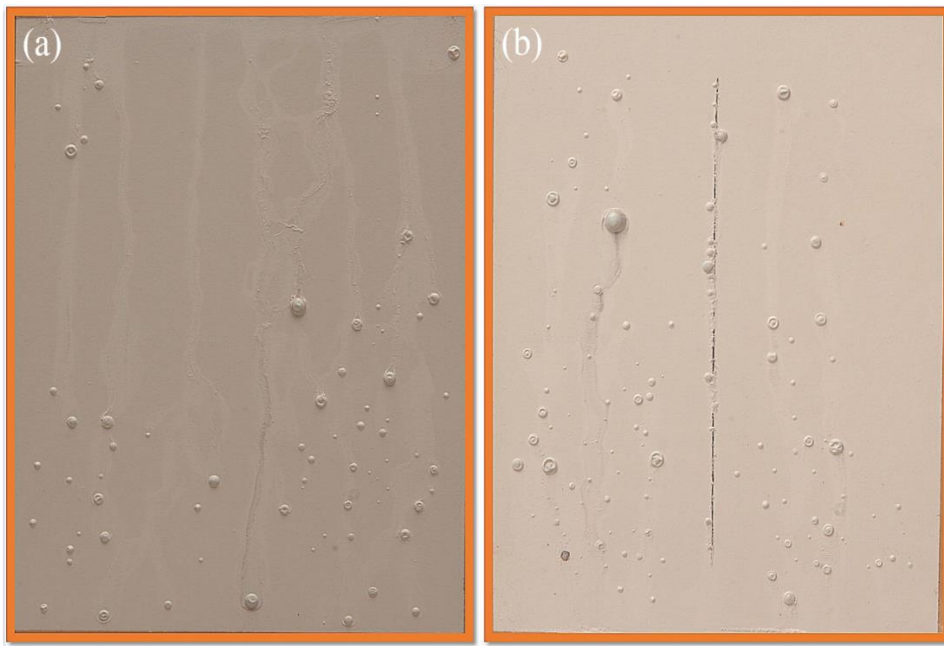


Figure 3.47 Images of (a) primer coating (b) primer coating with scribe after salt spray tests for 1000 h.

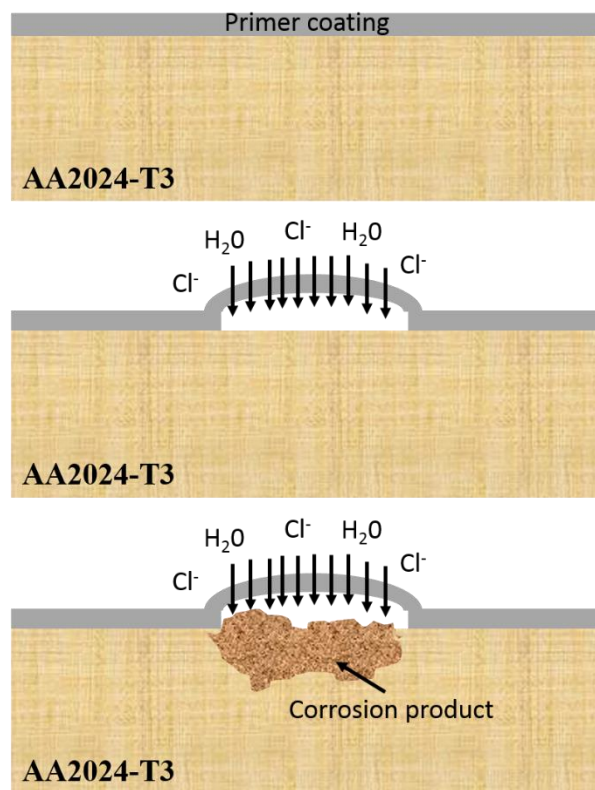


Figure 3.48 Schematic representation of blister formation and corrosion of the alloy surface under primer coating.

Figure 3.49 shows the cross-section images of the blisters. The substrate thickness of approximately 1.611 mm, decreases to about 1.530 mm under the blister due to the degradation of the substrate. The corresponding EDX results are shown in Figure 3.49b. Higher concentration of oxygen content confirms the presence of corrosion product. The results are affirmative of the fact that the blank primer coating offers poor barrier properties.

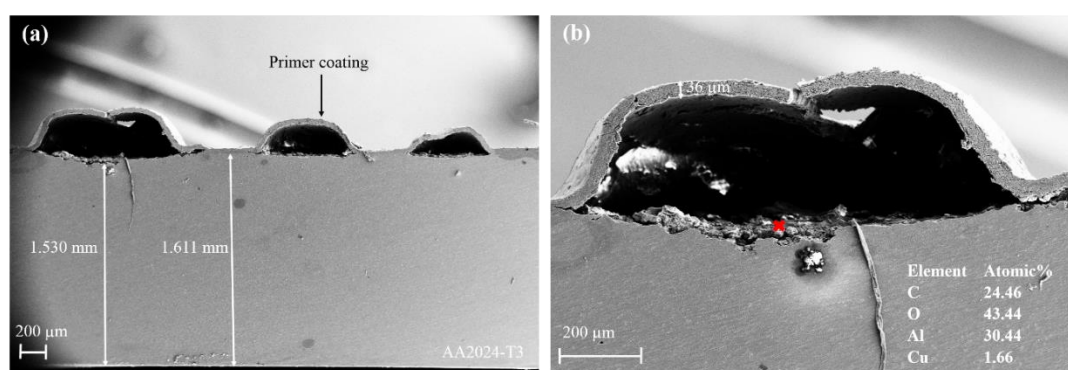


Figure 3.49 FE-SEM cross sectional images of the primer coating after salt spray test for 1000 h.

Figure 3.50 shows the images of the alloy surfaces coated with inhibitor doped primer, post salt spray exposure of 1000 h. The inhibitors doped primer coatings are blister free. These results corroborate with the EIS results on the order of inhibition efficiency of the coatings.

The active corrosion inhibition efficiencies of the inhibitor doped primer coatings with artificial damages were evaluated by salt spray test for 1000 h. The images of the artificially damaged coatings are shown in Figure 3.51. The FE-SEM images of the alloy surfaces with artificially damaged coatings are presented in Figure 3.52. The images show that in the presence of 3,4-DCT and 3,4-DHC, delamination and blistering of the coating are initiated around the scribe area. These results indicate that the presence of 3,4-DCT, 3,4-DHC in the coating negatively effects the coating adhesion, and the inhibitors do not show the active corrosion protection efficiency. 2,3,4-THC doped primer coating performed better in 1000 h salt spray test, as no delaminating was observed around the scribe area. The results corroborate with the EIS

results that 2,3,4-THC doped primer coating offers the active corrosion inhibition efficiency.

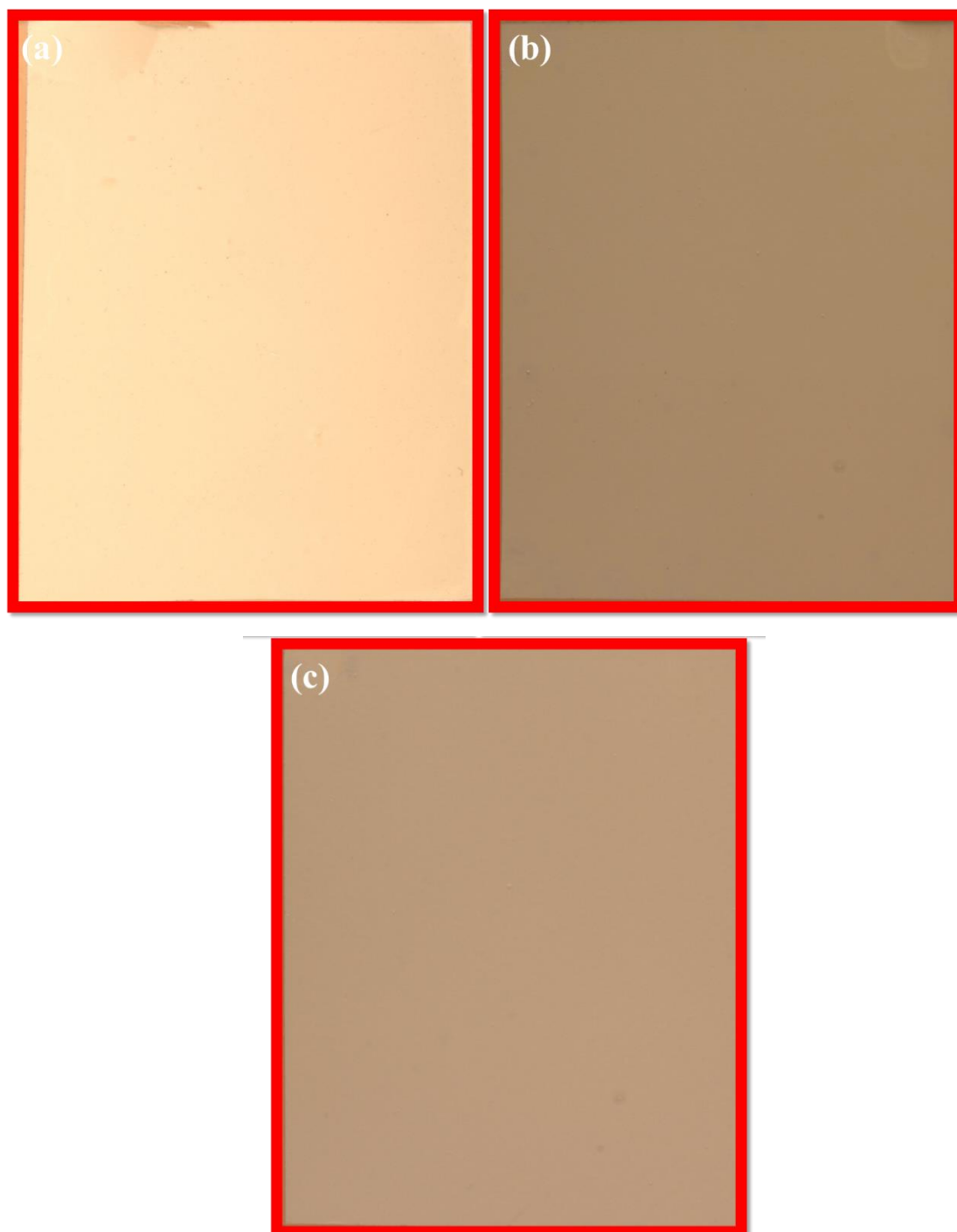


Figure 3.50 Images of (a) 3,4-DCT doped primer coating, (b) 3,4-DHC doped primer coating and (c) 2,3,4-THC doped primer coating after salt spray tests for 1000 h.

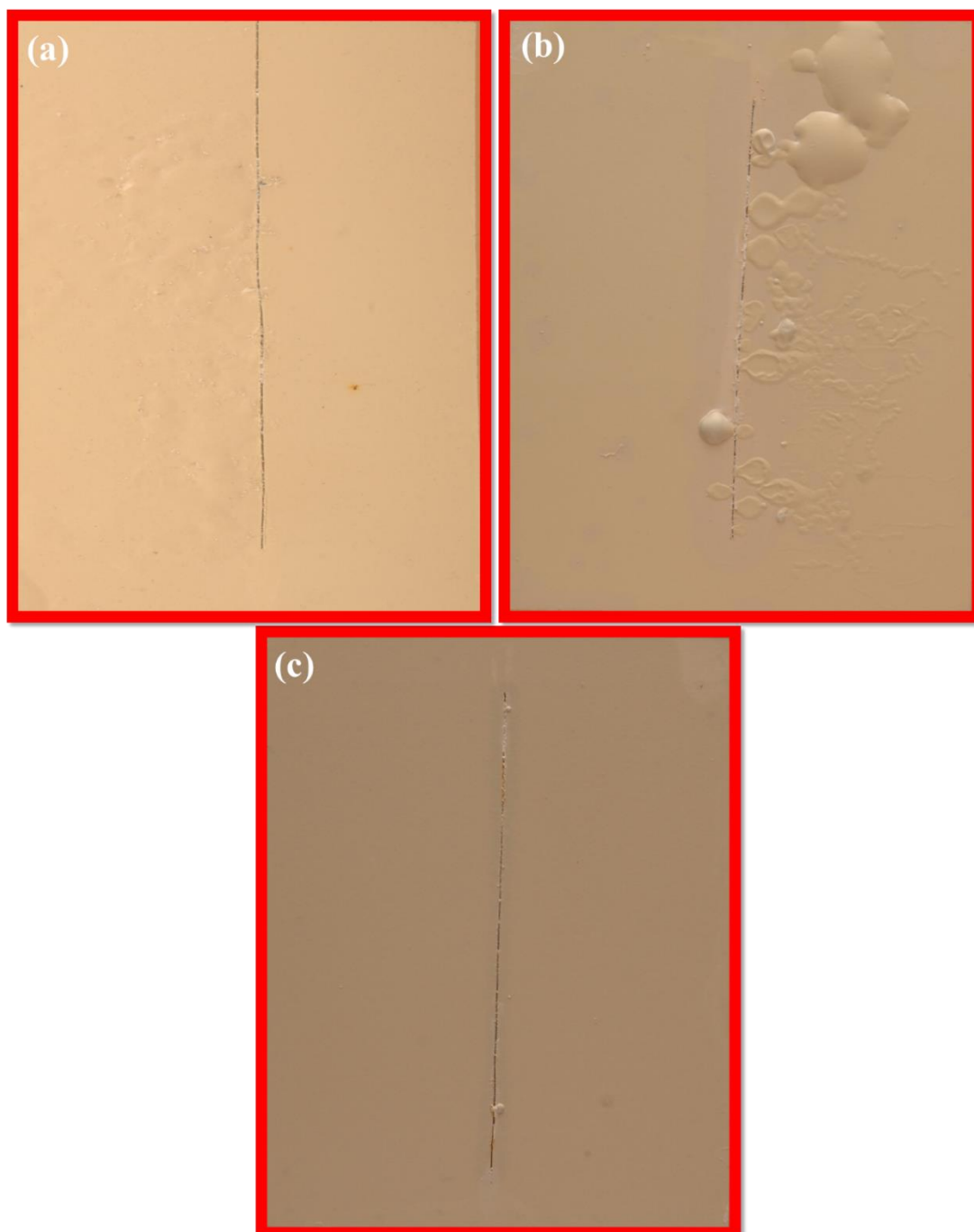


Figure 3.51 Images of (a) 3,4-DCT doped primer coating, (b) 3,4-DHC doped primer coating and (c) 2,3,4-THC doped primer coating, with scribes after salt spray tests for 1000 h.

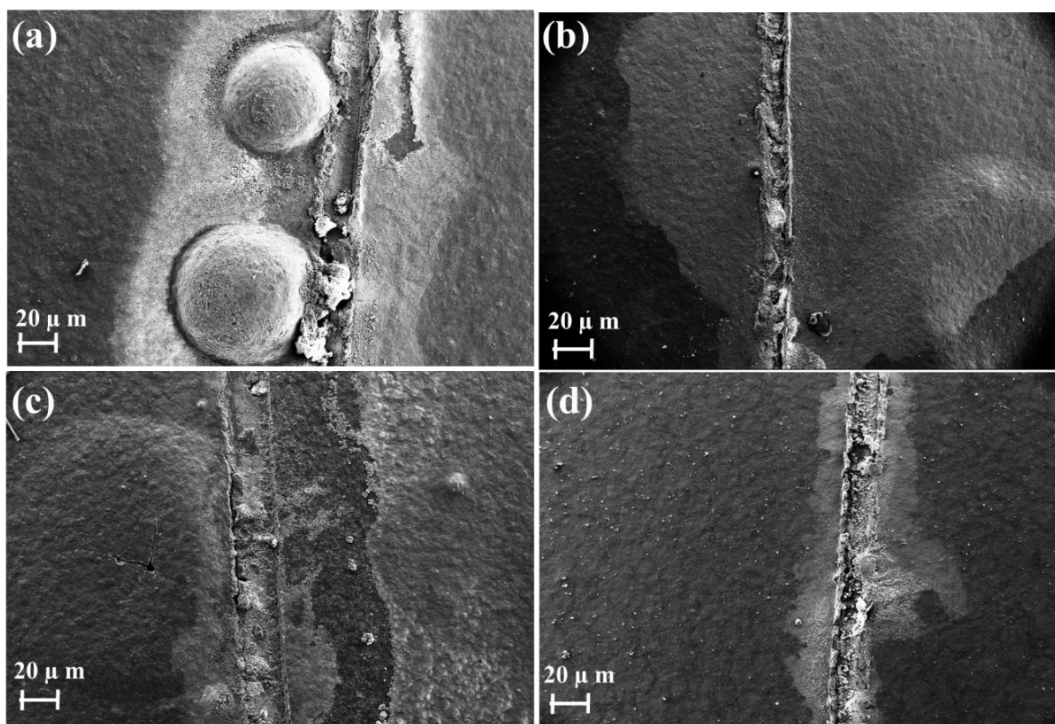


Figure 3.52 FE-SEM images of the scribe area taken after 1000 h salt spray test, (a) primer coating, (b) 3,4-DCT doped primer coating, (c) 3,4-DHC doped primer coating, (d) 2,3,4-THC doped primer coating.

Anticorrosion performance of the coatings is mainly decided by the interaction between the coating and the surface of the alloy. Interfacial surface adhesion was analyzed with the help of FE-SEM cross-sectional images of the primer and inhibitor doped primer coatings on the alloy substrate, post salt spray analysis (Figure 3.49 and Figure 3.53). Blank primer, 2,4-DHC doped, and 3,4-DHC doped primer coatings showed the delamination of the layer. 2,3,4-THC doped primer coating showed good adhesion, as no delamination is observed around the scribe area. Above results confirm that the addition of 2,3,4-THC improves the barrier properties of the primer coating.

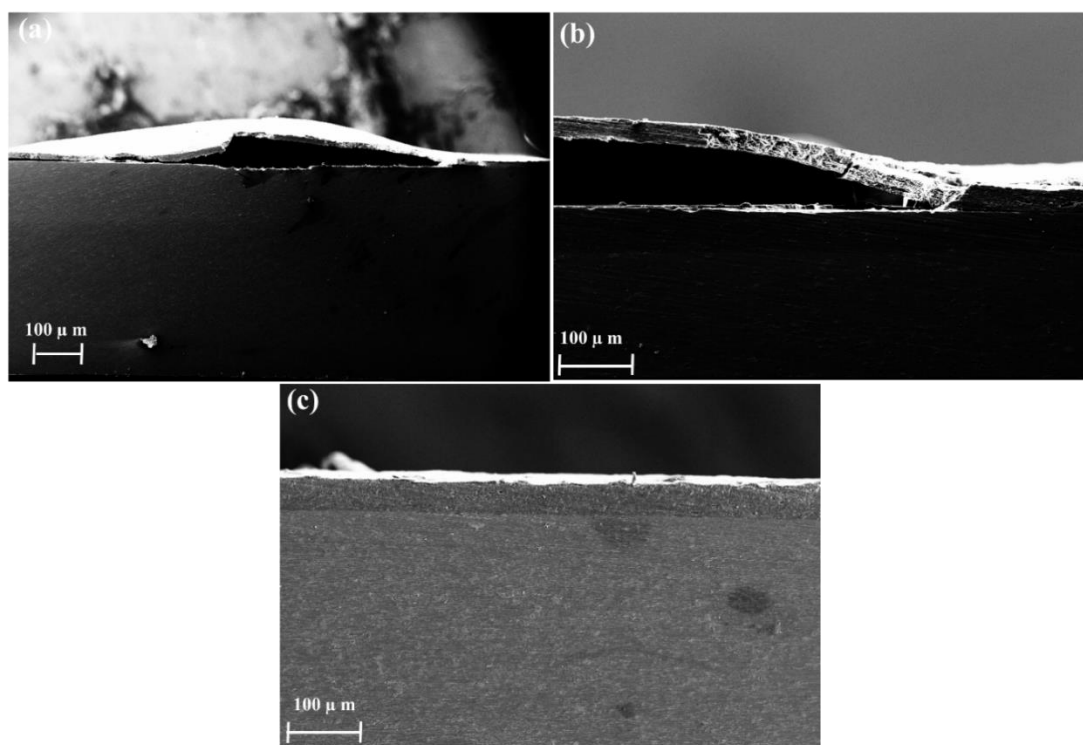


Figure 3.53 FE-SEM cross sectional images of (a) 3,4-DCT doped primer coating, (b) 3,4-DHC doped primer coating, (c) 2,3,4-THC doped primer coating, post salt spray analysis.

3.5 EFFECT OF INHIBITORS ON THE ANTICORROSION PROPERTIES OF SOL-GEL COATING ON ALUMINIUM ALLOY AA2024-T3

The synthesised inhibitors 3,4-DHC and 2,3,4-THC were added to the hybrid sol to study their effect on the corrosion protection efficiency of the sol-gel coating. As the addition of 3,4-DCT, formed the precipitated sol-gel, it was not used in these studies.

3.5.1 Electrochemical impedance spectroscopy

Corrosion resistance and degradation properties of the uncoated, sol-gel coated and sol-gel + inhibitor (2,3,4-THC, 3,4-DHC) coated AA2024-T3 were characterized by electrochemical impedance spectroscopy (EIS) method at different immersion times from 1 h to 168 h. The impedance spectra for the uncoated and coated aluminium alloy, represented as Nyquist plots, are presented in Figure 3.54 and Figure 3.55.

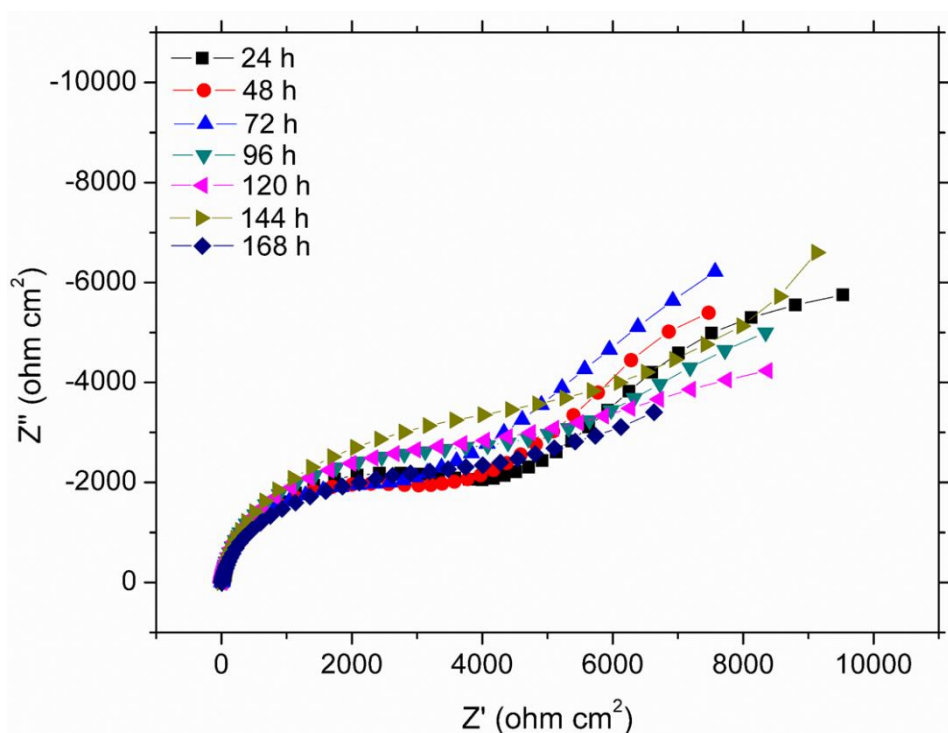


Figure 3.54 Nyquist plots for the corrosion of surface treated AA2024-T3 (uncoated) at different immersion times in 3.5 % NaCl solution.

The Nyquist plots for the uncoated substrate are associated with a large capacitive loop at higher frequency (HF) region and a small capacitive loop at lower frequency

(LF) region. The HF capacitive loop could be accounted for the naturally formed oxide layer resistance. The second capacitive loop at the LF region could be due to the charge transfer reaction during the corrosion process occurring at the metal/oxide/electrolyte interface. The charge transfer occurs through the formation of Al^{3+} , OH^- and O^{2-} at the metal/surface film/electrolyte interface and diffusion of ions.

The Nyquist plots for the sol-gel coated substrate are shown in Figure 3.55 a, are associated with two capacitive loops, first capacitive loop observed at higher frequency (HF) region and the second capacitive loop observed at lower frequency (LF) region. The HF capacitive loop could be accounted for the sol-gel coating resistance. The second capacitive loop at the LF region could be due to the charge transfer reaction. The diameter of the capacitive loop increases for the sol-gel coated system, implying that the coating acts as a passive barrier for the aggressive corrosion environment. During the immersion studies, the diameter of the capacitive loop decreases due to the penetration of electrolyte, which is accounted for the degradation of the protective sol-gel coating on the alloy surface, leading to increased ingress of the electrolyte into alloy surface and subsequent increase in the corrosion on the alloy surface.

The addition of inhibitors to the sol-gel coating significantly affects the hydrolytic stability (resistance to electrolyte penetration) of the sol-gel layer. The time-dependent Nyquist plots for the inhibitor incorporated sol-gel coating are presented in Figures 3.55 b and c. These results show that the addition of 2,3,4-THC and 3,4-DHC, leads to the increase in the diameters of the capacitive loop, indicating that addition of inhibitors increases the hydrolytic stability of the sol-gel coating. Although, in both cases, the diameters of the capacitive loops decrease with immersion time, the diameters of the capacitive loops are comparatively larger than those of the uncoated and undoped sol-gel coated samples.

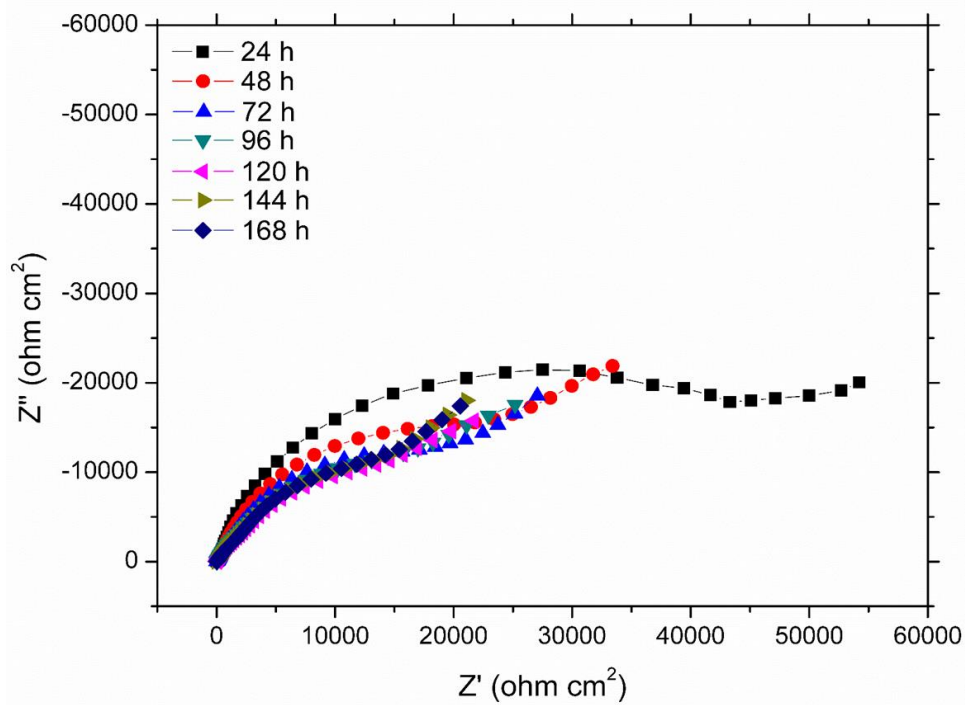


Figure 3.55 (a) Nyquist plots for the corrosion of sol-gel coated AA2024-T3 at different immersion times in 3.5 % NaCl solution.

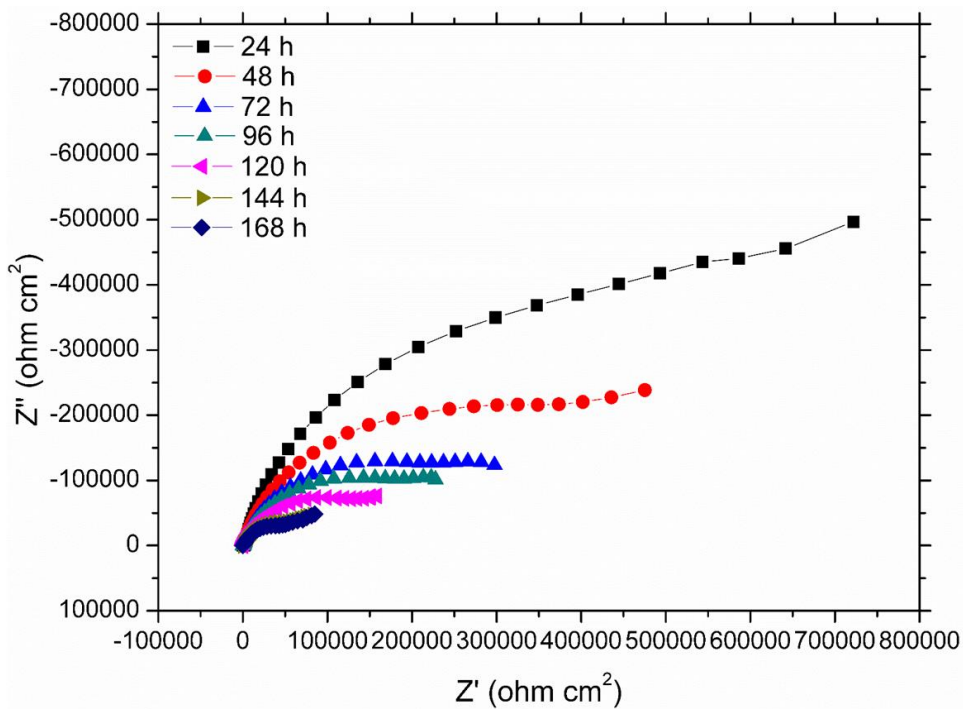


Figure 3.55 (b) Nyquist plots for the corrosion of 2,3,4-THC doped sol-gel coated AA2024-T3 at different immersion times in 3.5 % NaCl solution.

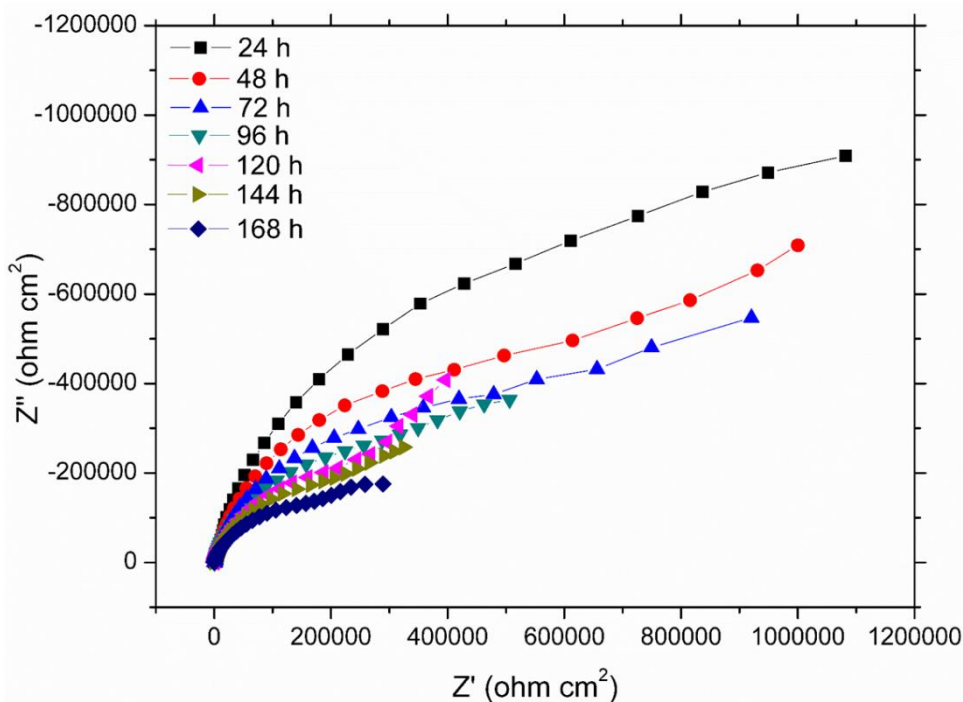


Figure 3.55 (c) Nyquist plots for the corrosion of 3,4- DHC doped sol-gel coated AA2024-T3 at different immersion times in 3.5 % NaCl solution.

The impedance spectra were fitted with the appropriate equivalent electrical circuit model for understanding the degradation nature of the different sol-gel coating systems. The equivalent electrical circuit model for the corrosion of uncoated and coated AA2024-T3 in sodium chloride solution are shown in Figure 3.56. The impedance spectra obtained for uncoated substrate is fitted with two time constants associated equivalent circuit (Figure 3.56a) and it is composed of, the solution resistance R_s , the oxide layer resistance R_{ox} , the oxide layer capacitance Q_{ox} , the charge transfer resistance R_{ct} , the double layer capacitance Q_{dl} , and the Warburg element W .

The impedance spectra obtained for the sol-gel coating is associated with three time constants and a Warburg resistance (Figure 3.56b). The extra time constant appears due to the presence of coating layer. The additional circuit components include the coating resistance (R_{coat}) and capacitance due to the dielectric nature of the coating layer (Q_{coat}). In 2,3,4-THC doped sol-gel coating, the Warburg resistance disappears at initial immersion time from 24 h to 48 h, probably due to the inhibitor molecules preventing the ion diffusion (Figure 3.56c). However, with further exposure time, the Warburg

impedance reappears due to the corrosion process occurring on the alloy surface and fitted with the equivalent circuit given in Figure 3.56b.

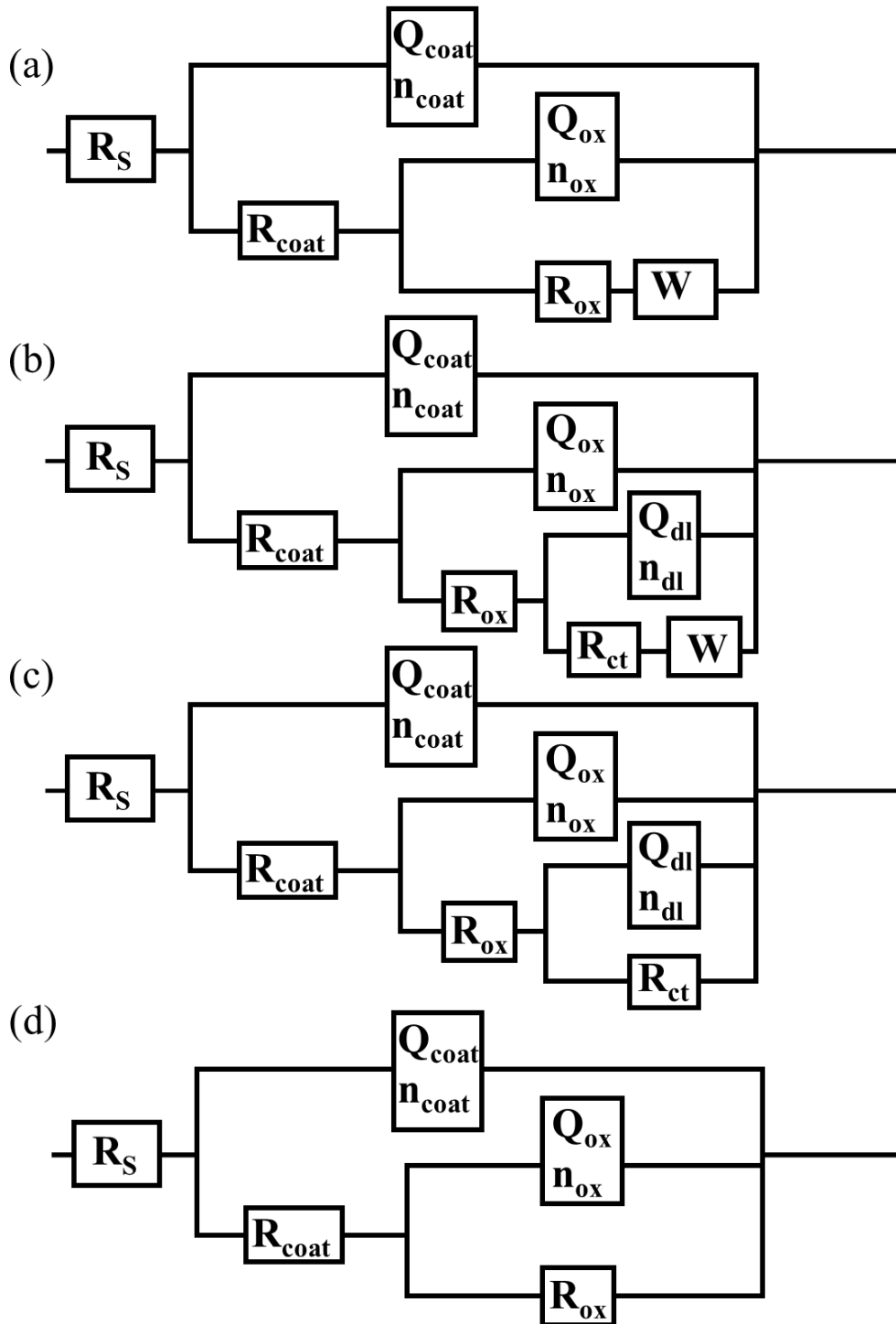


Figure 3.56 Equivalent circuit used to fit the experimental data for the sol-gel coating in the absence and in the presence of the inhibitors.

The impedance spectra for 3,4-DHC doped sol-gel coating, at the onset of exposure (from 24 to 72 h) the impedance curve is fitted by the equivalent circuit model that contains only two time constants representing the capacitive behaviour of 3,4-DHC doped sol-gel coating and native oxide layer (Figure 3.56d). With further exposure time from 96 h to 168 h, an additional time constant appeared due to the defect created on the 3,4-DHC incorporated sol-gel coating and native oxide layer, which may allow contact of the corrosive ions to the alloy surface. Corrosive ions cause initiation of the corrosion process, which could be accounted to the charge transfer resistance and double layer capacitance. The relevant equivalent electrical circuit model is given in Figure 3.56c.

The impedance parameters including sol-gel coating resistance (R_{coat}), naturally formed oxide layer resistance (R_{ox}), charge transfer resistance (R_{ct}) and polarization resistance ($R_{\text{p}}=R_{\text{ox}}+R_{\text{ct}}$ or $R_{\text{p}}=R_{\text{coat}}+R_{\text{ox}}$, or $R_{\text{p}}=R_{\text{coat}}+R_{\text{ox}}+R_{\text{ct}}$) are tabulated in Table 3.9.

The hydrolytic stability of the sol-gel coating during exposure in aqueous sodium chloride solution can be determined from the evaluation of the polarization resistance of the sol-gel layer. The results of polarization resistance variation with time for different sol-gel coatings are given in Figure 3.57. Over the entire immersion period, 3,4-DHC doped sol-gel coating shows higher polarization resistances compared to the remaining coatings, implying good protection properties and higher hydrolytic resistance of the coating layer. The inhibition efficiencies of the coatings in the present study are in the order: Uncoated < sol-gel coated < sol-gel + 2,3,4-THC coated < sol-gel + 3,4-DHC coated.

Table 3.9 Impedance parameters for the corrosion of different sol-gel coated AA2024-T3 alloy in 3.5 % NaCl solution.

Sample	Immersion time (h)	R _{coat} (Ω cm ²)	R _{ox} (Ω cm ²)	R _{ct} (Ω cm ²)	W (S cm ⁻²)	R _p (Ω cm ²)
Uncoated	24	-	4.92×10 ³	5.49×10 ³	5.087×10 ⁻⁴	1.04×10 ⁴
	48	-	4.54×10 ³	4.39×10 ³	6.816×10 ⁻⁴	8.93×10 ³
	72	-	4.41×10 ³	3.46×10 ³	4.396×10 ⁻⁴	7.87×10 ³
	96	-	5.82×10 ³	4.31×10 ³	8.002×10 ⁻⁴	1.01×10 ⁴
	120	-	5.81×10 ³	7.46×10 ³	-	1.33×10 ⁴
	144	-	6.83×10 ³	7.29×10 ³	-	1.41×10 ⁴
	168	-	4.41×10 ³	9.02×10 ³	-	1.34×10 ⁴
Sol-gel coated	24	3.012×10 ¹	3.812×10 ³	2.234×10 ⁴	1.825×10 ⁻⁴	2.618×10 ⁴
	48	2.572×10 ¹	3.767×10 ³	1.864×10 ⁴	1.425×10 ⁻⁴	2.243×10 ⁴
	72	2.581×10 ¹	3.541×10 ²	2.737×10 ⁴	2.217×10 ⁻⁴	2.774×10 ⁴
	96	2.148×10 ¹	6.73×10 ²	2.596×10 ⁴	1.975×10 ⁻⁴	2.665×10 ⁴
	120	1.942×10 ¹	4.955×10 ²	2.382×10 ⁴	1.988×10 ⁻⁴	2.433×10 ⁴
	144	1.675×10 ¹	4.133×10 ²	2.714×10 ⁴	1.739×10 ⁻⁴	2.757×10 ⁴
	168	1.612×10 ¹	3.364×10 ²	2.91×10 ⁴	1.771×10 ⁻⁴	2.945×10 ⁴
Sol-gel + 2,3,4 THC coated	24	1.625×10 ³	2.635×10 ⁶	3.787×10 ⁵	-	3.015×10 ⁶
	48	7.374×10 ²	7.119×10 ⁵	2.022×10 ⁵	-	9.148×10 ⁵
	72	1.594×10 ²	9.296×10 ²	2.687×10 ⁵	3.159×10 ⁻⁵	2.697×10 ⁵
	96	1.209×10 ²	3.182×10 ²	2.142×10 ⁵	3.767×10 ⁻⁵	2.146×10 ⁵
	120	8.308×10 ¹	3.731×10 ²	1.451×10 ⁵	4.624×10 ⁻⁵	1.455×10 ⁵
	144	7.210×10 ¹	4.100×10 ²	1.231×10 ⁵	4.123×10 ⁻⁵	1.235×10 ⁵
	168	6.429×10 ¹	6.867×10 ²	4.736×10 ⁴	6.689×10 ⁻⁵	4.811×10 ⁴
Sol-gel + 3,4- DHC coated	24	3.662×10 ³	2.019×10 ⁶	-	-	2.022×10 ⁶
	48	1.753×10 ³	1.409×10 ⁶	-	-	1.410×10 ⁶
	72	1.031×10 ³	1.081×10 ⁶	-	-	1.082×10 ⁶
	96	7.404×10 ²	6.244×10 ⁵	7.167×10 ⁵	-	1.341×10 ⁶
	120	5.012×10 ²	5.140×10 ⁵	8.165×10 ⁵	-	1.331×10 ⁶
	144	4.055×10 ²	4.237×10 ⁵	9.031×10 ⁵	-	1.327×10 ⁶
	168	3.272×10 ²	2.716×10 ⁵	2.258×10 ⁵	-	4.977×10 ⁵

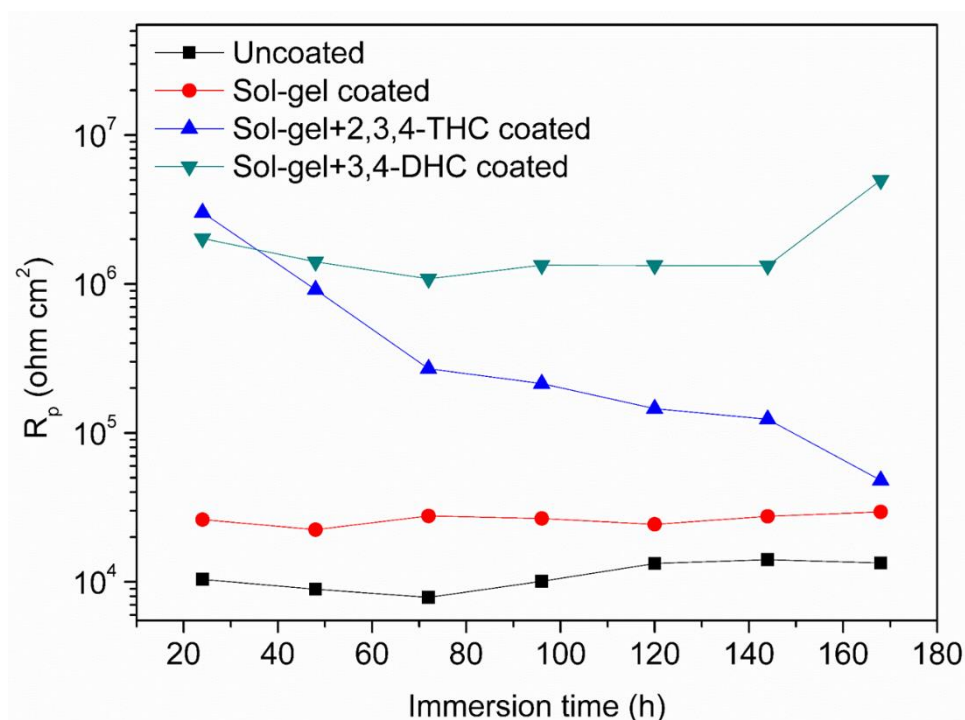


Figure 3.57 Variation of polarization resistance of the uncoated and sol-gel coated AA2024-T3 with immersion time in 3.5 % NaCl solution.

The impedance spectra for the corrosion of uncoated and coated Aluminium alloy, can also be represented as Bode magnitude and Bode phase angle plots. Figure 3.58 represents the Bode magnitude and Bode phase angle plots for the corrosion of sol-gel coated AA 2024-T3 in 3.5% NaCl solution, at different exposure times. The low frequency impedance explains the corrosion related alterations of the coating system. The 3,4-DHC and 2,3,4-THC doped sol-gel coatings show higher impedance at lower frequency (Figure 3.58 c & d), suggesting that the addition of these inhibitors to the sol-gel coatings, enhances the anticorrosion behaviour of the coating system. Figure 3.58 b represents, Bode magnitude plots for the sol-gel coating on the aluminium alloy at different immersion periods in 3.5 % NaCl solution. The total impedance value decreases with increase of the exposure time, suggesting the degradation of the coating system. Bode phase angle plots for the sol-gel film at different immersion times are shown in Figure 3.58 b, in which three time constants can be clearly seen. The high frequency impedance time constant is assigned to the capacitance of the sol-gel layer. The middle frequency time constant is attributed to the capacitance of the intermediate

aluminium oxide layer. The third time constant observed in the lower frequency region corresponding to the charge transfer process. These results suggest poor barrier properties of the coating due to the formation of defects on the coating system during immersion.

The Bode plots presented in Figures 3.58 c and d are for the inhibitors (2,3,4-THC and 3,4-DHC) doped sol-gel coated AA2024-T3. The impedance modules at $|Z|_{0.01\text{Hz}}$ was comparatively high during immersion studies compared with sol-gel coating. This observation suggests that, the corrosion rate is impeded with the incorporation of the inhibitors to the sol-gel film. Similarly, it is observed that the higher frequency phase angle increases in the presence of the inhibitors. This result suggests that, the addition of inhibitor increases the hydrolytic stability of the coating system. According to the obtained results, the order of inhibition efficiencies are: uncoated < sol-gel coated < sol-gel + 2,3,4-THC coated < sol-gel + 3,4-DHC coated.

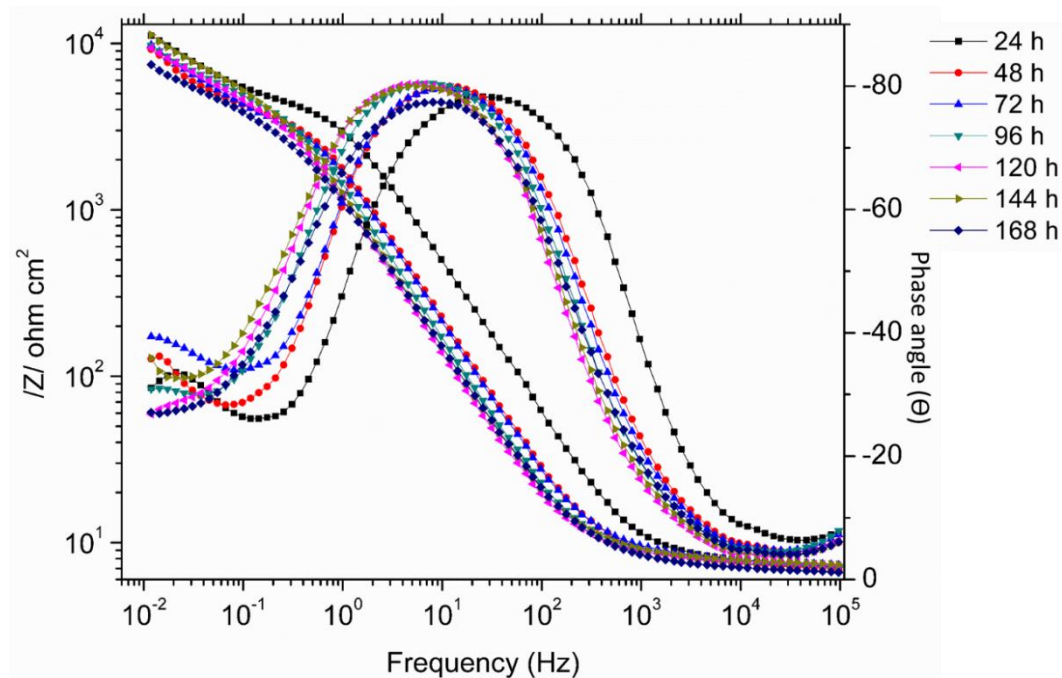


Figure 3.58 (a) Bode magnitude and phase angle plots for the corrosion of uncoated AA 2024-T3 Aluminium alloy at different immersion times in 3.5 % NaCl solution.

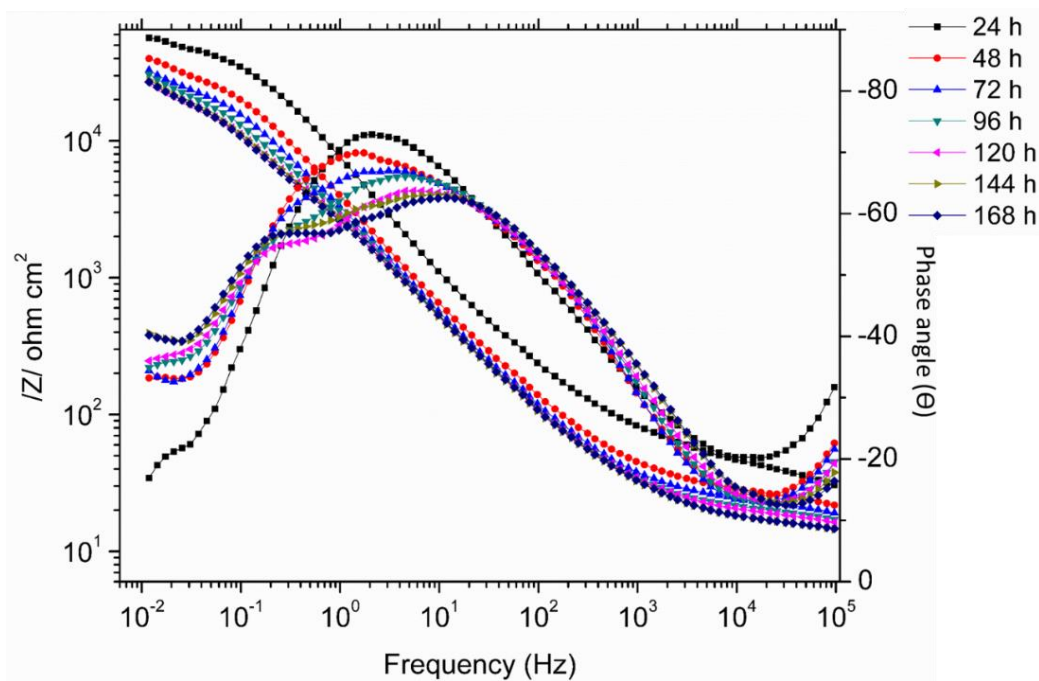


Figure 3.58 (b) Bode magnitude and phase angle plots for the corrosion of sol-gel coated AA 2024-T3 Aluminium alloy at different immersion times in 3.5 % NaCl solution.

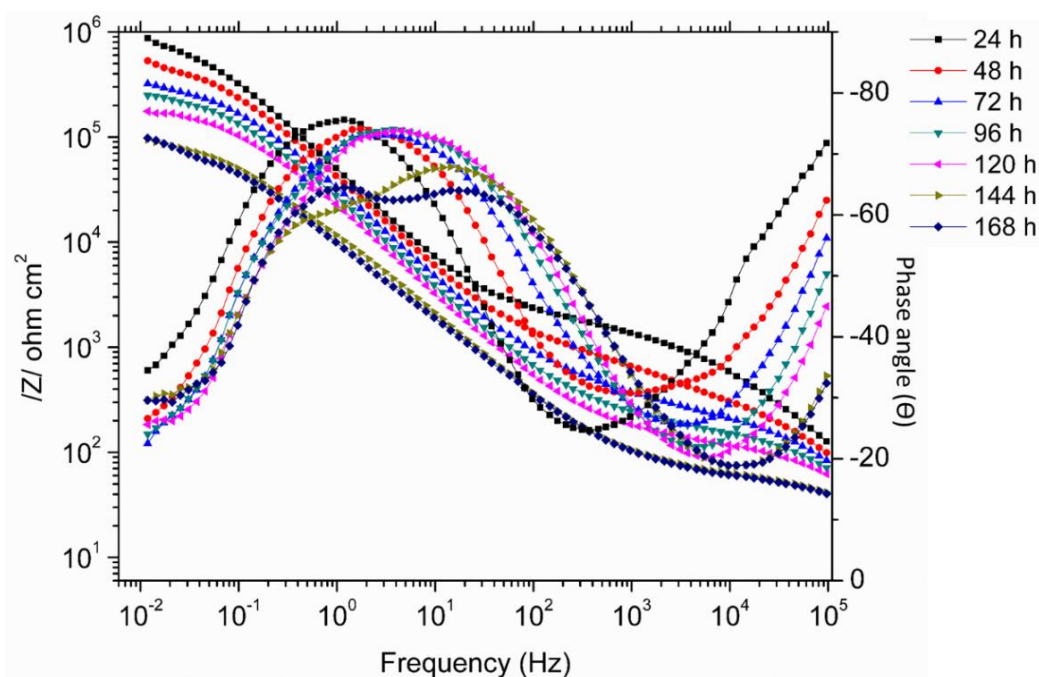


Figure 3.58 (c) Bode magnitude and phase angle plots for the corrosion of 2,3,4-THC doped sol-gel coated AA 2024-T3 Aluminium alloy at different immersion times in 3.5 % NaCl solution.

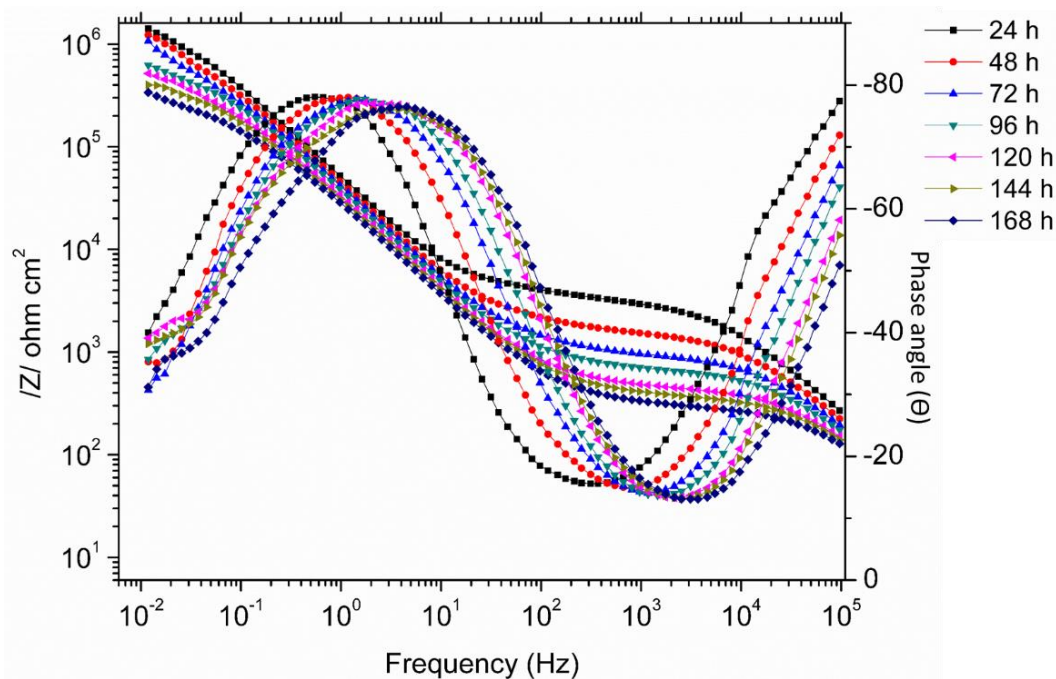


Figure 3.58 (d) Bode magnitude and phase angle plots for the corrosion of 3,4-DHC doped sol-gel coated AA 2024-T3 Aluminium alloy at different immersion times in 3.5 % NaCl solution.

3.5.2 Surface characterization after corrosion

The photographs of the sol-gel coated AA2024-T3 surfaces after 168 h immersion in 3.5 wt% sodium chloride solution, are shown in Figure 3.59. The deterioration of sol-gel coating and presence of certain number of large pits were visually observed for the sol-gel coated and 2,3,4-THC doped sol-gel coated (Fig 3.59 a and b) surface. On 3,4-DHC doped sol-gel coated surface, there is no evidence of sol-gel deterioration and visual pitting corrosion. Thus, demonstrating the higher corrosion protection compared to the undoped sol-gel coating and 2,3,4-THC doped sol-gel coating.

The surface morphology of the sol-gel coatings was analysed by FESEM technique, after immersion in the corrosive media. Figure 3.60 presents FESEM images for different sol-gel coated substrates after corrosion. Pits and cracks around the pit zone were observed on the undoped and 2,3,4- THC doped sol-gel coated samples (Figure 3.60). The deterioration of the sol-gel layer could be related to strong corrosion activity. No evidence of pit corrosion and cracking on 3,4-DHC doped sol-gel coated surface.

These results suggest that, 3,4-DHC doped sol-gel coating have better corrosion resistance compared to undoped and 2,3,4- THC doped sol-gel coated samples.

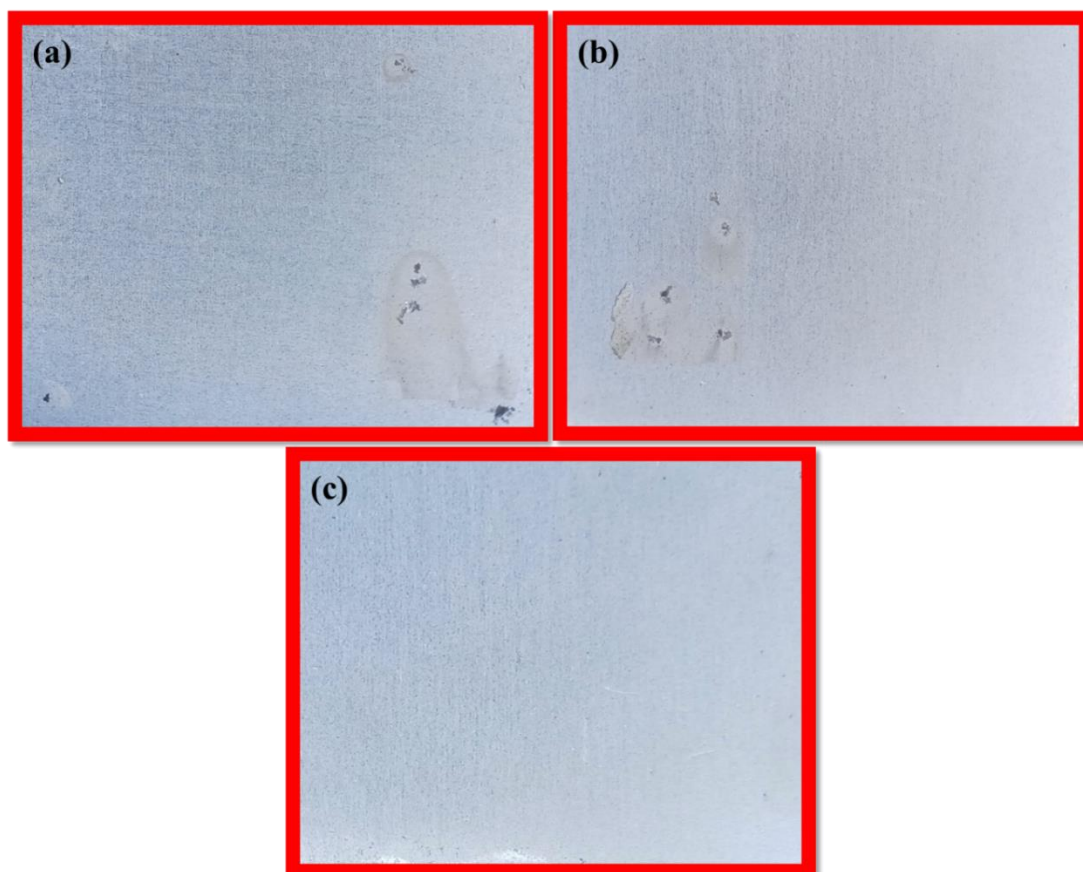


Figure 3.59 Photographs of (a) Sol-gel coated, (b) Sol-gel + 2,3,4-THC coated, (c) Sol-gel + 3,4-DHC coated sample surfaces after 168 h of immersion in 3.5 % NaCl solution.

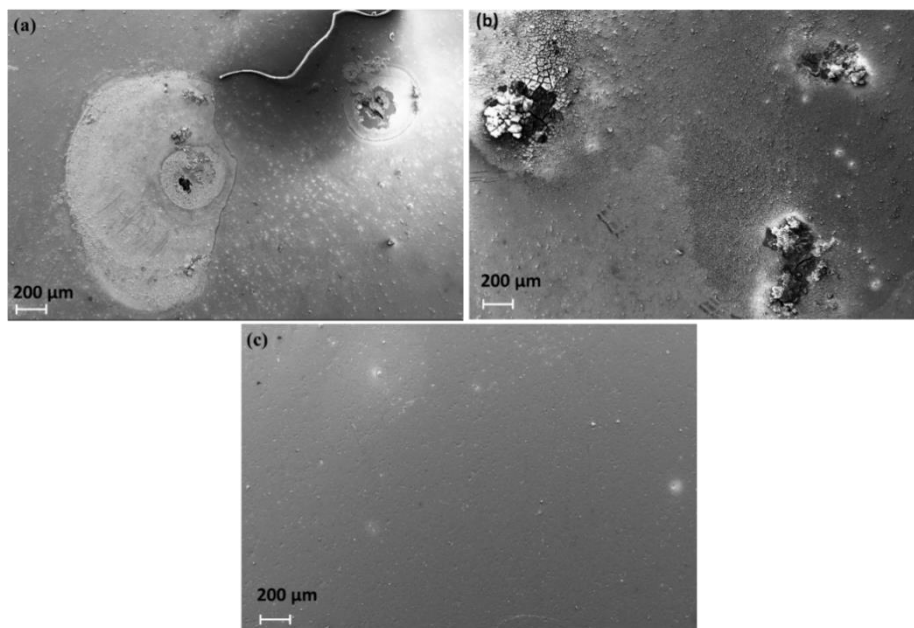


Figure 3.60 FESEM images of (a) Sol-gel coated, (b) 2,3,4-THC doped sol-gel coated and (c) 3,4-DHC doped sol-gel coated sample surfaces after 168 h of immersion in 3.5 % NaCl solution.

3.5.3 Adhesion strength of the sol-gel coating

The adhesion strengths of the sol-gel layers on AA2024-T3 substrates were measured by cross hatch test according to the ASTM D3359. The photographs of the samples after cross hatch test are shown in Figure 3.61. All the coatings qualified as 5B class (the highest adhesion strength and percent of the removed area is 0%).

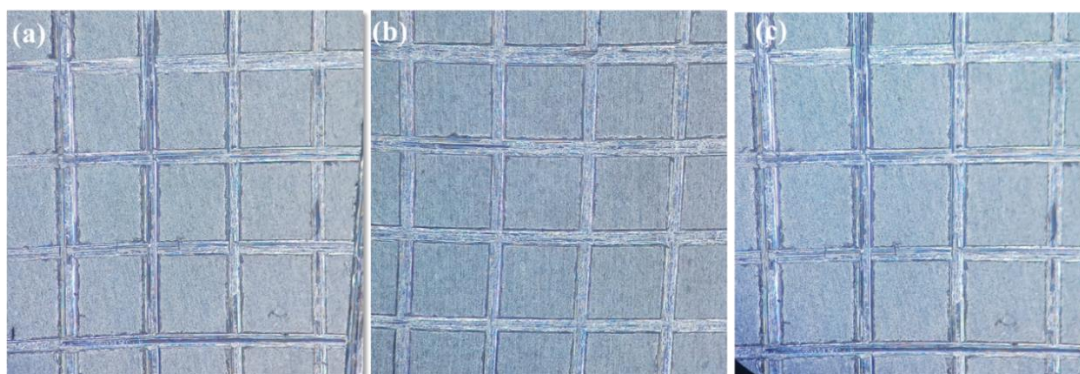


Figure 3.61 Optical images of the different sol-gel coated samples after the cross-hatch test according to ASTM D3359: (a) Sol-gel coating, (b) 2,3,4-THC doped sol-gel coating, (c) 3,4-DHC doped sol-gel coating.

4.1 SUMMARY

Five organic molecules, namely, (E)-2-(2-hydroxybenzylidene) hydrazinecarbothioamide (2-MHC), (E)-2-(2,4-dihydroxybenzylidene) hydrazinecarbothioamide (2,4-DHC), (E)-2-(3,4-dihydroxybenzylidene) hydrazinecarbothioamide (3,4-DHC), (E)-2-(2,3,4-trihydroxybenzylidene) hydrazinecarbothioamide (2,3,4-THC) and Bis[[3,4-Dihydroxyphenylmethylene]-carbonothioic dihydrazide] (3,4-DCT) were synthesised and their corrosion inhibition action on 2024-T3 Aluminium alloy was studied in 3.5% NaCl solution. The surface morphology and surface composition of the corroded alloy were examined using FESEM, EDX spectroscopy and X-ray photoelectron spectroscopy. The synthesised inhibitors were found to provide corrosion protection on AA2024-T3 by forming an adsorbed layer.

3,4-DHC act as a smart indicator for the early detection of corrosion and as an effective corrosion inhibitor on Aluminium alloy in 3.5% NaCl solution. The visible detection of corrosion on the AA2024-T3 was examined by using optical microscopy images, after exposure in 3.5 % NaCl solution containing 3,4-DHC.

The oxide layer created on the Aluminium alloy using 10 wt % sulphuric acid (plain oxide layer- Ox) was sealed with (E)-2-(2,3,4-trihydroxybenzylidene) hydrazinecarbothioamide (Ox-2,3,4-THC), (E)-2-(3,4-dihydroxybenzylidene) hydrazinecarbothioamide (Ox-3,4-DHC) and Bis [[3,4-Dihydroxyphenylmethylene] carbonothioicdihydrazide] (Ox-3,4-DCT) to enhance the corrosion resistance. The electrochemical behaviour of the sealed and unsealed anodized Aluminium alloy samples were evaluated by using electrochemical impedance spectroscopy and potentiodynamic polarization studies. Accelerated corrosion studies were carried out by salt spray test.

Effect of the addition of organic molecule on the anticorrosion properties of epoxy primer coatings on Aluminium alloy 2024-T3 was investigated. 2,3,4-THC, 3,4-DHC, 3,4-DCT were supplemented to epoxy primer that is generally used in aircraft paint systems; and its anticorrosion property was examined by electrochemical impedance

spectroscopy and salt spray test. FE-SEM and EDX were used to study the surface topology of the coating system. 3,4-DCT and 3,4-DHC doped primer coatings exhibit good barrier properties, while 2,3,4-THC doped primer coating exhibits good barrier properties along with active corrosion protection.

The sol-gel coatings are alternate for chromium free coatings. The hybrid sols were prepared by mixing of two sols. The first sol consists of 3-glycidoxypropyltrimethoxysilane (GPTMS), another sol consists of zirconium (IV) propoxide (TPOZ). The synthesised inhibitors, 3,4-DHC and 2,3,4-THC were added to the hybrid sol to improve the corrosion protection efficiency. The surface morphology of the coatings were examined by FESEM attached with EDX. Anticorrosion behaviour of uncoated and coated substrates were characterized by the electrochemical impedance spectroscopy (EIS) at different immersion times for understanding the degradation nature of the coatings. The acquired results revealed that, the addition of inhibitor into the coatings leads to the enhancement of the barrier properties of the sol-gel coatings.

4.2 CONCLUSIONS

Based on the results of the present investigation, the following conclusions are drawn

1. The synthesised five inhibitors 2-MHC, 2,4-DHC, 2,3,4-THC, 3,4-DHC and 3,4-DCT act as effective mixed type corrosion inhibitors on AA2024-T3 in 3.5 % NaCl solution.
2. The order of inhibition efficiency on the alloy surface is 2-MHC < 2,4-DHC < 2,3,4-THC < 3,4-DHC < 3,4-DCT.
3. 3,4-DHC exhibits dual functionality of corrosion detection and inhibition on the surface of Aluminium alloy AA2024-T3. The initiation of corrosion is detectable by the “naked eye”, as a bright red spots on the bare substrate.
4. The inhibitors 2,3,4-THC, 3,4-DHC and 3,4-DCT when incorporated in the oxide layer, enhance the anticorrosion performance of the oxide layer.
5. The order of corrosion protection efficiencies of the anodised layer is: Ox < Ox-2,3,4-THC < Ox-3,4-DHC < Ox-3,4-DCT.

6. The addition of synthesised inhibitors, 2,3,4-THC, 3,4-DHC, 3,4-DCT to the primer coatings improves the coating barrier nature and anticorrosion property of the coating.
7. The addition of 3,4-DCT and 3,4-DHC to primer coating, offers only good barrier properties, while the addition of 2,3,4-THC provides active corrosion protection along with good barrier properties,
8. Addition of corrosion inhibitors, 2,3,4-THC and 3,4-DHC enhance the corrosion protection abilities of sol-gel coatings.
9. The order of corrosion protection efficiencies is: Uncoated < sol-gel coated < sol-gel + 2,3,4-THC coated < sol-gel + 3,4-DHC coated.

4.3 SCOPE FOR FUTURE WORK

1. The synthesised inhibitors could be used as inhibitors for other metal alloys such as steel used in oil industries. Our preliminary results have shown encouraging results.
2. A promising replacement to the carcinogenic strontium chromate for aerospace paint coating system.
3. New derivatives of the inhibitors could be synthesised.

REFERENCES

Abdullayev, E. and Lvov, Y. (2010). "Clay nanotubes for corrosion inhibitor encapsulation: release control with end stoppers." *J. Mater. Chem.*, 20(32), 6681-6687.

Balaraju, J.N., Srinivasan, A., Yoganandan, G., Grips, V.W. and Rajam, K.S. (2011). "Effect of Mn/Mo incorporated oxide layer on the corrosion behavior of AA 2024 alloy." *Corros. Sci.*, 53(12), 4084-4092.

Bentiss, F., Lebrini, M. and Lagrenée, M. (2005). "Thermodynamic characterization of metal dissolution and inhibitor adsorption processes in mild steel/2, 5-bis (n-thienyl)-1, 3, 4-thiadiazoles/hydrochloric acid system." *Corros. Sci.*, 47(12), 2915-2931.

Bierwagen, G.P. and Tallman, D.E. (2001). "Choice and measurement of crucial aircraft coatings system properties." *Prog. Org. Coat.*, 41(4), 201-216.

Birbilis, N., Buchheit, R.G., Ho, D.L and Forsyth, M. (2005). "Inhibition of AA2024-T3 on a phase-by-phase basis using an environmentally benign inhibitor, cerium dibutyl phosphate." *Electrochem. Solid-State Lett.*, 8(11), C180-C183.

Birbilis, N., Zhu, Y.M., Kairy, S.K., Glenn, M.A., Nie, J.-F., Morton, A.J., Gonzalez-Garcia, Y., Terryn, H., Mol, J.M.C. and Hughes, A.E. (2016). "A closer look at constituent induced localised corrosion in Al-Cu-Mg alloys." *Corros. Sci.*, 113, 160-171.

Bo, W., Shiyan, Y., Daosen, J. and LiXin, Z. (1993). "Lanthanide complexes of a sulphur-nitrogen-oxygen ligand derived from thiosemicarbazones." *Polyhedron*, 12(14), 1805-1809.

Boag, A., Hughes, A.E., Glenn, A.M., Muster, T.H. and McCulloch, D. (2011). "Corrosion of AA2024-T3 Part I: Localised corrosion of isolated IM particles." *Corros. Sci.*, 53(1), 17-26.

Boag, A., Hughes, A.E., Wilson, N.C., Torpy, A., MacRae, C.M., Glenn, A.M. and Muster, T.H. (2009). "How complex is the microstructure of AA2024-T3?" *Corros. Sci.*, 51(8), 1565-1568.

Boisier, G., Pébère, N., Druetz, C., Villatte, M. and Suel, S. (2008). "FESEM and EIS study of sealed AA2024 T3 anodized in sulfuric acid electrolytes: Influence of tartaric acid." *J. Electrochem. Soc.*, 155(11), C521–C529.

Borisova, D., Akçakayıran, D., Schenderlein, M., Möhwald, H. and Shchukin, D.G. (2013). "Nanocontainer-Based Anticorrosive Coatings: Effect of the Container Size on the Self-Healing Performance." *Adv. Funct. Mater.*, 23(30), 3799–3812.

Buchheit, R.G., Gran, R.P., Hiava, P.F., Mckenzie, B. and Zender, G.L. (1997). "Local Dissolution Phenomena Associated with S Phase (Al₂CuMg) Particles in Aluminium Alloy 2024-T3." *J. Electrochem. Soc.*, 144(8), 2621-2628.

Capelossi, V., Poelman, M., Recloux, I., Hernandez, R.P.B., De Melo, H. and Olivier, M. (2014). "Corrosion protection of clad 2024 aluminum alloy anodized in tartaric-sulfuric acid bath and protected with hybrid sol–gel coating." *Electrochimica Acta*, 124, 69–79.

Coelho, L.B., Cossement, D. and Olivier, M.G. (2018). "Benzotriazole and cerium chloride as corrosion inhibitors for AA2024-T3: An EIS investigation supported by SVET and ToF-SIMS analysis." *Corros. Sci.*, 130, 177–189.

Danilidis, I., Hunter, J., Scamans, G.M. and Sykes, J.M. (2007). "Effects of inorganic additions on the performance of manganese-based conversion treatments." *Corros. Sci.*, 49(3), 1559–1569.

Dinodi, N. and Shetty, A.N. (2014). "Alkyl carboxylates as efficient and green inhibitors of magnesium alloy ZE41 corrosion in aqueous salt solution." *Corros. Sci.*, 85, 411–427.

Djebaili, K., Mekhalif, Z., Boumaza, A. and Djelloul, A. (2015) "XPS , FTIR , EDX , and XRD Analysis of Al₂O₃ Scales Grown on PM2000 Alloy." *Journal of Spectroscopy*.

- Elabar, D., Monica, G.R.L., Santamaria, M., Quarto, F.D., Skeldon, P. and Thompson, G.E. (2017). "Anodizing of aluminium and AA 2024-T3 alloy in chromic acid: Effects of sulphate on film growth." *Surf. Coat. Technol.*, 309, 480–489.
- Elaish, R., Curioni, M., Gowers, K., Kasuga, A., Habazaki, H., Hashimoto, T. and Skeldon, P. (2018). "Effect of fluorozirconic acid on anodizing of aluminium and AA 2024-T3 alloy in sulphuric and tartaric-sulphuric acids." *Surf. Coat. Technol.*, 342, 233–243.
- Fonseca, I.T.E., Lima, N., Rodrigues, J.A., Pereira, M.I.S., Salvador, J.C.S. and Ferreira, M.G.S. (2002). "Passivity breakdown of Al 2024-T3 alloy in chloride solutions: a test of the point defect model." *Electrochem. Commun.*, 4(5), 353–357.
- Gao, H., Li, Q., Dai, Y., Luo, F. and Zhang, H.X. (2010). "High efficiency corrosion inhibitor 8-hydroxyquinoline and its synergistic effect with sodium dodecylbenzenesulphonate on AZ91D magnesium alloy." *Corros. Sci.*, 52(5), 1603–1609.
- García-Rubio, M., Ocón, P., Climent-Font, A., Smith, R.W., Curioni, M., Thompson, G.E., Skeldon, P., Lavía, A. and García, I. (2009). "Influence of molybdate species on the tartaric acid/sulphuric acid anodic films grown on AA2024 T3 aerospace alloy." *Corros. Sci.*, 51(9), 2034–2042.
- Habazaki, H., Konno, H., Shimizu, K., Nagata, S., Skeldon, P. and Thompson, G.E. (2004). "Incorporation of transition metal ions and oxygen generation during anodizing of aluminium alloys." *Corros. Sci.*, 46(8), 2041–2053.
- Hashimoto, T., Zhang, X., Zhou, X., Skeldon, P., Haigh, S.J. and Thompson, G.E. (2016). "Investigation of dealloying of S phase (Al_2CuMg) in AA 2024-T3 aluminium alloy using high resolution 2D and 3D electron imaging." *Corros. Sci.*, 103, 157–164.
- Ho, D., Brack, N., Scully, J., Markley, T., Forsyth, M. and Hinton, B. (2006). "Cerium Dibutylphosphate as a Corrosion Inhibitor for AA2024-T3 Aluminum Alloys." *J. Electrochem. Soc.*, 153(9), B392-B401.

- Shi, H., Han, E.H. and Liu, F. (2011). "Corrosion protection of aluminium alloy 2024-T3 in 0.05 M NaCl by cerium cinnamate." *Corros. Sci.*, 53(7), 2374–2384.
- Hu, N., Dong, X., He, X., Browning, J.F. and Schaefer, D.W. (2015). "Effect of sealing on the morphology of anodized aluminum oxide." *Corros. Sci.*, 97, 17–24.
- Hu, T., Shi, H., Fan, S., Liu, F. and Han, E.H. (2017). "Cerium tartrate as a pigment in epoxy coatings for corrosion protection of AA 2024-T3." *Prog. Org. Coat.*, 105, 123–131.
- Huang, Y., Shih, H., Huang, H., Daugherty, J., Wu, S., Ramanathan, S., Chang, C. and Mansfeld, F. (2008). "Evaluation of the corrosion resistance of anodized aluminum 6061 using electrochemical impedance spectroscopy (EIS)." *Corros. Sci.*, 50(12), 3569–3575.
- Hughes, A.E., Boag, A., Glenn, A.M., McCulloch, D., Muster, T.H., Ryan, C., Luo, C., Zhou, X. and Thompson, G.E. (2011). "Corrosion of AA2024-T3 Part II: Co-operative corrosion." *Corros. Sci.*, 53(1), 27–39.
- Iannuzzi, M. and Frankel, G.S. (2007). "Inhibition of aluminum alloy 2024 corrosion by vanadates: an in situ atomic force microscopy scratching investigation." *Corrosion*, 63(7), 672–688.
- Jüttner, K. (1990). "Electrochemical impedance spectroscopy (EIS) of corrosion processes on inhomogeneous surfaces." *Electrochimica Acta*, 35(10), 1501–1508.
- Kartsonakis, I. A., Koumoulos, E.P., Balaskas, a. C., Pappas, G.S., Charitidis, C. a. and Kordas, G.C. (2012). "Hybrid organic-inorganic multilayer coatings including nanocontainers for corrosion protection of metal alloys." *Corros. Sci.*, 57, 56–66.
- King, P.C., Cole, I.S., Corrigan, P.A., Hughes, A.E. and Muster, T.H. (2011). "FIB/SEM study of AA2024 corrosion under a seawater drop: Part I." *Corros. Sci.*, 53(3), 1086–1096.

- King, P.C., Cole, I.S., Corrigan, P.A., Hughes, A.E., Muster, T.H. and Thomas, S. (2012). "FIB/SEM study of AA2024 corrosion under a seawater drop, part II." *Corros. Sci.*, 55, 116–125.
- Kopeć, M., Szczepanowicz, K., Mordarski, G., Podgórna, K., Socha, R.P., Nowak, P., Warszzyński, P. and Hack, T. (2015). "Self-healing epoxy coatings loaded with inhibitor-containing polyelectrolyte nanocapsules." *Prog. Org. Coat.*, 84, 97–106.
- Kuznetsov, B., Serdechnova, M., Tedim, J., Starykevich, M., Kallip, S., Oliveira, M.P., Hack, T., Nixon, S., Ferreira, M.G.S. and Zheludkevich, M.L. (2016). "Sealing of tartaric sulfuric (TSA) anodized AA2024 with nanostructured LDH layers." *Rsc Adv.*, 6(17), 13942–13952.
- Lakshmi, R.V., Yoganandan, G., Kavya, K.T. and Basu, B.J. (2013). "Effective corrosion inhibition performance of Ce³⁺ doped sol–gel nanocomposite coating on aluminum alloy." *Prog. Org. Coat.*, 76(2-3), 367–374.
- Lamaka, S.V., Zheludkevich, M.L., Yasakau, K.A., Montemor, M.F. and Ferreira, M.G.S. (2007). "High effective organic corrosion inhibitors for 2024 aluminium alloy." *Electrochimica Acta*, 52(25), 7231–7247.
- Lebrini, M., Bentiss, F., Vezin, H. and Lagrenee, M. (2006). "The inhibition of mild steel corrosion in acidic solutions by 2, 5-bis (4-pyridyl)-1, 3, 4-thiadiazole: structure–activity correlation." *Corros. Sci.*, 48(5), 1279–1291.
- Lei, H., Diao, H., Liu, W., Xie, J., Wang, Z. and Feng, L. (2016). "A facile Al(III)-specific fluorescence probe and its application in biological systems." *RSC Adv*, 6(81), 77291–77296.
- Liu, Z., Chong, P.H., Butt, A.N., Skeldon, P. and Thompson, G.E. (2005). "Corrosion mechanism of laser-melted AA 2014 and AA 2024 alloys." *Appl. Surf. Sci.*, 247(1-4), 294–299.

Maia, F., Tedim, J., Bastos, C., Ferreira, M.G.S. and Zheludkevich, M.L. (2013). "Nanocontainer-based corrosion sensing coating." *Nanotechnology*, 24(41), 415502-415511.

Maia, F., Tedim, J., Lisenkov, A.D., Salak, A.N., Zheludkevich, M.L. and Ferreira, M.G.S. (2012). "Silica nanocontainers for active corrosion protection." *Nanoscale*, 4(4), 1287-1298.

Mansfeld, F. and Kendig, M.W. (1988). "Evaluation of anodized aluminum surfaces with electrochemical impedance spectroscopy." *J. Electrochem. Soc.*, 135(4), 828–833.

Mansfeld, F., Tsai, C.H. and Shih, H. (1992). Software for simulation and analysis of electrochemical impedance spectroscopy (EIS) data. *In Computer Modeling in Corrosion*, (ASTM International).

Marcelin, S. and Pébère, N. (2015). "Synergistic effect between 8-hydroxyquinoline and benzotriazole for the corrosion protection of 2024 aluminium alloy: A local electrochemical impedance approach." *Corros. Sci.*, 101, 66–74.

Markley, T.A., Forsyth, M. and Hughes, A.E. (2007). "Corrosion protection of AA2024-T3 using rare earth diphenyl phosphates." *Electrochimica Acta*, 52(12), 4024–4031.

Matter, E.A., Kozhukharov, S., Machkova, M. and Kozhukharov, V. (2012). "Comparison between the inhibition efficiencies of Ce (III) and Ce (IV) ammonium nitrates against corrosion of AA2024 aluminum alloy in solutions of low chloride concentration." *Corros. Sci.*, 62, 22–33.

Miera, M.S.D., Curioni, M., Skeldon, P. and Thompson, G.E. (2008). "Modelling the anodizing behaviour of aluminium alloys in sulphuric acid through alloy analogues." *Corros. Sci.*, 50(12), 3410–3415.

Miera, M.S.D, Curioni, M., Skeldon, P. and Thompson, G.E. (2010). "The behaviour of second phase particles during anodizing of aluminium alloys." *Corros. Sci.*, 52(7), 2489–2497.

Moutarlier, V., Gigandet, M.P., Normand, B. and Pagetti, J. (2005). "EIS characterisation of anodic films formed on 2024 aluminium alloy, in sulphuric acid containing molybdate or permanganate species." *Corros. Sci.*, 47(4), 937–951.

Paussa, L., Andreatta, F., Navarro, N.C.R., Durán, A. and Fedrizzi, L. (2012). "Study of the effect of cerium nitrate on AA2024-T3 by means of electrochemical micro-cell technique." *Electrochimica Acta*, 70, 25-33.

Pearlstein, F. and Agarawala, V.S. (1994). "Trivalent chromium conversion coatings for aluminum." U.S. Patent 5,304,257.

Qafsaoui, W., Kendig, M.W., Perrot, H. and Takenouti, H. (2015). "Effect of 1-pyrrolidine dithiocarbamate on the galvanic coupling resistance of intermetallics – Aluminum matrix during corrosion of AA 2024-T3 in a dilute NaCl." *Corros. Sci.*, 92, 245–255.

Qi, J.T., Hashimoto, T., Walton, J.R., Zhou, X., Skeldon, P. and Thompson, G.E. (2015). "Trivalent chromium conversion coating formation on aluminium." *Surf. Coat. Technol.*, 280, 317–329.

Quinet, M., Neveu, B., Moutarlier, V., Audebert, P. and Ricq, L. (2007). "Corrosion protection of sol–gel coatings doped with an organic corrosion inhibitor: Chloranil." *Prog. Org. Coat.*, 58(1), 46–53.

Raps, D., Hack, T., Wehr, J., Zheludkevich, M.L., Bastos, A., Ferreira, M.G.S. and Nuyken, O. (2009). "Electrochemical study of inhibitor-containing organic–inorganic hybrid coatings on AA2024." *Corros. Sci.*, 51(5), 1012–1021.

Rosero-Navarro, N.C., Pellice, S. A, Duran, A and Aparicio, M. (2008). "Effects of Ce-containing sol-gel coatings reinforced with SiO₂ nanoparticles on the protection of AA2024." *Corros. Sci.*, 50(5), 1283–1291.

Shi, H., Han, E.H., Lamaka, S.V., Zheludkevich, M.L., Liu, F. and Ferreira, M.G.S. (2014). "Cerium cinnamate as an environmentally benign inhibitor pigment for epoxy coatings on AA 2024-T3." *Prog. Org. Coat.*, 77(4), 765–773.

Shi, H., Liu, F. and Han, E. (2010). "Corrosion behaviour of sol–gel coatings doped with cerium salts on 2024-T3 aluminum alloy." *Mater. Chem. Phys.*, 124(1), 291–297.

Shi, H., Wu, L., Wang, J., Liu, F. and Han, E. (2017). "Sub-micrometer mesoporous silica containers for active protective coatings on AA 2024-T3." *Corros. Sci.*, 127, 230–239.

Suay, J.J., Gimenez, E., Rodriguez, T., Habbib, K. and Saura, J.J. (2003). "Characterization of anodized and sealed aluminium by EIS." *Corros. Sci.*, 45(3), 611–624.

Tian, Z., Shi, H., Liu, F., Xu, S. and Han, E.H. (2015). "Progress in Organic Coatings Inhibiting effect of 8-hydroxyquinoline on the corrosion of silane-based sol – gel coatings on AA 2024-T3." *Prog. Org. Coat.*, 82, 81–90.

Tianhui, H., Hongwei, S., Tao, W., Fuchun, L., Shihua, F. and En-Hou, H. (2015). "Cerium tartrate as a corrosion inhibitor for AA 2024-T3." *Corros. Sci.*, 95, 152–161.

Torrescano-Alvarez, J.M., Curioni, M. and Skeldon, P. (2018). "Effects of oxygen evolution on the voltage and film morphology during galvanostatic anodizing of AA 2024-T3 aluminium alloy in sulphuric acid at –2 and 24 °C." *Electrochimica Acta*, 275, 172–181.

Twite, R.L. and Bierwagen, G.P. (1998). "Review of alternatives to chromate for corrosion protection of aluminum aerospace alloys." *Prog. Org. Coat.*, 33(2), 91–100.

Visser, P., Liu, Y., Zhou, X., Hashimoto, T., Thompson, G.E., Lyon, S.B., Ven, L.G.J. van der, Mol, A.J.M.C. and Terryn, H. A (2015). "The corrosion protection of AA2024-T3 aluminium alloy by leaching of lithium-containing salts from organic coatings." *Faraday Discuss.*, 180, 511–526.

Visser, P., Terryn, H. and Mol, J.M.C. (2018). "On the importance of irreversibility of corrosion inhibitors for active coating protection of AA2024-T3." *Corros. Sci.*, 140, 272-285.

Wang, R., Wang, L., He, C., Lu, M. and Sun, L. (2018). "Studies on the sealing processes of corrosion resistant coatings formed on 2024 aluminium alloy with tartaric-sulfuric anodizing." *Surf. Coat. Technol.*, 360, 369-375.

Wei, H., Wang, Y., Guo, J., Shen, N.Z., Jiang, D., Zhang, X., Yan, X., Zhu, J., Wang, Q., Shao, L., Lin, H., Wei, S. and Guo, Z. (2015). "Advanced micro/nanocapsules for self-healing smart anticorrosion coatings." *J Mater Chem A*, 3(2), 469–480.

Williams, G., Coleman, A.J. and McMurray, H.N. (2010). "Inhibition of Aluminium Alloy AA2024-T3 pitting corrosion by copper complexing compounds." *Electrochimica Acta*, 55(20), 5947–5958.

Yasakau, K.A., Tedim, J., Zheludkevich, M.L., Drumm, R., Shem, M., Wittmar, M., Veith, M. and Ferreira, M.G.S. (2012). "Cerium molybdate nanowires for active corrosion protection of aluminium alloys." *Corros. Sci.*, 58, 41–51.

Yasakau, K.A., Zheludkevich, M.L., Karavai, O.V. and Ferreira, M.G.S. (2008). "Influence of inhibitor addition on the corrosion protection performance of sol-gel coatings on AA2024." *Prog. Org. Coat.*, 63(3), 352–361.

Yasakau, K.A., Zheludkevich, M.L., Lamaka, S.V. and Ferreira, M.G.S. (2006). "Mechanism of Corrosion Inhibition of AA2024 by Rare-Earth Compounds." *J. Phys. Chem. B*, 110(11), 5515–5528.

Yoganandan, G., Balaraju, J.N., Low, C.H., Qi, G. and Chen, Z. (2016). "Electrochemical and long term corrosion behavior of Mn and Mo oxyanions sealed anodic oxide surface developed on aerospace aluminum alloy (AA2024)." *Surf. Coat. Technol.*, 288, 115–125.

Yu, X. and Cao, C. (2003). "Electrochemical study of the corrosion behavior of Ce sealing of anodized 2024 aluminum alloy." *Thin Solid Films*, 423(2), 252–256.

Zhang, H., Yao, G., Wang, S., Liu, Y. and Luo, H. (2008). "A chrome-free conversion coating for magnesium–lithium alloy by a phosphate–permanganate solution." *Surf. Coat. Technol.*, 202(9), 1825–1830.

Zhang, X., Hashimoto, T., Lindsay, J. and Zhou, X. (2016). "Investigation of the de-alloying behaviour of θ -phase (Al₂Cu) in AA2024-T351 aluminium alloy." *Corros. Sci.*, 108, 85–93.

Zheludkevich, M.L., Serra, R., Montemor, M.F., Yasakau, K., Salvado, I.M. and Ferreira, M.G.S. (2005). "Nanostructured sol–gel coatings doped with cerium nitrate as pre-treatments for AA2024-T3: corrosion protection performance." *Electrochimica Acta*, 51(2), 208–217.

Zheludkevich, M.L., Yasakau, K.A., Poznyak, S.K. and Ferreira, M.G.S. (2005). "Triazole and thiazole derivatives as corrosion inhibitors for AA2024 aluminium alloy." *Corros. Sci.*, 47(12), 3368–3383.

RESEARCH PUBLICATIONS**(a) In journals**

1. Prakashaiah, B.G., Vinayakumara, D., Pandith, A., Shetty, A.N., and Amitha Rani, B.E. (2018), "Corrosion inhibition of 2024-T3 aluminum alloy in 3.5 % NaCl by thiosemicarbazone derivatives" *Corros. Sci.* 136 326-338.
2. Prakashaiah. B.G., Shetty, A.N. and Amitha Rani, B.E. (2018) "2-(4-(Diethylamino)-2-hydroxybenzylidene) hydrazinecarboamide as Corrosion Inhibitor on AA2024-T3 Aluminum Alloy in 0.5 M Hydrochloric Acid Solution." *Surface Engineering and Applied Electrochemistry*, 54 (3) 286-296.
3. Prakashaiah. B.G., Shetty, A.N. and Amitha Rani, B.E. (2019) "Improvement of anticorrosion properties of epoxy primer coating on aluminum alloy 2024-T3 by thiosemicarbazone derivatives." *JOM*, 1-11.
4. Prakashaiah, B.G., Shetty, A.N. and Amitha Rani, B.E. "Enhancement of anticorrosion properties of epoxy based primer coating by bis[[3,4-dihydroxyphenylmethylene]carbonothioicdihydrazide] on AA2024-T3 alloy" *Journal Coatings Technology and Research*. (under revision- 4 Oct 2018).
5. Prakashaiah. B.G., Shetty, A.N. and Amitha Rani, B.E. "(E)-2-(3,4-Dihydroxybenzylidene)hydrazinecarbothioamide-A dual functionality molecule for corrosion detection and inhibition on aluminum alloy AA2024-T3 in aqueous sodium chloride medium" *JOM*, (under review- 17 Jun 2019)

(b) International conference presentation

1. Prakashaiah, B.G, Shetty, A.N and Amitha Rani, B.E "Anticorrosion potential of thiosemicarbazone derivative on AA2024-T3 aluminum alloy in 0.5 M hydrochloric acid", IWCEM 2017, Jaipur, India, 3-5 June 2017.
2. Prakashaiah, B. G, Shetty, A.N and Amitha Rani, B.E "Anticorrosion potential of thiosemicarbazone derivative on AA2024-T3 aluminum alloy in 3.5 % NaCl solution", ICONEST 2017, Bangalore, India, 10-12 August, 2017.

Mr. Prakashaiah B G

Personal data

First name Prakashaiah
Family name Basavanalu Gowdru
Date of birth June 1st 1989
Nationality Indian
Email bgprakash97@gmail.com
Address S/O Shivamurthaiah B G, Basavanalu (P), Davanagere (D)(T),
Karnataka
Phone No 9901729710, 7019263621

Education

2013–2019 (Ph.D). **Chemistry**, *Dept. of Chemistry, NITK, Suratkal, Mangaluru.*
2009–2011 **M.Sc. Industrial Chemistry**, *Dept. of Industrial Chemistry, Kuvempu University, Shankaraghatta, India.* 6th rank
First Class with Distinction
2006–2009 **B.Sc. (Biotechnology + Botany + Chemistry)**,
Sahyadri Science College [Autonomous], Shimoga.
First Class with Distinction

Scholarships and awards

August 2013 Junior Research Fellowship –CSIR,
August 2015 Senior research Fellowship
2014 Best paper cash award –IWCEM, Jaipur.

Doctoral thesis

Title Development of corrosion resistant coatings for aerospace aluminum alloy
AA2024-T3

Experience

2017 – present Project Assistant, SED, NAL, Bengaluru, Karnataka, India.

RESEARCH PUBLICATIONS

(a) In journals

1. **Prakashaiah. B. G**, Vinay Kumara, D Anup Pandith, A. Nityananda Shetty and B.E. Amitha Rani, (2018) "Corrosion inhibition of 2024-T3 aluminum alloy in 3.5 % NaCl by thiosemicarbazone derivatives." *Corrosion Science*, 136, 326-338
2. **Prakashaiah. B. G**, A. Nityananda Shetty and B.E. Amitha Rani, (2018), "2-(4-(Diethylamino)-2-hydroxybenzylidene) hydrazine carboamide as Corrosion Inhibitor on AA2024-T3 Aluminum Alloy in 0.5 M Hydrochloric Acid Solution". *Surface Engineering and Applied Electrochemistry*. 54, 286-296.
3. **Prakashaiah. B. G**, A. Nityananda Shetty and B.E. Amitha Rani (2019), "Improvement of anticorrosion properties of epoxy primer coating on aluminum alloy 2024-T3 by thiosemicarbazone derivatives." *JOM*, 1-11.
4. K. Nishchitha, M. K. Deepa, **B. G. Prakashaiah**, J. N. Balaraju and B. E. Amitha rani. (2018). "Effect of Surface Treatment on Bio-Corrosion in Aluminium Alloy 2024-T3." *Journal of Materials Engineering and Performance*, 27, 5778-5787.
5. A Viswanathan, **B G Prakashaiah**, V Subburaj, and A Nityananda Shetty (2019). "High energy reduced graphene oxide/vanadium pentoxide/polyaniline hybrid supercapacitor for power backup and switched capacitors." *Journal of Colloid and Interface Science*, 545, 82-93.
6. **Prakashaiah. B. G**, A. Nityananda Shetty and B.E. Amitha Rani, "(E)-2-(3,4-Dihydroxybenzylidene)hydrazinecarbothioamide-A dual functionality molecule for corrosion detection and inhibition on aluminum alloy AA2024-T3 in aqueous sodium chloride medium" *Materials Chemistry and Physics*. (under review)
7. **Prakashaiah. B. G**, A. Nityananda Shetty and B.E. Amitha Rani, "Enhancement of anticorrosion properties of epoxy based primer coating by

bis[[3,4-dihydroxyphenylmethylene]carbonothioicdihydrazide] on AA2024-T3 alloy" *Surface and Coatings Technology*. (under revision)

International conference presentations

1. **Prakashaiah. B. G**, B.E. Amitha Rani, Quick detection of incipient corrosion in AA2024-T3, IWCEM 2014, Pune, India, 24-26 May 2014
2. **Prakashaiah. B. G**, B.E. Amitha Rani, Evaluation of synthesised cerium molybdate nanowires for corrosion protection of aluminium alloy AA2024-T3, CORCON 2016, New Delhi, India, 18-21 September, 2016.
3. **Prakashaiah. B. G**, A. Nityananda Shetty and B.E. Amitha Rani, Anticorrosion potential of thiosemicarbazone derivative on AA2024-T3 aluminium alloy in 0.5 M hydrochloric acid, IWCEM 2017, Jaipur, India, 3-5 June 2017.
4. **Prakashaiah. B. G**, A. Nityananda Shetty and B.E. Amitha Rani, Anticorrosion potential of thiosemicarbazone derivative on AA2024-T3 aluminium alloy in 3.5 % NaCl solution, ICONEST 2017, Bangalore, India, 10-12 August, 2017